UNIVERSITY of CALIFORNIA
Santa Barbara

Failure of Ceramic Composites in Non-Uniform Stress Fields

A Dissertation submitted in partial satisfaction of the
requirements for the degree

Doctor of Philosophy
in
Materials

by

Varun P. Rajan

Committee in charge:

Professor Frank W. Zok, Chair
Professor Carlos G. Levi
Professor Matthew R. Begley
Professor Robert M. McMeeking

March 2014

The dissertation of Varun P. Rajan is approved.

Professor Carlos G. Levi

Professor Matthew R. Begley

Professor Robert M. McMeeking

Professor Frank W. Zok, Committee Chair

February 2014

Failure of Ceramic Composites in Non-Uniform Stress Fields *for Mom, Dad, and my friends.*

Acknowledgements

My success at UCSB can be attributed in large part to my relationship with my advisor, Frank Zok. He has inspired me to think about interesting and difficult problems, given me the free rein to tackle them, and provided the expertise needed to refine my ideas into a coherent and publishable form. Conversations with other faculty, including Matthew Begley and John Hutchinson, have also been helpful in resolving the knotty problems that inevitably arise when doing theoretical work. I would also like to thank members of my committee for providing useful advice on post-doctoral opportunities and scholarships. Financial support, from the National Defense Science and Engineering Graduate Fellowship and from the Pratt & Whitney Center of Excellence at the University of California, Santa Barbara, is also greatly acknowledged.

My colleagues in the Zok, Levi, Begley, and McMeeking groups have been extraordinarily helpful. Theory-oriented researchers, such as myself, benefit greatly from working with talented experimentalists, and I couldn't have asked for better partners than John Shaw and Michael Rossol. Nell Gamble, Brett Compton, and Chris Hammetter should also be thanked for their willingness to assist with ABAQUS-related problems, small and large. I acknowledge anyone (in particular, Rajlakshmi Purkayastha and Nick Bedi) willing to listen to my rants and whining about graduate school or life in general. I am also deeply grateful to Nicole Wolfson, who has been both my most annoying friend and my most treasured.

Finally, I would like to thank my parents, Vanitha and Subramaniam Rajan, for their constant love and support.

Curriculum Vitæ

Varun P. Rajan

Education

2006–2009	B.S. in Mechanical Engineering Rice University Houston, TX
2010–2014	Ph.D. in Materials University of California, Santa Barbara Santa Barbara, CA

Publications

V. P. Rajan, M. N. Rossol, and F. W. Zok. Optimization of Digital Image Correlation for High-Resolution Strain Mapping of Ceramic Composites. *Experimental Mechanics*, 52(9):1407–1421, 2012.

V. P. Rajan and F. W. Zok. Effects of Non-Uniform Strains on Tensile Fracture of Fiber-Reinforced Ceramic Composites. *Journal of the Mechanics and Physics of Solids*, 60(12):2003–2018, 2012.

V. P. Rajan and F. W. Zok. Remediation of a Constitutive Model for Ceramic Composite Laminates. *Composites Part A*, 52:80–88, 2013.

V. P. Rajan and F. W. Zok. Stress Distributions in Bluntly-Notched Ceramic Composite Laminates. *Composites Part A*, 60:15–23, 2014.

J. H. Shaw, V. P. Rajan, M. Blacklock, and F. W. Zok. Towards a Virtual Test for C/SiC Textile Composites: Calibration of Thermoelastic Tow Properties. *In press, Journal of the American Ceramic Society*.

B. N. Cox, H. A. Bale, M. Begley, M. Blacklock, B. C. Do, T. Fast, M. Naderi, M. Novak, V. P. Rajan, R. G. Rinaldi, R. O. Ritchie, M. Rossol, J. H. Shaw, O. Sudre, Q. D. Yang, F. Zok, and D. B. Marshall. Stochastic Virtual Tests for High Temperature Ceramic Matrix Composites. *In press, Annual Review of Materials Research*.

V. P. Rajan and F. W. Zok. Matrix Cracking of Fiber-Reinforced Ceramic Composites in Shear. *Submitted, Journal of the Mechanics and Physics of Solids*.

V. P. Rajan, J. H. Shaw, and F. W. Zok. A New Elastic-Plastic Constitutive Model for Ceramic Composite Laminates. *Submitted, Composites Part A*.

Y. Swolfs, R. M. McMeeking, V. P. Rajan, F. W. Zok, L. Gorbatikh, and I. Verpoest. Global Load Sharing Model for Unidirectional Hybrid Fibre-Reinforced Composites. *In preparation*.

M. N. Rossol, V. P. Rajan, and F. W. Zok. Effect of Woven Architecture on Damage Initiation and Evolution in Ceramic Composites. *In preparation*.

J. H. Shaw, V. P. Rajan, and F. W. Zok. Failure of Woven Ceramic Composites in Biaxial and Uniaxial Flexure *In preparation*.

M. N. Rossol, V. P. Rajan, and F. W. Zok. Notch Sensitivity of Woven Ceramic Composites. *In preparation*.

Abstract

Failure of Ceramic Composites in Non-Uniform Stress Fields

by

Varun P. Rajan

Continuous-fiber ceramic matrix composites (CMCs) are of interest as hot-section components in gas turbine engines due to their refractoriness and low density relative to metallic alloys. In service, CMCs will be subjected to spatially inhomogeneous temperature and stress fields. Robust tools that enable prediction of deformation and fracture under these conditions are therefore required for component design and analysis. Such tools are presently lacking. The present work helps to address this deficiency by developing models for CMC mechanical behavior at two length scales: that of the constituents and that of the components. Problems of interest are further divided into two categories: '1-D loadings,' in which the stresses are aligned with the fiber axes, and '2-D loadings,' in which the stress state is more general.

For the former class of problems, the major outstanding issue is material fracture, not deformation. A fracture criterion based on the attainment of a global load maximum is developed, which yields results for pure bending of CMCs in reasonable agreement with available experimental data. For the latter class of problems, the understanding of both the micro-scale and macro-scale behavior is relatively immature. An approach based upon analysis of a unit cell (a single fiber surrounded by a matrix jacket) is pursued. Stress fields in the constituents of the composite are estimated using analytical models, the accuracy of which is confirmed using finite element analysis. As part of a fracture mechanics analysis, these fields enable estimation of the steady-state matrix cracking stress for arbitrary in-plane loading of a unidirectional ply. While insightful at the micro-scale, unit cell models are difficult to extend to coarser scales. Instead, material deformation is typically predicted using phenomenological constitutive models. One such model for CMC laminates is investigated and found to predict material instability where none should exist. Remedies to the model to correct this deficiency are proposed; the remediated model is subsequently utilized in conjunction with an analytical model to probe stress fields adjacent to holes and notches in CMC panels. However, even the revised model is incapable of capturing the range of experimental behavior reported for CMCs with both stiff and compliant matrices. To ameliorate this deficiency, a new elastic-plastic constitutive model is developed. It extends the deformation theory of plasticity from metals to CMCs, and its predictions of near-notch strain fields in an open-hole tension test compare favorably to strains measured using digital image correlation. Based on these developments, future experimental and modeling work is proposed. With respect to the latter, cohesive interface simulations seem particularly suited for capturing multiple interacting damage mechanisms at multiple length scales in a physically sensible manner. In principle, they can function as virtual tests, guiding both engineering design and materials development.

Contents

List of Figures

List of Tables

Chapter 1

Introduction

1.1 Background

Composites comprising ceramic matrices, continuous ceramic fibers, and weak fiber-matrix interfaces have been proposed as materials for use in gas turbines in military and commercial aircraft engines and land-based power generation systems. The superior high-temperature capability of ceramic matrix composites (CMCs) relative to metals enables turbine engines to operate at higher temperatures, thereby increasing their thermodynamic efficiency. The resulting fuel savings can be enormous. For instance, in integrated gasification combined-cycle power plants, a mere 30 °C increase in the firing temperature of the gas turbine can increase the combined cycle efficiency by roughly

1 % (Eldrid et al., 2001). CMCs have the potential to increase firing temperatures by 100–200 °C or more, saving millions of dollars in fuel over the lifetime of the turbine. In addition to enabling higher operating temperatures, CMCs have the potential for significant weight reductions due to their low density: an attribute particularly important in aeroengine applications.

After almost three decades of development, CMCs are now beginning to be integrated into commercial aircraft engines (Figure 1.1). In General Electric's Passport 20 engine, an oxide-oxide CMC is being used to replace metallic components in the rear of the engine, reducing the mass of each engine by 20 kg (Epstein, 2013). The engine in the Boeing 787 Dreamliner will use a similar material for exhaust nozzles (Wood, 2013). Non-oxide CMCs will also be incorporated into gas turbine engines in the upcoming years: General Electric's LEAP Engine is expected to include a high-pressure turbine shroud made from a SiC/SiC composite (Wood, 2013). Looking further into the future, CMCs are also being targeted for use in turbine blades and vanes, where the savings arising from their lower density and refractoriness are potentially even larger.

In the aforementioned applications, CMC components are subjected to complex thermal and/or mechanical loads. Because the resulting stress fields are multidirectional, fiber architectures must also be multidirectional (the strength of unidirectional CMCs subjected to transverse loads being very poor). Two types of architectures are of particular interest: [0°/90°] cross-ply laminates and [0°/±45°/90°] quasi-isotropic laminates. Both types of composite can be manufactured by laying up either unidirectional plies or 2-D woven fabric. Typically, the lay-ups are both symmetric and balanced—i.e. involving equal numbers of plies corresponding to each angle of reinforcement. The present work focuses primarily on cross-ply materials and their constituent unidirectional plies or tows, although extension of the results to other fiber architectures should, in principle, be possible.

Design of CMC components with multidirectional fiber architectures that experience spatially inhomogeneous stress and temperature fields is a significant challenge. Although the elastic behavior of a CMC can be readily predicted from laminate theory, prediction of inelastic behavior is much more difficult. Not only are several (possibly interacting) damage mechanisms present, but models for these damage mechanisms must span multiple length scales: from that of the constituents (μm) to that of the components (cm) (see Figure 1.2). Furthermore, stresses that give rise to damage are not necessarily aligned with the fiber axes.

With respect to loadings, it is conceptually useful to divide the problems of interest into two classes, based on the complexity of the stress state. In the first class, termed '1-D problems,' the principal stresses are aligned with the fiber axes (at 0° and 90°). 1-D problems have received a great deal of study in the literature, both experimental (Beyerle et al., 1992a,b; Marshall and Evans, 1985; McNulty and Zok, 1997; Prewo, 1986; Jansson and Leckie, 1992) and theoretical (Zok and Spearing, 1992; Spearing and Zok, 1993; Curtin, 1993; He et al., 1994; Aveston et al., 1971; Marshall et al., 1985; Budiansky et al., 1986; Curtin, 1991a; Neumeister, 1993a; Hui et al., 1995; Zhou and Curtin, 1995; Landis et al., 2000; Hild et al., 1994). In the second class, termed '2-D problems,' stresses are oriented at an arbitrary angle to the fiber axes. Both the on-axis (tensile) and off-axis (shear) responses of the CMC govern the macroscopic behavior. Relatively little experimental work (Brøndsted et al., 1994; Cady et al., 1995a; Turner et al., 1995), and essentially no theoretical work, has been conducted on this class of problems.

1.2 1-D loadings

The 1-D problem describes many loading scenarios of practical interest: notably, uniaxial tension and in-plane and through-thickness flexure. Particular attention has been paid in the literature to the simplest possible system: a unidirectional CMC subjected to uniaxial tension (Figure 1.3(a)). This system provides a useful starting point because it exhibits many of the damage mechanisms that govern CMC inelasticity: matrix cracking, interfacial slip, and fiber fragmentation. The current understanding of its mechanical behavior is as follows.

- Initially, the composite responds elastically with a modulus well described by the rule of mixtures: $E_c = V_f E_f + V_m E_m$, where V is volume fraction, E is Young's modulus, and the subscripts f and m refer to fiber and matrix, respectively.

- At a critical stress, matrix cracks form and propagate long distances transverse to the tensile axis. The cracks deflect at the (weak) fiber-matrix interfaces, causing slip of the fibers relative to the matrix and bridging of the cracks by intact fibers. (If the fiber-matrix interfaces were strong and tough, such cracks would cause catastrophic fracture.) The stress needed to grow a *steady-state*, fully-bridged matrix crack was derived from energy arguments in the seminal paper of Aveston et al. (1971). Their model was later extended by Marshall et al. (1985), Budiansky et al. (1986), and Marshall and Cox (1988) to account for effects of non-zero interface debond toughness and residual stress. Upon further loading, the density of matrix cracks increases and eventually reaches saturation with an average spacing of, typically, (5–20)d, where d is the fiber diameter. The mechanics of the interactions between neighboring matrix cracks were addressed by Zok and Spearing (1992). After crack saturation, the matrix bears no additional load and the composite tangent modulus approaches that of the fibers alone ($\mathrm{d}\sigma/\mathrm{d}\epsilon \approx V_f E_f$).

- Additional non-linearity is obtained once the fibers begin to break. The composite strength is the stress required to rupture the fiber bundle. Exact solutions for the bundle fragmentation in the case where the fibers are frictionally coupled to a cracked matrix were developed by Hui et al. (1995) and useful approximations were derived by Curtin (1991b).

Essentially the same failure mechanisms are operative in cross-ply laminates subjected to uniaxial tension (Figure 1.3(b)) and hence similar mechanics analyses can be employed to describe the composite response. But here two additional features arise. First, tensile cracking of the *transverse plies* is usually the first inelastic event. Once the length of a transverse ply crack exceeds the ply thickness, the crack grows by 'tunneling' between adjacent axial plies under steady-state conditions (Beyerle et al., 1992b; Xia et al., 1993). Furthermore, multiple cracks are formed in each ply, eventually saturating when their spacing becomes comparable to the ply thickness. Second, at higher stresses, the cracks penetrate the axial plies. Because the segments of the cracks within the transverse plies are unbridged, the stress needed for full penetration into the axial plies is lower than the steady-state matrix cracking stress in unidirectional materials (adjusting the stress to account for the reduced fraction of axial plies) (Xia and Hutchinson, 1994). The fiber fragmentation process that controls ultimate strength is largely unaffected by the presence of the transverse plies, apart from their effects on the volume fraction of fibers aligned with the loading direction (Beyerle et al., 1992b).

To summarize, sophisticated models exist for the mechanical behavior of unidirectional and cross-ply composites in uniform uniaxial tension, which is the most basic type of '1-D problem.' However, few studies have modeled effects of *non-uniform strains* in 1-D problems. These arise in many cases of practical interest: for instance, in flexure or when temperature gradients are present. The experimental evidence suggests that there are two distinct effects of non-uniform strains.

First, inelastic strain associated with matrix cracking and fiber fragmentation leads to *stress re-distribution* (Cady et al., 1995a; McNulty et al., 1999). In the case of bending of a rectangular beam, for instance, inelasticity leads to a non-linear stress distribution and a progressive shift in the neutral axis from the beam center towards the compressive face. Even making the conservative assumption that failure occurs upon attainment of a critical tensile strain, the predicted nominal bending strength (calculated on the basis of elastic analysis) exceeds the uniaxial tensile strength by a large margin (Beyerle et al., 1992a; Marshall and Evans, 1985; McNulty and Zok, 1997). Indeed, experimental measurements show that the bending strengths of typical CMCs are about 50–120 % greater than their respective tensile strengths (Beyerle et al., 1992a; Marshall and Evans, 1985; McNulty and Zok, 1997; Prewo, 1986).

A second effect (not broadly recognized) is manifested as a disparity between the peak tensile strain attained in pure bending and the failure strain in uniaxial tension. Typical data for one CMC, investigated by McNulty and Zok (1997), is shown in Figure 1.5; here the failure strain in bending is about 50 % greater than that in tension. Yet higher values of tensile strains have been measured in the vicinity of notches or holes in tensile coupons of the same CMC (McNulty et al., 1999). Similar trends have been reported for fiber-reinforced metal-matrix composites. For instance, in SiC-fiber titanium-matrix systems, the peak tensile strains attained in bending exceed that the uniaxial tensile fracture strain by more than 60 % (Ramamurty, 2004). These results demonstrate that the tensile strain for fracture of fiber-reinforced composites is not unique and thus models based on a critical strain criterion are likely to underestimate their full potential.

Therefore, although the constitutive description of *deformation* in 1-D problems can be extended straightforwardly from uniaxial tension to the general case (of non-uniform strains), the *fracture* criterion is not so readily extended. The critical strain criterion is inadequate, and another fracture criterion must be employed. One such criterion, which yields predictions in markedly better agreement with experimental data, is investigated in Chapter 2.

1.3 2-D loadings

Significantly less attention has been devoted to 2-D loadings, wherein the stresses are not aligned with the fiber axes. Predicting deformation and fracture in these loadings requires that the off-axis response of the composite, as manifested in its 45° tensile and shear behavior, be accurately captured.

Once again, it is useful to review the experimental evidence (see Figure 1.4). Studies of cross-ply laminates in shear (Brøndsted et al., 1994; Cady et al., 1995a; Turner et al., 1995) have shown that the principal damage mechanism involves matrix cracking at approximately 45° to the fibers, i.e. perpendicular to the direction of maximum principal stress. As in tension, the cracks are initially fully bridged by intact fibers and propagate long distances without catastrophic fracture. The average crack spacing at saturation is approximately (10–20)d. For cross-ply laminates with dense matrices, typical values of matrix cracking stress in shear are comparable to those in tension. (The cracking stress in tension for a *unidirectional* material with the same fiber volume fraction tends to be significantly greater, for the reasons mentioned previously.) In shear, the matrix cracking stress increases with the matrix stiffness. For the specific example of SiC/CAS (Brøndsted et al., 1994), matrix cracking ultimately saturates at a strain of roughly 1 %[1]: only slightly below the corresponding fracture strain. This observation suggests the absence of a fiber-dominated regime such as that observed in uniaxial tension. For cross-ply laminates, failure strains in shear are somewhat larger than those in tension and are inversely related to the matrix stiffness. Brøndsted et al. (1994) attempted to explain the latter observation by considering local bending of fibers at matrix cracks, although a rigorous mechanistic understanding of the phenomenon was lacking in that work.

While the experimental results reveal intriguing similarities (and notable differences) between the tensile and shear responses of cross-ply laminates, no mechanistic model yet exists for predicting the initiation and evolution of damage in 2-D problems. The cracking stress appears to be the critical quantity governing inelasticity in shear loading (and in tension at 45° to the fibers), since the composite exhibits little hardening thereafter. In Chapter 3, a model for steady-state cracking in 2-D problems is developed, assuming that the fibers and matrix are initially unbonded from one another. The model yields a result analogous to that of Aveston et al. (1971) and Budiansky et al. (1986) for on-axis loading.

---

[1] All shear strains referred to herein are *engineering* shear strains.

1.4 Component-level analysis

The previous sections have emphasized micromechanics-based models that relate the properties of the constituents to the overall response of the composite. These models are useful because they represent damage in a physically realistic way: i.e., by explicitly modeling matrix cracks or fiber breaks. They necessarily operate at the length scale of the constituents of the composite (see Figure 1.2). However, such models are difficult to extend to coarser length scales. The principal problem is that explicit representation of damage (matrix crack formation in transverse plies, extension of cracks into axial plies, debonding/slip, fiber fragmentation, etc.) is not possible at the coarse scale. Instead, the inelasticity due to damage must be 'smeared out' over a volume element representative of the microstructure of the CMC. While significant progress on this front has been made for on-axis stressing of CMCs (see, for instance, the constitutive law of Curtin (1991a)), comparable work for off-axis stressing has yet to be conducted.

The latter is essential for prediction of, for instance, stresses arising in CMC plates with geometric features such as holes or notches. Many experimental studies have demonstrated that CMCs exhibit some degree of notch insensitivity (McNulty et al., 1999; Cady et al., 1995b; Genin and Hutchinson, 1997; Heredia et al., 1994; Levi et al., 1998; Mackin et al., 1995, 1996; Kramb et al., 1999; Mall et al., 1994): a desirable feature for component design. However, the theoretical understanding of notch insensitivity in CMCs remains immature. It must arise from near-notch stress redistribution, which, in turn, is governed by the interplay between inelasticity arising from (on-axis) tension and (off-axis) shear (Evans et al., 1994). Modeling near-notch stress redistribution and predicting notch insensitivity in CMC laminates thus requires a *component-level* constitutive model that incorporates on-axis and off-axis inelasticity.

Given the previous discussion, it should be unsurprising that existing constitutive models for this task have been phenomenological, not micromechanical, in nature (Cox and Zok, 1996). That is, the models take as inputs not the constituent properties, but instead other quantities, such as macroscopic stress-strain curves. One class of models relies on concepts from continuum damage mechanics (Talreja, 1991; Camus, 2000; Chaboche and Maire, 2001). The state of damage within the composite is assumed to be described by internal damage variables that can be scalars, vectors, or tensors. As these damage variables evolve with the applied load, the stiffness of the composite is degraded. The damage evolution laws are calibrated using experimental data. In some models, such as that of Talreja (1991), the damage variables are measurable quantities, such as crack density; in other models, such as that of Camus (2000), the damage variables are not measurable and must instead be inferred from macroscopic stress-strain data. The fundamental tradeoff in all such models is between the sophistication of the representation of damage and the amount of experimental data needed to calibrate the model. For instance, the model of Talreja (1991) requires evolution laws for four different damage tensors that represent crack densities, debond lengths, etc. A very extensive experimental program is thus required to calibrate the model for general multiaxial loading. Despite the complexity of the calibration procedure, it remains unclear whether the *predictive* capability of such models is actually enhanced by utilizing such a large number of internal variables.

A second modeling approach dispenses with internal damage variables, and instead assumes that the degradation of the composite stiffness can be related to macroscopic stress-strain functions from simple mechanical tests, such as uniaxial tension and shear. Typically, it also assumes proportional loading. This approach, in theory, should yield a mathematically simple model that can be calibrated with little experimental data, since there are far fewer 'fitting constants' than in damage mechanics models. Models of this type, developed mainly for use with polymer matrix composites, have been presented by Hahn (1973); Jones (1977); Sandhu (1976). An attempt to extend the approach to CMC laminates was made by Genin and Hutchinson (1997). However, as demonstrated in Chapter 4, calculations employing the Genin-Hutchinson

(GH) model frequently suffer from numerical convergence problems. Furthermore, for reasons elaborated upon in Chapter 6, even after modifications to remedy these problems, the modified GH model suffers from an additional deficiency: notably, it presupposes a particular form of the yield/cracking surface that is approximately satisfied by certain systems (notably, CMCs with relatively stiff matrices), but not others. A new approach for constitutive modeling of CMCs that enables a broader range of material behavior to be captured is introduced in Chapter 6.

1.5 Objectives and dissertation outline

The overarching goal of this work is to advance the understanding of the mechanics of CMC deformation and fracture and to develop tools that can aid in CMC component design and analysis. Two schemes for categorizing problems in CMC mechanics underpin this body of work. The first (introduced earlier) is based on the complexity of the stress state: 1-D vs. 2-D. Given the extra level of complexity inherent to 2-D problems, it is not surprising that the field of CMC micromechanics for off-axis loading is essentially barren. The second key distinction concerns the scales at which the phenomena are described and analyzed. These are categorized as being either at the ‘micro-scale,’ i.e., tens to hundreds of μm, or at the ‘macro-scale,’ typically greater than 1 mm.

The dissertation is organized in the following way. Chapters 2 and 3 deal with two problems at the micro-scale. The first, in Chapter 2, addresses the issue of the failure condition in CMCs when non-uniform strains are present. A constitutive model based on the analysis of fiber fragmentation and a failure criterion based on the attainment of a global load maximum is used to examine the effects of non-uniformity in strain on fracture. Chapter 3 focuses on steady-state matrix cracking in CMCs under pure shear and mixed shear/tension loadings. Although this work represents an important step forward, much work remains to be done in the area of micromechanics of CMCs (some of which is discussed in Chapter 7). This includes the development of a modeling framework that integrates the constitutive descriptions that arise from micromechanical models for on- and off-axis loading with constitutive models for analyses at the component scale.

Chapters 4–6 address phenomenological constitutive models at the macro-scale. In Chapter 4, the origin of the the numerical stability problems in calculations employing the Genin-Hutchinson model is identified. Accordingly, modifications are made to the model to remedy its physical and numerical deficiencies. The resulting modified GH model is used in Chapter 5 to investigate near-notch stress distributions in laminates subjected to (global) uniaxial tension. An analytical model is also developed and compared with finite element predictions. The analytical model is shown to capture the stress distributions with excellent accuracy. Its main advantage over numerical simulations is that it enables rapid calculation of stress concentration factors, inelastic zone sizes, and possibly even material fracture (associated with the onset of fiber bundle rupture and localization of deformation). Then, in Chapter 6, a new approach for constitutive modeling of CMCs is introduced. It allows a broader range of material behavior to be captured. The efficacy of this framework is demonstrated using a case study: an open-hole tension test. The model is validated by comparing predicted strain fields from finite element simulations with those measured experimentally by digital image correlation.

Finally, Chapter 7 summarizes the key findings of the work and identifies opportunities for future research, in both the experimental and modeling arenas. Virtual tests of CMCs, based on cohesive element simulations of representative volume elements, are identified as an important area for future research. They enable multiple interacting inelastic mechanisms to be simulated in a physically realistic manner, without recourse to the simplifying assumptions (global load sharing, steady-state cracking, etc.) commonly employed in the CMC mechanics literature.

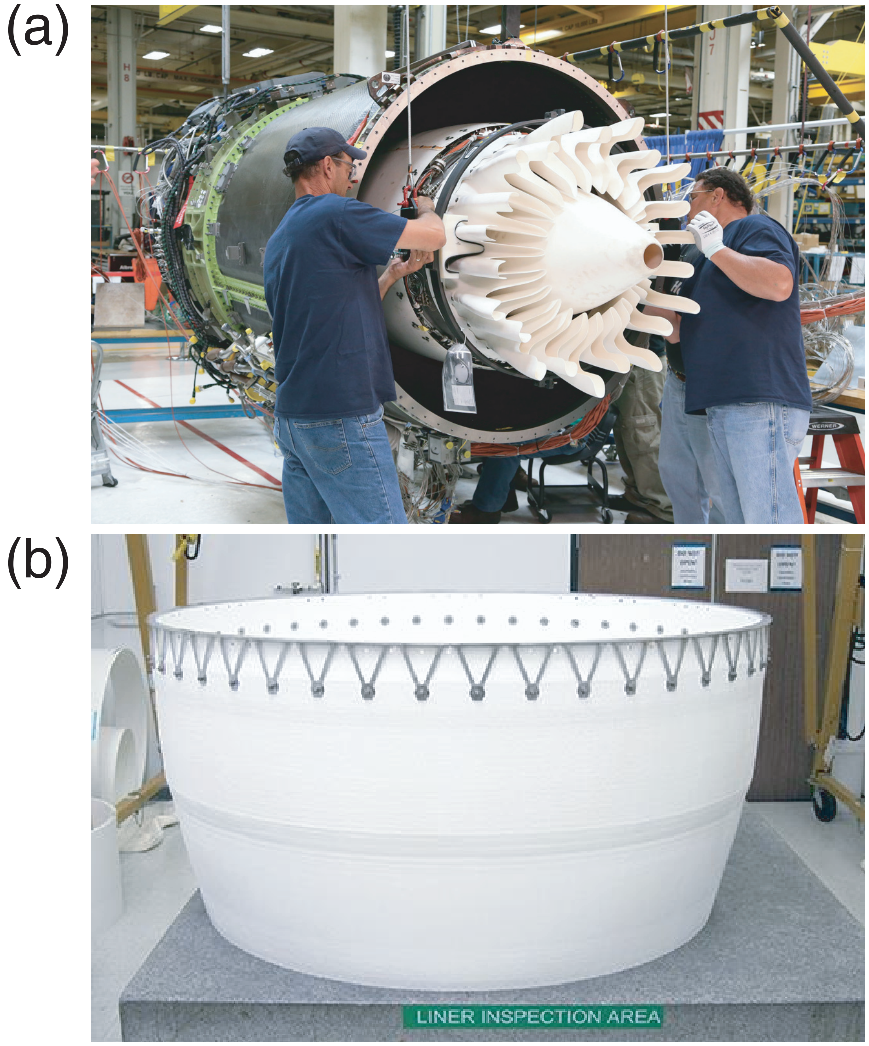

Figure 1.1: Examples of CMCs in commercial engines: (a) all-oxide CMC for mixer and center body assemblies in General Electric Passport 20 engine (Epstein, 2013); (b) all-oxide CMC for exhaust nozzle in the Boeing 787 Dreamliner engine (Wood, 2013).

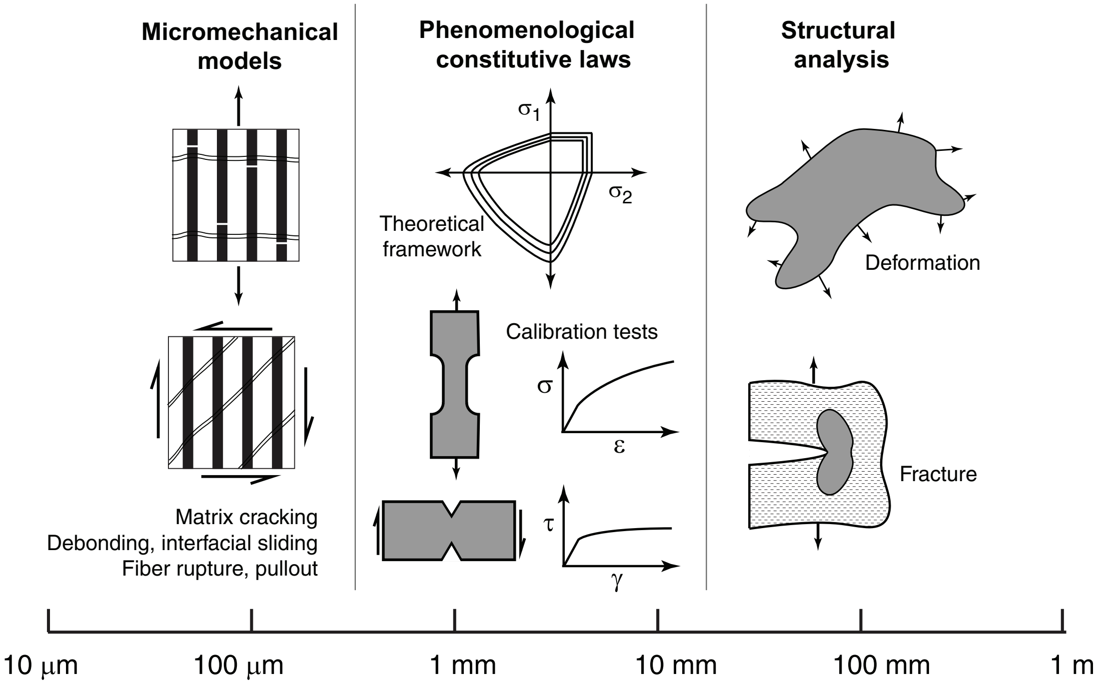

Figure 1.2: Length scales of interest in CMC mechanics.

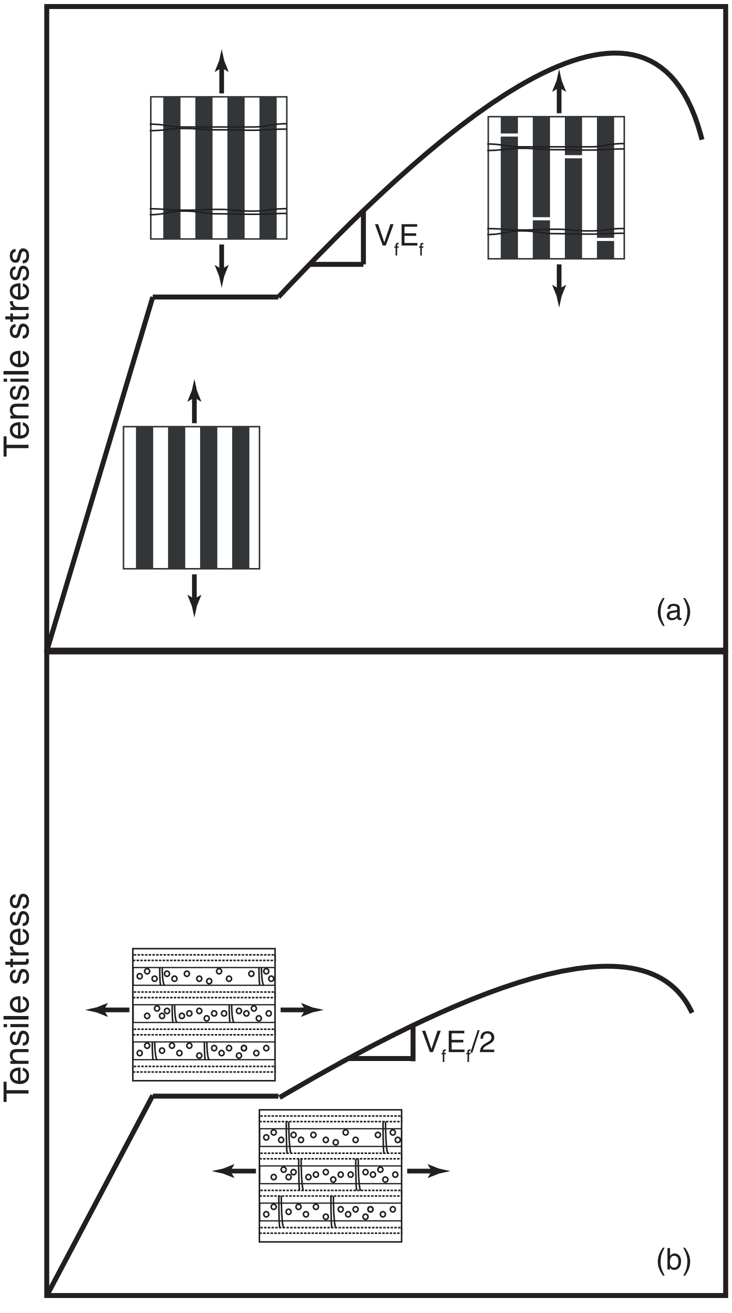

Figure 1.3: Schematics of stress-strain curves in uniaxial, on-axis tension of (a) a unidirectional CMC and (b) a cross-ply CMC.

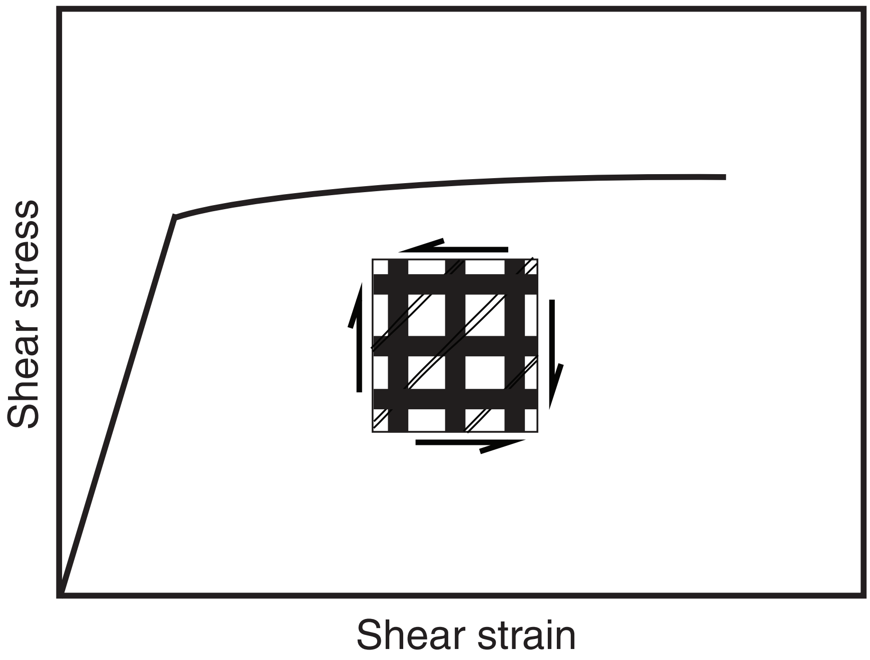

Figure 1.4: Schematic of a stress-strain curve of a cross-ply CMC in shear.

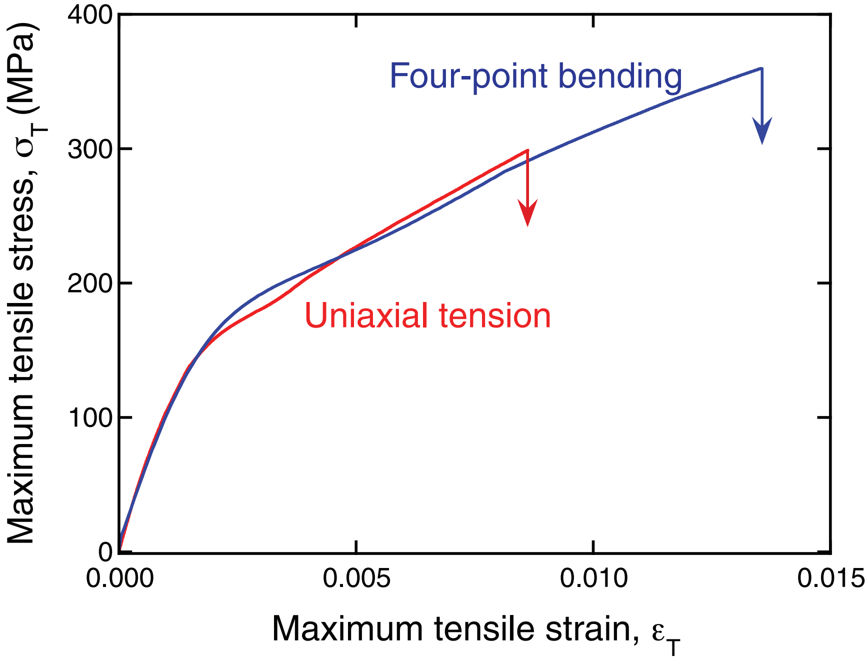

Figure 1.5: Comparison of the stress-strain curve in uniaxial tension with the tensile face stress-strain curve in four-point bending for a Nicalon/MAS composite (from McNulty and Zok (1997)).

Chapter 2

Tensile fracture of CMCs in 1-D problems

2.1 Introduction

As discussed in Chapter 1, fracture of CMCs in 1-D loadings is related not to the development of matrix cracks, but instead to the mechanics and statistics of fiber fragmentation, which dictate the fiber bundle strength. Numerous

---

This chapter is adapted from a peer-reviewed publication: V. P. Rajan and F. W. Zok. Effects of Non-Uniform Strains on Tensile Fracture of Fiber-Reinforced Ceramic Composites. *Journal of the Mechanics and Physics of Solids*, 60(12):2003–2018, 2012. Available at: `http://dx.doi.org/10.1016/j.jmps.2012.07.006` studies have addressed this problem (Curtin, 1991a; Neumeister, 1993a; Hui et al., 1995; Curtin, 1991b; Thouless and Evans, 1988; Phoenix, 1993; Curtin et al., 1998), and a review article by Curtin (1998) summarizes many of the important developments. Most of the studies have been based on a one-dimensional shear lag analysis to describe the stress build-up around broken fibers, assuming that the frictional resistance between the fibers and matrix is constant within the region in which the fibers have slipped past the matrix. Furthermore, most have been based on the assumption of global load sharing; that is, the load carried previously by a broken fiber is shed equally to all other fibers in the plane of the break without generating stress concentrations in neighboring fibers. Notable exceptions to the latter include the work of Ibnabdeljalil and Curtin (1997a).

As also discussed in Chapter 1, the constitutive law that arises from aforementioned analyses of fiber fragmentation must be coupled with a fracture criterion in order to predict fracture in 1-D loadings. This approach was, for instance, utilized by Hild et al. (1994) to analyze the mechanical response of a unidirectional CMC in flexure. In this analysis, a failure criterion based on a critical local strain was employed. Although some of the effects of inelasticity on the stress distribution in bending were captured, the differing failure strains in bending and tension were obviously not. Neumeister (1993b) used a similar approach to address the same problem but with an alternate (*ad hoc*) fracture criterion: notably, one based on the attainment of a critical number of fiber breaks within a prescribed volume element. In addition to lacking a sound fundamental basis, the fracture criterion leads to a predicted tensile-face failure strain in bending comparable to the failure strain in tension: again inconsistent with experimental measurements (McNulty and Zok, 1997). Yet others have attempted to rationalize the effects of non-uniform strains on the basis of weakest link scaling laws, wherein strength increases as the volume of stressed material decreases (McNulty and Zok, 1997; Bullock, 1974; Whitney and Knight, 1980). Although this approach has been made to bring some experimental results into agreement with the model—by tuning the parameters in an assumed Weibull distribution, for instance—it is purely phenomenological and lacks predictive power.

Steif and Trojnacki (1994) presented an analysis of the bending problem that was based on a purely phenomenological representation of the tensile response of a composite (without any explicit connection to fiber properties) but proved to be useful in demonstrating the role of the post-peak strain-softening rate on the composite bending strength. To this end, they used a one-dimensional tri-linear constitutive law for the composite. The three parts were intended to depict: (i) the linear-elastic portion before matrix cracking in tension as well as that in compression; (ii) the reduction in tangent modulus due to matrix cracking; and (iii) the strain softening beyond the peak stress. They then used standard Euler-Bernoulli beam theory coupled with a fracture criterion based on the *attainment of a maximum bending moment* to compute the nominal bending strength. They concluded that the degree to which the bending strength exceeds the tensile strength is governed predominantly by the rate of post-peak strain softening. In the present chapter, it is shown, using a similar analysis but with a mechanistic model for fiber fragmentation, that there are indeed circumstances in which the bending/tension strength differential can be attributed to the post-peak softening. It is also shown that there are other circumstances in which this is not the case; instead, the dominant effect is associated with the attainment of a plateau flow stress after fiber fragmentation is complete (a feature not captured by the model of Steif and Trojnacki (1994)). The effects of strain softening and plateau flow on failure in other loading scenarios in which strain gradients are present are also examined.

An argument could be made that, once the stress in a composite structure locally reaches the peak in its tensile stress-strain curve, the deformation would localize into a narrow band and thus the assumption of deformation homogeneity implicit to the load-maximum failure criterion would break down. If this were the case, the preferred approach to failure prediction would involve use of a cohesive zone model. Later in the chapter, it is argued that, if the localization spreads under a progressively increasing macroscopic load (i.e. with structural hardening), then other potential localization sites remote from the first can be triggered, leading to an array of such bands with a characteristic spacing controlled by the fragment length. Thus, although the deformation would not be homogeneous over distances comparable to the crack spacing, the displacements could be averaged over an appropriate length scale so as to compute a physically-meaningful strain.

Assessments of the fidelity of predicted bending strengths have been based on comparisons between such predictions and experimental measurements. However, some of these assessments are tainted by the fact that failure in the experiments had not occurred in a purely tensile mode. For example, in the studies of Marshall and Evans (1985), Prewo (1986), and Jansson and Leckie (1992) on unidirectional SiC/LAS, tensile fracture was preceded by compressive crushing at the loading points in the bend tests. In another study, by Beyerle et al. (1992a) on unidirectional SiC/CAS, fracture in bending occurred via delamination in the regions between the inner and outer loading points: not in the region of maximum moment. Consequently, conclusions drawn from such comparisons (Hild et al., 1994; Neumeister, 1993b; Steif and Trojnacki, 1994) should be judged skeptically. (It is noted parenthetically that, because of the very high tensile strength of unidirectional CMCs coupled with their low resistance to in-plane shear loads, true tensile failure is generally difficult to attain under flexural loading. The problem is less pronounced in multidirectional laminates.)

The principal objective of this chapter is to develop a mechanics framework capable of capturing the effects of non-uniform strains on fracture of fiber-reinforced CMCs in 1-D loadings (assuming monotonic loading). The outline of the chapter is as follows. First, the constitutive law for the composite tensile stress-strain response, based on the fiber fragmentation model of Hui et al. (1995), is described. Next, we present a framework that utilizes this constitutive law to ascertain the maximum load-bearing capacity of composite structures in the presence of non-uniform strains. The key assumption (as noted earlier) is that failure occurs upon attainment of a global load maximum. This framework is then applied to three model problems of engineering interest: (i) an end-constrained plate subjected to a linear transverse temperature gradient; (ii) a cylindrical thin-walled tube with a linear through-thickness temperature gradient and internal pressure; and (iii) a beam with rectangular cross-section undergoing combined bending and tension. Each problem produces a constant strain gradient in one of the directions transverse to the fibers. It is found that the peak tensile strain at the load maximum increases with the magnitude of the strain gradient; the sensitivity of the failure strain to the strain gradient is not unique but rather depends on the loading path. Furthermore, in order to glean insights into the characteristics of the tensile response that control failure, approximate representations that decouple the effects of strain softening from the plateau flow stress at large strains are developed. Finally, calculations of failure strain and stress for the problem of pure bending are assessed against the experimental data of McNulty and Zok (1997).

2.2 Constitutive laws

2.2.1 Fiber fragmentation

The inelasticity in the post matrix-cracking tensile response is governed by the process of fiber fragmentation and sliding along the fiber-matrix interfaces. A convenient description of the statistical variation in fiber strength is the two-parameter Weibull distribution:

$$F = 1 - \exp\left[\frac{L}{L_0}\left(\frac{\sigma_f}{\sigma_0}\right)^{\rho}\right] \tag{2.1}$$

where F is the cumulative failure probability of a fiber of length L at a stress σ_f, L_0 and σ_0 are reference values of length and strength, respectively, and ρ is the Weibull modulus. Shear-lag theory describes how fiber stress away from a break is restored to its far-field value, via the frictional resistance τ_s of the fiber-matrix interface (Cox, 1952). Assuming that τ_s is a constant, the fiber stress varies linearly within a 'recovery zone' adjacent to the fiber break, over a length $l = 2R\sigma_f/\tau_s$, where σ_f is the fiber stress remote from the break, given by $\sigma_f = E_f\epsilon$, with E_f being the fiber modulus and ϵ the applied strain.

The fiber fragmentation problem has been analyzed approximately by Curtin (1991a,b) and Neumeister (1993a), and solved exactly by Hui et al. (1995). The differences in the resulting constitutive laws from the exact and the approximate analyses arise from differing assumptions about two physical phenomena: shadowing of fiber defects within the recovery zone and overlap of recovery zones adjacent to neighboring breaks (Neumeister, 1993a). Neglecting these phenomena leads to erroneous predictions in the post-peak softening regime (Neumeister, 1993a). The constitutive law employed here is the one based on Hui's solution. The model is based on the assumptions that: (i) the frictional resistance of the fiber/matrix interface is uniform along the length of the fibers (unaffected by local perturbations associated with discrete matrix cracks); (ii) the characteristic terminal fragment length is small compared to the gauge length of stressed material; and (iii) the fiber strength follows a Weibull distribution (Equation 2.1). Suitable normalizations yield three key parameters: (i) a non-dimensional stress, $S = \overline{\sigma}/V_f\sigma_c$ where $\overline{\sigma}$

is the average composite stress, V_f is the volume fraction of fibers aligned with the tensile loading direction and σ_c is a characteristic strength defined by $\sigma_c = \left(\frac{\sigma_0^\rho \tau_s L_0}{R}\right)^{\frac{1}{\rho+1}}$; (ii) the corresponding tensile strain, $\Delta = \epsilon E_f/\sigma_c$; and (iii) a characteristic length, given by $\delta_c = \left(\frac{R\sigma_0}{\tau_s L_0^{1/\rho}}\right)^{\frac{\rho}{\rho+1}}$. The full analytical description of the stress-strain response is presented in Appendix A. The integrals contained therein were computed numerically in MATLAB (Mathworks, 2009) using adaptive Simpson quadrature.

Tensile stress-strain curves computed from Hui's model for representative values of ρ are depicted in Figure 2.1. The notable features include the gradual strain softening following the peak and a 'plateau' flow stress at large strains (once the fragmentation process is complete). Also shown for comparison are the stress-strain curves from Curtin's approximate model. The latter yields reasonably accurate results up to the peak stress but not in the post-peak (softening) regime.

2.2.2 Complete constitutive law

To ensure that the composite is modeled in a physically-realistic manner in the elastic regime as well as under compressive loading, the preceding fragmentation model is supplemented with a *pre*-matrix cracking constitutive law.

The compressive response of the composite is taken to be elastic for all strains, and the elastic moduli in compression and tension are assumed to be equal to one another. The ratio E' of the post-matrix cracking tangent modulus to the longitudinal composite modulus E_c is defined by $E' = V_f E_f / E_c$. For typical fiber volume fractions and fiber/matrix moduli, E' falls between 1/4 and 1/2. In addition, although matrix cracking is experimentally observed to commence and saturate at somewhat different stress levels (Evans and Zok, 1994), the constitutive law used in the present analysis assumes that these stresses are the same. The consequence is that the stress-strain curve exhibits a strain burst upon matrix cracking, in accord with the prediction of the well-known micromechanical model of Aveston et al. (1971). A non-dimensional matrix cracking stress is defined by $S_{mc} = \sigma_{mc} / V_f \sigma_c$. The complete constitutive law can thus be expressed in piecewise form as

$$S(\Delta) = \begin{cases} \Delta / E' & \Delta < S_{mc} E' \\ S_{mc} & S_{mc} E' < \Delta < S_{mc} \\ f(\Delta) & S_{mc} < \Delta \end{cases} \tag{2.2}$$

where $f(\Delta)$ is the stress-strain response in the post-matrix cracking regime.

In the model problems considered in the present article, the structures do not undergo unloading either globally or locally. Consequently, differences in the loading/unloading response (common in CMCs) are neglected.

2.2.3 Approximate representations

In order to glean insights into the important post-peak characteristics that govern failure, two approximate formulations of the constitutive law obtained from Hui's model (Figure 2.2) are developed. In the first, termed the plateau model, the post-peak response is represented by instantaneous softening from the peak to the plateau and the subsequent flow stress is assumed to remain at the plateau level for higher strains. This representation neglects the strain-softening portion of the curve and is expected to yield a lower bound on the predicted failure stress and strain. In the second, termed the softening model, the post-peak response is assumed to follow a linear softening law, with the rate of softening obtained from a linear fit of the exact results in the regime between the peak and the plateau (Figure 2.2). The expectation is that, for small strain gradients, failure will occur at strains only slightly beyond the peak and hence the linear softening model should yield reasonably accurate results. Conversely, for large gradients, the failure strain will fall well within the plateau regime, and thus the perfectly-plastic post-peak representation should yield more accurate results. A further expectation is that the suitability of the two approximate representations will depend on ρ. This is because, as ρ decreases, the ratio of the plateau stress to the peak stress increases and the rate of strain softening decreases.

Assessments of the two approximate representations are made on the basis of the errors in the predicted strengths of the composite structures relative to those obtained from the exact Hui model. The results are presented as maps in coordinates of fiber Weibull modulus and a measure of the strain gradient. The maps depict the regimes in which the approximate models yield sufficiently accurate results: an error of less than 5 % being deemed to be adequate. For comparison, a model based on the attainment of a critical fracture strain is also considered. Consequently, in general, three (potentially overlapping) domains emerge, one for each of the three approximate representations. A fourth domain — one in which none of the three approximations provide adequate accuracy — can also be present.

2.3 Model problems

2.3.1 Approach

The approach for solving the problem of fracture with non-uniform strains is as follows. Equation 2.2 defines a constitutive law that relates normal strains and stresses in the fiber direction, x. The axial strain is permitted to vary only in the transverse directions, y and z. The reaction force, r_x, in the fiber direction can therefore be expressed as

$$r_x = \iint_A \sigma_{xx}(\epsilon_{xx}(y, z))\, \mathrm{d}y\, \mathrm{d}z \tag{2.3}$$

The y and z coordinates are non-dimensionalized as $Y = y/h_y$ and $Z = z/h_z$, where h_i is the dimension of the specimen in the i direction. Then, utilizing the normalizations introduced in Section 2.2, Equation 2.3 reduces to

$$R_x = \frac{r_x}{h_y h_z V_f \sigma_c} = \iint_A S(\Delta(Y, Z))\, \mathrm{d}Y\, \mathrm{d}Z \tag{2.4}$$

The strain distribution, $\Delta(Y, Z)$, is assumed to be known *a priori*. The loading trajectory is expressed in terms of a single parameter, t: for instance, an applied displacement, a rotation, or a temperature gradient. Fracture is deemed to have occurred once the load-bearing capacity attains a maximum (*not* when a material element *locally* reaches the peak in its stress-strain curve). Under this assumption, the non-dimensional fracture strength, S^f, is thus obtained by maximizing R_x with respect to t. Similarly, the fracture strain, Δ^f_{max}, is taken as the maximum value of $\Delta(Y, Z)$ anywhere within the body when the critical value of t is reached. Numerical solutions were obtained using a minimization algorithm in the optimization toolbox of MATLAB (Mathworks, 2009).

For problems involving bending, a non-dimensional moment is defined as

$$M_z = \frac{m_z}{h_y^2 h_z V_f \sigma_c} = \iint_A (Y - Y_t) S(\Delta(Y, Z))\, \mathrm{d}Y\, \mathrm{d}Z \tag{2.5}$$

Y_t is the Y-coordinate of the axis of applied tension. Proportional loading is assumed, with $M_z/R_x = \tan\lambda$, where λ characterizes the mixity of loading; the loading reduces to pure bending for $\lambda = \pi/2$ and pure tension for $\lambda = 0$. Intermediate values of λ describe combined bending and tension. Numerical solutions were again obtained using MATLAB (Mathworks, 2009). Since the moment and the axial load are proportional, either quantity can be used as the objective function for maximization. The loading parameter was taken to be the tensile-face strain Δ_{max}. For each prescribed value of Δ_{max}, a subroutine was used to solve numerically for the strain gradient, Ψ, that satisfies the proportional loading equation

$$M_z\left(\Delta_{max}, \Psi\right) = R_x\left(\Delta_{max}, \Psi\right)\tan\lambda \tag{2.6}$$

For pure bending, the quantities of interest obtained from the numerical solution are the tensile-face strain at failure, Δ_{max}^f, and the failure moment, M_z^f. The flexural strength, σ_b^f, can be expressed in non-dimensional form in accordance with

$$S_b^f = \frac{\sigma_b^f}{V_f \sigma_c} = 6M_z^f \tag{2.7}$$

where S_b^f is the non-dimensional flexural strength. For combined bending and tension, a failure locus can be constructed at a constant value of ρ. The moment at failure, M_z^f, is converted into a flexural strength using Equation 2.7, while the axial load at failure, R_x^f, becomes the tensile strength, S_t^f.

In each of the three model problems considered below, the strain distribution is linear and varies in only the Y-direction. The strain distribution can therefore be expressed as

$$\Delta(Y, Z) = \Delta_{max} - \Psi \cdot Y \tag{2.8}$$

where Δ_{max} is the maximum tensile strain; the origin of the Y-axis is positioned so that the maximum strain is located at $Y = 0$; and Ψ characterizes the strain gradient. Both Δ_{max} and Y are functions of the loading parameter t.

2.3.2 Constrained plate with temperature gradient

The first model problem is that of a composite plate with rectangular cross-section, fixed between two rigid supports and initially at a uniform (stress-free) temperature T_0 (Figure 2.3(a)). The left side of the plate is positioned at $Y = 0$, and its temperature, T_L, is then reduced at a constant rate so that $T_L = -\dot{T}_L \tau + T_0$, where τ is time. Similarly, the right side of the plate is cooled at a different rate in accordance with $T_R = -\dot{T}_R \tau + T_0$. Without loss of generality, it is assumed that $\dot{T}_L \geq \dot{T}_R$. Further assuming that the temperature gradient thereby developed is linear, the thermal strain field becomes

$$\epsilon_{th}(Y, t) = \alpha[T_L(1 - Y) + T_R Y - T_0] = -\alpha\tau[\dot{T}_L(1 - Y) + \dot{T}_R Y] \tag{2.9}$$

where α is the coefficient of thermal expansion of the composite in the fiber direction. Since the total strain is zero, the mechanical strain is $\epsilon_m = -\epsilon_{th}$. Its maximum value, written in the form of Equation 2.8, is

$$\Delta_{max}(\tau) = \frac{E_f \alpha \dot{T}_L \tau}{\sigma_c} \tag{2.10}$$

The corresponding strain gradient is

$$\Psi(\tau) = \Theta \cdot \Delta_{max}(\tau) \tag{2.11}$$

and

$$\Theta = 1 - \frac{\dot{T}_R}{\dot{T}_L} \tag{2.12}$$

All physically-plausible scenarios fall in the domain $0 \leq \Theta \leq 1$.

Illustrative numerical results showing the effects of ρ, E', and S_{mc} on the fracture strength and strain are presented in Figures 2.4 and 2.5. They show that the fracture strain increases monotonically with strain gradient (characterized by Θ). The effects are most pronounced for small Weibull moduli ($\rho \leq 5$, typical of SiC fibers). The fracture stress, however, decreases with Θ. The results also indicate that the fracture stress and strain are insensitive to both E' and S_{mc}. This insensitivity arises because, at fracture, the majority of the material resides in the post-matrix-cracking regime.

Also shown for comparison in Figure 2.4(b) are the predictions based on the linear softening model and the plateau model. Here the softening model yields accurate results over the entire range of ρ and Θ. The plateau model, in contrast, is adequate at low strain gradients but underestimates the strength for $\Theta \geq 0.3$.

A map showing the domains in which the approximate models yield accurate results is presented in Figure 2.6. It comprises three regimes. (i) For small gradients, characterized approximately by $\Theta \leq 1/3$, fracture occurs shortly after the peak in the stress-strain curve. Consequently, all three of the approximate models yield adequate results. The boundary of this domain is almost independent of ρ. (ii) The plateau model is also accurate in the domain of very low values of ρ and high strain gradients. This result arises because the plateau stress is a significant fraction of the peak value at low values of ρ and thus, under large strain gradients, failure occurs when the peak strain is well within the plateau domain. (iii) The linear softening model provides adequate results over the entire parameter space. The inference is that the additional load-bearing capacity (beyond that at the attainment of the peak stress locally) is attributable largely to the finite post-peak strain-softening rate; the plateau flow stress plays a decidedly secondary role.

2.3.3 Pressurized tube with temperature gradient

The next model problem is that of a thin-walled cylindrical tube. It is subject, first, to a linear through-thickness temperature gradient, and, second, to a monotonically increasing internal pressure. Fibers are oriented in the circumferential direction. The rotational symmetry of the problem precludes bending; however, a net mechanical stress must develop over the cross-section to counterbalance the internal pressure (Figure 2.3(b)). Combining this equilibrium condition with the result in Equation 2.4 yields the reaction force R_x:

$$R_x = \frac{pd}{2h_y V_f \sigma_c} \tag{2.13}$$

where p is the internal pressure, d is the diameter of the tube, and h_y is the thickness of the wall. With the wall mid-plane held at the stress-free temperature, the thermal strain distribution is $\epsilon_{th} = \frac{\alpha \Delta T}{2}(2Y - 1)$, where ΔT is the through-thickness temperature difference and $Y = y/h_y$. The mechanical strain therefore becomes $\epsilon_{mech} = \epsilon_{tot} + \frac{\alpha \Delta T}{2}(1 - 2Y)$, where the total strain is independent of Y since the tube is thin-walled. Upon normalization this expression can be rewritten in the form of Equation 2.8, with

$$\Psi = \frac{E_f \alpha \Delta T}{\sigma_c} \tag{2.14}$$

and

$$\Delta_{max} = \Delta_{tot} + \frac{\Psi}{2} = \frac{\epsilon_{tot} E_f}{\sigma_c} + \frac{\Psi}{2} \tag{2.15}$$

Taking the temperature difference to be constant, the parameter describing the loading trajectory is Δ_{max}, which increases monotonically with pressure.

Select numerical results are plotted in Figure 2.7. Here again the failure strain increases with the gradient (characterized in this case by Ψ), albeit with a significantly weaker dependence on ρ. Also, the failure stress and strain exhibit an even weaker dependence on S_{mc} and E' (not shown) because only a small portion of the tube wall remains in the elastic domain at fracture.

The failure map for this problem is shown in Figure 2.8. It exhibits characteristics similar to those seen in the previous problem. Notably, for low strain gradients, all three of the approximate models are adequate since failure occurs shortly after the peak stress is attained locally. The predictions of the plateau model and the critical strain model begin to break down at a critical strain gradient, characterized by $\Psi \leq 0.2$ (almost independent of ρ), while the softening model yields accurate results over most of the parameter space. However, the softening model also eventually breaks down, at very high gradients and high ρ. The increasing error in the predictions from the softening model with increasing ρ are evident in Figure 2.7(b) for the case $\Psi = 0.9$.

2.3.4 Combined bending and tensile loading

The final model problem is that of a beam with rectangular cross-section subjected to proportional bending plus tension (Figure 2.3(c)). From Euler-Bernoulli bending theory, the strain distribution is linear through the cross-section and can be written in the form of Equation 2.8, with

$$\Delta_{max} = \frac{\epsilon_{max} E_f}{\sigma_c} \tag{2.16}$$

and

$$\Psi = \frac{\kappa h_y E_f}{\sigma_c} \tag{2.17}$$

where ϵ_{max} is the tensile-face strain, κ is the curvature and h_y is the beam thickness.

Results for the limiting case of pure bending ($\lambda = \pi/2$) are plotted in Figure 2.9. In contrast to the preceding model problems, bending failure occurs in one of two ways:

(i) At low ρ, a *limit moment* is obtained. Consequently, the tensile-face strain approaches infinity. Moreover, in the limit state, the stress throughout the beam is essentially uniform and equal to the plateau flow stress, S_{pl}: the exception being the compressive face itself, where the stress approaches $-\infty$. In this domain the *plateau model yields exact results*; the limit stress is simply $S_b^f = 3S_{pl}$.

(ii) At higher values of ρ, a *maximum moment* is obtained. In this domain, failure occurs while the peak strain is on the softening portion of the stress-strain curve and thus the softening model yields highly accurate results. Furthermore, the failure stress is almost independent of ρ and given to high accuracy by $S_b^f = C/(1+\sqrt{E'})$, with $C = 1.92$ ($< 2\,\%$ error for $1/4 \leq E' \leq 1, \rho \leq 20$)[1]. Note that in contrast to the other two problems, the failure load in bending is somewhat sensitive to the elastic modulus, because much of the material is in compression. Similar results were obtained by Steif and Trojnacki (1994) using a tri-linear representation of the stress-strain curve. But, because of the absence of an explicit connection between the post-peak softening rate and the fiber properties as well as the absence of a plateau flow stress, their model is unable to predict the behavior at low ρ, especially the nature of the failure condition.

The transition between the two domains is discontinuous and occurs at a critical value of ρ; for the case shown in Figure 2.9, it occurs at $\rho \approx 4$. The plateau model also predicts a discontinuity, but *not* at the correct value of ρ. The softening model, on the other hand, does not predict the discontinuity, though it is accurate at high ρ. A key conclusion is that, despite the merits of the two approximate models in certain domains, neither satisfactorily predicts the be-

---

[1] The functional dependence of S_b^f on E' was obtained using Curtin's approximate model. The parameter C was then obtained by fitting this equation to the exact results from the Hui model.

havior across the entire parameter range of interest.

The failure loci for combined bending/tension are plotted in Figure 2.10. The corresponding map showing the domains in which the approximate models yield adequate results is in Figure 2.11. For the latter, the gradient is characterized by the tension/bending loading mixity parameter λ. The failure loci in S_t^f–S_b^f space are approximately linear for fixed ρ. Indeed, for low ρ and moderately high values of λ, wherein failure occurs via a limit condition, one can readily show using the plateau model that the failure locus is *exactly linear* and given by

$$S_t^f + \frac{S_b^f}{3} = S_{pl} \tag{2.18}$$

Interestingly, this result is independent of the peak stress in the fiber bundle response. But it breaks down at higher ρ and lower λ, wherein failure occurs while the peak strain is in the softening regime, as evident in the map in Figure 2.11. This behavior is seen in Figure 2.10. For $\rho = 3$, a discontinuity in the bending and tensile strengths occurs at low tension/bending mixity λ, since the failure condition transitions from a limit load to a load maximum.

2.3.5 Comparisons of results from the three model problems

Comparisons of the results from each of the three model problems are made on the basis of the variation in failure strain Δ_{max}^f with the strain gradient Ψ^f

at failure (Figure 2.12). Though the trends are qualitatively similar, there are significant differences in the details. This result is not unexpected, given the differences in loading trajectories. That is, in the linear temperature gradient problem, the strain gradient increases proportionally with strain; in the pressurized tube problem, the strain gradient is applied first and remains fixed while the pressure is increased; and for combined bending/tension, the loads are applied proportionally and thus the strain gradient is neither constant nor proportional to the maximum strain.

2.4 Discussion

A preliminary assessment of the present model has been made through comparisons with experimental measurements of failure stresses and strains under tensile and bending loads. Because of issues of delamination and/or compressive failure, the data on unidirectional CMCs is neglected. Instead, only data for composites with multidirectional architectures that are known to fail in a tensile mode under bending (McNulty and Zok, 1997) are considered. The data employed here are for a composite consisting of Nicalon fibers in a [0°/90°] layup and a magnesium aluminosilicate (MAS) matrix (Table 2.1). Both the tensile and compressive surfaces of the bend specimens had been instrumented with strain gauges. The ratios of bending/tension strengths and failure strains are 1.85–2.2 and 1.4–1.6, respectively. For the model predictions, a range of values of E' and S_{mc} that realistically match those obtained from the measured tensile stress-strain curves (E' = 0.17–0.25, S_{mc} = 0.3–0.4) is selected. Furthermore, a fiber Weibull modulus $\rho = 4$ (typical of Nicalon fibers (McNulty and Zok, 1997)) is assumed. The predicted ratios of bending/tension strength and failure strain are 1.85–2 and 1.5–1.6, respectively. The predictions agree quite well with the experimental results. By comparison, using the same parameter values along with a critical strain criterion for fracture, the predicted strength and failure strain ratios are 1.5–1.7 and 1, respectively. The latter results indicate that neglecting the contribution from the post-peak regime results in the flexural strength being underestimated by approximately 20 %. The ratio of failure strains is (naturally) underestimated by an even larger margin. Other mechanics-based models for composite fracture also fail to accurately predict the ratio of failure strains (Hild et al., 1994; Neumeister, 1993b).

As noted at the outset, the present analysis is predicated on the assumption of global load sharing (GLS) among fibers: a condition obtained when the interface toughness and sliding stress are low. Otherwise, some degree of stress concentration is obtained around a fiber failure site (Hedgepeth and van Dyke, 1967). The effects of local load sharing (LLS) on fiber bundle properties have been studied by Curtin and co-workers (Zhou and Curtin, 1995; Ibnabdeljalil and Curtin, 1997a) using three-dimensional lattice spring models. Their results show that, for spring constants that yield realistic values of stress concentrations around fiber breaks, the fiber bundle strength is reduced only slightly relative to the GLS prediction and exhibits only a small amount of variability and volume-sensitivity. Furthermore, the bundle properties follow the same scalings with the characteristic strength σ_c and the characteristic length δ_c. The inference is that, although the present work has been based on the GLS assumption, the results for LLS conditions are likely to be similar. Furthermore, the *ratios* of quantities, such as flexural/tensile strengths, should be predicted with reasonable accuracy.

Finally, the issue of deformation localization once the stress locally reaches the peak in the stress-strain curve is discussed. As argued earlier, if a localization band were to spread under an increasing macroscopic load, then other potential localization sites remote from the first could be triggered. Averaging the displacements over an appropriate length scale would yield a physically-meaningful strain. Indeed, this situation is the same as that of a matrix crack in a CMC bridged by fully-intact fibers under uniaxial tensile loading. In the latter scenario, the deformation is clearly localized in the vicinity of the crack (manifested as a crack opening displacement). But, because of structural hardening (in this case resulting from a rising traction law), other cracks form in an approximately periodic manner, ultimately reaching a spacing dictated by the slip length along the fiber-matrix interface; the displacements are averaged accordingly to yield a macroscopic inelastic strain. There is no reason to believe that the same macroscopic response—with multiple periodic cracks—should not be obtained in cases where the traction law associated with a crack exhibits a softening portion *provided the loading is such that crack extension occurs under an increasing macroscopic load*. The expectation therefore is that a cohesive approach should yield a peak macroscopic load that is virtually identical to that obtained from a continuum description of the inelastic deformation.

The latter equivalence can be demonstrated using a specific example: the problem of pure bending of a composite with a low fiber Weibull modulus and hence a high plateau flow stress. The results in Section 2.3.4 show that, in this scenario, a limit moment is obtained, with a predicted bending strength of $S_b^f = 3S_{pl}$. Arguably the problem could be tackled equivalently by considering the extension of a single localized deformation band from the tensile face towards the compressive face, with a bridging stress equal to S_{pl}. The growth of the band can be readily computed using a standard cohesive zone approach[2].

---

[2] The results were computed using the analytical formulae for weight functions on pages 2.13 and 2.27 of Tada et al. (1985), assuming zero crack tip toughness. Note that, since the bridging stress is constant, there is no additional (bridging) length scale in the problem. A corollary to this statement is the tacit assumption that the peak crack opening displacement remains small in relation to the characteristic fiber pull-out length.

The corresponding fracture resistance curve, couched in terms of the macroscopic bending stress and the current length of the localized band, is plotted in Figure 2.13. The band grows stably from a stress of S_{pl} at its inception to a maximum value of $3S_{pl}$ when it reaches the back face: the latter being identical to that predicted from the limit moment calculation. Despite the utility of the cohesive zone model in predicting the ultimate bending strength of such a composite, the model provides no information about the density of localized bands and the associated macroscopic strain. This aspect of the problem would require consideration of the pull-out lengths of fiber fragments and the interactions between adjacent localized bands. The result is likely to be very similar to that obtained from Hui's fragmentation model.

Table 2.1: Measured failure strains and stresses in uniaxial tension, four-point bending, and open-hole tension of a Nicalon/MAS composite (McNulty and Zok, 1997)

Test	Maximum local strain at failure (%)	Strength (MPa)
Uniaxial tension	0.86–0.93	299–324
Four-point bending	1.30–1.40	600–650 (flexural)
Open-hole tension	1.60	–

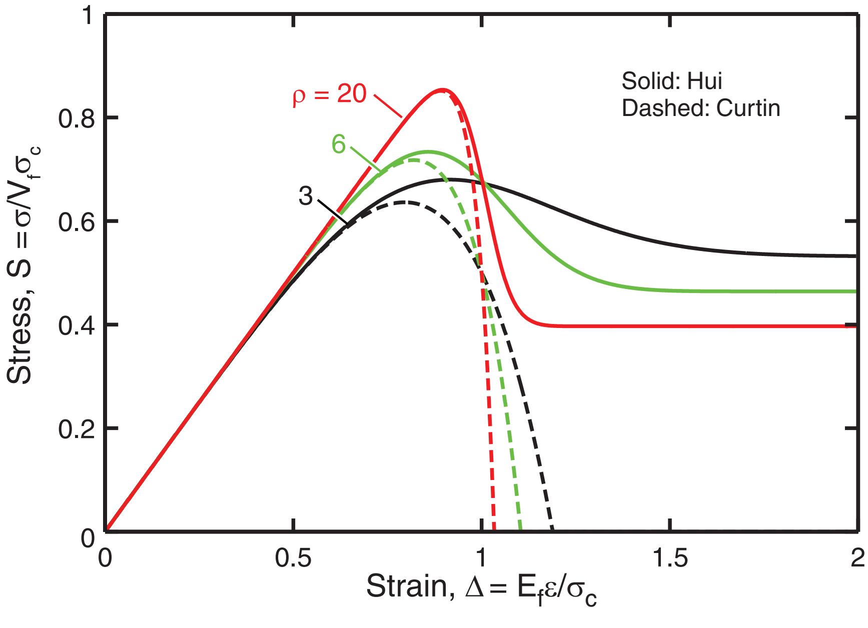

Figure 2.1: Comparison of constitutive laws for three typical values of ρ.

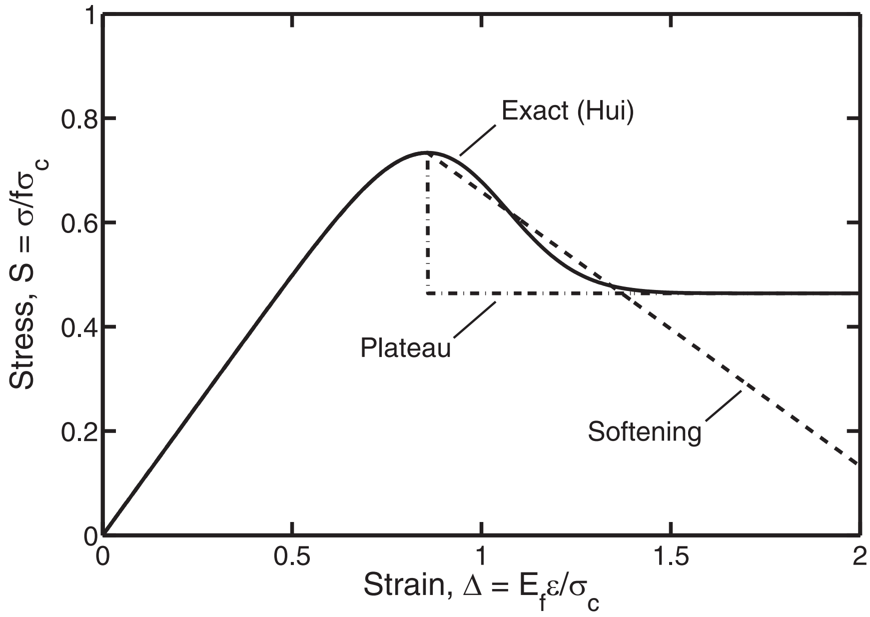

Figure 2.2: Two approximate representations of the post-peak response: perfectly-plastic flow at the plateau stress and linear softening ($\rho = 6$).

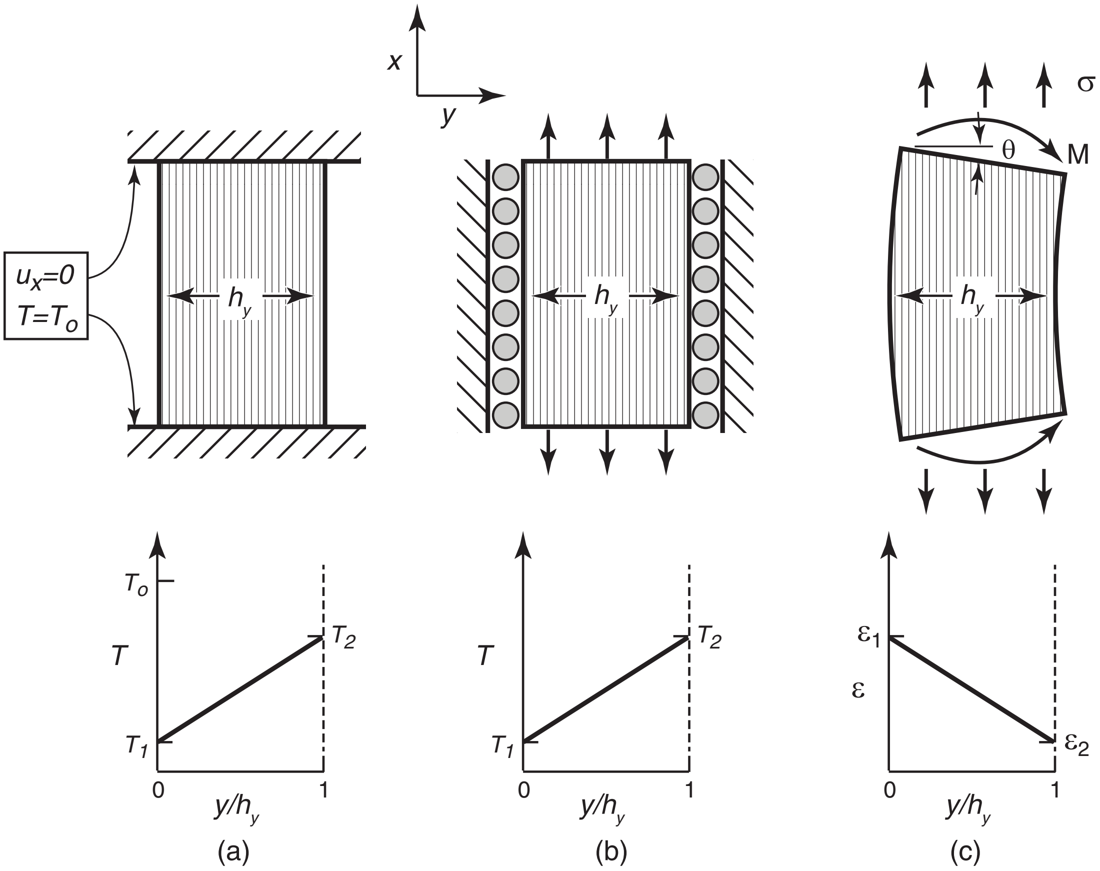

Figure 2.3: Schematics of the three model problems of interest: (a) linear temperature gradient across an end-clamped plate, (b) pressurized tube with linear temperature gradient through the wall, and (c) combined bending and tension of a rectangular beam.

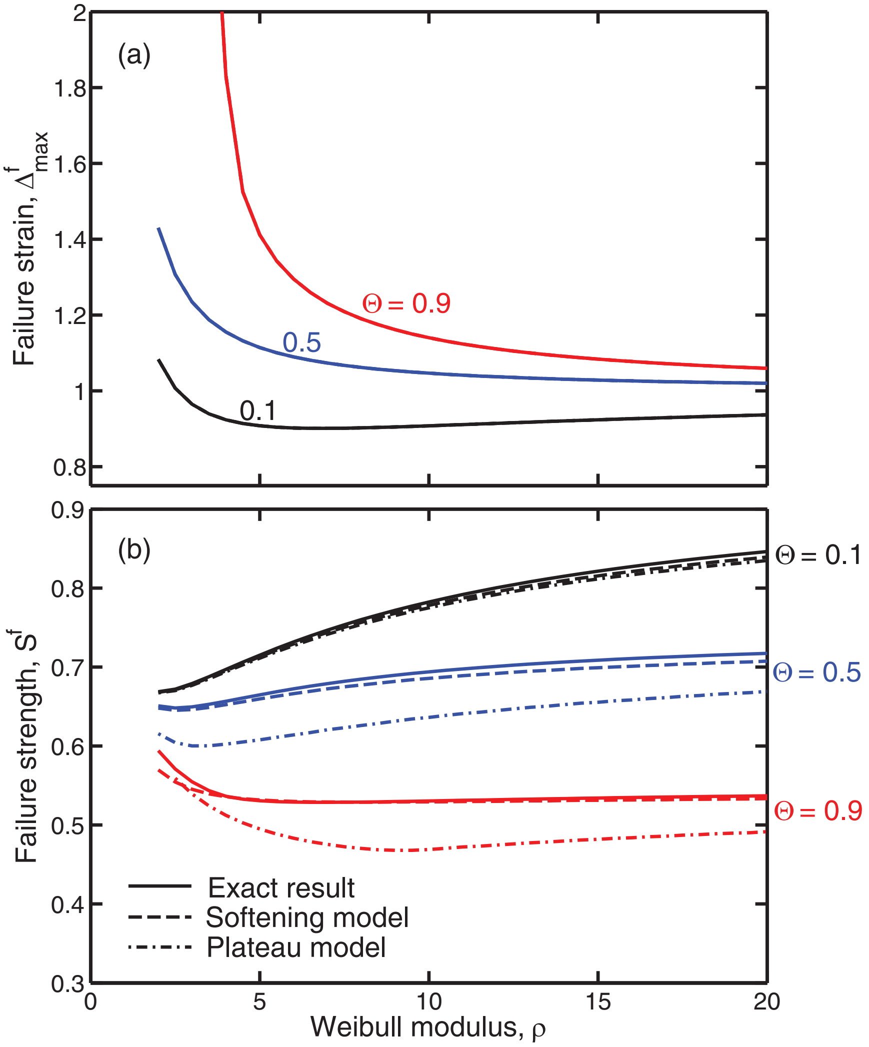

Figure 2.4: Effects of Weibull modulus ρ and strain gradient Θ on (a) the maximum strain at peak load and (b) the corresponding peak stress for the linear temperature gradient problem ($E' = 1/3$ and $S_{mc} = 0$).

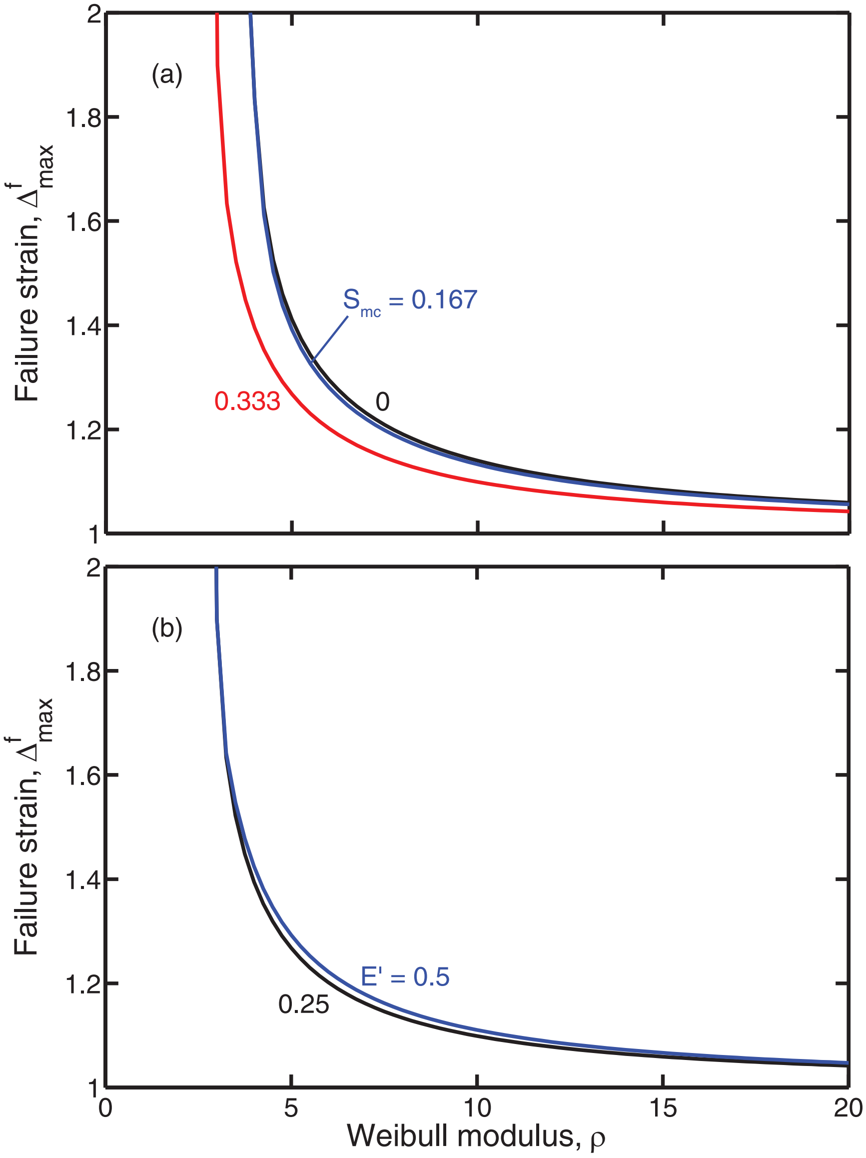

Figure 2.5: Effects of (a) matrix cracking stress S_{mc} (for $\Theta = 0.9$ and $E' = 1/3$) and (b) the modulus ratio E' (for $\Theta = 0.9$ and $S_{mc} = 1/3$) on the maximum strain at the peak stress for the linear temperature gradient problem.

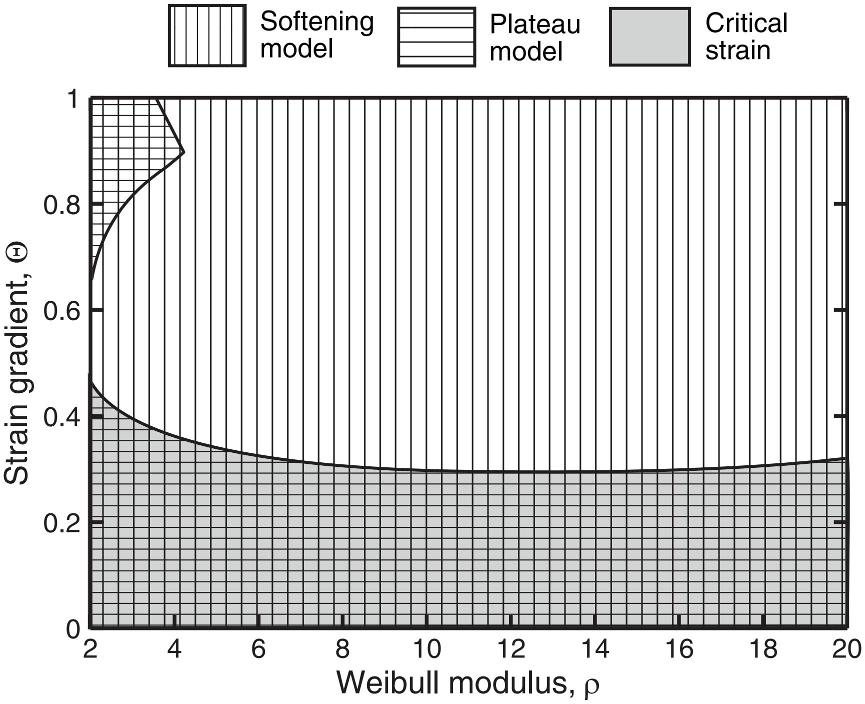

Figure 2.6: Failure map for the linear temperature gradient problem ($E' = 1/3$ and $S_{mc} = 0$).

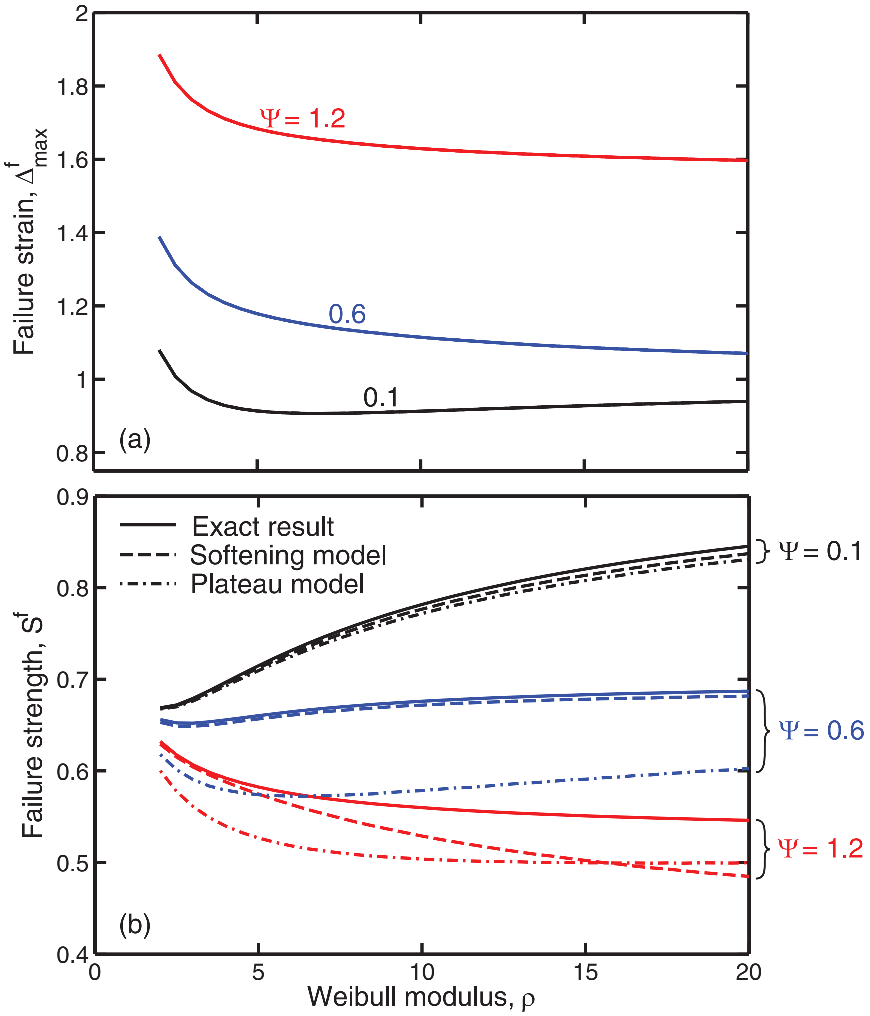

Figure 2.7: Effects of Weibull modulus ρ and strain gradient Ψ on (a) failure strain and (b) failure strength (i.e. average hoop stress at failure) for the pressurized tube problem ($E' = 1/3$ and $S_{mc} = 0$).

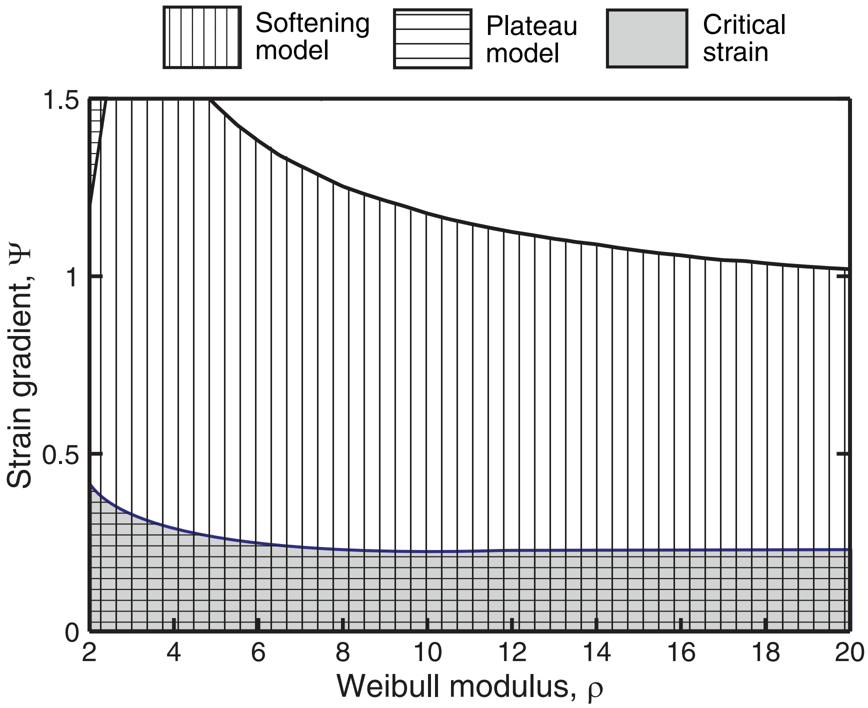

Figure 2.8: Failure map for the pressurized tube problem ($E' = 1/3$ and $S_{mc} = 0$).

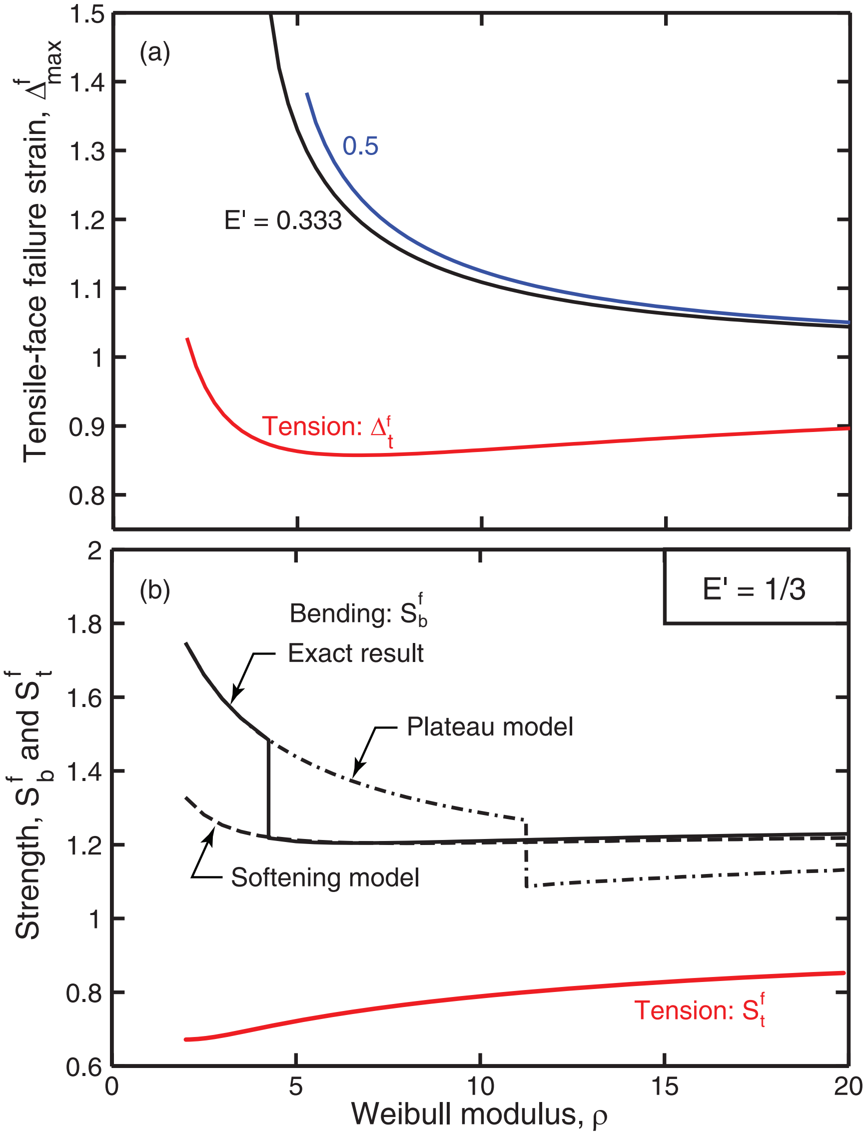

Figure 2.9: (a) Failure strain and (b) strength in pure bending ($S_{mc} = 0$). Shown for comparison in red are the results for uniaxial tension.

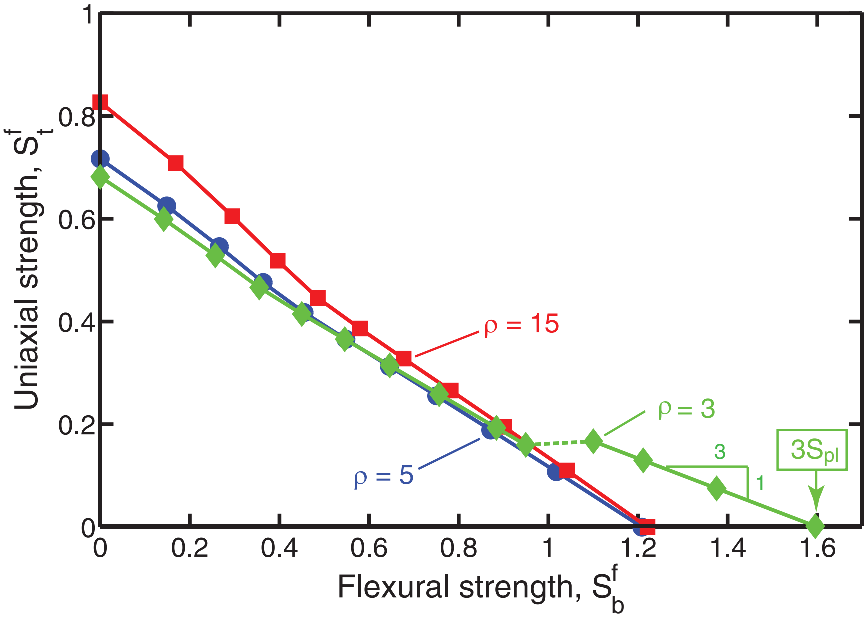

Figure 2.10: Failure loci for combined bending and tension ($E' = 1/3$ and $S_{mc} = 0$).

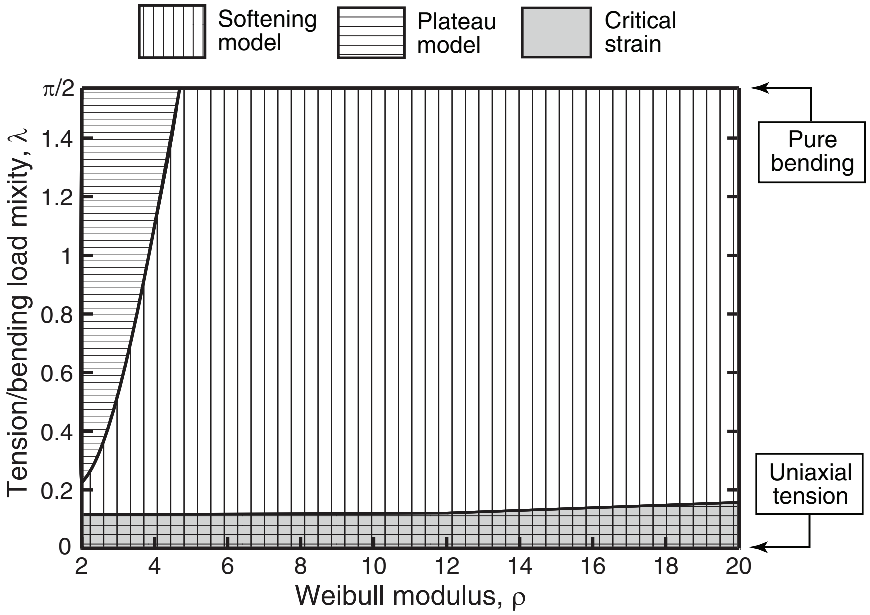

Figure 2.11: Failure map for combined bending and tension ($E' = 1/3$ and $S_{mc} = 0$). The right branch of the solid line for $\rho = 3$ is obtained from Equation 2.18.

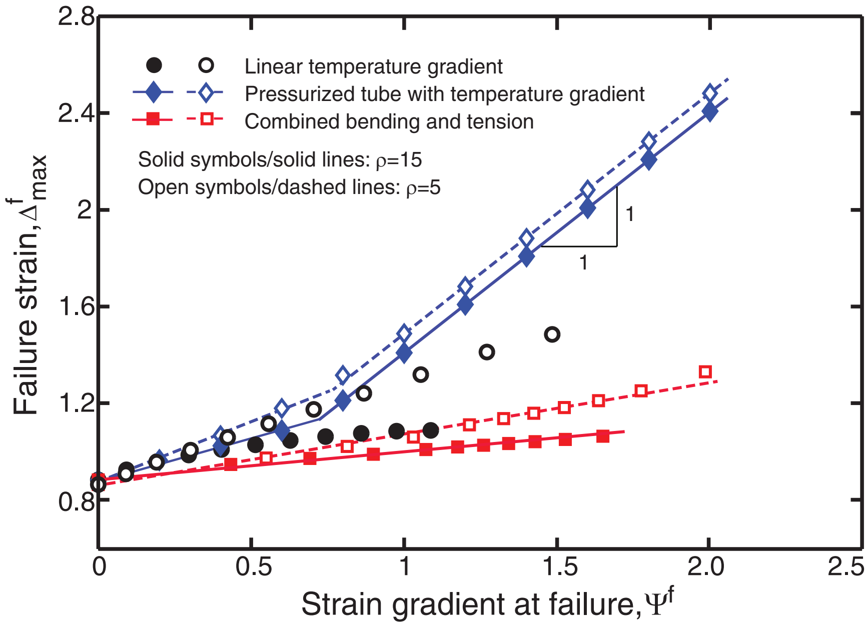

Figure 2.12: Variation in the maximum strain at failure with the strain gradient at failure for the three model problems ($E' = 1/3$ and $S_{mc} = 0$).

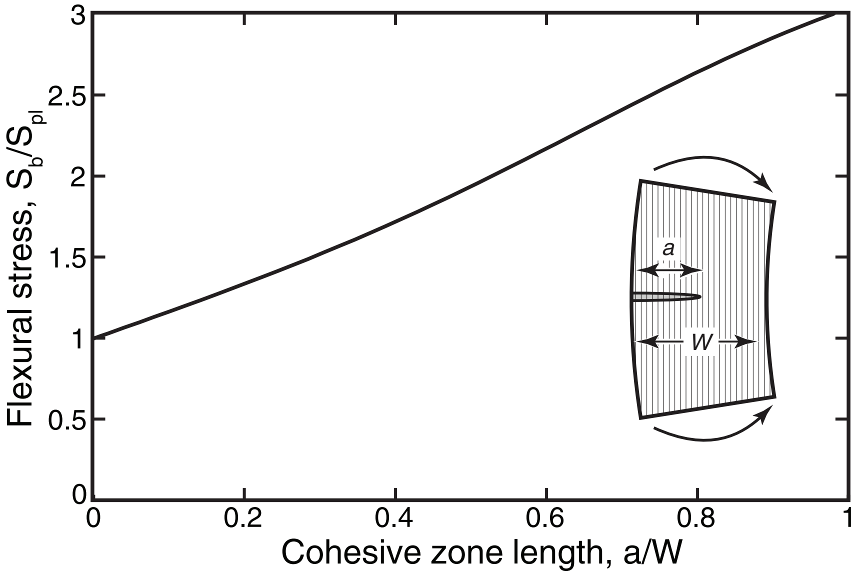

Figure 2.13: Flexural stress corresponding to the growth of a localized deformation band through a bend specimen.

Chapter 3

Steady-state matrix cracking of unidirectional CMCs in shear

3.1 Introduction

As intimated in Chapter 1, a general constitutive model for the inelastic mechanical response of fiber-reinforced ceramic composites must account for both on- and off-axis loading. Therefore, with respect to ply response, the key inelastic properties are those measured in tension and in shear parallel to the fiber axis. The latter is the focus of the present chapter. Specifically, the principal objective is to develop the mechanics underlying the onset of matrix cracking in fiber-reinforced ceramic composites under shear loading. The study is restricted to *unidirectional* materials, with the understanding that some modification will be required to adapt the results to multidirectional laminates. The focus is on the stress distributions in the fibers and matrix before and after matrix cracking. The corresponding differences in total potential energy are used to determine the critical applied shear stress for cracking under steady-state conditions.

The outline of the chapter is as follows. First, a governing equation, adapted from the work of Budiansky et al. (1986), is presented for the steady-state matrix cracking stress in shear. The driving force for crack growth is seen to depend upon the differences in stresses in the uncracked and cracked states. Second, the stresses in the *uncracked* composite are approximated using an analytical model, originally developed by Hashin and Rosen (1964), for a cylindrical unit cell undergoing shear loading. Third, the stresses in the *cracked* composite are obtained from finite element (FE) analyses of a representative volume element (RVE). The model employs periodic boundary conditions that ensure stress and displacement continuity between adjacent RVEs. The approach is highly versatile: effects of fiber volume fraction, fiber and matrix constitutive properties, matrix crack spacing, and interface constitutive behavior can be readily explored. Fourth, the results of the FE model are used to guide the development of approximate analytical solutions for fiber and matrix stresses in a cracked composite. Comparison with the FE results shows that the analytical results yield the correct scalings with constituent properties. Finally, using the analytical results for the stresses within the fibers and the matrix in the cracked and uncracked states, expressions are derived for the steady-state matrix cracking stress in shear. The cracking stress in shear and that in tension (Aveston et al., 1971; Budiansky et al., 1986) are found to exhibit similar (though not identical) scalings with the constituent properties.

As a prelude to the results that follow, two key differences between the shear cracking problem considered here and the tensile cracking problem addressed by Aveston et al. (1971) and Budiansky et al. (1986) are highlighted. The discussion is restricted to cases where the fiber/matrix interfaces are initially unbonded but frictionally-coupled. (Additional complications arise if the interfaces are initially bonded.) Accompanying schematic illustrations are shown in Figure 3.1. (i) In tension, prior to cracking, there is no driving force for interfacial separation or slip and thus the material response is purely elastic: obtaining stresses and strain energies for this state is trivial. In contrast, when the composite is loaded in shear, the fiber-matrix interface experiences a shear stress that varies linearly across the fiber diameter: the maximum occurring at the the two 'poles' and zero stress occurring along the fiber midplane. This raises the possibility of interfacial slip prior to matrix cracking.

Furthermore, the non-uniformity of the shear stresses adds complexity to the prediction of the slip processes. (ii) In tension, after cracking, frictional slip occurs in an axisymmetric manner, significantly simplifying the stress analysis. In contrast, in shear, frictional slip manifests itself in two distinct ways. In the first, termed 'antisymmetric slip', the average axial displacements of the fiber and the matrix are identical. (The 'average' is computed by integrating the quantity over the interface at a particular value of the axial coordinate x). In this case, the matrix slips positively relative to the fiber along one half of the interface and negatively with respect to the fiber along the other half. In the second, termed 'axial slip,' the average axial displacements of the fiber and the matrix differ. It is shown below that this occurs as a consequence of the *tensile* stresses developed within the fiber after matrix cracking in shear.

3.2 Matrix cracking model

The critical stress for steady-state matrix cracking in shear is derived using a fracture mechanics-based approach, closely analogous to that presented by Budiansky et al. (1986) for matrix cracking in axial tension. The driving force for crack growth is the potential energy difference between the cracked and uncracked segments; crack growth occurs when this energy difference is equal to the fracture resistance. Computation of the potential energy difference requires stresses in the 'upstream' and the 'downstream' locations with respect to the crack tip.

The fibers are assumed to be frictionally-coupled but initially *unbonded* from the matrix (i.e., the interfacial toughness is zero). It is shown below that, in cases where the conditions for frictional slip are met in the uncracked state, the introduction of a matrix crack leaves the shear stresses in the fibers and the matrix largely unaffected. However, the presence of the matrix crack creates axial tension in the fibers and axial compression in the matrix. The differences in these stresses provide the driving force for cracking; the corresponding resistance is the energy needed to create the matrix crack surfaces. The governing equation for steady-state growth of a shear crack is found through an adaptation of Equation 11 in Budiansky et al. (1986), notably:

$$\frac{1}{2A_c}\int_{-\infty}^{\infty}\int_{A_c}(\boldsymbol{\sigma}^U-\boldsymbol{\sigma}^D):(\boldsymbol{\epsilon}^U-\boldsymbol{\epsilon}^D)\,\mathrm{d}A\,\mathrm{d}x=\sqrt{2}V_m\mathcal{G}_m \tag{3.1}$$

Here, $\boldsymbol{\sigma}$ and $\boldsymbol{\epsilon}$ are stress and strain tensors, respectively, in the upstream (U) and downstream (D) locations. The area integral is taken over a representative cross-sectional area of the composite, A_c, comprising a fiber and the surrounding matrix jacket. The x-direction is aligned with the fiber axis, $\mathcal{G}_m$ is the fracture energy of the matrix, and the factor $\sqrt{2}$ accounts for the fact that the crack is oriented at 45° to the fiber axis. Equation 3.1 assumes that no point on the fiber-matrix interface experiences variable-direction slip between the upstream and downstream states, and that the slip process at each point occurs at a constant sliding stress.

As demonstrated in a forthcoming section, the upstream stresses can be well approximated using an analytical model of a cylindrical unit cell (Section 3.4). In contrast, the downstream stresses are not amenable to a fully analytical solution. Consequently, finite element analyses (Section 3.3) are used to generate numerical results that are then used to guide the formulation of semi-analytical solutions that capture the dominant stress components (Section 3.5). The stresses are then combined with Equation 3.1 in order to ascertain the steady-state matrix cracking stress (Sections 3.6 and 3.7).

3.3 Finite element model

3.3.1 Geometry and mesh

One crucial consideration in computational micromechanical modeling is the fidelity with which heterogeneities in microstructure are captured. In laminates undergoing shear loading, the fibers and the matrix cracks are generally distributed non-uniformly. Capturing these heterogeneities requires that at least tens of fibers and several matrix cracks comprise the RVE; the minimum size of the resulting RVE for a typical composite with fiber diameter $d = 10\,\mu\text{m}$

would be approximately 100 μm × 100 μm × 1 mm. Assuming that an element size of $d/10$ is necessary to properly resolve local stresses, a conservative estimate of the number of elements within such a model is 10^7: beyond that which is computationally feasible. (Note that this situation contrasts markedly with RVE models used to compute the deformation response of *polymer* matrix composites (PMCs). In PMCs undergoing plastic deformation, the length of the RVE can be taken to be arbitrarily small, thereby allowing for a large number of fibers with non-uniform spacing to be readily tackled with existing computational capabilities (see, for instance, Totry et al. (2010)).)

In order to strike a balance between computational efficiency and model accuracy, the fibers are assumed to be are arranged in a regular, square array and the matrix cracks are assumed to be evenly spaced. The RVE thus becomes a parallelepiped unit cell, composed of a single fiber enclosed in a cracked matrix jacket (Figure 3.2(a)). The unit cell is tiled in space in a staggered manner to generate the entire unidirectional composite. The two cell dimensions transverse to the fiber axis, $L_y = L_z$, are equivalent to the center-to-center fiber spacing and the fiber volume fraction is related to the dimensions by $V_f = \pi d^2/4L_y^2$. The third RVE dimension, L_x, represents the matrix crack spacing. In principle, the matrix crack can be positioned anywhere within the RVE; here it is located centrally to preserve the antisymmetry of the deformation. The origin of the coordinate system defining material locations is taken to be the intersection of the matrix crack plane with the fiber axis.

Finite element simulations were conducted in ABAQUS Standard (Version 6.9-EF1, Dassault Systèmes). The mesh was carefully constructed to enable application of periodic boundary conditions (Section 3.3.2). Specifically, when a node exists on the boundary of the RVE, all points equivalent to it—i.e., points that are periodically related to it—must also exist as nodes on the boundary of the RVE. This condition was operationally realized using the following procedure. First, a 2-D mesh was generated of a fiber enclosed by a matrix jacket. In the 2-D mesh, both the left and right edges as well as the top and bottom edges contained periodic pairs of nodes. Furthermore, the fiber and matrix nodes were constructed to be coincident at the fiber-matrix interface; this choice was found to greatly reduce numerical oscillations in contact pressure along the interface. The mesh was then transformed to create the (45°) right face of the unit cell, and was swept in the x-direction to generate the entire parallelepiped. Because the mesh is swept, the 4-noded elements that comprise the 2-D mesh become 8-noded bricks within the 3-D mesh. Finally, the matrix crack was inserted by dividing the matrix jacket into two separate parts. A typical finite element simulation used first-order, reduced integration elements (C3D8R) with a characteristic length of 5 % of the fiber diameter; for typical matrix crack spacings (e.g. $L_x/d = 10$), the total number of elements within the model was approximately 120 000. For a limited number of representative simulations, a study was performed to ensure that the quantities of interest (e.g. fiber bending stress) converged with respect to mesh density.

3.3.2 Boundary conditions

The boundary conditions were designed to create a state of simple shear and to enforce stress and displacement continuity between adjacent RVEs. Both objectives are met by utilizing the periodicity condition (Suquet, 1987; Xia et al., 2003). Displacements on the boundary of a RVE are decomposed into two parts: a systematic component, which is related to the applied strain field, and a periodic component, which is generally unknown. The condition can be expressed as (Suquet, 1987; Xia et al., 2003):

$$u_i = \hat{\epsilon}_{ik} x_k + u_i^* \tag{3.2}$$

where u_i is the displacement of the point in the i-direction, $\hat{\epsilon}_{ik}$ is the tensor of *average* applied strains, x is the position of the point, and u_i^* is the periodic component of displacement in the i-direction. For points within the RVE that are equivalent (i.e., periodically related to one another), u_i^* must be identical. This ensures that the deformations of neighboring RVEs are compatible. By considering *differences* in displacements between equivalent points, the periodic component of displacement cancels out, which results in a simple relationship between the displacement difference and the applied strain.

To formulate the displacement difference for the parallelepiped unit cell, the three pairs of surfaces in the unit cell that are equivalent/periodic (see Figure 3.2(b)) are identified: (i) the right (R) and left (LF) surfaces of the fiber and matrix; (ii) the top (T) and bottom (BM) surfaces of the matrix; and (iii) the front (F) and back (BK) surfaces of the matrix. For surface pair (i), the following expressions are obtained:

$$\begin{aligned} u_x(R) - u_x(LF) &= \hat{\epsilon}_{xx} L_x \\ u_y(R) - u_y(LF) &= \hat{\epsilon}_{yx} L_x \\ u_z(R) - u_z(LF) &= \hat{\epsilon}_{zx} L_x \end{aligned} \tag{3.3}$$

Similarly, for surface pair (ii),

$$\begin{aligned} u_x(T) - u_x(BM) &= -\hat{\epsilon}_{xx} \Delta x + \hat{\epsilon}_{xy} L_y \\ u_y(T) - u_y(BM) &= -\hat{\epsilon}_{yx} \Delta x + \hat{\epsilon}_{yy} L_y \\ u_z(T) - u_z(BM) &= -\hat{\epsilon}_{zx} \Delta x + \hat{\epsilon}_{zy} L_y \end{aligned} \tag{3.4}$$

where $\Delta x = L_y$ since the left and right surfaces are oriented at 45° to the x-axis.

Ideally, the boundary conditions would be written so that either average *strains* or average *stresses* could be prescribed. In their current form, Equations 3.3 – 3.4 allow only average strains to be imposed. To correct this deficiency, three 'fictitious' nodes, denoted Fx, Fy, and Fz, are constructed. The nodes are fictitious in the sense that they are not part of either the fiber or matrix meshes. Instead, they are connected to 'real' nodes on the RVE boundary through constraint equations. A length, $L(Fj) = L_j$, and an area, $A(Fj) = V/L_j$, are associated with each fictitious node Fj (where $V = L_x L_y L_z$). Each strain component is written in terms of the displacement of a fictitious node, $u(Fj)$:

$$\hat{\epsilon}_{ij} = \frac{u_i(Fj)}{L(Fj)} \tag{3.5}$$

Combining with Equation 3.4, for instance, yields:

$$\begin{aligned} u_x(T) - u_x(BM) &= -\frac{\Delta x}{L_x} u_x(Fx) + u_x(Fy) \\ u_y(T) - u_y(BM) &= -\frac{\Delta x}{L_x} u_y(Fx) + u_y(Fy) \\ u_z(T) - u_z(BM) &= -\frac{\Delta x}{L_x} u_z(Fx) + u_z(Fy) \end{aligned} \tag{3.6}$$

Similarly, each stress component is written in terms of the force applied to a fictitious node, $F(Fj)$:

$$\hat{\sigma}_{ij} = \frac{F_i(Fj)}{A(Fj)} \tag{3.7}$$

To impose an average strain, a displacement is applied to the appropriate fictitious node according to Equation 3.5; to impose an average stress, a force is applied according to Equation 3.7. In the case of zero average stress, zero force is applied to the fictitious node: the node relaxes to ensure that the net reaction force is zero. The fictitious node approach is versatile in that a mixture of stress and strain conditions can be enforced. In the case of simple shear loading considered here, two *strain* components are prescribed ($\hat{\epsilon}_{xy} = 0$, $\hat{\epsilon}_{yx} = \gamma$), and all stress components apart from σ_{xy} (= σ_{yx}) are set to zero.

3.3.3 Constitutive behavior

The fibers and matrix were assumed to be linear elastic and isotropic with a Poisson's ratio of 0.2 (a value representative of ceramics). Two surface interactions were specified: that between the matrix crack faces (when present) and that between the fiber and the matrix. The matrix crack faces were allowed to undergo frictionless slip in the tangential direction and were subjected to 'hard contact' in the normal direction. (As a practical matter, the crack faces are found to separate during shear loading and thus the results are unaffected by the prescribed contact interaction.) Frictional slip between the fiber and the matrix was allowed to occur at a critical value of the interfacial shear stress τ_s, as in the works of Aveston et al. (1971) and Curtin (1991b). This interaction was implemented in ABAQUS using a Coulomb friction law with a shear stress 'cap.' In this model, no interaction occurs between the fiber and the matrix when the interface is open. In contrast, when the interface is closed, with contact pressure $p > 0$, either a 'sticking' or a 'slip' condition obtains, depending on the interfacial shear stress. The critical shear stress for slip is defined as $\tau_{cr} = \min(\mu p, \tau_s)$ where μ is the friction coefficient and τ_s is the shear stress 'cap.' When the equivalent shear stress[1] along the interface exceeds τ_{cr}, the fiber slides relative to the matrix and the sliding stress along the interface is equal to τ_{cr}; conversely, 'sticking' occurs if the shear stress is less than τ_{cr}. Operationally, a positive contact pressure between fiber and matrix was effected by specifying a mismatch in thermal expansion coefficients of the two phases, and subsequently imposing an isothermal temperature change that yielded the desired average interfacial pressure, $\hat{p}$. This process also yields residual axial compression in the fiber and residual axial tension in the matrix (in the x-direction). The latter stresses are on the order of $\hat{p}$ (Budiansky et al., 1986). In order to obtain an approximately constant interfacial sliding stress, the friction coefficient μ is selected to be large enough so that, when slip occurs, it does so essentially *at* τ_s.

3.4 Response of uncracked composite

3.4.1 Preliminaries

Here solutions are presented for the stress distributions in both phases and the global response of the uncracked composite under shear loading. The solu-

---

[1] The equivalent shear stress is $\tau_{eq} = \sqrt{\tau_{xr}^2 + \tau_{\theta r}^2}$, where τ_{xr} and $\tau_{\theta r}$ are the components of shear stress in the two tangential directions along the interface. The results of the simulation demonstrate that $\tau_{\theta r} = 0$ almost everywhere; τ_{eq} is dominated by the τ_{xr}, the shear stress in the axial direction.

tions rely on formulae obtained from analyses of a cylindrical unit cell (Hashin and Rosen, 1964). The diameter of the matrix jacket in this cell is taken as $d_m = d/\sqrt{V_f}$. Displacements (in cylindrical coordinates) are taken to have the form:

$$\begin{aligned} u_r &= Cx \sin\theta \\ u_\theta &= Cx \cos\theta \\ u_x &= \left(Ar + \frac{B}{r}\right) \sin\theta \end{aligned} \tag{3.8}$$

All stress components are zero, except:

$$\begin{aligned} \sigma_{x\theta} &= G\left(A + C + \frac{B}{r^2}\right) \cos\theta \\ \sigma_{xr} &= G\left(A + C - \frac{B}{r^2}\right) \sin\theta \end{aligned} \tag{3.9}$$

where G is the shear modulus of the appropriate phase. There are six unknown constants: A, B, and C for each of the two phases. They are obtained by assigning appropriate boundary conditions. Continuity of radial displacement (u_r) and shear stress (σ_{xr}) must hold at the fiber-matrix interface ($r = d/2$). The shear stress σ_{xr} at the external boundary ($r = d_m/2$) must equal the applied shear traction, which has the form $\tau^0_{app}(r,\theta) = \tau_{app} \sin\theta$. Also, the applied shear traction must be in equilibrium with the resultant of the shear stresses along a plane of constant x. The condition for *axial* displacements (u_x) at the fiber-matrix interface depends on the state of the interface. That is, when the applied stress is sufficiently small, the interface remains unslipped and the axial displacements in the fiber and the matrix are equal. The solutions for this scenario are presented in Section 3.4.2. Conversely, when the applied stress is large, antisymmetric slip occurs between the fiber and the matrix, and the condition of continuity of u_x is no longer met. The pertinent solutions are presented in Section 3.4.3. The analytical predictions are assessed through comparisons with results from finite element solutions for several cases of practical interest.

With the stresses and strains in hand, the tangent modulus of the unit cell is derived using the principle of virtual work. All stresses, strains and displacements are expressed in terms of the applied shear load P (for a unit cell in shear, $P = \pi d_m^2 \tau_{app}/4$). The statement reads:

$$\int\limits_V \boldsymbol{\sigma}(P) : \delta\boldsymbol{\epsilon}(P)\,\mathrm{d}V + \int\limits_S \tau\delta\Delta u_\tau(P)\,\mathrm{d}S = P\delta u_P(P) \tag{3.10}$$

where Δu_τ is the difference in axial (u_x) displacement between the fiber and matrix, and u_P is the shear displacement of the cell (i.e., the work conjugate to P).

Using the chain rule,

$$\int\limits_V \boldsymbol{\sigma}(P) : \frac{\mathrm{d}\boldsymbol{\epsilon}(P)}{\mathrm{d}P}\delta P\,\mathrm{d}V + \int\limits_S \tau\frac{\mathrm{d}\Delta u_\tau(P)}{\mathrm{d}P}\delta P\,\mathrm{d}S = P\frac{\mathrm{d}u_P(P)}{\mathrm{d}P}\delta P \tag{3.11}$$

Since δP is arbitrary,

$$\frac{\mathrm{d}\tau_{app}}{\mathrm{d}\gamma} = \frac{4L_x}{\pi d_m^2}\frac{\mathrm{d}P}{\mathrm{d}u_P} = \frac{4L_x}{\pi d_m^2}\frac{P}{\int\limits_V \boldsymbol{\sigma}(P) : \frac{\mathrm{d}\boldsymbol{\epsilon}(P)}{\mathrm{d}P}\,\mathrm{d}V + \int\limits_S \tau\frac{\mathrm{d}\Delta u_\tau(P)}{\mathrm{d}P}\,\mathrm{d}S} \tag{3.12}$$

3.4.2 Elastic response

For small applied stresses, the composite response is elastic. In this scenario, analytical solutions for the constants A, B, and C (previously presented by Hashin and Rosen (1964)) are:

$$\begin{aligned}
A_m &= \frac{\tau_{app}(G_m + G_f)}{G_m(G_m V_m + G_f(1+V_f))} - C_0 \\
B_m &= \frac{d^2 \tau_{app}(G_m - G_f)}{4G_m(G_m V_m + G_f(1+V_f))} \\
A_f &= \frac{2\tau_{app}}{G_m V_m + G_f(1+V_f)} - C_0 \\
B_f &= 0 \\
C_f &= C_m = C_0
\end{aligned} \tag{3.13}$$

where C_0 is an unknown constant related to rigid body rotation that does not affect the stresses. Combining with Equation 3.9 yields the pertinent stresses:

$$\begin{aligned}
\sigma_{xr,f} &= \frac{2G_f}{G_m V_m + G_f(1+V_f)} \tau_{app} \sin\theta \\
\sigma_{x\theta,f} &= \frac{2G_f}{G_m V_m + G_f(1+V_f)} \tau_{app} \cos\theta \\
\sigma_{xr,m} &= \frac{G_m(1-(d/2r)^2) + G_f(1+(d/2r)^2)}{G_m V_m + G_f(1+V_f)} \tau_{app} \sin\theta \\
\sigma_{x\theta,m} &= \frac{G_f(1-(d/2r)^2) + G_m(1+(d/2r)^2)}{G_m V_m + G_f(1+V_f)} \tau_{app} \cos\theta
\end{aligned} \tag{3.14}$$

Further combining these results with Equation 3.12 recovers the result for the shear modulus from the composite cylinder assemblage (CCA) model (Hashin, 1983):

$$G_{xy} = \frac{\mathrm{d}\tau_{app}}{\mathrm{d}\gamma} = G_m \frac{G_f(1+V_f) + G_m V_m}{G_f V_m + G_m(1+V_f)} \tag{3.15}$$

Comparisons of stress distributions for one specific case are shown in Figure 3.3. Very good agreement is obtained within the entire fiber and over most of the matrix volume; differences naturally arise at the cell boundaries because of the differing cell cross-sections (circular vs. square). Moreover, stress components predicted to be zero by the analytical model (σ_{xx}, σ_{yy}, σ_{zz}, and σ_{yz}) are indeed very small (after subtracting the residual stresses) in the finite element simulations (not shown). Analogous comparisons for other material property combinations yielded similarly good agreement.

Comparisons of the global shear response are presented in Figure 3.4. Here the fiber is assumed to be ceramic grade Nicalon (210 GPa), the fiber volume fraction is 0.2 or 0.4, and the matrix modulus E_m is selected to be representative of one of three common matrix materials: 37 GPa for carbon, 100 GPa for glass-ceramics, and 400 GPa for SiC. For all cases, the analytical predictions and the computational results agree to within 0.6 %. The agreement indicates that the difference in the unit cell geometry in the finite element and analytical models is inconsequential for prediction of macroscopic properties.

3.4.3 Inelastic response

For sufficiently large applied stresses, the composite response is inelastic because antisymmetric slip occurs between the fiber and matrix. The condition of continuity of u_x at $r = d/2$ is replaced by the condition that the shear stress σ_{xr} at $r = d/2$ must equal the frictional sliding stress, which must take the form $\tau(r,\theta) = \tau_{s2}\sin\theta$. To maintain consistency with the FE model, where $|\tau(r,\theta)| = \tau_s$ everywhere, the effective sliding stress τ_{s2} is selected to be that which gives the equivalent frictional dissipation during sliding, notably $\tau_{s2} = 4\tau_s/\pi$. Using these formulae yields:

$$\begin{aligned} A_m &= \frac{\tau_{app} - \tau_{s2}V_f}{G_m V_m} - C_0 \\ B_m &= \frac{d^2(\tau_{app} - \tau_{s2})}{4G_m V_m} \\ A_f &= \frac{\tau_{s2}}{G_f} - C_0 \\ B_f &= 0 \\ C_f = C_m &= C_0 \end{aligned} \tag{3.16}$$

Combining with Equation 3.9 gives the stresses as:

$$\begin{aligned} \sigma_{xr,f} &= \tau_{s2}\sin\theta \\ \sigma_{x\theta,f} &= \tau_{s2}\cos\theta \\ \sigma_{xr,m} &= \frac{(\tau_{app} - \tau_{s2}V_f) - (\tau_{app} - \tau_{s2})(d/2r)^2}{V_m}\sin\theta \\ \sigma_{x\theta,m} &= \frac{(\tau_{app} - \tau_{s2}V_f) + (\tau_{app} - \tau_{s2})(d/2r)^2}{V_m}\cos\theta \end{aligned} \tag{3.17}$$

Additionally, the tangent modulus at large applied stresses becomes

$$\frac{\mathrm{d}\tau_{app}}{\mathrm{d}\gamma} = G_m \frac{V_m}{1 + V_f} \tag{3.18}$$

This is identical to the shear modulus predicted by the CCA model (Equation 3.15) when $G_f \to 0$. The applied stress, τ_{app}^{tr}, at which the response transitions from Equation 3.15 to Equation 3.18 can be derived by equating the interfacial shear stress for the unslipped composite to the shear sliding stress. Doing so yields:

$$\tau_{app}^{tr} = \frac{G_f(1 + V_f) + G_m V_m}{2G_f} \tau_{s2} \tag{3.19}$$

For typical constituent properties, τ_{app}^{tr} is of the same order as τ_s.

Comparisons of stress distributions in the fiber and the matrix for one case are shown in Figure 3.5. Again, very good agreement is obtained between analytical predictions and computational results over most of the unit cell volume; differences arise at the cell boundaries because of differences in cell geometry. The predicted global responses (plotted in Figure 3.6) are also in close agreement. Specifically, the tangent moduli in the high stress domain agree within 2 % for all cases. The stress at which the behavior transitions from elastic to inelastic is also predicted fairly well, although the computational stress-strain curve is somewhat ‘smeared’ at the transition point. The latter occurs because the interfacial shear stress distribution must transition from the sinusoidal spatial variation to a step-like one over a finite strain range.

3.5 Response of cracked composite

3.5.1 Preliminaries

No simple analytical model exists for the stresses in the cracked unit cell. Consequently, finite element simulations are employed to establish the form of the dominant stress components for cases of practical interest, and, in turn, to develop approximate analytical solutions for these stress components. The baseline FE simulation assumes a matrix crack spacing of $L_x/d = 10$, which is large enough to differentiate the stresses arising from the presence of the matrix crack from the far-field stresses. The parameter values for this and other simulations are summarized in Table 3.1.

The principal result that arises from the FE simulations is that large bending and tensile stresses develop within the fiber adjacent to the matrix crack, as conjectured by Brøndsted et al. (1994). To illustrate, the distribution of σ_{xx} within the fiber (at $z = 0$) for the baseline simulation is shown in Figure 3.7. The maximum tensile stress within the fiber, roughly 1.3 GPa, is more than an order of magnitude larger than the applied shear stress (100 MPa). Furthermore, the difference between the magnitude of stresses on the tensile and compressive faces indicates that a net tensile stress—again, significantly in excess of the applied shear stress—is also present.

3.5.2 Free body analysis

The origin of the tensile and bending stresses in the fibers can be understood through a two-dimensional free body analysis of the unit cell (Figure 3.8(a)). (For convenience, the unit cell selected for this analysis differs slightly from the one depicted in Figure 3.2, in that the matrix crack planes lie along the left and right surfaces rather than in the cell center.) The R vectors are force resultants, obtained by integrating the traction over the surface. As discussed by Xia et al. (2003), the average stress within the unit cell, $\hat{\sigma}$, can be expressed as

$$\hat{\sigma}_{ij} = \frac{1}{V}\int\limits_V \sigma_{ij}\,\mathrm{d}V = \frac{1}{V}\int\limits_S \sigma_{ik}x_j n_k\,\mathrm{d}S = \frac{1}{V}\int\limits_S T_i x_j\,\mathrm{d}S \tag{3.20}$$

where V is the volume of the unit cell ($V = L_x L_y L_z$), n is the surface normal, and T is the surface traction. Combining this equation with the condition of stress periodicity yields the following relationships:

$$\begin{aligned}
\hat{\sigma}_{xx} &= \frac{1}{V}(R_{fx}L_x - R_{mx}L_y) \\
\hat{\sigma}_{xy} &= \frac{1}{V}R_{mx}L_y \\
\hat{\sigma}_{yx} &= \frac{1}{V}(R_{fy}L_x - R_{my}L_y) \\
\hat{\sigma}_{yy} &= \frac{1}{V}R_{my}L_y
\end{aligned} \tag{3.21}$$

Solving (with $\hat{\sigma}_{xy} = \hat{\sigma}_{yx}$),

$$\begin{aligned} R_{fx} &= (\hat{\sigma}_{xx} + \hat{\sigma}_{xy}) L_y L_z \\ R_{mx} &= \hat{\sigma}_{xy} L_x L_z \\ R_{fy} &= (\hat{\sigma}_{yy} + \hat{\sigma}_{xy}) L_y L_z \\ R_{my} &= \hat{\sigma}_{yy} L_x L_z \end{aligned} \tag{3.22}$$

For shear loading, $\hat{\sigma}_{xx} = \hat{\sigma}_{yy} = 0$ and $\hat{\sigma}_{xy} = \hat{\sigma}_{yx} = \tau_{app}$. Therefore, the force resultants become

$$\begin{aligned} R_{fx} &= \tau_{app} L_y L_z \\ R_{mx} &= \tau_{app} L_x L_z \\ R_{fy} &= \tau_{app} L_y L_z \\ R_{my} &= 0 \end{aligned} \tag{3.23}$$

The net tension arises because R_{fx} is not zero. Rearranging Equation 3.23 (using $L_y = L_z$ and $V_f = \pi d^2 / 4L_y^2$) reveals that both the average tensile and average shear stresses on the fiber at the matrix crack plane equal τ_{app}/V_f.

Ancillary relationships are established by enforcing mechanical equilibrium for the individual phases (fiber and matrix) of the composite (Figures 3.8(b) and (c)). Considering first the matrix, a pressure distribution must develop along the fiber-matrix interface in order to preserve angular equilibrium. The results of the finite element simulation indicate that the 'contact patch' between fiber and matrix is confined to a small region around the matrix crack of length ≈ (1–1.5)d (in the x-direction). This is indicated schematically by a distributed load in Figure 3.8(b). The fiber must be subjected to a distributed load of equal magnitude and of opposite sign. Inspection of Figure 3.8(c) clearly reveals that local bending of the fiber in the vicinity of the matrix crack will result.

3.5.3 Fiber stress distribution

The importance of the various stress components within the fiber can be parsed in an approximate way by considering their relative contributions to the total elastic strain energy. This analysis (which neglects the Poisson effect) reveals that, for the unit cell with crack spacing $L_x/d = 10$, σ_{xx} accounts for 75–80 % of the strain energy in the fiber and σ_{xy} accounts for an additional 10 %. The strain energy from the remaining stress components is mostly confined to a narrow 'core' adjacent to the matrix crack, where contact stresses are significant: approximately 95 % of this remaining strain energy lies within a distance $\overline{L}_y$ of $\overline{x} = 0$.

In light of the preceding results, the dominant stresses within the fiber can be captured by accounting for bending and axial tension in the following way. Shear stresses within the fiber are entirely attributable to bending; these stresses are significant compared to the bending stresses because the length over which bending persists is not very large compared to the fiber diameter (i.e., the Bernoulli-Euler assumption does not hold). Equation 3.23 implies, crucially, that both the average shear and the average axial stress in the fiber at $x = 0$ scale with τ_{app}/V_f. Therefore, a suitable normalization (denoted by an overbar) for fiber stresses is $\overline{\sigma} = \sigma V_f / \tau_{app}$. Positions and other geometrical quantities are normalized by the fiber diameter: e.g. $\overline{x} = x/d$, $\overline{A} = A/d^2 = \pi/4$, $\overline{I} = I/d^4 = \pi/64$, where x is the axial coordinate, A is the area of the fiber, and I is the second moment of area. Two functions are taken as unknown: the normalized moment, $\overline{M}(\overline{x}) = M(\overline{x}) V_f / (\tau_{app} d^3)$, and the normalized axial stress, $\overline{\sigma}(\overline{x}) = \sigma(\overline{x}) V_f / \tau_{app}$. Using these normalizations, σ_{xx} and σ_{yy} within the fiber can be expressed as

$$\overline{\sigma}_{xx}(\overline{x},\overline{y}) = \frac{V_f}{\tau_{app}} \sigma_{xx}(\overline{x},\overline{y}) = \frac{\overline{M}(\overline{x})}{\overline{I}} \overline{y} + \overline{\sigma}(\overline{x}) \tag{3.24}$$

and

$$\overline{\sigma}_{xy}(\overline{x}) = \frac{V_f}{\tau_{app}} \sigma_{xy}(\overline{x}) = \frac{1}{\overline{A}} \frac{\mathrm{d}\overline{M}(\overline{x})}{\mathrm{d}\overline{x}} \tag{3.25}$$

where σ_{xy} is the average shear stress over the fiber cross-section. The normalized distributions $\overline{M}(\overline{x})$ and $\overline{\sigma}(\overline{x})$, depicted in Figures 3.9 and 3.10, are obtained by fitting the σ_{xx} stresses from the FE simulations to the form suggested by Equation 3.24. That Equation 3.24 describes the stress distribution well can be seen in Figure 3.7: at a given value of x, the distribution in σ_{xx} is approximately linear in y. The agreement between $\overline{M}$ obtained from Equation 3.24

and that obtained from Equation 3.25 (not shown) is also quite good. Taken together, these results indicate that fiber bending and tension are indeed the dominant deformation modes.

The results for $\overline{M}(\overline{x})$ for the base simulation are shown by the solid line in Figure 3.9; those for all other simulations (summarized in Table 3.1) are shown by the dashed lines. Evidently, $\overline{M}(\overline{x})$ is insensitive to the interfacial sliding stress, interfacial pressure, and matrix crack spacing (provided it is large enough that no interaction between matrix cracks occurs), and only weakly sensitive to the ratio of the matrix modulus to fiber modulus. Any effect arising from these variables reflects minor changes in the shape of the pressure distribution at the fiber-matrix contact patch. Furthermore, normalization of the fiber stress by τ_{app}/V_f essentially eliminates the effects of both τ_{app} and V_f, consistent with the conclusions drawn from the free body analysis.

Representative numerical results for the axial fiber stress distribution $\overline{\sigma}(\overline{x})$ are shown in Figure 3.10 for the base simulation with $L_x/d = 15$. (Results for the other simulations (not shown) are similar, with exceptions discussed below.) The axial stress in the fiber is largest at $x = 0$ and decays away from the matrix crack plane because of frictional slip between the fiber and the matrix. The distribution of axial stress in the fiber can be rationalized using a basic shear-lag model. In this model, the stress decays away from the matrix crack at a rate $\mathrm{d}\sigma/\mathrm{d}x = -4\tau_s/d$ until it reaches its initial (residual) value. The resulting stress distribution is given by

$$\overline{\sigma}(\overline{x}) \approx \begin{cases} 1 - \dfrac{4\tau_s V_f}{\tau_{app}}|\overline{x}|, & |\overline{x}| < \overline{L}_{ax} \\ \dfrac{\sigma_{xx}^{f,I} V_f}{\tau_{app}}, & |\overline{x}| \geq \overline{L}_{ax} \end{cases} \tag{3.26}$$

where $\sigma_{xx}^{f,I}$ is the residual stress in the fiber and $\overline{L}_{ax} = L_{ax}/d$ is the normalized axial slip length. Equating the two expressions in Equation 3.26 yields the slip length:

$$\overline{L}_{ax} \approx \frac{\tau_{app}/V_f - \sigma_{xx}^{f,I}}{4\tau_s} \tag{3.27}$$

The predictions of the shear-lag model are in excellent agreement with the FE results over much of the slip zone; discrepancies arise only in the 'core' region (within a distance of about ± (1–2)d from the crack plane) and in the transition zone to the residual stress. The latter is a consequence of elastic shear transfer where the interfacial shear stress is insufficient for axial slip. (Additional discrepancies arise when the axial slip length exceeds the length of the RVE, but these are merely artifacts of the finite RVE length, selected for computational expediency; the real composite would be essentially infinitely long before the first steady-state matrix crack would emerge and thus there would be no interactions with the boundaries.)

The agreement between the shear-lag model and the FE results breaks down when partial separation between the fiber and matrix occurs. This behavior is observed in the 'core' region, as well as when as the interfacial pressure, $\hat{p}$, becomes vanishingly small. If the interface is partially separated, the stress decay occurs at a rate lower than that predicted by the shear-lag model, which is based on full contact. But the results in this limit are not expected to be representative of real composite materials. The reason is that, whereas the model assumes that no shear stresses can be transmitted along the interface for even an infinitesimal separation distance, the finite roughness of real interfaces will enable such transfer even after separation is predicted to occur. Thus, the shear-lag model should provide a satisfactory description of the axial stresses even in regions where the computational model predicts partial separation.

3.5.4 Matrix stress distribution

The dominant stress components in the matrix are σ_{xx}, σ_{xy}, and σ_{xz}; the cumulative strain energy from these components comprises 70–85 % of the total strain energy in the matrix (for $L_x/d = 10$), depending somewhat on the fiber volume fraction. (The contribution is even larger for larger matrix crack spacings.) The axial compressive stress σ_{xx} counterbalances the axial tension in the fiber. The shear stresses σ_{xy} and σ_{xz} arise from shearing of the matrix jacket, and are present even in the uncracked unit cell (Section 3.4). The remaining stress components are again confined to the 'core' region surrounding the crack: approximately 85 % of the strain energy from σ_{yy}, σ_{yz}, and σ_{zz} lies within $\pm\overline{L}_y$ of $\overline{x} = 0$.

Figure 3.11 shows comparisons of the shear stresses (σ_{xy} and σ_{xz}) in the matrix of the cracked body at the edge of the core region (at $|\overline{x}| = \overline{L}_y$) and those in the uncracked body, at an applied stress significantly larger than the interfacial sliding stress. Evidently the matrix shear stresses are almost identical before and after matrix cracking. Moreover, at greater distances from the crack plane ($|\overline{x}| > \overline{L}_y$), the stresses grow ever closer and become identical in the limit as $|\overline{x}| \to \infty$. The key implication is that the potential energy difference associated with matrix shear stresses is negligible (apart from that inside the core region).

The axial compressive stress in the matrix can be estimated reasonably well by utilizing the approximate[2] condition for force equilibrium: $\sigma^f_{xx}(\overline{x})V_f + \sigma^m_{xx}(\overline{x})V_m = 0$. Rearranging this equation yields the matrix stress in terms of the axial tension in the fiber:

$$\sigma^m_{xx}(\overline{x}) = -\frac{V_f}{V_m}\sigma^f_{xx}(\overline{x}) = -\frac{\tau_{app}}{V_m}\overline{\sigma}(\overline{x}) \tag{3.28}$$

In the context of the potential energy change given by Equation 3.1, the stress in Equation 3.28 represents the only significant contribution from the matrix.

---

[2] The exact force equilibrium condition involves equilibrium on planes oriented at 45°, as discussed in Section 3.5.2. However, the approximate load equilibrium condition is highly accurate outside of the core region.

3.6 Matrix cracking in shear

The preceding results for stresses are utilized to determine the matrix cracking stress in the limit of large axial slip lengths. (The same limit was considered by Aveston et al. (1971) in deriving their classical result for the matrix cracking stress in uniaxial tension.) In this limit, the potential energy change arising from stress components confined to the near-crack ('core') region are neglected.[3] Furthermore, provided the stress for cracking is sufficiently high to cause slip to occur before cracking, the shear stresses in the constituents outside of the core region are largely unaffected by the presence of the crack and thus the only relevant stress differences, $\sigma^U - \sigma^D$, derive from the axial stresses σ_{xx}. The governing equation for steady-state matrix cracking, Equation 3.1, becomes:

$$\frac{d}{2}\int_{-\infty}^{\infty}\left[\frac{V_f}{E_f}\left(\sigma_{xx}^{f,U}-\sigma_{xx}^{f,D}\right)^2+\frac{V_m}{E_m}\left(\sigma_{xx}^{m,U}-\sigma_{xx}^{m,D}\right)^2\right]\mathrm{d}\bar{x}=\sqrt{2}V_m\mathcal{G}_m \tag{3.29}$$

Clearly, the upstream axial stresses are simply the residual stresses:

$$\begin{aligned}\sigma_{xx}^{f,U}&=\sigma_{xx}^{f,I}\\ \sigma_{xx}^{m,U}&=\sigma_{xx}^{m,I}\end{aligned} \tag{3.30}$$

where

$$V_f\sigma_{xx}^{f,I}+V_m\sigma_{xx}^{m,I}=0 \tag{3.31}$$

---

[3] Note that consideration of these energies would reduce the estimate of the matrix cracking stress.

The downstream axial stresses in the slipped region ($|\overline{x}| < \overline{L}_{ax}$) are given approximately by Equations 3.26 and 3.28. Upon combining the expressions for the upstream and downstream stresses with the governing equation for crack growth (Equation 3.29), the steady-state matrix cracking stress is obtained:

$$\tau_{cr} = \left(\frac{12\sqrt{2} V_f^2 V_m^2 E_f E_m \tau_s \mathcal{G}_m}{E_c d} \right)^{1/3} - V_m \sigma_{xx}^{m,I} \tag{3.32}$$

For comparison, the tensile cracking stress in the absence of residual stress, σ_1^0, originally derived by Aveston et al. (1971), is:

$$\sigma_1^0 = \left(\frac{12 V_f^2 E_f E_c^2 \tau_s \mathcal{G}_m}{V_m E_m^2 d} \right)^{1/3} \tag{3.33}$$

Combining with Equation 3.32 yields:

$$\tau_{cr} = \frac{2^{1/6} V_m E_m}{E_c} \sigma_1^0 - V_m \sigma_{xx}^{m,I} \tag{3.34}$$

This equation represents one of the key results of the present work. In the absence of residual stress, the ratio of cracking stresses in shear and in tension is given by

$$\frac{\tau^{cr,0}}{\sigma_1^0} = \frac{2^{1/6} V_m E_m}{E_c} \tag{3.35}$$

For typical values of constituent properties, this ratio equals 0.2–0.6.

3.7 Matrix cracking stress for arbitrary in-plane loading

The preceding results for matrix cracking in shear and in tension are extended to cracking under *arbitrary in-plane loadings*, again subject to the assumptions of large-scale slip and of slip preceding matrix cracking. Two further assumptions are made. (i) The matrix crack normal is oriented an angle θ to the fiber axis. (ii) The normal stress *transverse* to the fiber axis does not affect the cracking stress. The latter assumption is justified on the basis that this stress component does not alter the axial stresses in the fiber or the matrix. This assumption also implies that the transverse stress does not alter the interfacial constitutive behavior (e.g. by causing interfacial separation). A free-body analysis of a unit cell with a crack oriented at θ (analogous to that in Section 3.5.2) shows that the average fiber stress at the crack plane is given by

$$\sigma_{xx}^{f}(0) = \frac{\sigma_{app} + \tau_{app}\tan\theta}{V_f} \tag{3.36}$$

where σ_{app} and τ_{app} are the applied normal and shear stresses, respectively. The governing equation for steady-state matrix cracking, Equation 3.1, becomes:

$$\frac{d}{2}\int_{-\infty}^{\infty}\left[\frac{V_f}{E_f}\left(\sigma_{xx}^{f,U}-\sigma_{xx}^{f,D}\right)^2+\frac{V_m}{E_m}\left(\sigma_{xx}^{m,U}-\sigma_{xx}^{m,D}\right)^2\right]\mathrm{d}\bar{x} = V_m\mathcal{G}_m\sec\theta \tag{3.37}$$

where the term $\sec\theta$ accounts for the area associated with an inclined crack. The upstream axial stresses are given simply by the elastic solution (incorporating residual stresses):

$$\begin{aligned} \sigma_{xx}^{f,U} &= \frac{E_f \sigma_{app}}{E_c} + \sigma_{xx}^{f,I} \\ \sigma_{xx}^{m,U} &= \frac{E_m \sigma_{app}}{E_c} + \sigma_{xx}^{m,I} \end{aligned} \tag{3.38}$$

The downstream axial stresses in the slipped region are given by the shear-lag result (Equations 3.26 and 3.28), modified using Equation 3.36 to account for an arbitrarily oriented crack:

$$\sigma_{xx}^{f,D} = \begin{cases} \dfrac{\sigma_{app} + \tau_{app}\tan\theta}{V_f} - 4\tau_s|\overline{x}|, & |\overline{x}| < \overline{L}_{ax} \\ \dfrac{E_f \sigma_{app}}{E_c} + \sigma_{xx}^{f,I}, & |\overline{x}| \geq \overline{L}_{ax} \end{cases} \tag{3.39}$$

and

$$\sigma_{xx}^{m,D}(\overline{x}) = \frac{\sigma_{app} - V_f \sigma_{xx}^{f,D}(\overline{x})}{V_m} \tag{3.40}$$

Proportional loading, characterized by $\lambda = \sigma_{app}/\tau_{app}$, is assumed. Upon substituting the expressions for the upstream and downstream stresses (Equations 3.38–3.40) into the governing equation for crack growth, the steady-state cracking stresses, σ_{app}^{cr} and τ_{app}^{cr}, are obtained:

$$\begin{aligned} \sigma_{app}^{cr} &= \frac{\lambda V_m E_m \sigma_1^0 (\sec\theta)^{1/3} - \lambda V_m E_c \sigma_{xx}^{m,I}}{E_c \tan\theta + \lambda V_m E_m} \\ \tau_{app}^{cr} &= \frac{V_m E_m \sigma_1^0 (\sec\theta)^{1/3} - V_m E_c \sigma_{xx}^{m,I}}{E_c \tan\theta + \lambda V_m E_m} \end{aligned} \tag{3.41}$$

In the limit of uniaxial tension ($\lambda \to \infty$, $\theta = 0$), Equation 3.41 reduces to the tensile cracking stress derived by Budiansky et al. (1986):

$$\sigma^{cr} = \sigma_1^0 - \frac{E_c}{E_m}\sigma_{xx}^{m,I} \tag{3.42}$$

Also, in the limit of pure shear ($\lambda \to 0$, $\theta = \pi/4$), it reduces to Equation 3.34 in the preceding section. An additional case of interest is one in which tension is applied at 45° to the fiber axis. Here the steady-state cracking stress (again, in the fiber coordinate system) becomes:

$$\sigma_{app}^{cr} = \tau_{app}^{cr} = \frac{2^{1/6} V_m E_m \sigma_1^0 - V_m E_c \sigma_{xx}^{m,I}}{E_c + V_m E_m} \tag{3.43}$$

so that the 45° tensile cracking stress is:

$$\sigma_{45}^{cr} = 2\sigma_{app}^{cr} = 2\frac{2^{1/6} V_m E_m \sigma_1^0 - V_m E_c \sigma_{xx}^{m,I}}{E_c + V_m E_m} \tag{3.44}$$

In the absence of residual stress, each of these stresses scales with σ_1^0. Since $V_m E_m < E_c$, the order of the cracking stresses follows: $\sigma^{cr} > \sigma_{45}^{cr} > \tau^{cr}$.

The results in Equation 3.41 can also be expressed in the form of a 'yield surface' in σ-τ space by eliminating λ. The result is

$$\sigma_{app}^{cr} + \frac{E_c}{V_m E_m}\tau_{app}^{cr} \tan\theta = \sigma_1^0 (\sec\theta)^{1/3} - \frac{E_c}{E_m}\sigma_{xx}^{m,I} \tag{3.45}$$

The form of the yield surface is illustrated in Figure 3.12 for representative values of $V_m E_m / E_c$ (absent residual stress). The surfaces are constructed by assuming that the matrix crack is oriented normal to the maximum principal stress.

3.8 Discussion

Extension of the preceding results on unidirectional plies to composites with *multi-directional* reinforcement (e.g. cross-ply laminates) requires accounting for stresses induced by the incompatibility between deformations of individual plies. Consider, for instance, a cross-ply laminate loaded in uniaxial tension at ±45° to the fibers. A continuum-level treatment, in which each ply is treated as a homogeneous, elastic, orthotropic medium, reveals the following effects (Pipes and Pagano, 1970). Each ply experiences not only σ_{45}, the macroscopic applied tension at 45°, but also a shear stress that arises from the incompatibility of ply deformations. Its magnitude is $C\sigma_{45}$, where C is proportional to the difference between the axial and transverse stiffnesses of an individual ply. However, at a crack (or any free surface) oriented perpendicular to the direction of loading, the shear stress must vanish. Therefore, interlaminar stresses must arise at the intersection of the crack with the inter-ply boundary. These stresses decay rapidly away from the crack, over a length scale proportional to the ply thickness.

To our knowledge, a micromechanical analysis of stresses arising from incompatible ply deformations has yet to be conducted. The preceding continuum-level analysis, however, implies that these stresses can be neglected if either (i) the external state of loading does not give rise to macroscopic ply deformations that are incompatible (a notable example being shear loading); or (ii) the axial and transverse ply stiffnesses are similar, or, equivalently, the fiber and matrix moduli are similar. Therefore, the results presented in Section 3.6 (on matrix cracking in pure shear) are expected to be applicable to all cross-ply laminates (regardless of constituent properties); conversely, those in Section 3.7 (on cracking under arbitrary in-plane loads) would be restricted to cross-ply laminates in which the matrix and the fibers exhibit similar stiffness. When the 'incompatibility stresses' are non-negligible, as can be deduced from an analysis similar to that in Pipes and Pagano (1970), they provide another contribution to the crack driving force and thus reduce the estimate of the steady-state matrix cracking stress.

Table 3.1: Parameters used for FE simulations of cracked unit cell.

	V_f	L_x/d	E_f (GPa)	E_m (GPa)	τ_s (MPa)	$\hat{p}$ (MPa)	τ_{app} (MPa)
Base simulation	0.4	10	210	100	10	50	100
Other	0.2	15	100	37, 400	2	5	40

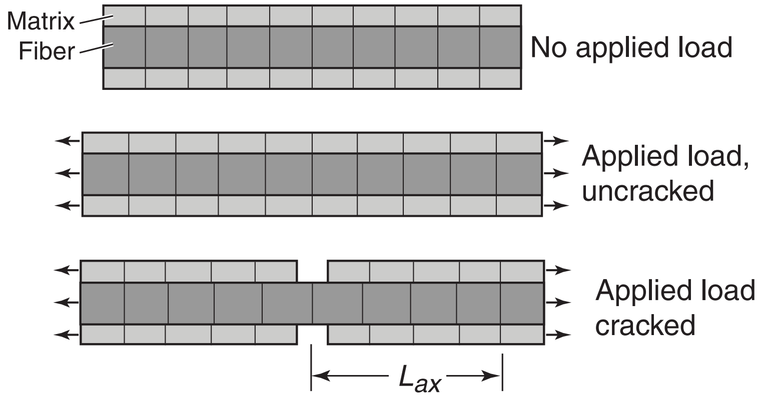

(a) TENSION

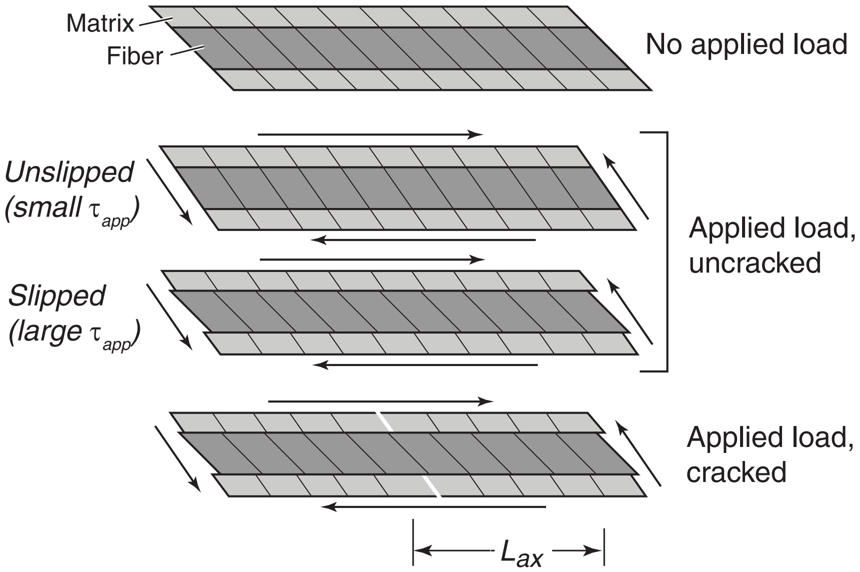

(b) SHEAR

Figure 3.1: Development of frictional slip in a unidirectional CMC in (a) tension and (b) shear.

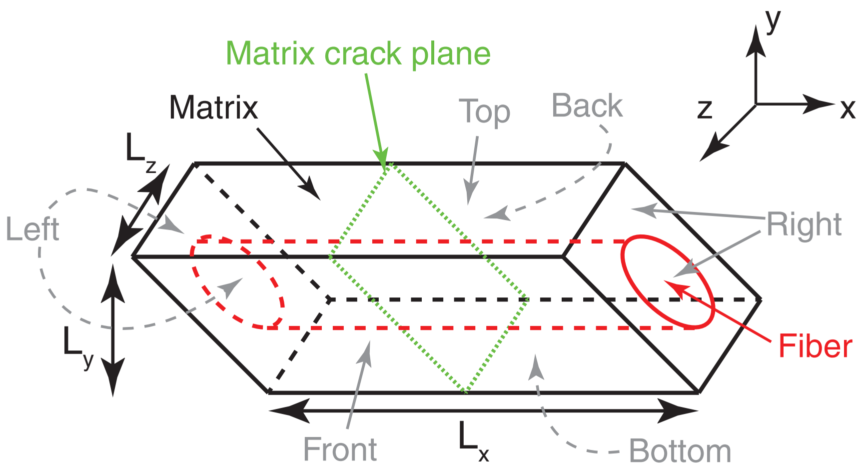

Figure 3.2: Parallelepiped unit cell used in finite element model.

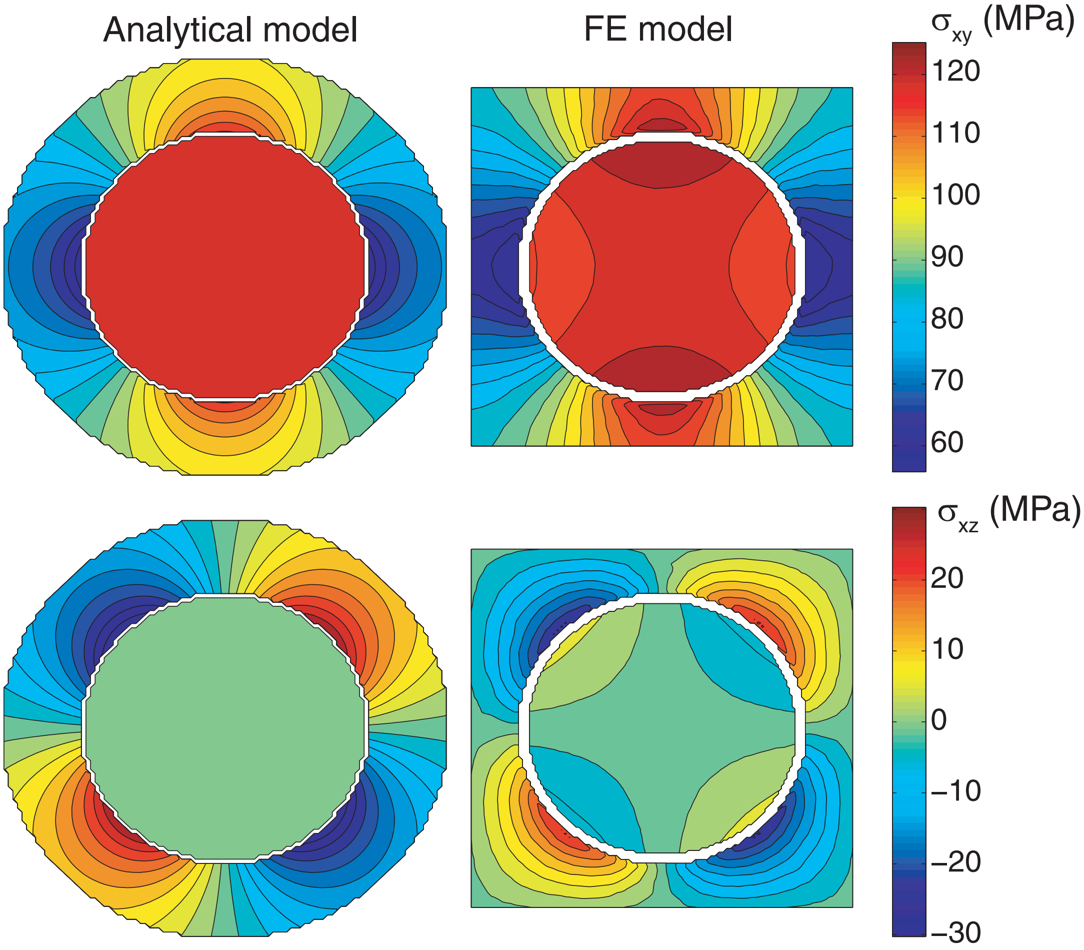

Figure 3.3: Contour plots of σ_{xy} and σ_{xz} from the analytical model (cylindrical unit cell) and the finite element model for the uncracked, elastic composite ($V_f = 0.4$, $E_f = 210\,\text{GPa}$, $E_m = 100\,\text{GPa}$, $\hat{p} = 50\,\text{MPa}$, and $\tau_{app} = 100\,\text{MPa}$).

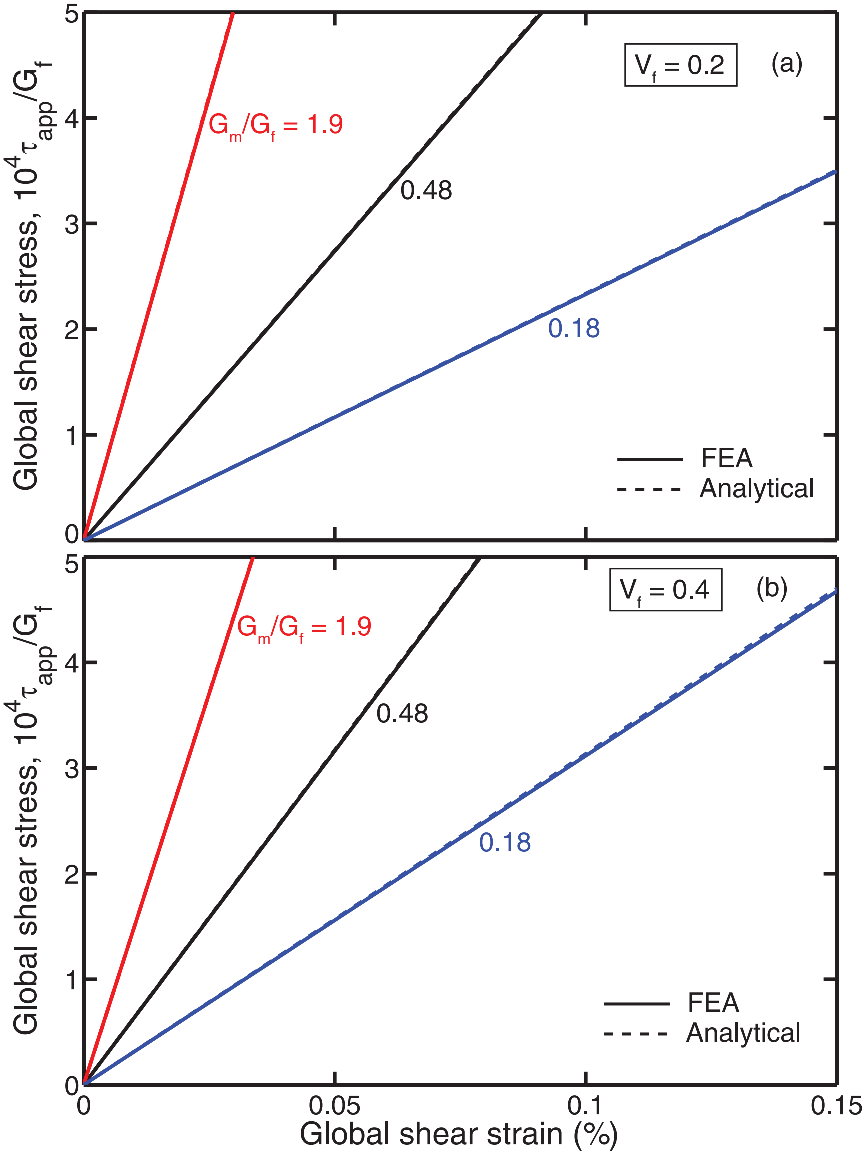

Figure 3.4: Analytical predictions and finite element results of the global stress-strain behavior of the uncracked, elastic composite for various values of matrix modulus and fiber volume fraction ($E_f = 210\,\text{GPa}$ and $\hat{p} = 50\,\text{MPa}$).

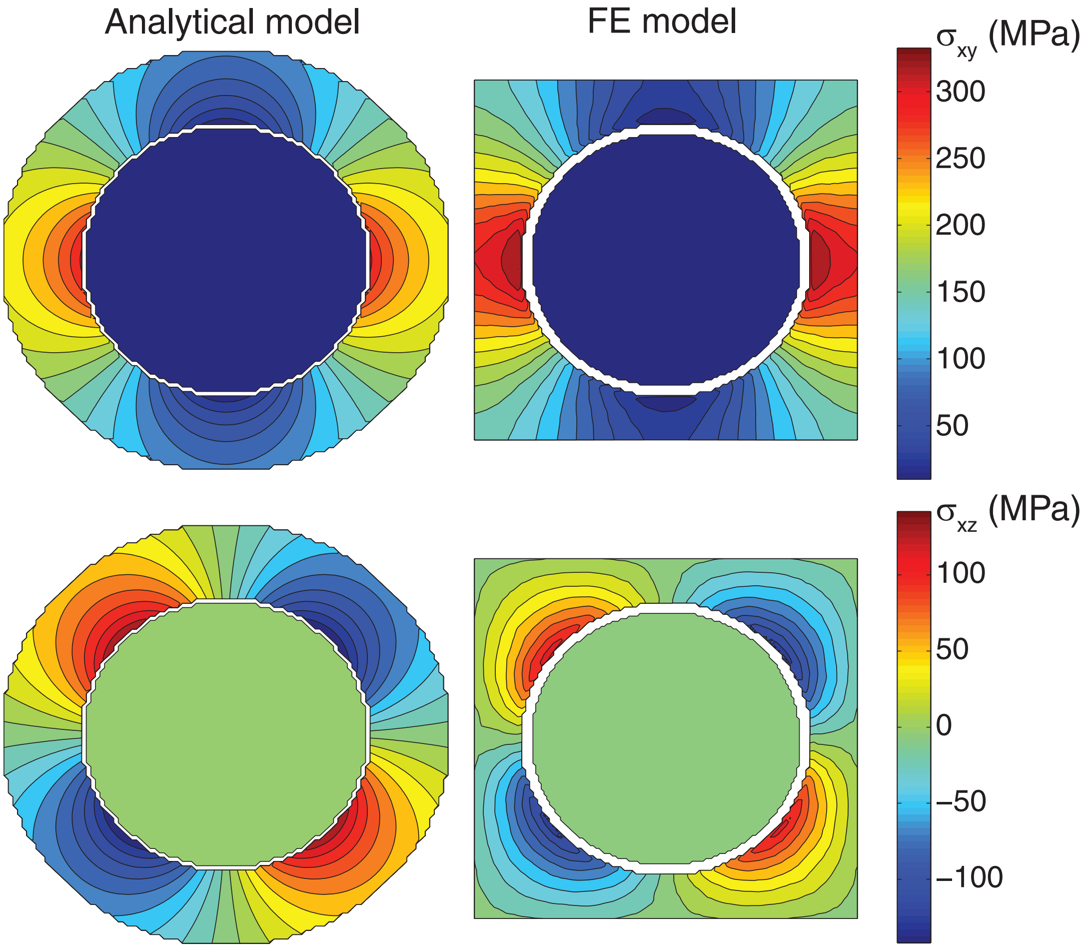

Figure 3.5: Contour plots of σ_{xy} and σ_{xz} from the analytical model (cylindrical unit cell) and the finite element model for the uncracked, inelastic composite ($\tau_{app} = 100\,\text{MPa}$, $V_f = 0.4$, $E_f = 210\,\text{GPa}$, $E_m = 100\,\text{GPa}$, $\hat{p} = 50\,\text{MPa}$, and $\tau_s = 10\,\text{MPa}$).

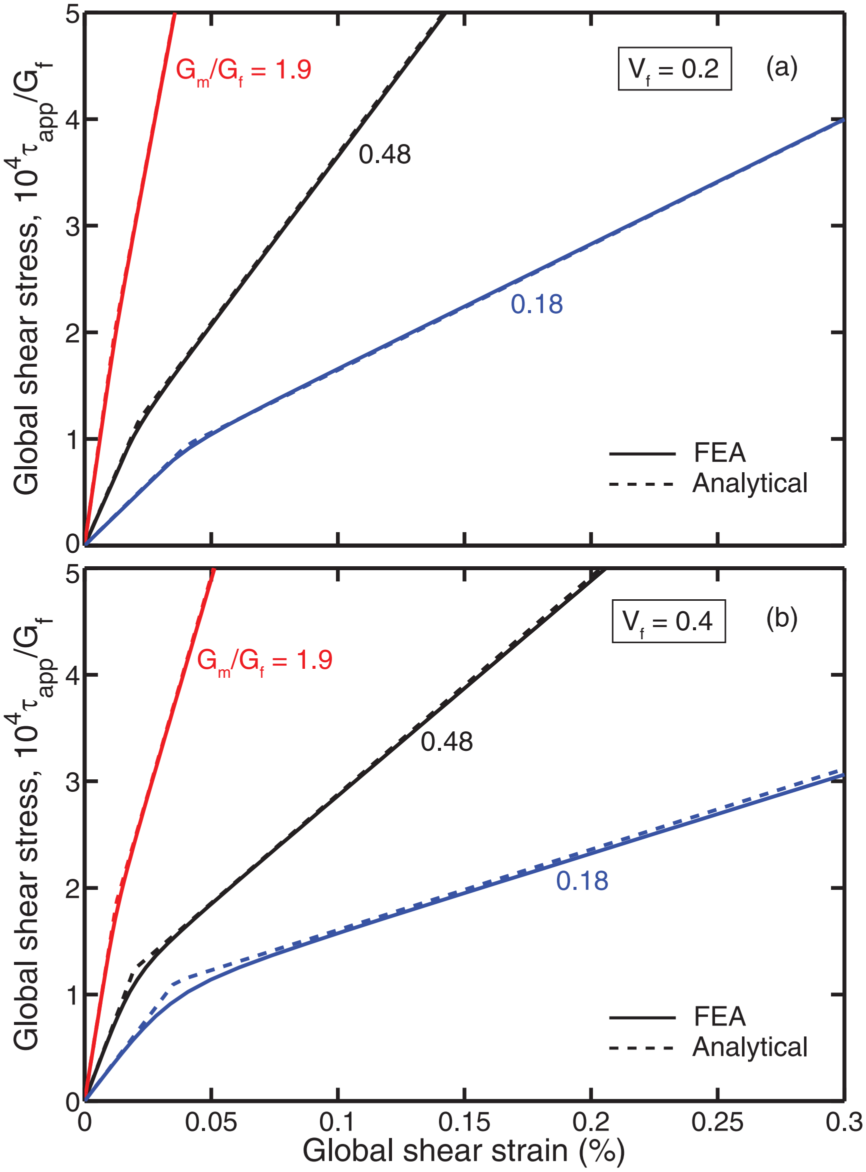

Figure 3.6: Analytical predictions and finite element results of the global stress-strain behavior of the uncracked, inelastic composite for various values of matrix modulus and fiber volume fraction ($E_f = 210\,\text{GPa}$, $\hat{p} = 50\,\text{MPa}$, and $\tau_s = 10\,\text{MPa}$).

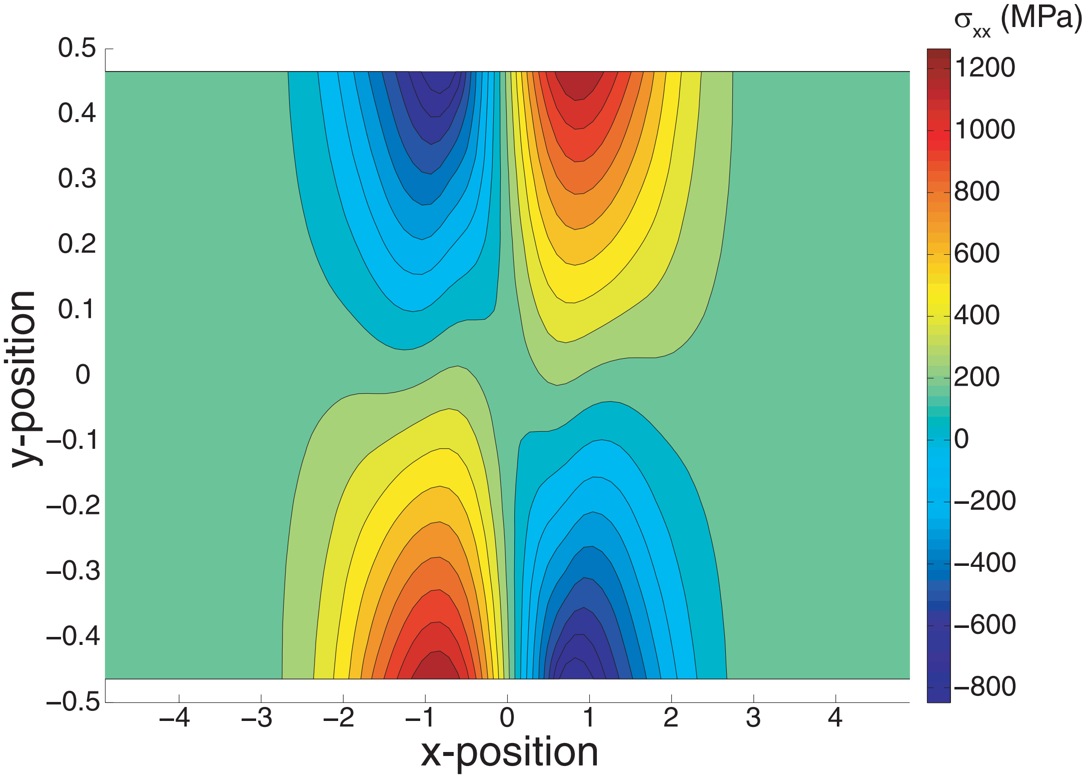

Figure 3.7: Axial stress (σ_{xx}) in the fiber at $z = 0$ for the baseline simulation of the cracked unit cell ($\tau_{app} = 100\,\text{MPa}$).

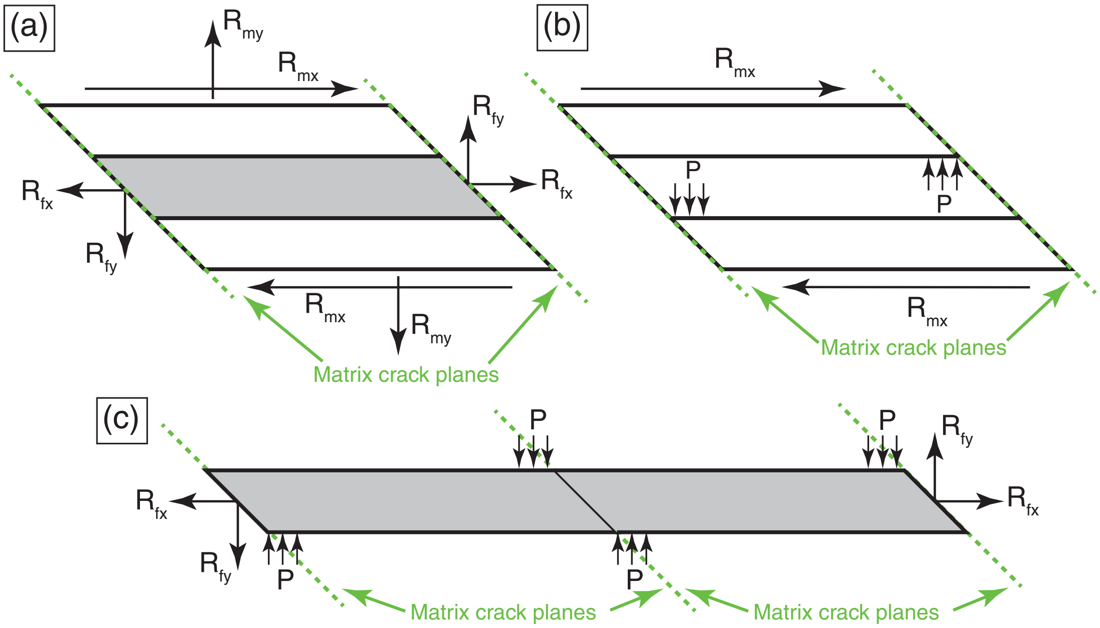

Figure 3.8: Free body diagrams for (a) the entire unit cell, (b) the matrix jacket, and (c) the fiber for the cracked composite.

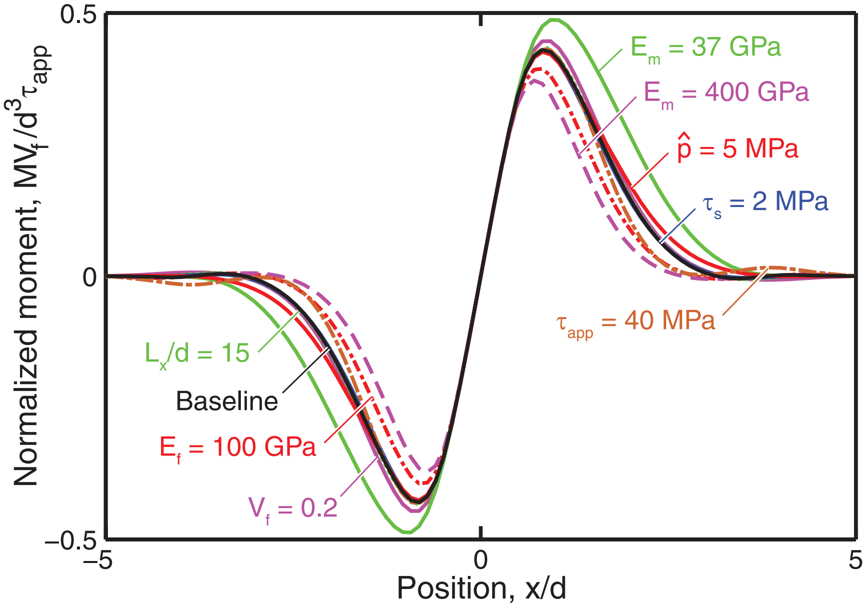

Figure 3.9: Normalized moment vs. position for the simulations summarized in Table 3.1. (The curves corresponding to $\tau_s = 2\,\text{MPa}$ and $L_x/d = 15$ are not easily seen, being almost coincident with that corresponding to the baseline simulation.)

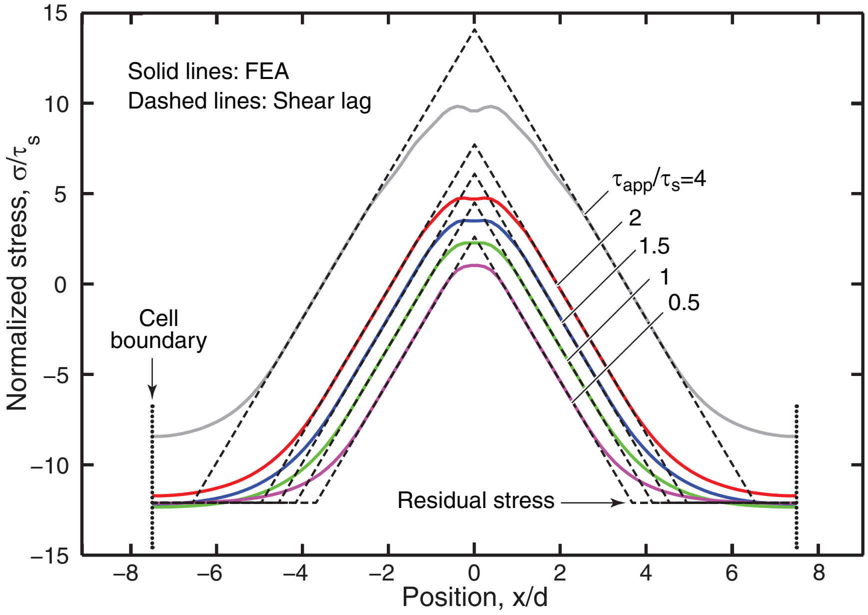

Figure 3.10: Normalized axial stress vs. position for the base simulation (with $L_x/d = 15$) with various values of applied stress.

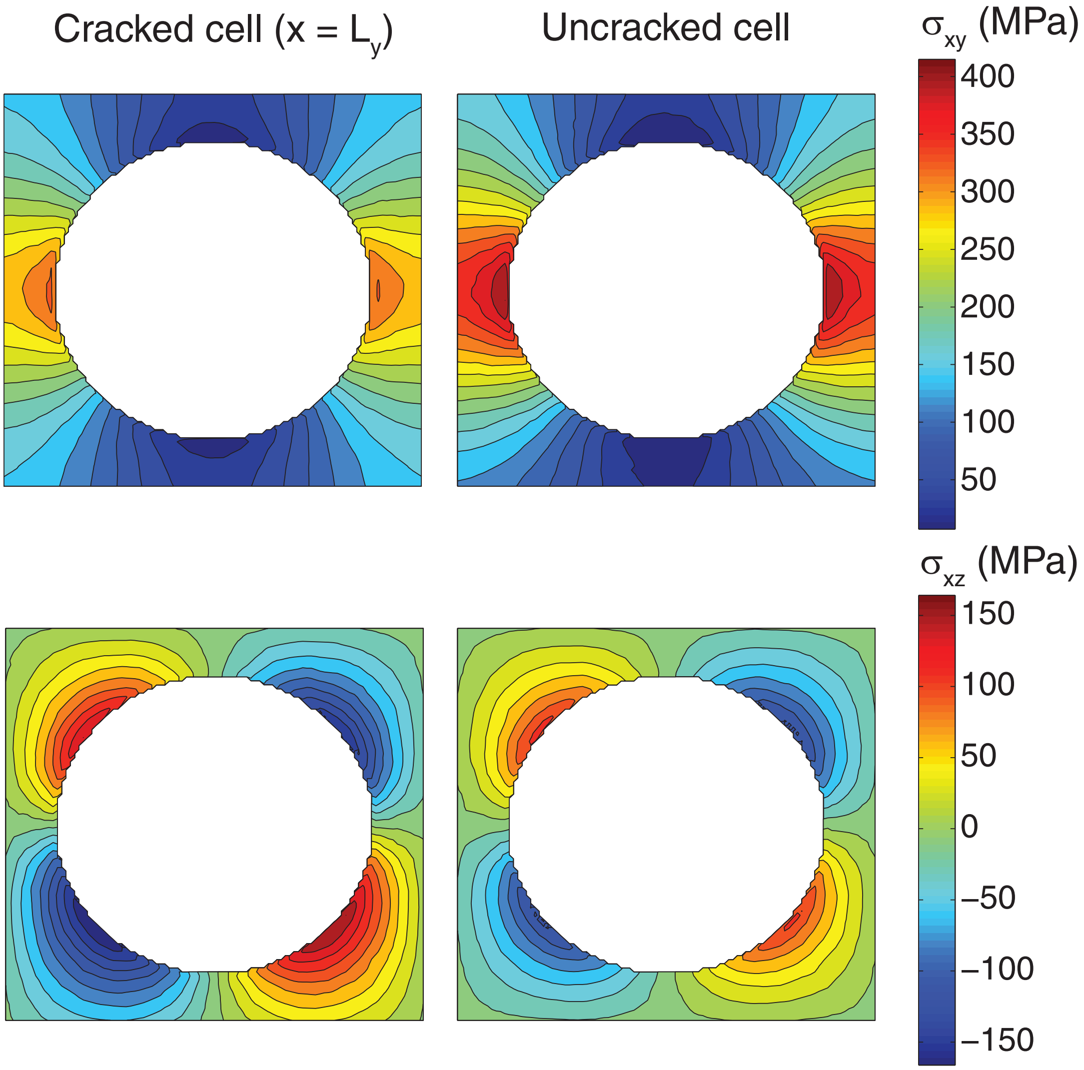

Figure 3.11: Contour plots of σ_{xy} and σ_{xz} from the FE models of the uncracked and cracked unit cells. Results for the cracked unit cell are plotted the edge of the core region ($\overline{x} = \overline{L}_y$). The applied stress, $\tau_{app} = 100\,\text{MPa}$, is much larger than the interfacial sliding stress ($V_f = 0.4$, $E_f = 210\,\text{GPa}$, $E_m = 100\,\text{GPa}$, $\hat{p} = 50\,\text{MPa}$, and $\tau_s = 10\,\text{MPa}$).

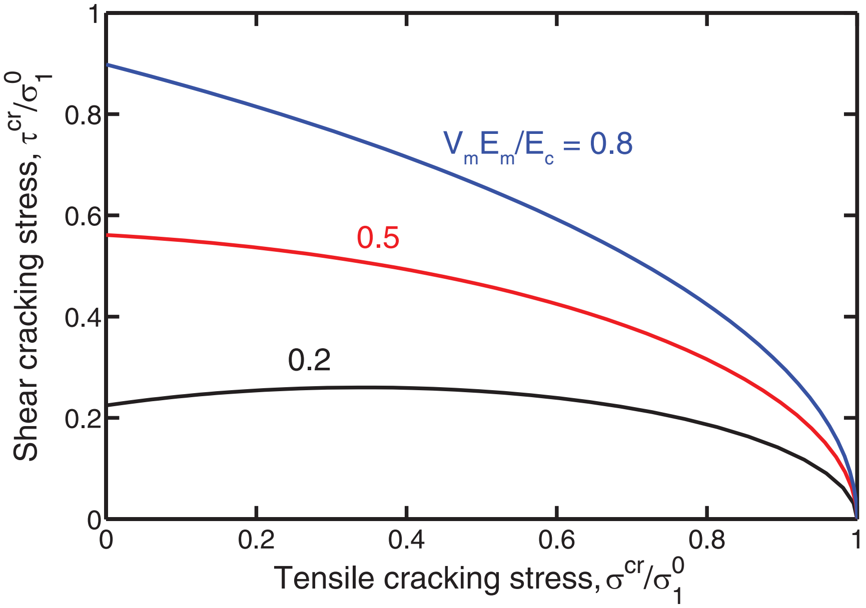

Figure 3.12: 'Yield' surfaces (assuming zero residual stress) in σ-τ space, for representative values of relative matrix modulus.

Chapter 4

Remediation of the Genin-Hutchinson constitutive model for CMC laminates

---

This chapter is adapted from a peer-reviewed publication: V. P. Rajan and F. W. Zok. Remediation of a Constitutive Model for Ceramic Composite Laminates. *Composites Part A*, 52:80–88, 2013. Available at: http://dx.doi.org/10.1016/j.compositesa.2013.05.010

4.1 Introduction

Chapter 1 provided motivation for the development of a physically-valid, experimentally-validated constitutive model for CMC laminates *at the component scale*. It would enable, for instance, prediction of knockdown factors due to stress concentrations such as holes and notches: a result that presently cannot be obtained from micro-scale mechanics analyses. Genin and Hutchinson (1997) attempted to develop such a constitutive model. The Genin-Hutchinson (GH) model is closely analogous in many respects to deformation theory for metal plasticity; it can be readily calibrated using standardized mechanical tests and implemented in finite element codes as a user-defined material model. However, the model suffers from numerical convergence problems, which arise from the fact that the model predicts strain-softening in the post-matrix cracking regime even when the stress-strain curves used for calibration exhibit strain hardening.

In this chapter, the source of instability in the GH model is identified, and the model formulation is remedied to ensure stability for strain-hardening materials. The modifications to the original model are necessarily *minimal*, in order to retain the positive features of the original formulation: notably, the excellent agreement between experimental and predicted stress-strain curves for 45° tension and pure shear (Genin and Hutchinson, 1997), as well as between experimental and predicted strains in notched tension tests (McNulty et al., 1999).

The outline of the chapter is as follows. First, the essential features of the original GH model are recapitulated. Second, a mathematically-equivalent incremental version of the model is derived. Here the increments in stress are related to increments in strain via a tangential stiffness matrix that depends on the current stress state. Third, it is demonstrated that, for certain anisotropic laminates, the incremental model, and hence the original model, can be unstable after matrix cracking. Fourth, the incremental formulation is modified to ensure stability. This is accomplished by judiciously adjusting the entries in the tangential stiffness matrix so it is positive-definite for all strain-hardening laminates. The remedy has been devised to not only ensure stability but also satisfy a number of additional conditions, notably, that: (i) the stress-strain relationships in the elastic domain are preserved exactly; (ii) the responses in 0° tension, 45° tension, equibiaxial tension, and pure shear are recovered; (iii) it reduces to the original model for the special case of a quasi-isotropic laminate; and (iv) it be based in part on the mechanics of CMC laminates after matrix cracking (rather than being purely mathematical). The modified version of the model is shown to satisfy all of the aforementioned conditions. Finally, this model is applied to simulate open-hole tension tests of CMC plates. Whereas the finite element simulations employing the original model fail to converge for certain inelastically-anisotropic laminates, the new model exhibits no such convergence problems. Furthermore, the original and modified models yield identical results for quasi-isotropic laminates, as required.

The weakness of the remediation approach is that it is necessarily *ad hoc*. Ideally, in converting a deformation theory into an incremental theory, a yield surface and a flow rule would be utilized. However, our *ad hoc* incremental formulation should be sufficient for scenarios in which material elements undergo nearly proportional straining: a limitation also of the original GH formulation.

4.2 Original formulation of GH model

In its original formulation, the GH model expresses the stress state in terms of the *total* strain components. The procedure, described in Genin and Hutchinson (1997), is summarized below. It is restricted to loadings with proportional straining and thus the axes of principal strain are assumed not to rotate significantly during deformation.

The contributions of principal stresses to the principal strains are assumed to be additive when the principal strains are oriented along directions of material symmetry. For principal strains oriented at 0°, the strains are written as

$$\begin{aligned} \epsilon_I &= f_0(\sigma_I) + f_{0T}(\sigma_{II}) \\ \epsilon_{II} &= f_{0T}(\sigma_I) + f_0(\sigma_{II}) \end{aligned} \tag{4.1}$$

Similarly, for principal strains oriented at 45° to the fiber directions:

$$\begin{aligned} \epsilon_I &= f_{45}(\sigma_I) + f_{45T}(\sigma_{II}) \\ \epsilon_{II} &= f_{45T}(\sigma_I) + f_{45}(\sigma_{II}) \end{aligned} \tag{4.2}$$

Here the functions f are stress-strain curves measured in uniaxial tension tests conducted at either 0° or 45°. f_0 and f_{45} refer to normal strains aligned with the load axis, whereas f_{0T} and f_{45T} refer to normal strains transverse to the load axis. Considering the special case of equibiaxial loading ($\sigma_I = \sigma_{II} = \sigma$), wherein the axes of principal stress are indeterminate, the four functions f are found to be related by

$$f_0(\sigma) + f_{0T}(\sigma) = f_{45}(\sigma) + f_{45T}(\sigma) \tag{4.3}$$

Hence, only three of the four functions are independent. Equation 4.3 has been shown to be approximately satisfied by stress-strain curves measured on a SiC/CAS [0°/90°] laminate (Genin and Hutchinson, 1997).

Non-linearity in the GH model is couched in terms of so-called 'stress deficits': that is, differences between elastic and actual stress values. The elastic stresses are obtained from Hooke's law. For instance, when the principal strains are oriented at 0°, the elastic (principal) stresses are given by

$$\begin{bmatrix} \sigma^0_{el,I} \\ \\ \sigma^0_{el,II} \end{bmatrix} = \begin{bmatrix} \frac{E_0}{1-\nu_0^2} & \frac{\nu_0 E_0}{1-\nu_0^2} \\ \\ \frac{\nu_0 E_0}{1-\nu_0^2} & \frac{E_0}{1-\nu_0^2} \end{bmatrix} \begin{bmatrix} \epsilon_I \\ \\ \epsilon_{II} \end{bmatrix} = \boldsymbol{C^0_{el}} \begin{bmatrix} \epsilon_I \\ \\ \epsilon_{II} \end{bmatrix} \tag{4.4}$$

where $\boldsymbol{C^0_{el}}$ is the elastic stiffness matrix for principal strains oriented at 0°.

Similarly, the elastic (principal) stresses for principal strains oriented at 45° are

$$\begin{bmatrix} \sigma^{45}_{el,I} \\ \\ \sigma^{45}_{el,II} \end{bmatrix} = \begin{bmatrix} \frac{E_{45}}{1-\nu_{45}^2} & \frac{\nu_{45} E_{45}}{1-\nu_{45}^2} \\ \\ \frac{\nu_{45} E_{45}}{1-\nu_{45}^2} & \frac{E_{45}}{1-\nu_{45}^2} \end{bmatrix} \begin{bmatrix} \epsilon_I \\ \\ \epsilon_{II} \end{bmatrix} = \boldsymbol{C^{45}_{el}} \begin{bmatrix} \epsilon_I \\ \\ \epsilon_{II} \end{bmatrix} \tag{4.5}$$

Using these results, the stress deficits at 0° can be written as

$$\begin{bmatrix} \Delta\sigma^0_I \\ \\ \Delta\sigma^0_{II} \end{bmatrix} = \boldsymbol{C^0_{el}} \begin{bmatrix} \epsilon_I \\ \\ \epsilon_{II} \end{bmatrix} - \begin{bmatrix} \Sigma^0(\epsilon_I, \epsilon_{II}) \\ \\ \Sigma^0(\epsilon_{II}, \epsilon_I) \end{bmatrix} \tag{4.6}$$

The Σ terms in Equation 4.6 correspond to the solution (inversion) of Equation 4.1. A similar statement can be written for the 45° direction, with the Σ terms corresponding to the solution (inversion) of Equation 4.2.

To obtain the stress deficits at the angle of principal strains, θ_ϵ, the stress deficits at 0° and 45° are interpolated in accordance with

$$\begin{aligned} \Delta\sigma^{\theta_\epsilon}_I &= \Delta\sigma^0_I \cos^2(2\theta_\epsilon) + \Delta\sigma^{45}_I \sin^2(2\theta_\epsilon) \\ \Delta\sigma^{\theta_\epsilon}_{II} &= \Delta\sigma^0_{II} \cos^2(2\theta_\epsilon) + \Delta\sigma^{45}_{II} \sin^2(2\theta_\epsilon) \end{aligned} \tag{4.7}$$

Combining the previous results:

$$\begin{aligned}\begin{bmatrix}\sigma_I^{\theta_\epsilon}\\ \sigma_{II}^{\theta_\epsilon}\end{bmatrix} &= \boldsymbol{C}_{el}^{\theta_\epsilon}\begin{bmatrix}\epsilon_I\\ \epsilon_{II}\end{bmatrix} - \cos^2(2\theta_\epsilon)\left(\boldsymbol{C}_{el}^{\mathbf{0}}\begin{bmatrix}\epsilon_I\\ \epsilon_{II}\end{bmatrix} - \begin{bmatrix}\Sigma^0(\epsilon_I,\epsilon_{II})\\ \Sigma^0(\epsilon_{II},\epsilon_I)\end{bmatrix}\right)\\ &\quad - \sin^2(2\theta_\epsilon)\left(\boldsymbol{C}_{el}^{\mathbf{45}}\begin{bmatrix}\epsilon_I\\ \epsilon_{II}\end{bmatrix} - \begin{bmatrix}\Sigma^{45}(\epsilon_I,\epsilon_{II})\\ \Sigma^{45}(\epsilon_{II},\epsilon_I)\end{bmatrix}\right)\end{aligned} \tag{4.8}$$

It can further be shown through standard procedures of coordinate transformations that

$$\boldsymbol{C}_{el}^{\boldsymbol{\theta}} = \boldsymbol{C}_{el}^{\mathbf{0}}\cos^2(2\theta) + \boldsymbol{C}_{el}^{\mathbf{45}}\sin^2(2\theta) \tag{4.9}$$

so Equation 4.8 reduces to

$$\begin{bmatrix}\sigma_I^{\theta_\epsilon}\\ \sigma_{II}^{\theta_\epsilon}\end{bmatrix} = \cos^2(2\theta_\epsilon)\begin{bmatrix}\Sigma^0(\epsilon_I,\epsilon_{II})\\ \Sigma^0(\epsilon_{II},\epsilon_I)\end{bmatrix} + \sin^2(2\theta_\epsilon)\begin{bmatrix}\Sigma^{45}(\epsilon_I,\epsilon_{II})\\ \Sigma^{45}(\epsilon_{II},\epsilon_I)\end{bmatrix} \tag{4.10}$$

Because the shear stress deficit is assumed to be zero, the actual shear stress (again, oriented at θ_ϵ) is merely the elastic shear stress:

$$\tau^{\theta_\epsilon} = \frac{E_{45} - E_0}{2(1+\nu_{45})(1+\nu_0)}(\epsilon_I - \epsilon_{II})\sin(4\theta_\epsilon) \tag{4.11}$$

4.3 Incremental formulation of GH model

The objective in this section is to convert the original GH model into an incremental formulation. Not only is the incremental formulation useful for assessing stability, but it is also amenable to modification to correct instabilities, as demonstrated below.

4.3.1 Approach

Consider two strain/stress states: the current state, denoted by the superscript c, and the new state, denoted by the superscript n. The states are related to one another by a prescribed strain increment. The goal is to determine the new stress state (or, equivalently, the increments in each of the stress components) in terms of the strain increment and the current strain and stress states.

The current strain state is given by two principal strains oriented at the principal angle, θ_ϵ^c, expressed generally as:

$$\boldsymbol{\epsilon}^c = [\epsilon_I^c, \epsilon_{II}^c, 0] \tag{4.12}$$

The increment in strain is also oriented at θ_ϵ^c. Although proportional straining is assumed, a non-zero shear strain component is allowed in order to assess stability with respect to *any* incremental deformation. The incremental strain tensor is thus expressed as:

$$\mathbf{d}\boldsymbol{\epsilon} = [\mathrm{d}\epsilon_I, \mathrm{d}\epsilon_{II}, \mathrm{d}\gamma] \tag{4.13}$$

Increments in principal strains are first-order in $\mathrm{d}\epsilon_I$ and $\mathrm{d}\epsilon_{II}$, but are only second-order in $\mathrm{d}\gamma$. If the increment is small, the latter term is negligible.

Conversely, the increment in θ_ϵ (the orientation of the principal strain axes) is first-order in $\mathrm{d}\gamma$, and higher-order in the other components. Therefore, the shear strain increment rotates the principal axes while leaving the magnitudes of the principal strains unchanged, and vice versa for the normal strain increments.

The new strain state, oriented at an angle θ_ϵ^n, is thus given by

$$\boldsymbol{\epsilon^n} = [\epsilon_I^o + \mathrm{d}\epsilon_I, \epsilon_{II}^o + \mathrm{d}\epsilon_{II}, 0] \tag{4.14}$$

where

$$\theta_\epsilon^n = \theta_\epsilon^c + \mathrm{d}\theta_\epsilon \tag{4.15}$$

and

$$\mathrm{d}\theta_\epsilon = \frac{\mathrm{d}\gamma}{2(\epsilon_I^o - \epsilon_{II}^o)} \tag{4.16}$$

The stresses in the current state are also rotated into θ_ϵ^c. Since the principal axes of stress and strain do not necessarily coincide, a nonzero shear stress component may also be present, and thus the current stress state is written as

$$\boldsymbol{\sigma^c} = [\sigma_I^c, \sigma_{II}^c, \tau^c] \tag{4.17}$$

4.3.2 Formulation

The incremental model is derived by linearizing Equations 4.10 and 4.11 about $\mathbf{d}\boldsymbol{\epsilon} = 0$.

Using Equation 4.1, the following result is obtained:

$$\begin{bmatrix} \mathrm{d}\epsilon_I \\ \mathrm{d}\epsilon_{II} \end{bmatrix} = \begin{bmatrix} f_0'(\sigma_I^0) & f_{0T}'(\sigma_{II}^0) \\ f_{0T}'(\sigma_I^0) & f_0'(\sigma_{II}^0) \end{bmatrix} \begin{bmatrix} \mathrm{d}\sigma_I^0 \\ \mathrm{d}\sigma_{II}^0 \end{bmatrix} = \boldsymbol{S}^{\mathbf{0}}(\boldsymbol{\sigma}) \begin{bmatrix} \mathrm{d}\sigma_I^0 \\ \mathrm{d}\sigma_{II}^0 \end{bmatrix} \tag{4.18}$$

where the prime symbols denote derivatives. Similarly, using Equation 4.2,

$$\begin{bmatrix} \mathrm{d}\epsilon_I \\ \mathrm{d}\epsilon_{II} \end{bmatrix} = \begin{bmatrix} f_{45}'(\sigma_I^{45}) & f_{45T}'(\sigma_{II}^{45}) \\ f_{45T}'(\sigma_I^{45}) & f_{45}'(\sigma_{II}^{45}) \end{bmatrix} \begin{bmatrix} \mathrm{d}\sigma_I^{45} \\ \mathrm{d}\sigma_{II}^{45} \end{bmatrix} = \boldsymbol{S}^{\mathbf{45}}(\boldsymbol{\sigma}) \begin{bmatrix} \mathrm{d}\sigma_I^{45} \\ \mathrm{d}\sigma_{II}^{45} \end{bmatrix} \tag{4.19}$$

Expanding Equation 4.10 about $\mathbf{d}\boldsymbol{\epsilon} = 0$ yields

$$\begin{aligned} \begin{bmatrix} \sigma_I^n \\ \sigma_{II}^n \end{bmatrix} &= \cos^2(2(\theta_\epsilon^c + \mathrm{d}\theta_\epsilon)) \begin{bmatrix} \Sigma^0(\epsilon_I^c + \mathrm{d}\epsilon_I, \epsilon_{II}^c + \mathrm{d}\epsilon_{II}) \\ \Sigma^0(\epsilon_{II}^c + \mathrm{d}\epsilon_{II}, \epsilon_I^c + \mathrm{d}\epsilon_I) \end{bmatrix} \\ &\quad + \sin^2(2(\theta_\epsilon^c + \mathrm{d}\theta_\epsilon)) \begin{bmatrix} \Sigma^{45}(\epsilon_I^c + \mathrm{d}\epsilon_I, \epsilon_{II}^c + \mathrm{d}\epsilon_{II}) \\ \Sigma^{45}(\epsilon_{II}^c + \mathrm{d}\epsilon_{II}, \epsilon_I^c + \mathrm{d}\epsilon_I) \end{bmatrix} \end{aligned} \tag{4.20}$$

where $\sigma_{I,II}^n$ are normal stresses oriented at θ_ϵ^n. Substituting the previous results into Equation 4.20 and neglecting higher-order terms yields

$$\begin{aligned} \begin{bmatrix} \mathrm{d}\sigma_I \\ \mathrm{d}\sigma_{II} \end{bmatrix} &= 2\sin(4\theta_\epsilon^c)\mathrm{d}\theta_\epsilon \left(\begin{bmatrix} \Sigma^{45}(\epsilon_I^c, \epsilon_{II}^c) \\ \Sigma^{45}(\epsilon_{II}^c, \epsilon_I^c) \end{bmatrix} - \begin{bmatrix} \Sigma^0(\epsilon_I^c, \epsilon_{II}^c) \\ \Sigma^0(\epsilon_{II}^c, \epsilon_I^c) \end{bmatrix} \right) \\ &\quad + \left(\left[\boldsymbol{S}^{\mathbf{0}}(\boldsymbol{\sigma}^c)\right]^{-1} \cos^2(2\theta_\epsilon^c) + \left[\boldsymbol{S}^{\mathbf{45}}(\boldsymbol{\sigma}^c)\right]^{-1} \sin^2(2\theta_\epsilon^c) \right) \begin{bmatrix} \mathrm{d}\epsilon_I \\ \mathrm{d}\epsilon_{II} \end{bmatrix} \end{aligned} \tag{4.21}$$

Note that the first term scales with the product of a modulus and $\mathrm{d}\gamma$ (per Equation 4.16), whereas the second term scales with the product of a modulus and

$\mathrm{d}\epsilon_{I,II}$. For nearly proportional straining, the former term is negligible in comparison to the latter. Using this simplification yields the result:

$$\begin{bmatrix} \mathrm{d}\sigma_I \\ \mathrm{d}\sigma_{II} \end{bmatrix} = \left(\left[\boldsymbol{S}^{\mathbf{0}}(\boldsymbol{\sigma}^{\boldsymbol{c}}) \right]^{-1} \cos^2(2\theta_\epsilon^c) + \left[\boldsymbol{S}^{\mathbf{45}}(\boldsymbol{\sigma}^{\boldsymbol{c}}) \right]^{-1} \sin^2(2\theta_\epsilon^c) \right) \begin{bmatrix} \mathrm{d}\epsilon_I \\ \mathrm{d}\epsilon_{II} \end{bmatrix} \tag{4.22}$$

Finally, linearizing the shear stress equation yields

$$\mathrm{d}\tau = \frac{E_{45} - E_0}{2(1+\nu_{45})(1+\nu_0)} \left(4(\epsilon_I^c - \epsilon_{II}^c) \cos(4\theta_\epsilon^c) \mathrm{d}\theta_\epsilon + (\mathrm{d}\epsilon_I - \mathrm{d}\epsilon_{II}) \sin(4\theta_\epsilon^c) \right) \tag{4.23}$$

4.4 Assessment of stability

4.4.1 Stability criterion

As discussed by Hill (1958), a structure is stable if the condition

$$\mathrm{d}^2 W = \int_V \frac{1}{2} \mathbf{d}\boldsymbol{\sigma} : \mathbf{d}\boldsymbol{\epsilon} \, \mathrm{d}V \geq 0 \tag{4.24}$$

is satisfied for the strain increment $\mathbf{d}\boldsymbol{\epsilon}$ associated with *any* incremental displacement $\mathbf{d}\boldsymbol{q}$ of the structure (Bažant and Cedolin, 2010). For Equation 4.24 to hold, it is *sufficient* that the second-order work be positive 'in the small' (Maier and Hueckel, 1979; Bigoni and Hueckel, 1991). This implies that the condition

$$\mathbf{d}\boldsymbol{\sigma} : \mathbf{d}\boldsymbol{\epsilon} \geq 0 \tag{4.25}$$

should be satisfied *locally*, for every material element. Equation 4.25 imposes a condition on the constitutive law: notably, that the tangential stiffness matrix, $C_{ij} = \mathrm{d}\sigma_i / \mathrm{d}\epsilon_j$, be positive-definite (Bigoni and Hueckel, 1991), or, equivalently, that the symmetric part of the tangential stiffness, $(\boldsymbol{C} + \boldsymbol{C}^{\boldsymbol{T}})/2$, possess no negative eigenvalues. This condition will be used to assess stability in the present work. Since Equation 4.25 implies positive material stiffness in every strain direction, it is not expected to hold for strain states in which the input stress-strain curves exhibit strain-softening. Conversely, the stability condition should be satisfied when the input stress-strain curves exhibit strain-hardening.

The incremental formulation, described above, involves changes in the magnitudes of the stress components and rotation of the stress vector through the angle $\mathrm{d}\theta_\epsilon$. To assess stability using Equation 4.25, the incremental stress and strain vectors must be written with respect to the same coordinate axes. For this purpose, the new stress vector, oriented at θ_ϵ^n, is rotated back to the current principal axes, oriented at θ_ϵ^c. Neglecting higher-order terms, the principal stress increment (Equation 4.22) remains unchanged, but the shear stress increment has an additional term, now written as:

$$
\begin{aligned}
\mathrm{d}\tau^c = {} & \frac{E_{45} - E_0}{2(1+\nu_{45})(1+\nu_0)} \left(4(\epsilon_I^c - \epsilon_{II}^c)\cos(4\theta_\epsilon^c)\mathrm{d}\theta_\epsilon + (\mathrm{d}\epsilon_I - \mathrm{d}\epsilon_{II})\sin(4\theta_\epsilon^c)\right) \\
& + (\sigma_I^c - \sigma_{II}^c)\mathrm{d}\theta_\epsilon
\end{aligned}
\tag{4.26}
$$

Using Equations 4.22 and 4.26, he stability of the incremental formulation can now be assessed. Furthermore, since the two formulations of the model are mathematically equivalent, conclusions regarding the stability of the incremental formulation are also applicable to the original formulation.

Using the preceding framework, two types of instabilities are found in the inelastic regime: one associated with Equation 4.26, and the other with Equation 4.22. Each, in turn, is described below.

4.4.2 Shear strain instability

Establishing general conditions for stability is difficult (and not particularly enlightening), so a special case is examined here: notably, a uniaxial tension test conducted in the 0° direction. The material is assumed to have $\nu_0 = 0$ (not unreasonable for CMCs). Then, an incremental *shear* strain is applied. Obviously, $\epsilon_{II}^c = 0$, $\sigma_{II}^c = 0$, $\mathrm{d}\epsilon_I = \mathrm{d}\epsilon_{II} = 0$, $\theta_\epsilon^c = 0$ and $\nu_{45} = 1 - E_{45}/E_0$.

Defining $\beta = E_{45}/E_0$, Equation 4.26 simplifies to

$$d\tau^c = \frac{-2E_0(1-\beta)}{(2-\beta)}\epsilon_I^c d\theta_\epsilon + \sigma_I^c d\theta_\epsilon \tag{4.27}$$

A good approximation of the first principal stress is $\sigma_I^c = \alpha E_0(\epsilon_I^c - \epsilon_{mc}) + E_0\epsilon_{mc}$, where α is the ratio of the post-matrix cracking modulus to the pre-matrix cracking modulus in the 0° direction, and ϵ_{mc} is the matrix cracking strain. Since $d\theta_\epsilon$ is proportional to $d\gamma$, stability requires that $d\tau^c d\theta_\epsilon \geq 0$. Following some algebra, the stability condition is obtained:

$$1 - \alpha - \frac{1}{\epsilon_I^c/\epsilon_{mc} - 1} \leq \frac{\beta}{2-\beta} \tag{4.28}$$

It is trivial to show that, although this equation is automatically satisfied for elastically-isotropic materials ($\beta = 1$), it is not generally true for elastically-*anisotropic* materials. For one set of typical values of material parameters ($\alpha = 1/4$, $\epsilon_{mc} = 0.001$, $\epsilon_I^c = 0.006$), stability requires that β exceed 0.71. Laminates in which the fiber modulus is significantly higher than the matrix modulus (perhaps because of remnant porosity in the matrix) are unlikely to satisfy this condition.

4.4.3 Principal strain instability

Here, a uniaxial tension test conducted at 45° is examined. In this case, Equation 4.22 reduces to

$$\begin{bmatrix} \mathrm{d}\sigma_I^c \\ \mathrm{d}\sigma_{II}^c \end{bmatrix} = \left[\boldsymbol{S}^{\mathbf{45}}(\sigma^c) \right]^{-1} \begin{bmatrix} \mathrm{d}\epsilon_I \\ \mathrm{d}\epsilon_{II} \end{bmatrix} \tag{4.29}$$

and thus the stability condition is satisfied if $\boldsymbol{S}^{\mathbf{45}}$ is positive-definite. Note that, after matrix cracking, the compliances in the 45° and 45°-transverse directions are essentially equal and of opposite sign because of 'fiber scissoring' (see Equation 4.3). So:

$$\boldsymbol{S}^{\mathbf{45}} = \begin{bmatrix} f'_{45}(\sigma_I^{45}) & f'_{45T}(\sigma_{II}^{45}) \\ f'_{45T}(\sigma_I^{45}) & f'_{45}(\sigma_{II}^{45}) \end{bmatrix} = \begin{bmatrix} 1/E_{45,pmc} & -\nu_{45}/E_{45} \\ -1/E_{45,pmc} & 1/E_{45} \end{bmatrix} \tag{4.30}$$

where the subscript 'pmc' denotes post-matrix cracking. If the material is elastically-isotropic, but inelastically very anisotropic (for instance, $E_0 = E_{45} = 200\,\mathrm{GPa}$, $\nu_0 = \nu_{45} = 0.1$, and $E_{45,pmc} = 5\,\mathrm{GPa}$), it is readily seen that $\boldsymbol{S}^{\mathbf{45}}$ is non-positive-definite. This result arises because of the large dissimilarity in the off-diagonal terms that describe coupling between strains and stresses in orthogonal directions.

4.4.4 Numerical calculations

To illustrate the effects of the instabilities in finite element analyses, the uniaxial tension tests described above were simulated using ABAQUS Standard (Version 6-9.2, Dassault Systèmes) with the original GH model as a user-defined constitutive law. Relatively coarse meshes (16 four-noded, quadrilateral, plane stress elements), depicted in Figure 4.1(b) and 4.1(d), were used. (Note that mesh refinement does not fix, and can actually exacerbate, the convergence problems associated with unstable materials.) In an attempt to suppress local material instabilities, automatic stabilization (damping) was employed.

The input stress-strain curves for the 0° tension test of the elastically-anisotropic material are shown in Figure 4.1(a). The stress-strain curves are bi-linear, with elastic constants $E_0 = 200\,\mathrm{GPa}$, $\nu_0 = 0.1$, and $E_{45} = 100\,\mathrm{GPa}$. Thus $\beta = E_{45}/E_0 = 0.5$, below the predicted critical value for stability (0.71) in Equation 4.28. In the post-matrix cracking regime, the tangent moduli of the 0° and 45° stress-strain curves are equal.

The stress in the direction of loading is plotted in Figure 4.2(a) for all integration points within the mesh. In the elastic regime and in a portion of the inelastic regime, each element possesses a positive-definite tangential stiffness matrix. No instability results, and the stress-strain curve predicted by the finite element analysis therefore agrees with the 0° stress-strain curve (f_0) used as input. However, at a sufficiently large strain in the inelastic regime, the smallest eigenvalue of the symmetric part of the tangential stiffness matrix becomes negative (see Figure 4.2(c)), causing the stiffness matrix to lose positive-definiteness. When this occurs, the numerical solver (based on the Newton-Raphson method) encounters convergence difficulties. As a consequence, the stresses at the integration points diverge from the 0° stress-strain curve. The magnitude of the errors exceeds 25%.

Next the tensile response of an inelastically-anisotropic material (defined in Figure 4.1(c)) in the 45° orientation is examined. Once again, bi-linear behavior is assumed. The material is elastically-isotropic, so the shear strain-induced instability illustrated above does not arise. However, *inelastic* anisotropy is present: the ratio of the post-matrix cracking moduli being $E_{45,pmc}/E_{0,pmc} = 1/100$.

The normal stress in the 0° direction (*not* in the loading direction) is plotted in Figure 4.2(b) for all integration points within the mesh. Once again, the elastic behavior is correctly modeled by the finite element simulation, while the inelastic behavior is poorly modeled due to convergence problems. Loss of positive-definiteness occurs immediately after matrix cracking, as indicated in Figure 4.2(d). The errors in the computed stresses exceed 20% for several integration points. (The normal stress in the loading direction—at 45° to the fiber axes—displays lower error, because errors of opposite sign in the normal and shear stresses at 0° tend to cancel one another out.)

In the relatively simple loadings and geometries considered here, the finite element analyses yield inaccurate results. In other circumstances (such as those considered below), the finite element solver can fail to converge entirely. This can occur, for instance, when more complex geometries are simulated.

4.5 Remediation of instabilities

As demonstrated, the instabilities associated with the original model prevent accurate finite element simulations for certain anisotropic materials. The problem is remedied by adjusting the entries of the tangential stiffness matrix in the inelastic domain. The adjustments are physically motivated, as opposed to being purely mathematical. One adjustment corrects for the problem of the shear strain instability in elastically-anisotropic materials; the other addresses the problem of the principal strain instability in inelastically-anisotropic materials. Stability of the new model is ensured by verifying that the tangential stiffness matrix is positive-definite when the input stress-strain curves exhibit strain-hardening.

4.5.1 Shear strain instability

Prior to matrix cracking, shear-extension coupling can exist if $E_0 \neq E_{45}$. Specifically, a difference in principal strains causes shear stresses to develop if the orientation of the principal axes lies between 0° and 45°. The original GH model predicts that, even after matrix cracking, shear stresses within the material continue to rise with additional normal strain. This scenario is somewhat implausible, however, since matrix cracking alleviates the constraint that gives rise to shear-extension coupling. Contrary to the original model, it is expected that matrix cracking causes a de-coupling of shear and extension, and thus no additional shear stress should build up from this coupling. It is therefore assumed that increments in shear stress in the *inelastic* regime are caused *solely* by increments in shear strain. But the proportionality constant cannot be chosen arbitrarily: the requirement of objectivity must be enforced (Bažant, 1983). Specifically, for quasi-isotropic materials, the axes of principal stress and strain must be aligned. Therefore, in the incremental model, these axes must rotate by the same angle. As noted by Bažant (1983), this requirement is equivalent to the relationship

$$\mathrm{d}\tau^c = (\sigma_I^c - \sigma_{II}^c)\mathrm{d}\theta_\epsilon = \frac{\sigma_I^c - \sigma_{II}^c}{2\left(\epsilon_I^c - \epsilon_{II}^c\right)}\mathrm{d}\gamma \tag{4.31}$$

where both the stress and the stress increment are oriented at θ_ϵ^c. Since the proportionality constant is guaranteed to be positive, this modification resolves the problem of shear strain instability. Note that Equation 4.31 is identical to that in the original GH model for laminates that are elastically-isotropic ($E_0 = E_{45}$).

The elimination of the shear-extension coupling term renders the tangential stiffness matrix in the modified model orthotropic in the inelastic domain. Therefore, the modified model can be classified as an incrementally orthotropic model, as discussed by Bažant (1983).

4.5.2 Principal strain instability

As noted previously, the principal strain instability arises because the description of the coupling between stresses and strains in the two principal directions is incomplete. To properly describe this coupling, the phenomenon of fiber scissoring must be taken into account.

Scissoring represents a low-stiffness deformation mode in which fibers rotate and bend in order to align themselves with the load axis. It occurs in the inelastic domain, wherein matrix cracks partially alleviate the constraints on fiber motion. Scissoring does not operate in the elastic domain (provided the matrix is sufficiently stiff) nor when the load is aligned with one of the fiber axes (i.e. at 0° or 90°).

The GH model evidently fails to capture the scissoring mechanism. A particular example, shown in Figure 4.5, illustrates the point. A [0°/90°] laminate is first loaded in tension at 45° to the fiber axes, along the I-direction defined in Figure 4.5. This loading produces a series of periodic matrix cracks normal to the I-direction. The laminate is subsequently loaded by a pair of incremental stresses $\Delta\sigma$ in the I- and II-directions, with $\Delta\sigma_{II} \gg \Delta\sigma_I$. The compliance matrix from the original GH model, notably

$$\boldsymbol{S}^{\mathbf{45}} = \begin{bmatrix} f'_{45}(\sigma_I^{45}) & f'_{45T}(\sigma_{II}^{45}) \\ f'_{45T}(\sigma_I^{45}) & f'_{45}(\sigma_{II}^{45}) \end{bmatrix} \tag{4.32}$$

would predict that the incremental strain in the I-direction would be much greater than that in the II-direction. In contrast, upon consideration of the scissoring process, the magnitudes of the incremental strains are expected to be reversed.

Here an alternative compliance matrix to describe the strains resulting from fiber scissoring is proposed. To this end, the cracked matrix is conceptualized, to a first approximation, as a very compliant *elastic* medium with a large failure strain: an assumption also made in models of the post-cracking response of CMCs under 0° loading (Curtin, 1991b). In order for scissoring to be treated as an elastic phenomenon, the compliance matrix must be symmetric. (This symmetry makes sense in physical terms: when fiber scissoring is the predominant mode of deformation, large transverse strains should develop for stresses applied in *either* of the principal directions.) Additionally, the compliance matrix must preserve the 45°, 45°-transverse, and equibiaxial stress-strain relations. The simplest compliance matrix that satisfies these conditions is

$$\boldsymbol{S^{45}} = \begin{bmatrix} f'_{45}(\sigma_I^{45}) & f'_{45T}(\sigma_I^{45}) \\ f'_{45T}(\sigma_I^{45}) & f'_{45}(\sigma_I^{45}) \end{bmatrix} \tag{4.33}$$

Here the second principal stress plays no role because the first principal stress governs the state of damage and therefore the propensity for scissoring to occur.

The response of real laminates is expected to fall between the extremes of Equation 4.33, which accounts for fiber scissoring, and Equation 4.32, which accounts for fiber stretching and fragmentation. It is assumed that, for general loading in the θ-direction, the pertinent compliance is a weighted sum of those in Equations 4.32 and 4.33. Enforcing the condition that the stress-strain curves for uniaxial tension at 0° and 45° should be recovered, the new compliance matrix becomes

$$\boldsymbol{S^{\theta}} = D_\theta \begin{bmatrix} f'_{\theta}(\sigma_I^{\theta}) & f'_{\theta T}(\sigma_I^{\theta}) \\ f'_{\theta T}(\sigma_I^{\theta}) & f'_{\theta}(\sigma_I^{\theta}) \end{bmatrix} + (1 - D_\theta) \begin{bmatrix} f'_{\theta}(\sigma_I^{\theta}) & f'_{\theta T}(\sigma_{II}^{\theta}) \\ f'_{\theta T}(\sigma_I^{\theta}) & f'_{\theta}(\sigma_{II}^{\theta}) \end{bmatrix} \tag{4.34}$$

where D_θ is a constant that characterizes the tendency of the laminate to scissor in the θ-direction. It is defined such that, when $D_\theta = 1$, the compliance matrix is governed by fiber rotation (scissoring); conversely, when $D_\theta = 0$, it is governed by fiber stretching and fragmentation.

In implementing this modification in the GH model, only D_0 and D_{45} are required; in general, these quantities will be different from one another. In the 0° direction, the fibers are aligned with the load axis, so there is no tendency to scissor and thus $D_0 = 0$. In contrast, in the 45° direction, the laminate may undergo scissoring, so $0 \leq D_{45} \leq 1$. For a quasi-isotropic laminate, D_{45} must equal 0, since the 0° and 45° directions are equivalent. In contrast, for a [0°/90°] laminate, deformation is expected to be dominated by the scissoring mechanism; therefore, D_{45} should be close to unity. Determination of the precise value of D_{45} for the latter laminate is outside the scope of this work; micro-mechanical models may be required for this task. However, as shown in Section 4.6.2, stress distributions that arise during on-axis loading of [0°/90°] laminates are insensitive to D_{45}.

For $D_{45} = 1$, the modified compliance matrix, and therefore the tangential stiffness matrix, is positive-definite when $f'_{45}(\sigma_I^{45}) > -f'_{45T}(\sigma_I^{45})$. This condition is automatically satisfied, per Equation 4.3.

4.5.3 Material instability

The aforementioned approach remedies material instability in the GH constitutive model. It yields a tangential stiffness matrix that is guaranteed to be positive-definite provided the stress-strain curves used for calibration exhibit strain hardening. One possible criticism of this strategy is that physically realistic instabilities, resulting from fiber fragmentation or shear banding (Hui et al., 1995; Cady et al., 1995a), may be artificially suppressed. The counterargument is that the input stress-strain curves f_0 and f_{45} could be readily modified to account for phenomena that lead to instabilities in the $0°$ and $45°$ directions. If, for instance, a strain softening portion were included in f_{45}, the model would predict a negative shear stiffness and the formation of a shear band; if, on the other hand, a softening portion were included in f_0, the model would predict a negative tensile stiffness and the formation of a tensile crack. Furthermore, since the $0°$ and $45°$ tension tests probe the extremes of the composite response, it seems unlikely that instabilities would occur for loadings at intermediate angles if these instabilities were not present in the input stress-strain curves. Although this approach requires further experimental and theoretical study for validation, it appears to offer a promising route for modeling material instability in CMC laminates.

4.5.4 Criterion for inelasticity

The modified constitutive model requires a criterion to distinguish between the elastic and inelastic regimes, since the procedures for computing stresses differ in the two regimes. For instance, in the original GH model, inelasticity is deemed to occur if any of the stress deficits are non-zero. But, this criterion leads to contradictory results if the matrix cracking stresses or strains differ in the 0° and 45° directions. To demonstrate the contradiction, consider a material element undergoing equibiaxial stressing with a stress $\sigma = \sigma_I = \sigma_{II}$ in the range $\sigma_{mc}^{45} < \sigma < \sigma_{mc}^{0}$. The original GH model predicts a nonzero stress deficit in the 45° direction (since $\Delta\sigma_I^{45} > 0$) and a zero stress deficit in the 0° direction (since $\Delta\sigma_I^{0} = 0$). Therefore, per Equation 4.7, if the principal stresses are considered to be aligned at 45°, the material element is deemed to be inelastic, but if the principal stresses are considered to be aligned at 0°, the material element is deemed to be elastic. This result is contradictory since the axes of principal stress are arbitrary for equibiaxial stressing.

The contradiction arises from the assumption that matrix cracking is governed only by the largest principal stress: a natural consequence of the stress deficit criterion for matrix cracking. Therefore, if this criterion is used, both the original and modified GH models are appropriate *only* for materials that possess (nearly) identical matrix cracking stresses and strains in the 0° and 45°

directions. While this condition may be approximately satisfied in CMCs with relatively dense, stiff matrices, e.g. SiC/CAS, it will not be satisfied in CMCs with compliant, weak matrices, e.g. C/C. (According to the categorization scheme of Evans and co-workers, the former composites are Class II materials whereas the latter are Class III. The classes can be distinguished by the ratio of the matrix shear modulus to the fiber Young's modulus (Cady et al., 1995a).)

The modified GH model would be suitable for elastically-anisotropic materials provided that a different criterion for matrix cracking were employed. This criterion remains to be developed. As argued above, it would need to involve the second principal stress, to avoid the contradiction that arises for equibiaxial stressing.

In this work, the stress deficit criterion is used to assess the presence of matrix cracking within an element. Therefore, the finite element simulations that use the modified GH model are limited to elastically-isotropic laminates. For these materials, the shear strain instability discussed previously becomes irrelevant. However, the original GH model remains unsuitable for finite element calculations because of the principal strain instability that arises in inelastically-anisotropic materials.

4.5.5 Predictions for simple loading scenarios

By inspection, the modified model agrees with the original model for 0° and 45° tension. The models also agree for equibiaxial tension, according to Equation 4.3.

For the case of pure shear, the predictions of the original and modified models are somewhat different. In the original model, the tangent shear compliance in the inelastic domain is well approximated by

$$\frac{\mathrm{d}\gamma}{\mathrm{d}\tau} \approx f'_{45}(\tau) - f'_{45T}(\tau) \tag{4.35}$$

In the modified model, the material is somewhat more compliant in shear:

$$\frac{\mathrm{d}\gamma}{\mathrm{d}\tau} \approx (1 + D_{45})(f'_{45}(\tau) - f'_{45T}(\tau)) \tag{4.36}$$

Since the tangent modulus in the inelastic regime is usually very small (roughly 1–5 GPa)—that is, the response is nearly perfectly-plastic (McNulty et al., 1999; Genin and Hutchinson, 1997)—the factor $1 + D_{45}$ will have only a small influence on the shear flow stress. The predictions of the modified model are therefore expected to be almost indistinguishable from the experimental results for the loading scenarios considered in Genin and Hutchinson (1997): 0° tension, 45° tension, and pure shear.

For a quasi-isotropic laminate, the shear-extension coupling term is zero, and the material does not scissor in either the 0° or 45° direction, so $D_0 =$

$D_{45} = 0$. Therefore, not only is the pure shear behavior identical in the modified and original models, but the models are actually equivalent.

4.6 Open-hole tension simulations

4.6.1 Simulations

For ease of implementation, the constitutive equations in the modified model are integrated explicitly using the modified Euler scheme discussed by Sloan et al. (2001). The scheme utilizes automatic sub-stepping to limit the error arising from the integration procedure to within a prescribed error tolerance for each time step. It has been implemented in a user-material subroutine (UMAT) for use in ABAQUS.

The UMATs for the modified and original models are utilized to simulate an open-hole tension test of a composite laminate. Two materials are investigated. In one simulation, the laminate is elastically isotropic but inelastically anisotropic, with stress-strain curves identical to those depicted in Figure 4.1(c). In this simulation, the original GH model is expected to fail to converge in the inelastic domain, due to material elements that are unstable. In contrast, the modified GH model is expected to remain stable and encounter no convergence problems throughout the inelastic domain. In the second, the geometry and loading are identical to the first, but the laminate is quasi-isotropic. The 45° stress-strain curve is modified to have a tangent modulus of 50 GPa in the inelastic domain, so that $f_{45} = f_0$. As noted above, the modified and original models are expected to yield identical results for this material and, for both models, all material elements should be stable.

The finite element simulation was conducted in ABAQUS Standard (Version 6.9-2, Dassault Systèmes). The specimen geometry is depicted in Figure 4.3. The plate width is five times the hole diameter. A quarter-symmetry finite element model is employed, with four-noded, quadrilateral, plane-stress elements. Load is applied in the y-direction (i.e. at 90°). A study was performed to ensure that the stresses and strains converged with respect to mesh density. For the quasi-isotropic material, the scissoring parameters D_0 and D_{45} both equal 0, by definition. For the inelastically anisotropic material, these parameters were set to 0 and 1 for the 0° and 45° directions, respectively. To explore the sensitivity of the results to D_{45}, a simulation was also run using the minimum value of this parameter that guaranteed stability ($D_{45} = 0.76$).

4.6.2 Results

For the quasi-isotropic laminate, stresses and strains in the direction of loading for the modified and original models are virtually identical to one another (within 0.05 %) in both the elastic and inelastic regimes, as expected. The computed stress concentration factor k at the hole edge, normalized by that obtained in the elastic domain, k_{el}, is plotted in Figure 4.4(a) against the applied net-section stress, σ_{net}, normalized by the matrix cracking stress, σ_{mc}. The results show that stress redistribution due to inelasticity initially mitigates the stress concentration at the hole edge, thereby allowing the laminate to sustain larger loads before tensile fracture: a common feature in CMCs. More importantly, the stress concentration factors predicted by both models are identical. Furthermore, the tangential stiffness matrix for every element remains positive-definite throughout both simulations, and no convergence difficulties are encountered.

In contrast, for the anisotropic laminate, stresses and strains for the two models differ slightly, since the scissoring adjustment is present in the modified model but absent in the original model. Therefore, the stress concentration factors, shown in Figure 4.4(b), are also slightly different (by approximately 0.3–0.6 % after net-section matrix cracking). The original model yields unstable behavior after matrix cracking. As a consequence, the solver eventually fails to obtain a solution; in the present case, this occurs at an applied stress of $\sigma_{net}/\sigma_{mc} = 1.34$. The stress history for one unstable element (see Figure 4.3) is plotted in Figure 4.6. The stresses (σ_{yy}, in the direction of loading) initially increase monotonically and smoothly; however, at $\sigma_{net}/\sigma_{mc} = 1.15$, matrix cracking commences within the element. The tangential stiffness matrix loses positive-definiteness shortly thereafter, causing the stresses to diverge and the stress history to lose monotonicity. The stress history for the same element in the modified model is also plotted in Figure 4.6; the element is seen to exhibit stable behavior.

The simulation using the value $D_{45} = 0.76$ yields results almost identical to those for $D_{45} = 1$. The discrepancy between the axial stresses along the net-section symmetry plane (i.e. the incipient fracture plane) is very small: less than 0.2 % for all values of applied stress. Results for the stress concentration factor for $D_{45} = 0.76$ are shown in Figure 4.4(b). They indicate that the stress concentration factor is essentially independent of D_{45}. Physically, these results arise because, in notched tension simulations, the 0° properties dominate the behavior, whereas the shear properties have a decidedly secondary effect. This fact can be verified by comparing the stress concentration factor for the quasi-isotropic material (in which the laminate is stiff in shear) with that for the anisotropic material (in which the laminate is compliant in shear after matrix cracking). Recall that the only effect of D_{45} is to marginally alter the shear compliance in the post-matrix cracking regime; D_{45} leaves the 0° response unchanged. The implication is that, for open-hole tension tests, D_{45} can be set to unity without greatly affecting the accuracy of the results. However, for tests in which the shear properties predominate, the scissoring parameter must be selected more carefully.

The assumption of nearly proportional straining, used to derive the incremental model, was checked numerically for both the quasi-isotropic and anisotropic laminates. The orientation of the axes of principal strain (θ_ϵ) was found to rotate by less than 0.1 rad (5.7°) for almost all elements. In a few elements along the hole boundary, which experienced larger shear strains, θ_ϵ rotated by a larger angle, with the maximum rotation angle being 0.35 rad (20°). Therefore, the strains are nearly proportional for the vast majority of the laminate; the presence of mildly non-proportional straining in a small number of elements is surmised to negligibly affect the accuracy of the finite element analysis.

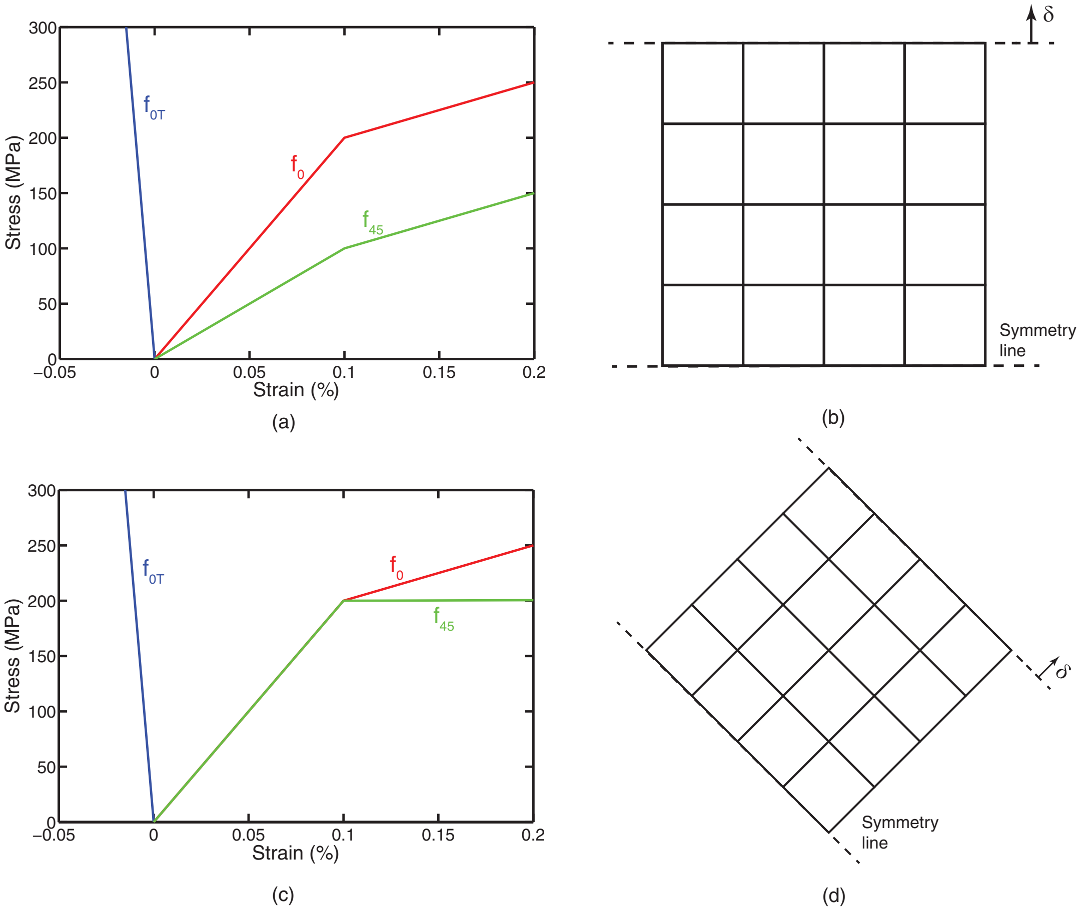

Figure 4.1: (a) Input stress-strain curves and (b) finite element mesh for a simulation of an elastically-anisotropic material in 0° tension. (c) Input stress-strain curves and (d) finite element mesh for a simulation of an inelastically-anisotropic material in 45° tension.

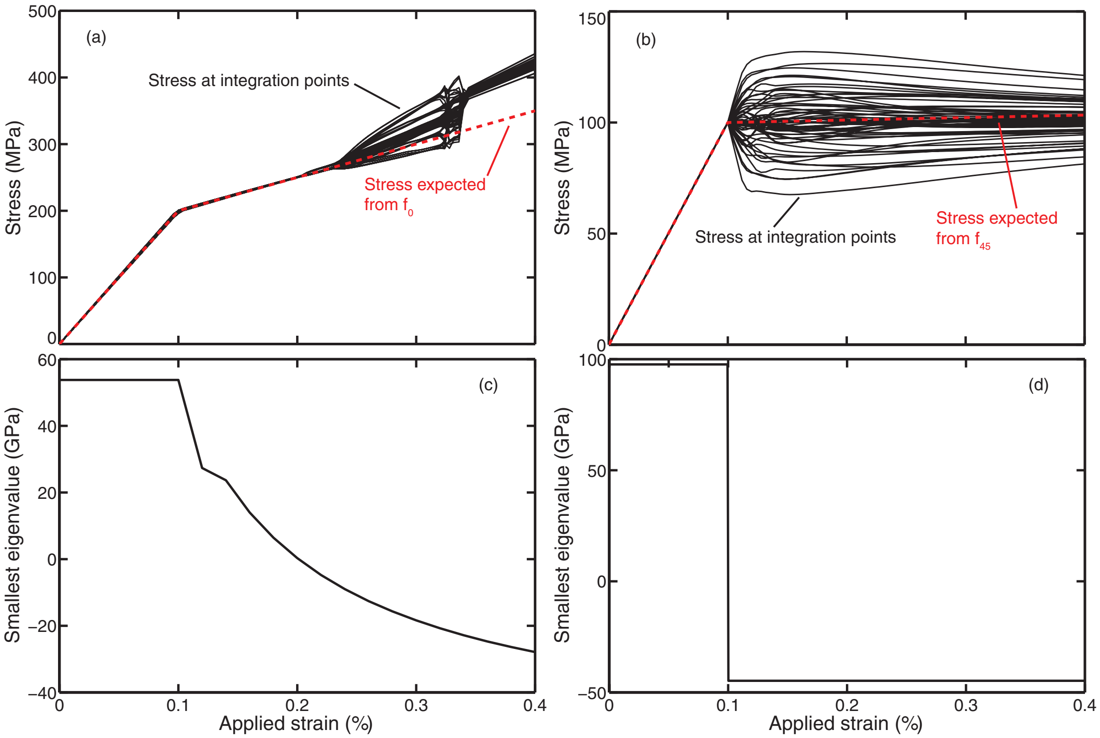

Figure 4.2: Normal stresses parallel to the fiber directions at all integration points within the two finite element models defined in Figure 4.1: (a) 0° tension of the material defined in Figure 4.1(a) and (b) 45° tension of the material defined in Figure 4.1(c). Smallest eigenvalue of the symmetric part of the tangential stiffness matrix in each test ((c) and (d)). Loss of positive-definiteness occurs when the smallest eigenvalue becomes negative.

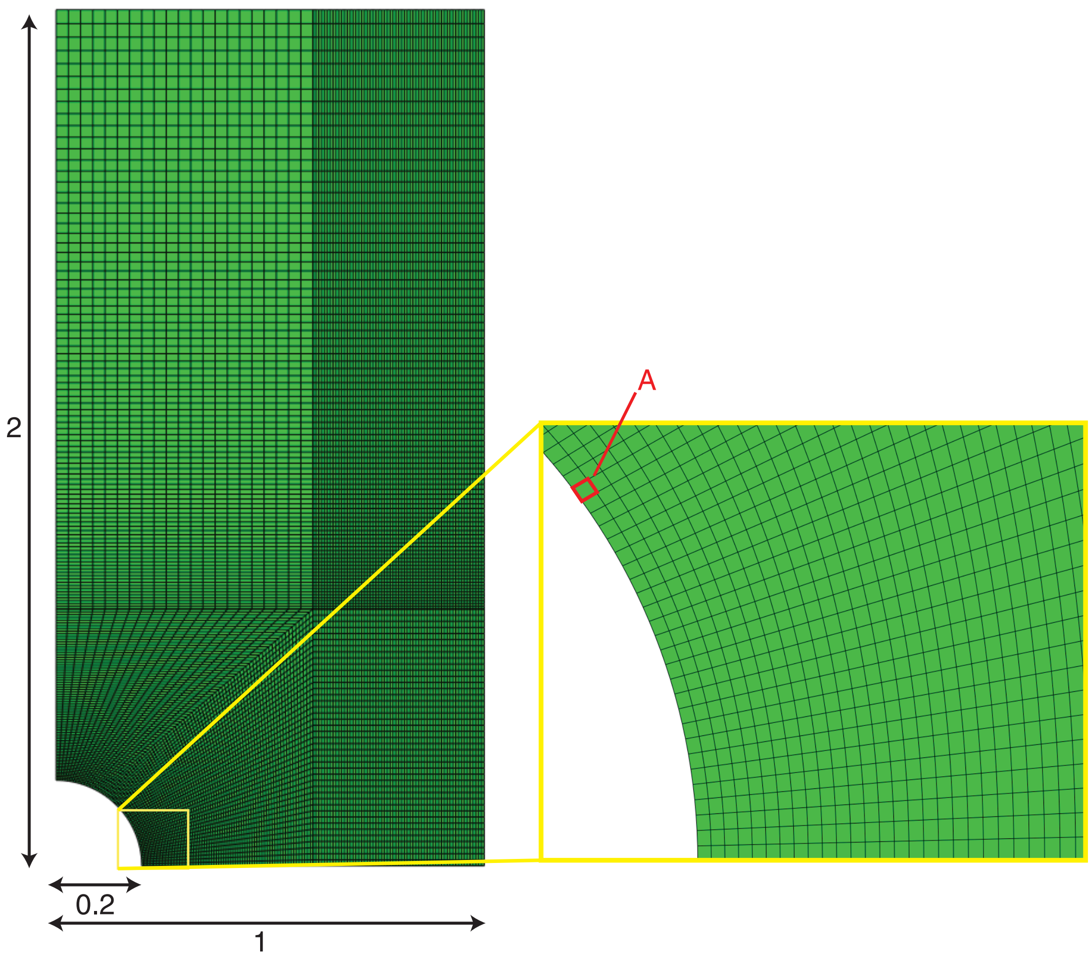

Figure 4.3: Finite element mesh used to compute stress concentrations in open-hole tensile specimens. The element labeled A is the one interrogated to obtain the results in Figure 4.6.

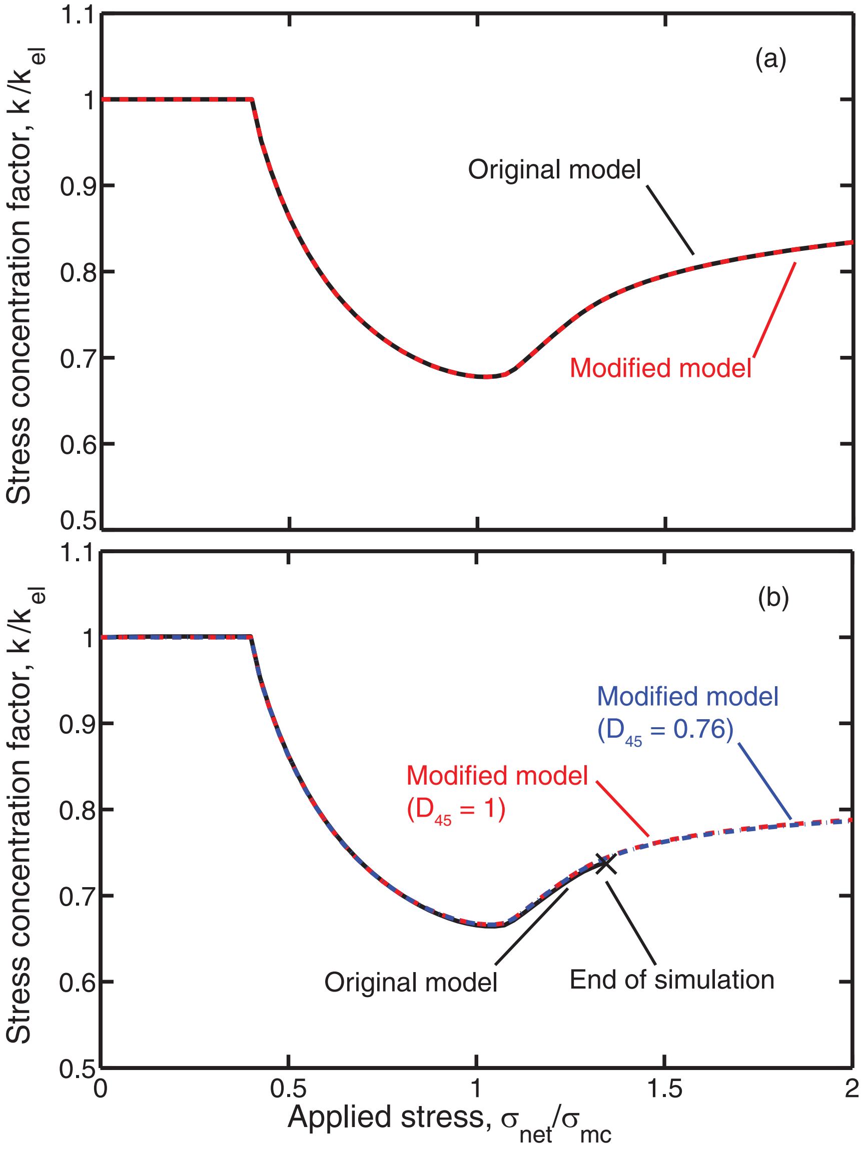

Figure 4.4: Stress concentration factor at hole edge vs. applied stress for (a) the quasi-isotropic material and (b) the inelastically-anisotropic material. Results for the original and modified GH models are shown. For the anisotropic material, two values of D_{45} (0.76 and 1) are examined. The stress concentration factor is normalized by that in the elastic domain. The applied stress is computed on a net-section basis and is normalized by the matrix cracking stress.

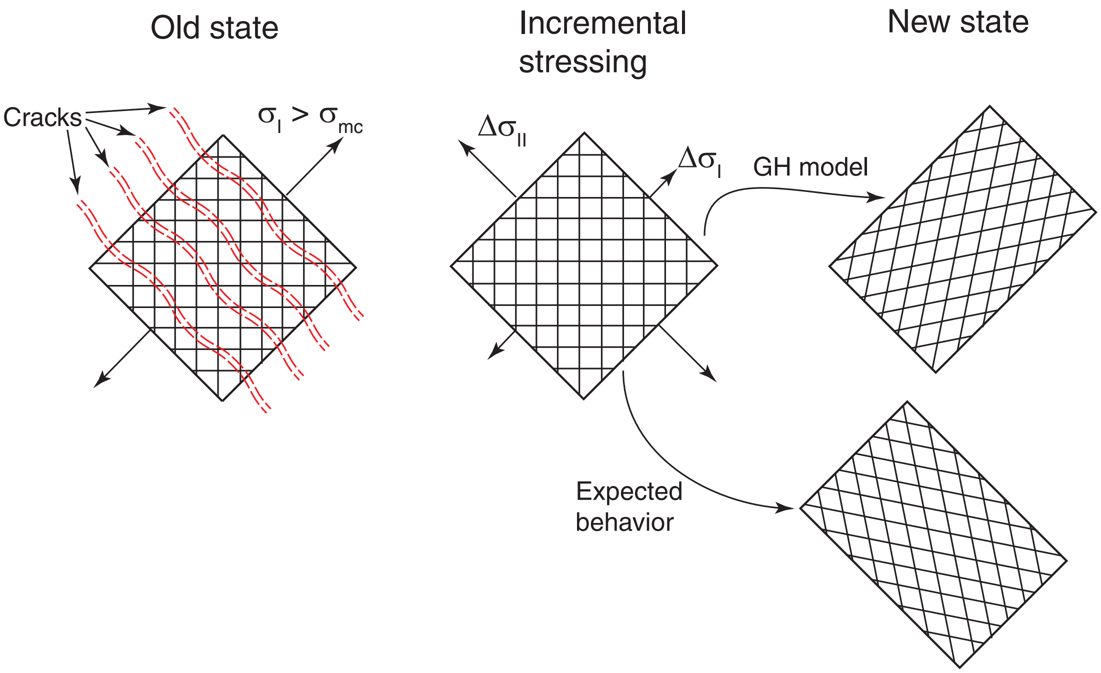

Figure 4.5: Deformation of a cracked crossply laminate undergoing fiber scissoring. The behavior predicted by the GH model is shown at top right; that expected from consideration of fiber scissoring is shown at bottom right.

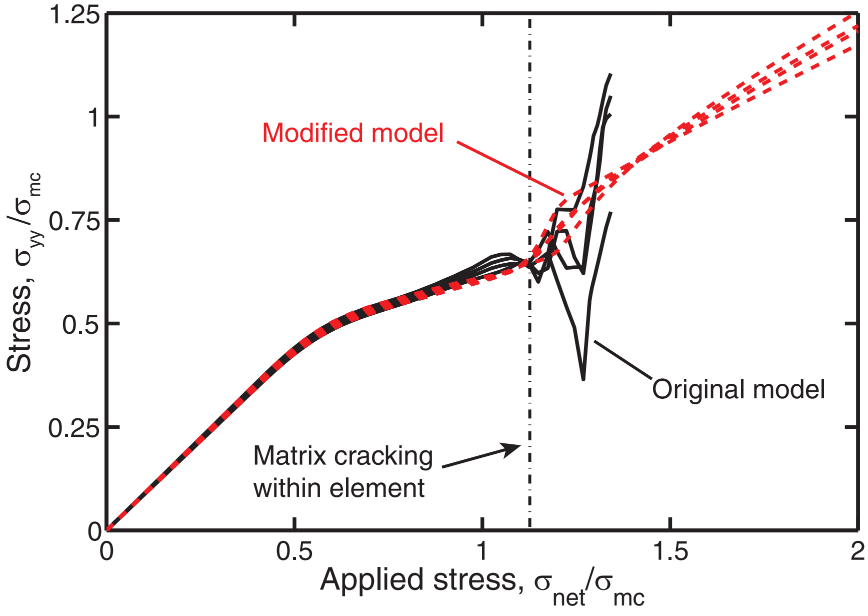

Figure 4.6: Evolution of normal stress in direction of loading (σ_{yy}) for one specific unstable element (indicated in Figure 4.3) in the notched tension simulation. Stresses are plotted at all four integration points within the element.

Chapter 5

Stress distributions in notched CMC laminates

5.1 Introduction

In this chapter, the effect of notches on stress distributions in CMC laminates is investigated. In tough CMCs, inelasticity arising from matrix cracking and fiber fragmentation redistributes stress away from notches, thus enabling

---

This chapter is adapted from a peer-reviewed publication: V. P. Rajan and F. W. Zok. Stress Distributions in Bluntly-Notched Ceramic Composite Laminates. *Composites Part A*, 60:15–23, 2014. Available at: `http://dx.doi.org/10.1016/j.compositesa.2014.01.010` design of components with complex geometric features and with attendant stress concentrations using *elastic* analyses and low 'knock-down' factors. The principal goal of this chapter is to predict these stress fields using an *analytical* framework, the accuracy of which is assessed by finite element simulations that utilize the modified GH model. As part of a broader effort to assess notch-sensitivity, the analytical stress fields could be used subsequently for predicting fracture (associated with the onset of fiber bundle rupture and localization of deformation).

The chapter is organized in the following way. Finite element analyses of notched CMC plates are conducted using the modified GH constitutive model, developed in Chapter 4. For the purpose of generating generally applicable results and identifying important trends, the tensile stress-strain curves used to calibrate the model are idealized as being bilinear. This is followed by presentation of the proposed analytical framework, which is based on Neuber's law (Neuber, 1961) for stress concentration factors (SCFs) in elastic-plastic materials. Using this framework, solutions are derived for both SCFs and near-notch stress distributions in CMC laminates exhibiting bilinear tensile behavior. The latter are based on a series of proposed linear transformations to the elastic stress distributions. The predicted SCFs and stress distributions are then assessed through comparisons with results from FEA. Effects of the post-cracking tangent modulus, the degree of in-plane anisotropy, and the notch size and shape are examined. The study is directed at systems in which the matrix modulus is of the same order as the fiber modulus and which therefore exhibit minimal *elastic* anisotropy. This behavior is obtained in SiC/SiC composites. Effects of elastic anisotropy, obtained in C/C, C/SiC and some oxide composites (Cady et al., 1995a; Heathcote et al., 1999), are not considered.

5.2 Finite element analysis

5.2.1 Constitutive law

The material response is taken to follow a modified form of the Genin-Hutchinson constitutive model for CMC laminates (Chapter 4). To recapitulate, the model is calibrated using measurements from two types of tensile tests: parallel to one of the fiber directions (in the 0°/90° orientation) and at 45° to this direction. For each test, both the longitudinal and the transverse (in-plane) strains are measured. The longitudinal and transverse strain-stress functions in the 0°/90° orientation are denoted f_0 and f_{0T}, respectively. Similarly, at 45°, the functions are denoted f_{45} and f_{45T}.

The subsequent numerical simulations are based on the assumption that f_0 and f_{45} are bilinear functions of applied stress, each characterized by: (i) a

Young's modulus, $E = E_0 = E_{45}$, (ii) a matrix cracking stress, $\sigma_{mc} = \sigma_{mc,0} = \sigma_{mc,45}$, and (iii) a post-cracking tangent modulus, E^P, which may differ in the 0° and 45° directions (Figure 5.1). The transverse strain function f_{0T} obtained in the $0^\circ/90^\circ$ orientation is assumed to be linear with applied stress in both the elastic and the post-cracking domains (Poisson's ratio = 0.1). This assumption is supported by experimental studies which have shown that, following cracking, the transverse strain in this orientation either remains constant or decreases only very slightly in magnitude (McNulty et al., 1999; Lynch and Evans, 1996). Since the Poisson's ratio of these composites is small (< 0.2), the elastic strains themselves are small and hence deviations from linearity have little effect on the notched composite behavior.

The baseline case is taken as one for which: (i) the normalized post-cracking tangent modulus in the $0^\circ/90^\circ$ orientation, defined as $\alpha \equiv E_0^P/E_0$, is $1/4$ (a value representative of $[0^\circ/90^\circ]$ elastically-isotropic laminates with a fiber volume fraction of 50 %); and (ii) the post-cracking response is isotropic ($\overline{E^P} \equiv E_{45}^P/E_0^P = 1$) and hence $f_{45} = f_0$. A limited parametric study is also conducted to assess the effects of both the post-cracking tangent modulus ($\alpha = 1/10$), and the *inelastic* anisotropy ($\overline{E^P} = 1/5$ and $1/50$).

When loaded in the ±45° direction beyond the cracking stress, the latter laminates exhibit some degree of 'scissoring': a deformation mode in which fibers rotate towards the direction of the largest principal stress. In the modified Genin-Hutchinson model, the propensity for scissoring in this orientation is characterized by a non-dimensional parameter, $0 \leq D_{45} \leq 1$, as discussed in Chapter 4. D_{45} is largely controlled by the *post-cracking* matrix properties, which is reflected in $\overline{E^P}$. When the matrix provides minimal constraint against scissoring, D_{45} tends towards unity; in the opposite scenario, D_{45} tends towards zero. In the present study, the values $D_{45} = 0, 0.5$, and 1 are selected for laminates with $\overline{E^P} = 1, 1/5$, and $1/50$, respectively.

5.2.2 Geometry and mesh

As in Chapter 4, finite element simulations were carried out in Abaqus Standard (Version 6.9-2, Dassault Systèmes) using the modified Genin-Hutchinson constitutive model as a user-material subroutine.

The specimen geometry is depicted in Figure 5.2. Quarter-symmetry models with four-noded, quadrilateral, plane-stress elements were used. The plate height H was set to twice the plate width (defined as $2W$); this ensures that significant bending stresses do not develop in the ligament between the loaded boundary and the notch (Genin and Hutchinson, 1999). For the circular holes, the hole radius, a, was varied between $a/W = 0.05$ and 0.5. For elliptical holes, the principal radius, a, in the x-direction was selected to be $a/W = 0.2$, and that in the y-direction, b, was set to either $b/a = 1/3$ or 3. Load was applied at the upper boundary in the y-direction. A study was performed to ensure that the stresses and strains converged with respect to mesh density.

5.3 Analytical models

5.3.1 Stress concentration factors

An analytical solution for the stress concentration factor (SCF) following the onset of inelastic straining is obtained from Neuber's law (Neuber, 1961). The law is based on the assumption that the stress and strain concentration factors, k_σ and k_ϵ, following the onset of local inelastic straining are related to the elastic stress concentration factor, k_{el}, through

$$\sqrt{k_\sigma k_\epsilon} = k_{el} \tag{5.1}$$

Neuber (1961) demonstrated this relation to be strictly valid for isotropic metals subject to anti-plane shear loading. Subsequently, the law has been used extensively for predicting stress concentrations in metallic specimens for a variety of notch shapes and loading configurations (Agnihotri, 1995; Guo et al., 1998; Jiang and Xu, 2001; Moftakhar et al., 1995; Zeng and Fatemi, 2001; Härkegård and Mann, 2003).

Operationally, the law is implemented by finding the intersection point between the tensile stress-strain curve and a hyperbola described by

$$\sigma\epsilon = k_{el}^2 \sigma_{net} \epsilon_{net} \tag{5.2}$$

where σ_{net} and ϵ_{net} are the nominal net-section values (calculated from the applied load and the uniaxial tensile stress-strain curve). The SCF is then given by the ratio of the stress at the intersection point of the two curves and the applied stress (Figure 5.3). In applying the Neuber law to CMCs loaded in the $0^\circ/90^\circ$ orientation, the relevant stress-strain curve is the one measured in that same orientation. A tacit assumption, therefore, is that the off-axis properties, as manifested in the $\pm 45^\circ$ tensile response, do not affect the SCF. The veracity of this assumption is addressed in due course.

For *isotropic* CMCs that exhibit a bilinear stress-strain response, the SCF can be evaluated analytically. Three solution regimes exist. (i) At low stresses, defined by $\beta = \sigma_{net}/\sigma_{mc} \leq 1/k_{el}$, the material remains elastic everywhere and thus $k_\sigma = k_{el}$. (ii) At higher stresses, in the range $1/k_{el} \leq \beta \leq 1$, cracking occurs *locally* around the hole. Following the procedure described above, the SCF is determined by combining Equation 5.2 with the tensile stress-strain curve. (That is, $\epsilon_{net} = f_0(\sigma_{net})$ and $\epsilon = f_0(\sigma)$.) This yields (after some algebra):

$$k_\sigma = \frac{1 - \alpha + \sqrt{(1-\alpha)^2 + 4\alpha\beta^2 k_{el}^2}}{2\beta} \tag{5.3}$$

(iii) At yet higher stresses, notably $\beta \geq 1$, cracking occurs across the entire section and the SCF is given by:

$$k_\sigma = \frac{1 - \alpha + \sqrt{(1-\alpha)^2 + 4\beta(\alpha + \beta - 1)k_{el}^2}}{2\beta} \tag{5.4}$$

5.3.2 Stress distributions

A first approximation to the longitudinal stress distribution, $\sigma(x)^1$, along the incipient fracture plane following the onset of inelastic straining is obtained through a straightforward modification of the elastic distribution. The modification involves application of Neuber's law to every point along this plane. This is accomplished by re-interpreting k_{el} in Equations 5.3 and 5.4 as the ratio of the (original) elastic stress at the point of interest, $\sigma_{el}^o(x)$, to the net-section stress, σ_{net}, and k_σ as the ratio of the actual stress, $\sigma(x)$, in the inelastic zone to σ_{net}. Accordingly, the modified stress along this plane in the inelastic zone is given by:

$$\frac{\sigma_{in}^o(x)}{\sigma_{net}} = \frac{1 - \alpha + \sqrt{(1-\alpha)^2 + 4\alpha\beta^2(\sigma_{el}^o(x)/\sigma_{net})^2}}{2\beta} \tag{5.5}$$

for $1/k_{el} \leq \beta \leq 1$, and

$$\frac{\sigma_{in}^o(x)}{\sigma_{net}} = \frac{1 - \alpha + \sqrt{(1-\alpha)^2 + 4\beta(\alpha + \beta - 1)(\sigma_{el}^o(x)/\sigma_{net})^2}}{2\beta} \tag{5.6}$$

---

[1] Throughout the article $\sigma(x)$ refers to the distribution in the normal stress acting in the direction of the applied load.

for $\beta \geq 1$.

A comparison of the Neuber-modified stress distribution with that obtained from FEA for a plate with a circular hole with $a/W = 0.2$ is shown in Figure 5.4. Although the proposed modification brings the elastic distribution into somewhat closer agreement with the FEA results, it underestimates both the stresses in the near-tip region and the size of the inelastic zone. The discrepancies arise because the spatial re-distribution of stress associated with inelastic straining is neglected.

The discrepancies are ameliorated through further transformations of the elastic stress distribution. The transformations build on the requirement that the net-section must support the same load before and after stress redistribution and, as a result, the size of the inelastic zone must increase in order to compensate for the reduction in stress at the notch tip. The transformations should yield stress distributions that satisfy the equilibrium condition:

$$\int\limits_{0}^{x_{in}} \sigma_{in}(x)\,\mathrm{d}x + \int\limits_{x_{in}}^{W-a} \sigma_{el}(x)\,\mathrm{d}x = (W-a)\sigma_{net} \tag{5.7}$$

where $\sigma_{el}(x)$ and $\sigma_{in}(x)$ refer to the stress distributions in the elastic and inelastic zones, respectively, *after transformation*, and x_{in} denotes the elastic-inelastic boundary. They must also satisfy the condition of continuity of stress at the inelastic zone boundary, notably

$$\sigma_{in}(x_{in}) = \sigma_{el}(x_{in}) \tag{5.8}$$

Numerous approaches for transforming stress distributions and estimating the size of inelastic zones have previously been proposed (Agnihotri, 1995; Guo et al., 1998; Glinka, 1985): the most well-known being Irwin's method for estimating the plastic zone size ahead of a crack in an elastic/plastic plate (Irwin, 1960). The transformations are typically linear, i.e. translation, scaling, or a combination thereof. To capture the stress within the *elastic* zone (away from the notch tip), a simple translation of the original elastic stress distribution, $\sigma_{el}^{o}(x)$, is employed. Specifically, as done by Irwin (1960):

$$\sigma_{el}(x) = \sigma_{el}^{o}(x + A) \tag{5.9}$$

where A is a positional shift along the x-direction, taken to be

$$A = x_{in}^{o} - x_{in} \tag{5.10}$$

Here x_{in}^{o} is the original estimate of the elastic-inelastic boundary, obtained by equating the elastic stress distribution to the matrix cracking stress (see Figure 5.5), and x_{in} is obtained in the manner described below.

For the stress distribution in the *inelastic* zone, the complete linear transformation is used:

$$\sigma_{in}(x) = \sigma_{in}^{o}(Bx + C) \tag{5.11}$$

where $\sigma_{in}^{o}(x)$ is obtained from Equation 5.5 or 5.6, as appropriate. The constants B and C are found by enforcing the continuity condition (Equation 5.8) in conjunction with the requirement that the stress at the notch tip (at $x = 0$) equal that predicted by Neuber's law (Equation 5.1). Doing so yields $C = 0$ and

$$B = \frac{x_{in}^{o}}{x_{in}} \tag{5.12}$$

This procedure is shown graphically in Figure 5.5. The only unknown variable is the new estimate of x_{in}. It can, in principle, be obtained from Equation 5.7, which is nonlinear and must be solved numerically. Alternatively, in order to facilitate the development of analytical solutions, it is noted that, by taking

$$B = \frac{k_{\sigma}}{k_{el}} \tag{5.13}$$

the resulting stress distributions (presented in Section 5.4.3) are in excellent agreement with those computed by FEA. Combining Equations 5.12 and 5.13 yields:

$$x_{in} = \frac{k_{el}}{k_{\sigma}} x_{in}^{o} \tag{5.14}$$

Combining the preceding results yields the final estimates of the stresses in the elastic and inelastic zones, notably:

$$\sigma_{el}(x) = \sigma_{el}^{o}\left(x - x_{in}^{o}\left[\frac{k_{el}}{k_{\sigma}} - 1\right]\right), \qquad x_{in} \le x \le W - a \tag{5.15a}$$

$$\sigma_{in}(x) = \sigma_{in}^{o}\left(\frac{k_{\sigma}}{k_{el}} x\right), \qquad 0 \le x \le x_{in} \tag{5.15b}$$

where the function $\sigma_{in}^{o}(x)$ is given by Equation 5.5, k_{σ} is from Equation 5.3, and x_{in} is from Equation 5.14.

Once the entire net-section has cracked, the inelastic zone size is taken to be $x_{in} = W - a$. The equilibrium condition in this domain is

$$\int_{0}^{W-a} \sigma_{in}(x)\,\mathrm{d}x = (W-a)\sigma_{net} \tag{5.16}$$

The stress distribution is again given by Equation 5.15b, but with k_σ and $\sigma_{in}^{o}(x)$ now obtained from Equations 5.4 and 5.6, respectively.

5.4 Assessment of analytical solutions

5.4.1 Preliminaries

The accuracy of the preceding analytical solutions is evaluated by comparing the predictions with the results obtained from FEA. To this end, several metrics are used: (i) the error in the SCF, (ii) the error in x_{in}, (iii) the error in satisfying the equilibrium condition (Equation 5.7), and (iv) the average error in stress along the net-section plane. In the results that follow, FEA is employed to ascertain both the inelastic *and* the elastic stress distributions. In principle, analytical solutions for the elastic fields could be used, thereby yielding fully-analytical solutions for the stress distributions after cracking.

Neuber's law, which forms the basis for the present model, is strictly applicable only for small-scale yielding, wherein the inelastic zone size is small compared to the notch size and the net-section width (Rice, 1967; Zappalorto and Lazzarin, 2007). However, it is found, surprisingly, that the resulting SCFs and stress distributions in bluntly-notched CMCs are in excellent agreement with the FEA results even for large-scale and net-section inelasticity. With few exceptions, this conclusion holds over the range of notch geometries considered in the present study. The basis for this conclusion follows.

5.4.2 Stress concentration factors

Comparisons of the SCFs obtained from Neuber's law (Equations 5.3 and 5.4) and those from FEA for the isotropic laminate ($\alpha = 1/4$, $\overline{E^P} = 1$) are shown in Figure 5.6. Results are for circular holes with three radii ($a/W = 0.05$, 0.2, or 0.5) and elliptical holes with two aspect ratios ($b/a = 1/3$ or 3, both with $a/W = 0.2$). Here the SCF is normalized by is elastic counterpart, k_{el}. Matrix cracking is seen to significantly reduce the stress concentration factor at the notch tip; at the nominal net-section cracking stress ($\beta = 1$), typical reductions in stress concentration are 20–50 %, with larger reductions being attained for sharper notches.

The comparisons also show that Neuber's law provides a reasonably accurate description of k_σ over the pertinent range of applied stress ($0 \leq \beta \leq 2$). For all notch geometries investigated, errors in k_σ are less than 10 %. Neuber's law performs especially well, with error less than 5 %, for plates with small, low aspect-ratio features. For notches that are large relative to the plate width (e.g. holes with $a/W = 0.5$), Neuber's law somewhat over-predicts the SCF after net-section cracking, likely because of the interaction of the stress field with the plate boundaries. For sharper features, such as the elliptical hole with $b/a = 1/3$, Neuber's law again yields slightly conservative estimates of k_σ at high stress. Qualitatively similar results have been reported for notched metallic plates by Guo et al. (1998), who proposed that a more accurate estimate of the SCF could be obtained by applying Neuber's law a small distance ahead of the notch-tip. However, since the errors in the present study are far lower than those reported by Guo et al. (1998), this additional *ad hoc* adjustment is deemed unnecessary.

5.4.3 Stress distribution and inelastic zones

The proposed method for calculating the stress distribution along the net-section works exceedingly well for stress concentrating features that are small in comparison to the plate width. Typical stress distributions are shown in Figure 5.7(a) for a plate with a circular hole of radius $a/W = 0.2$. For an applied stress sufficient to cause large-scale cracking ($\beta = 0.75$), the method accurately captures both the location of the elastic-inelastic boundary and the stress distributions in the elastic and inelastic zones. Even in the domain of net-section cracking ($\beta = 1.5$), the stresses close to the hole are captured very well, although those near the plate edge are slightly overestimated. Clearly, the utility of the method is not limited to the restrictive case of small-scale yielding.

The accuracy of the method improves as the hole size decreases. For net-section cracking ($1 \leq \beta \leq 2$), the normalized root-mean-squared error in the predicted stresses falls in the range 1–2.5 % for $a/W = 0.05$, 3.5–7 % for $a/W = 0.2$, and 6.5–19 % for $a/W = 0.5$. To understand this result, note that the length scale for stress decay away from the hole is governed by the hole radius, a. To compensate for the increase in stress near the notch (relative to the net-section stress), a reduction in stress (again, relative to the net-section stress) must occur near the plate edge. The magnitude of this stress drop is proportional to a/W. The present transformation method neglects this effect; consequently, stresses near the plate edge are overestimated in plates that have large stress concentrating features and that are subjected to high stresses. One important corollary is that the method should be highly accurate in the limit of infinite plates. Indeed, this conclusion is borne out by the present results.

The variations in the inelastic zone size with applied stress are plotted in Figure 5.8. For moderate stress levels ($\beta \leq 0.9$), excellent agreement is obtained between the model predictions and the FEA results. In this domain, the error between the two is less than 5 %. Similar agreement is obtained for the other notch geometries considered in this study (not shown); the one exception is the plate with an elliptical hole with $b/a = 3$, for which the error is still less than 10 %. Once the net-section cracking condition is met ($\beta = 1$), the analytical model predicts that the inelastic zone encompasses the entire net-section ($x_{in} = W - a$). In reality, because of the stress reduction effect that occurs for larger holes, this boundary may exist within the bounds of the plate even when $\beta = 1$. Thus the computed transition at and slightly beyond $\beta = 1$ is somewhat more gradual, especially for large a/W.

The models for the stress distribution and the inelastic zone size perform equally well for plates with elliptical holes (Figure 5.9). Here, again, the near-tip stresses are captured very well by the analytical model; the errors are slightly greater near the plate edge at high stress ($\beta \geq 1$).

Because stresses at the plate edge tend to be overestimated by the present model, the equilibrium condition (Equations 5.7 and 5.16) is only approximately satisfied. For plates with larger notches, the net-section reaction force predicted by the analytical model is approximately 2–6 % larger than the applied load at high applied stresses. Enforcing the equilibrium condition, by numerically solving Equation 5.7 to find x_{in}, brings the stresses near the plate edge into somewhat better agreement with the FEA results. However, this improvement is offset by poorer agreement in the stress near the notch tip, particularly for sharp notches. Since the near-tip stresses are arguably most important in failure prediction, this alternative approach is not recommended.

5.4.4 Effects of post-cracking tangent moduli

Neuber's law assumes isotropic mechanical response. When applied to anisotropic laminates, it tacitly neglects the off-axis properties (at 45°). This assumption is assessed by examining the effects of the post-cracking tangent moduli, E_0^P and E_{45}^P, on the correspondence between the predicted and computed stress fields and, in turn, on the accuracy of the proposed transformation method. Finite element results for the SCF for $\alpha = 1/10$ (shown in Figure 5.6(a)) reveal only slight increases in error relative to those obtained for the higher hardening laminate ($\alpha = 1/4$). Analogous results for the SCFs in a highly anisotropic laminate ($\overline{E^P} = 1/50$) are plotted on Figure 5.6(b) and the stress distribution at one stress level ($\beta = 2$) is plotted in Figure 5.11. Comparisons with the analytical results reveal that, for features with inherently low SCF (say, $b/a \geq 1$), the errors in the predicted SCFs are no greater than those for the isotropic laminate. For features that yield higher stress concentrations (e.g. elliptical hole with $b/a = 1/3$), the errors in SCF are somewhat greater than those of the isotropic laminate, although the predicted SCF values are conservative over the entire stress range (i.e. lower than those obtained from FEA).

The origin of the differences in behavior of the isotropic and anisotropic laminates at high stress can be elucidated from examination of strain distributions obtained from FEA. Two sets of results, for $\overline{E^P} = 1$ and $1/50$, are shown in Figure 5.10. The comparisons show that, at high stresses (well beyond the onset of cracking), the shear strain γ_{xy} in the notch-tip region adjacent to the net-section plane is almost twice that obtained at the same location in the isotropic laminate (see, for example, the points indicated on Figures 5.10(c) and (d)). The additional shear strain has the effect of mitigating the axial tensile strains directly ahead of the notch tip. Moreover, the somewhat elongated shape of the zone of high shear is reminiscent of the deformation preceding the formation of a shear band. Indeed, the increased propensity for shear banding in the anisotropic laminate gives rise to the reduced SCF. Analogous effects have been found in some anisotropic fiber-reinforced polymer-matrix composites (Yang and Cox, 2005) and ceramic/metal laminates (Chan et al., 1993). Examinations of other strain distributions (not shown) reveal that the notch shape also plays a role: sharp notches inducing larger shear strains than circular holes.

5.4.5 Extension to multiaxial loading

Here a preliminary assessment of the utility of the analytical method in predicting SCFs and stress distributions under multiaxial loading conditions is presented. It is motivated in part by reports that, in metallic alloys, Neuber's law yields inaccurate results when stress multiaxiality is significant (Guo et al., 1998; Moftakhar et al., 1995; Zeng and Fatemi, 2001; Glinka, 1985; Molski and Glinka, 1981; Hoffman and Seeger, 1985). The errors are attributed to effects of stress multiaxiality on plastic straining in metals (Zeng and Fatemi, 2001). Local stress multiaxiality can arise in plates that are sufficiently thick to create plane strain conditions at the notch tip or when the applied loads themselves are multiaxial. Our expectation at the outset is that such effects should be less important for isotropic ceramic composite laminates. This expectation is based on three observations. First, inelasticity (i.e. cracking) in ceramic composites is driven by the maximum principal tension (in contrast, metal plasticity is driven by the deviatoric stress). Second, the coupling of axial stresses with transverse strains is weak in ceramic composites, both in the elastic and the inelastic domains (Genin and Hutchinson, 1997). Third, plane strain conditions are not obtained in CMC plates. Thus the analytical method is expected to remain applicable when uniaxial tension is combined with other in-plane loadings, provided that the loading remains proportional.

To assess this hypothesis, a specific example is considered: that of proportional biaxial loading of a square plate ($W = H$) with a circular center hole ($a/W = 0.2$). The applied stress in the x-direction (at 0°) is half of that in the y-direction. The FEA is otherwise identical to that described previously. The variation in SCF with applied stress is plotted in Figure 5.12(a) and representative stress distributions are shown in Figure 5.12(b). The correlations between the analytical predictions and the FEA results are very good: comparable to those obtained for uniaxial tensile loading. Therefore, for isotropic CMC laminates, the current analytical method should find utility in predicting stress concentrations and stress distributions in scenarios involving multiaxial in-plane loading.

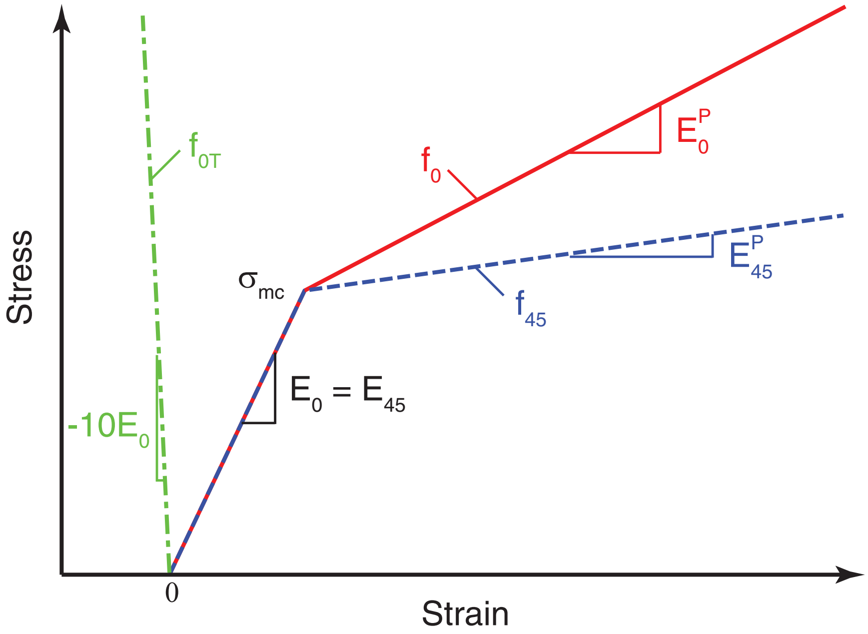

Figure 5.1: Idealized stress-strain curves used for calibrating the Genin-Hutchinson constitutive model.

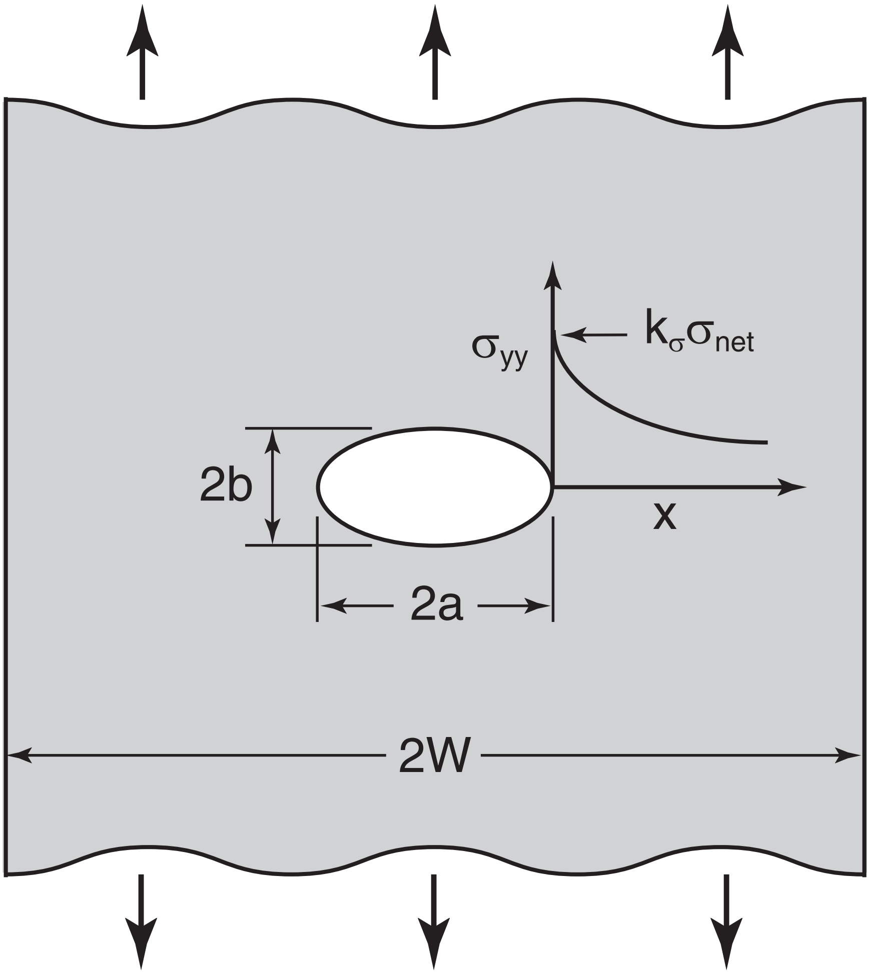

Figure 5.2: Geometry of center-notched plate subjected to uniaxial tensile loading.

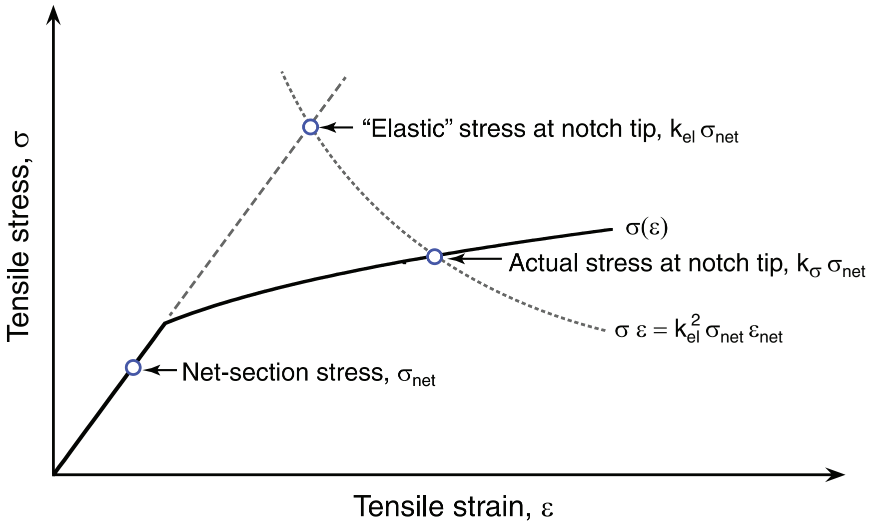

Figure 5.3: Schematic illustration of the procedure used to calculate SCFs from Neuber's law.

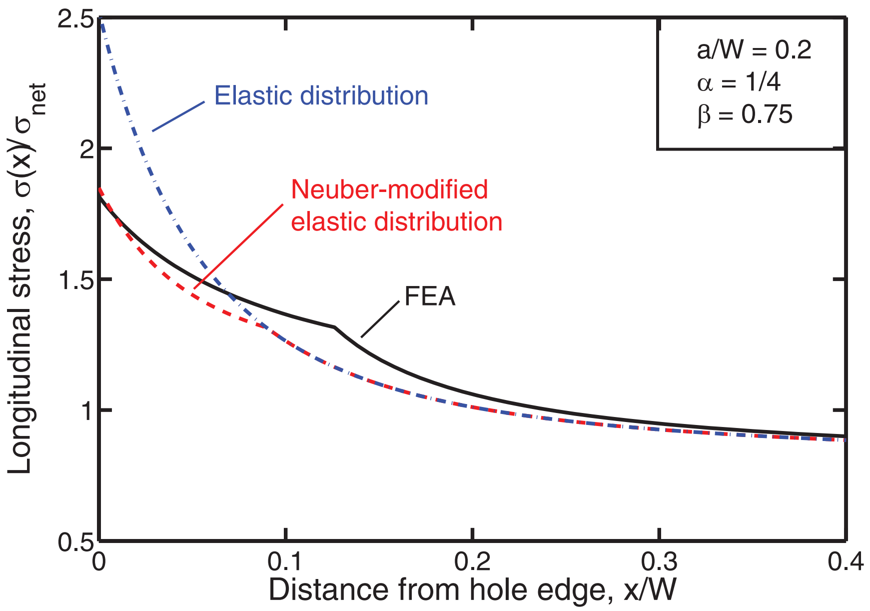

Figure 5.4: Comparison of the (untransformed) Neuber-modified stress distribution with the elastic distribution and that from FEA for a plate containing a circular hole.

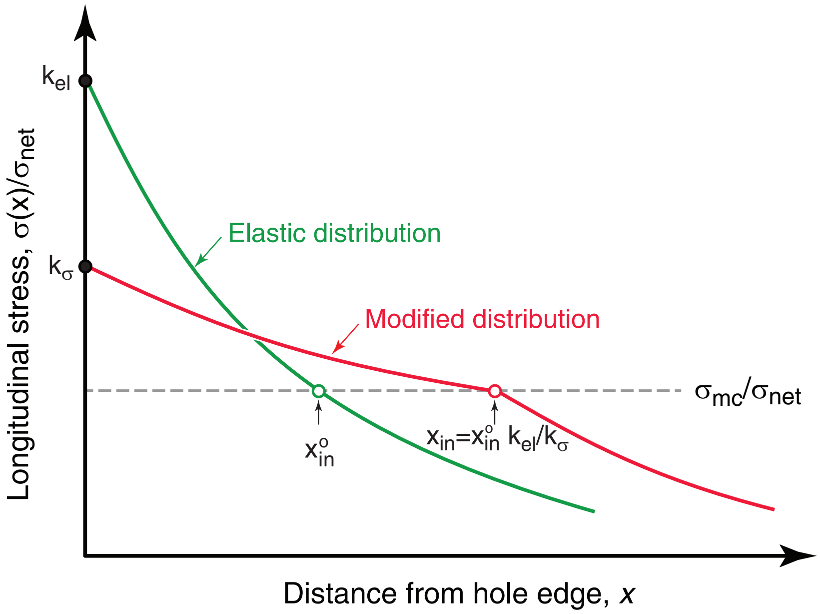

Figure 5.5: Schematic representation of the transformation of the elastic distribution to account for effects of stress redistribution on both the peak stress and the size of the inelastic zone.

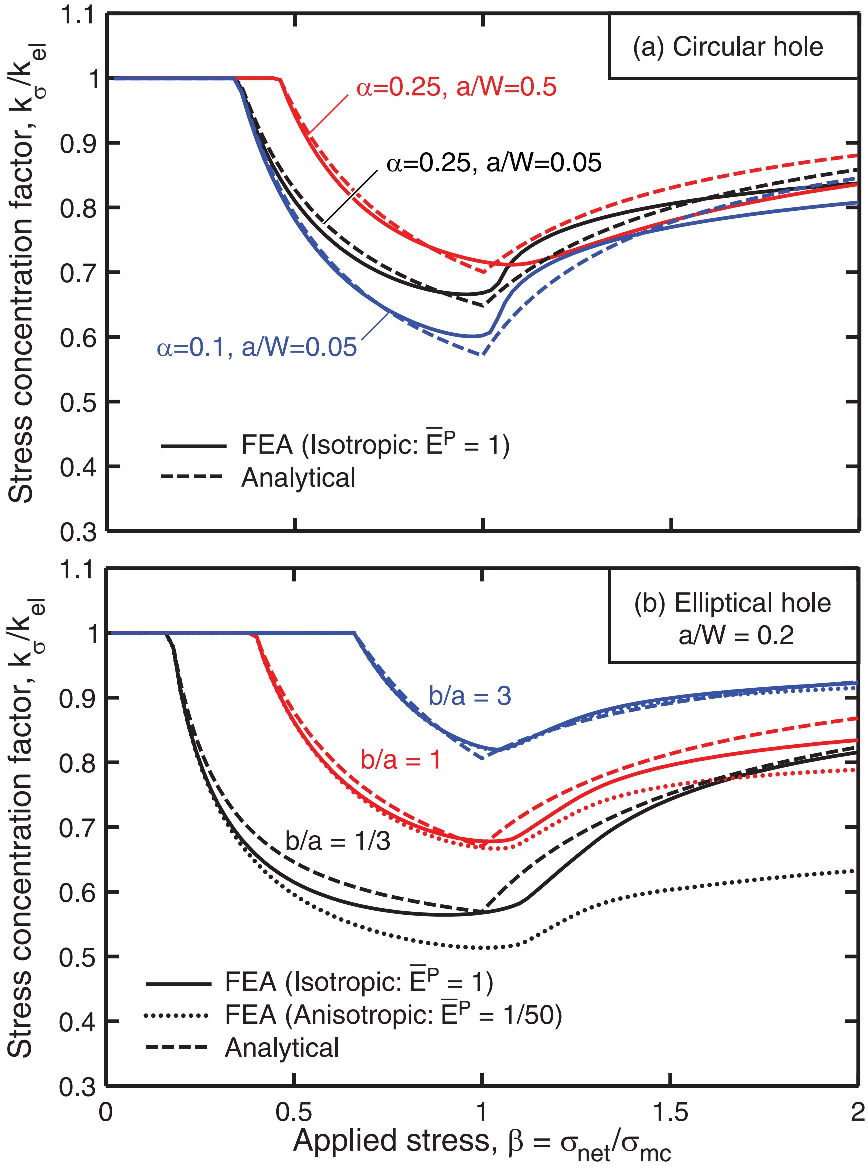

Figure 5.6: Normalized stress concentration factors, k_σ/k_{el}, for isotropic and anisotropic plates with (a) circular holes and (b) elliptical holes ($\alpha = 1/4$).

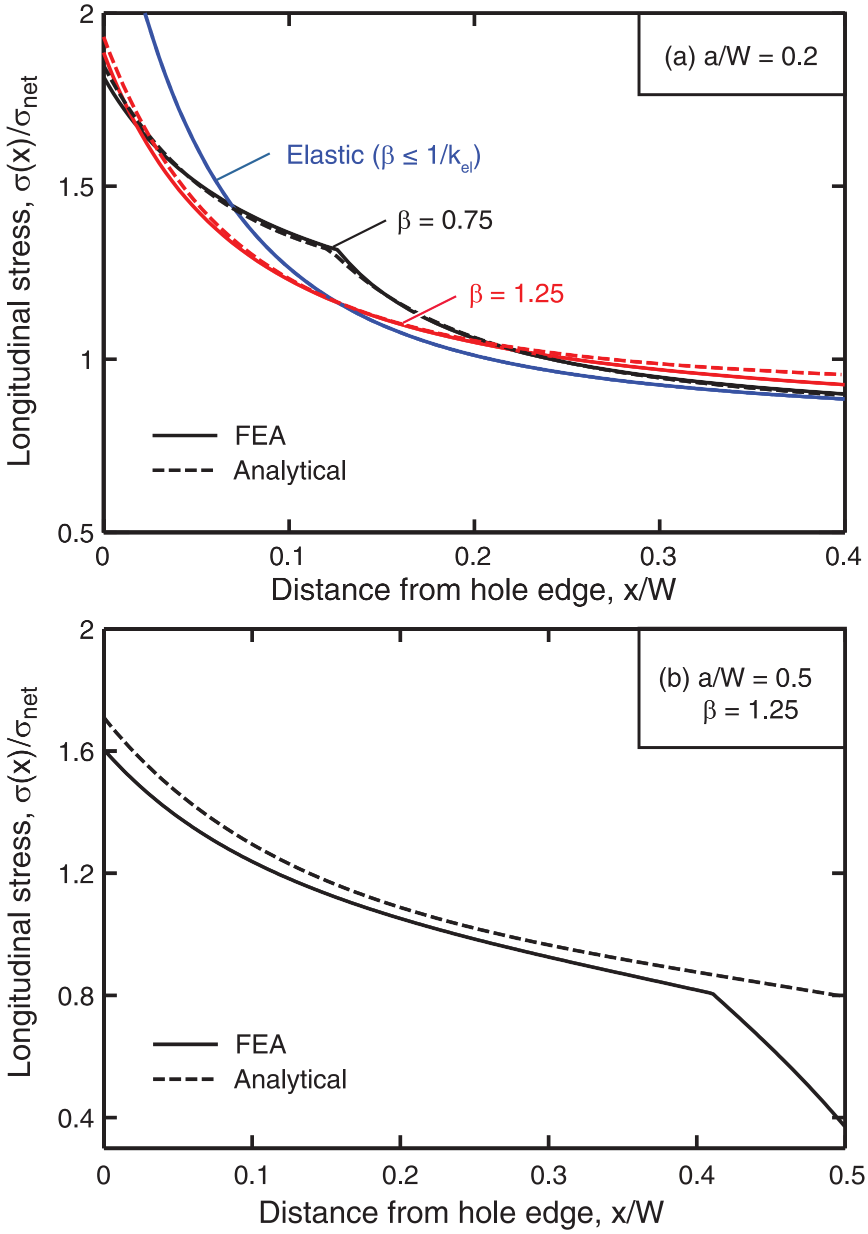

Figure 5.7: Stress distributions in isotropic plates ($\alpha = 1/4$, $\overline{E^P} = 1$) with circular holes of radius: (a) $a/W = 0.2$ and (b) $a/W = 0.5$. Results are shown for stress levels representative of both large-scale and net-section inelasticity.

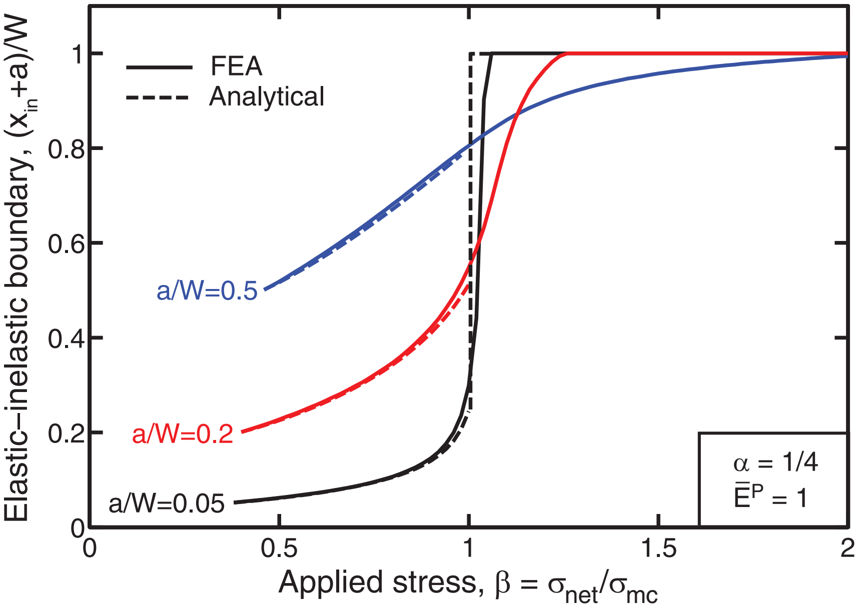

Figure 5.8: Variation in the elastic-inelastic boundary with applied stress for isotropic plates containing circular holes.

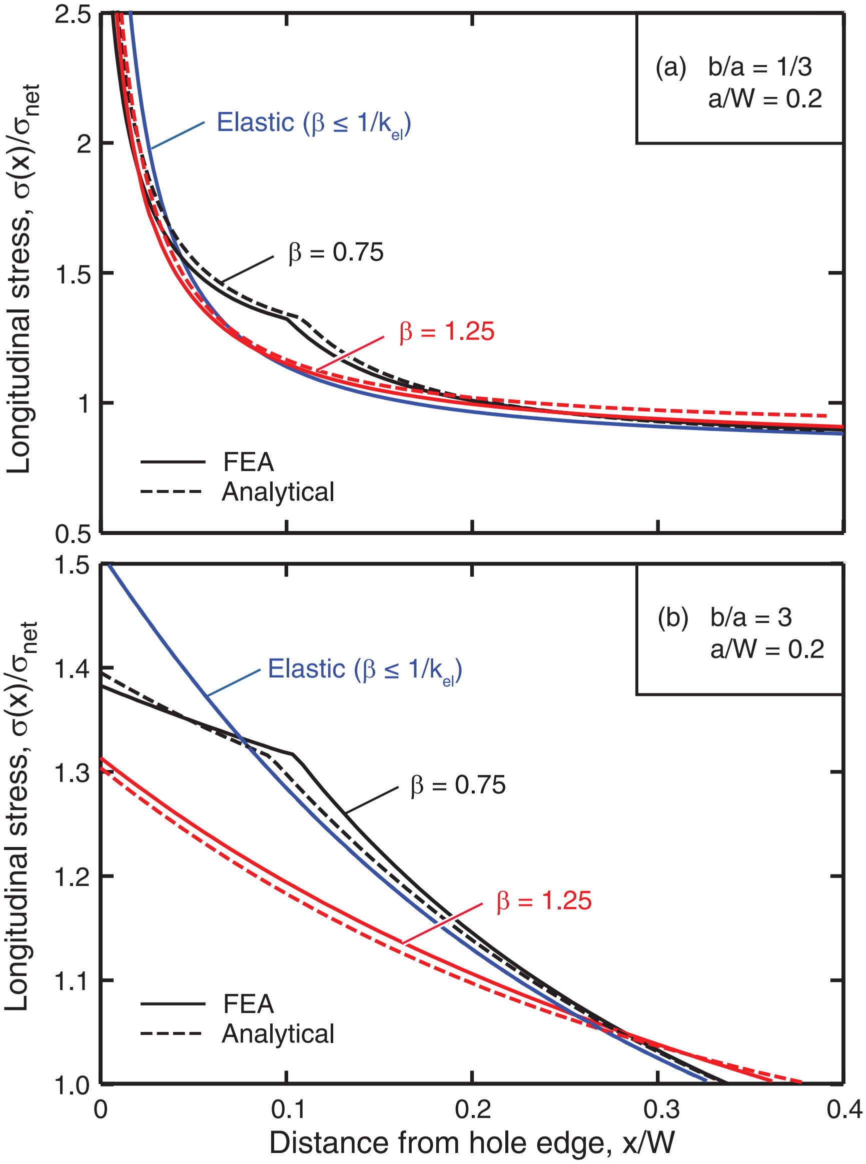

Figure 5.9: Stress distributions in isotropic plates ($\alpha = 1/4$, $\overline{E^P} = 1$) with elliptical holes of aspect ratio: (a) $b/a = 1/3$ and (b) $b/a = 3$. Results are shown for stress levels representative of both large-scale and net-section inelasticity.

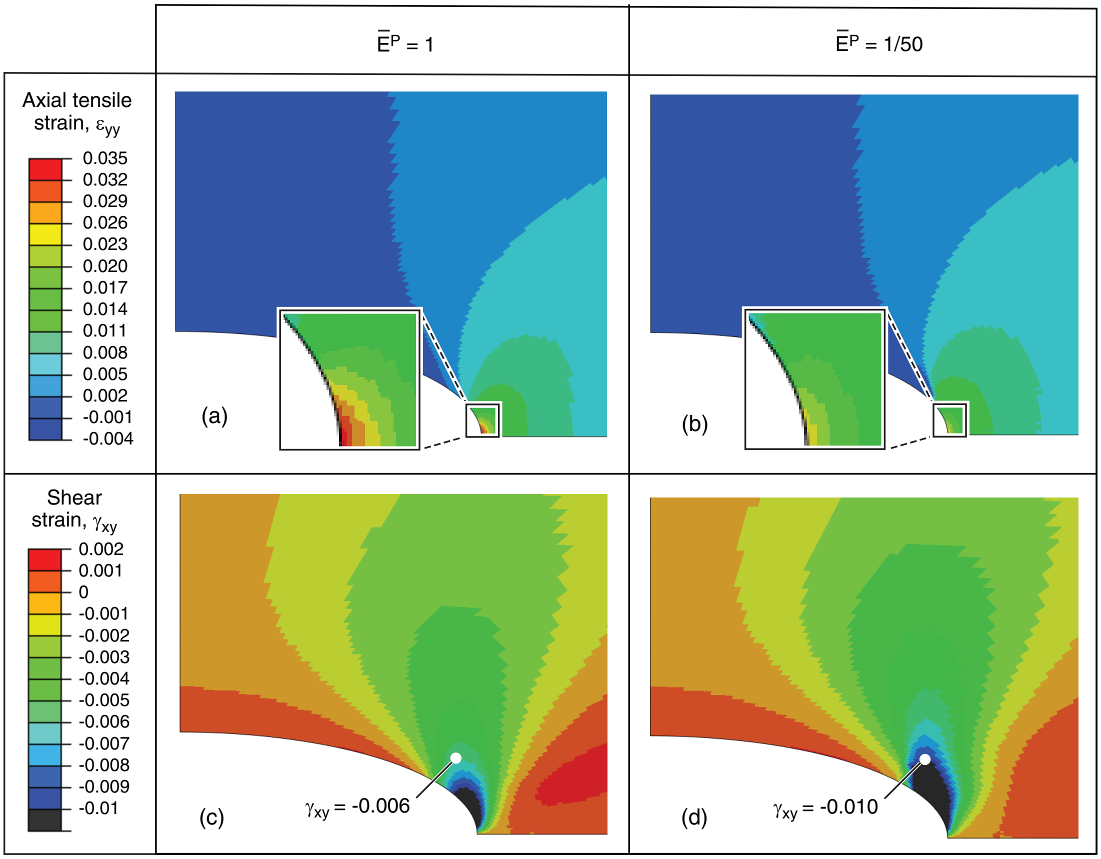

Figure 5.10: Effects of $\overline{E^P}$ on near-tip distributions of (a,b) axial tensile strain and (c,d) shear strain, in a plate with an elliptical hole ($a/W = 0.2$ and $b/a = 1/3$) at an applied stress of $\beta = 2$ ($\alpha = 1/4$).

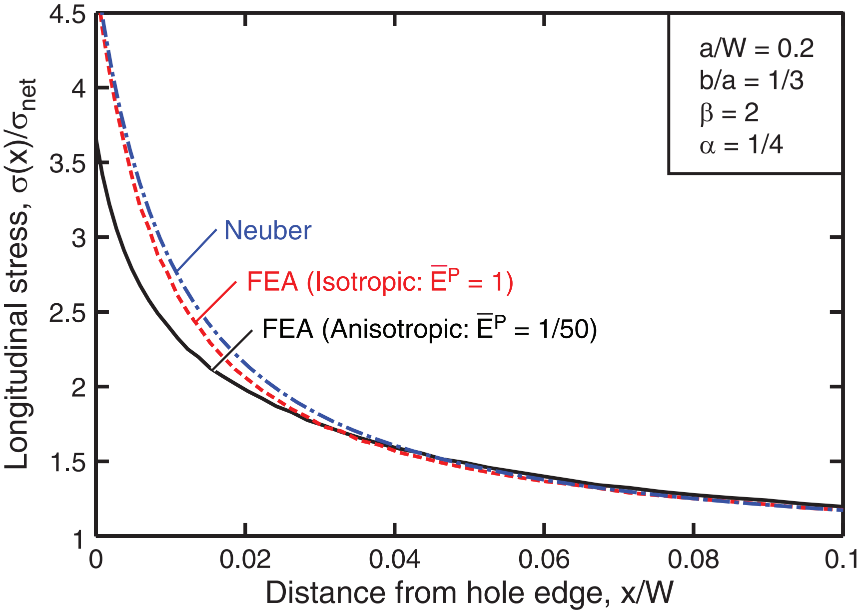

Figure 5.11: Near-tip stresses under net-section inelasticity in both isotropic and anisotropic laminates.

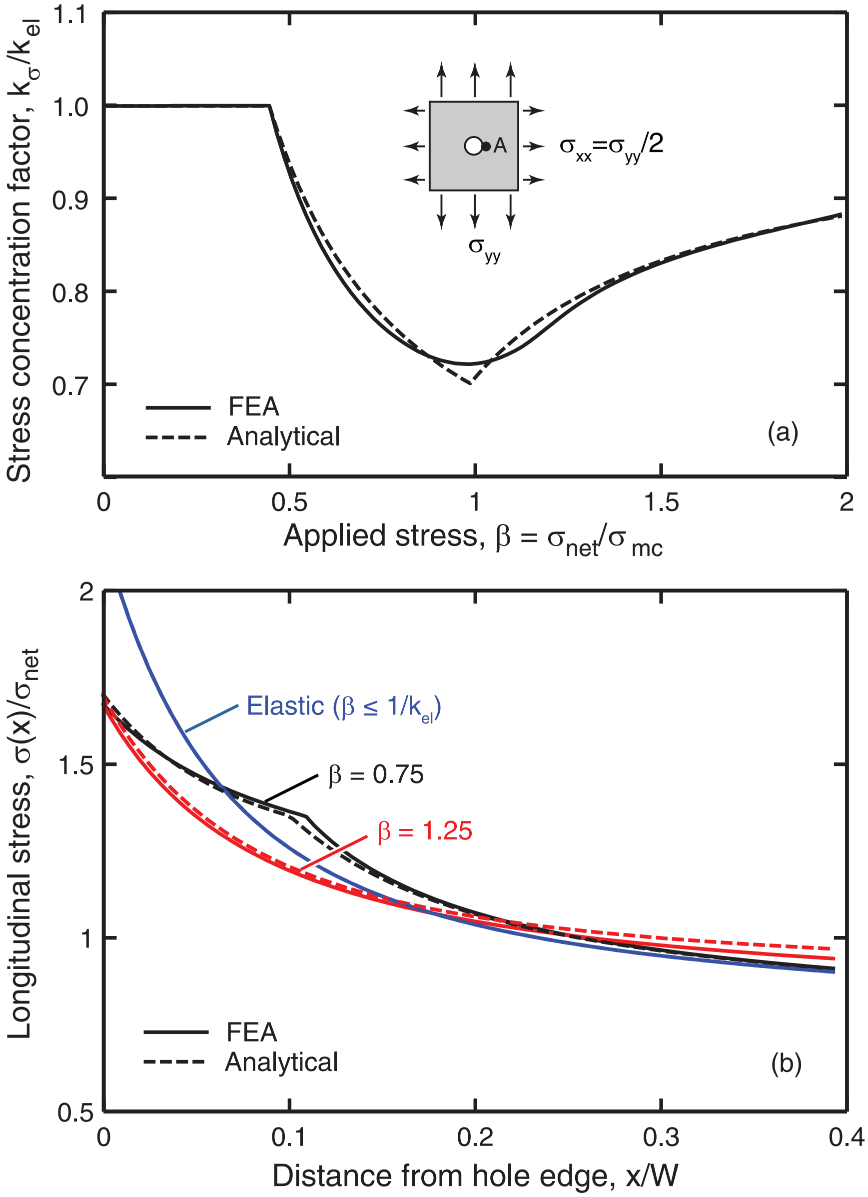

Figure 5.12: Effects of stress multiaxiality on (a) the SCF (at point A in the inset) and (b) the stress distribution in an isotropic plate with circular hole ($a/W = 0.2$, $\alpha = 1/4$).

Chapter 6

A new elastic-plastic constitutive model for CMC laminates

6.1 Introduction

As discussed in Chapter 1, notch insensitivity in CMCs results from near-notch inelasticity, just as notch insensitivity in metals arises from near-notch plastic deformation. A component-scale elastic-plastic constitutive model for CMCs should therefore enable less conservative designs of components that contain stress concentrating features.

In CMCs with matrices that are relatively stiff (e.g. SiC/SiC or SiC/CAS), near-notch inelasticity is associated with the formation of multiple matrix cracks oriented perpendicular to the axis of applied load. Cracking takes place over a large area of the composite in a spatially *distributed* manner (Cady et al., 1995b; Mackin et al., 1995; Evans et al., 1994). In contrast, CMCs with relatively compliant matrices (e.g. SiC/C or C/C), near-notch inelasticity has been attributed to spatially *localized* bands of shear damage that extend parallel to the axis of applied load (Heredia et al., 1994; Evans et al., 1994). The former type of composite has been termed 'Class II' and the latter type 'Class III' (Evans and Zok, 1994).

In Chapter 1, it was noted that efforts to model either type of inelasticity have typically been made using constitutive models that are *phenomenological* in nature. One notable model in this class is that of Genin and Hutchinson (1997), investigated in Chapter 4. As discussed therein, the original GH model suffers from numerical instability problems. For reasons elaborated upon in Section 6.3, however, even the *remediated* GH model (developed in Chapter 4) is somewhat deficient. Specifically, the model presupposes a particular form of the yield/cracking surface for the laminate: a condition which is approximately satisfied by certain material systems (notably, CMCs with relatively stiff matrices), but not others.

The principal objective of the present chapter is to develop and validate a new plane-stress, phenomenological elastic-plastic model for CMC laminates that overcomes the deficiencies of the previously discussed models. It should satisfy the following criteria:

1. It can be calibrated using experimental data from standard mechanical tests (e.g. tension, shear).
2. It is applicable to common CMC fiber architectures, notably cross-ply ($[0^\circ/90^\circ]_s$) and quasi-isotropic ($[0^\circ/\pm45^\circ/90^\circ]_s$) laminates.
3. It can capture the behavior of a range of CMCs, including those with stiff or compliant matrices.

The outline of the chapter is as follows. First, the results of mechanical tests (uniaxial tension at 0°, tension at 45°, and Iosipescu shear) for a commercial SiC/SiCN woven CMC are presented. Second, these data are combined with previously reported results for other material systems and used to assess two existing phenomenological models for CMC laminates: notably, that of Genin and Hutchinson (1997) and an adaptation of the model of Hahn (1973). The two models are distinguished by their respective predictions of the relationship between the mechanical responses in shear and in 45° tension. Notably, the shear/tensile cracking stress ratios from the GH model and the Hahn model are 1 and 1/2, respectively. The actual behavior, from both the experimental data and from theoretical considerations, is roughly bounded by these two extremes. Third, a new phenomenological elastic/plastic model is proposed. It is based on the deformation theory of plasticity and it combines features of both the GH and Hahn-type models. Importantly, it allows for arbitrary values of the shear/tensile cracking stress ratio. The predictive capabilities of the model are assessed in two ways: (i) by comparisons with measured inelastic responses in 45° tensile stress-strain curves, and (ii) comparisons of computed and measured displacement and strain fields in open-hole tension tests. The errors in the predicted open-hole tensile results are computed and rationalized in terms of the degree of non-proportional stressing that occurs during inelastic straining in the test geometry of interest.

6.2 Materials and experiments

6.2.1 Material

The material investigated in the present study comprises 8 plies of Hi-Nicalon (SiC) fibers in an 8-harness satin weave, a BN interface coating, and a SiCN matrix made through a combination of slurry infiltration and precursor impregnation and pyrolysis (S-200H, COI Ceramics, Inc., San Diego, CA). The finished composite panel was 2.25 mm thick. Optical micrographs (Figure 6.1) reveal some remnant porosity and extensive microcracking in the matrix. These defects play a significant role in the average matrix modulus and strength, as manifested in the mechanical test results presented below.

6.2.2 Experimental procedures

Three sets of mechanical tests were performed: uniaxial tension at 0° and at 45°, and shear parallel to the two fiber directions. Either two or three specimens were used for each set. The test specimens were designed to accommodate the limited quantity of available material.

For both sets of uniaxial tension tests, a dog-bone geometry was employed. For the test at 0°, the gauge width was 12.4 mm and the gauge length was 25.4 mm; for the test at 45°, the gauge width was 7 mm and the gauge length was 14 mm. Fiberglass tabs were adhered using a commercial epoxy to the ends of the tensile specimens to promote even load transfer. The specimens were loaded using hydraulic wedge grips.

Shear properties were measured using the Iosipescu test. Specimen design was broadly in accordance with the pertinent ASTM standard (ASTM D5379), with one notable exception: the V-notch angle was selected to be 105°, instead of 90° (Figure 6.2). A notch angle larger than 90° is desirable for testing orthotropic materials, since it produces somewhat smaller transverse stresses in the central ligament (Adams and Walrath, 1987). The specimen was loaded using a standard Iosipescu test fixture (Wyoming Test Fixtures, Inc.).

All specimens were instrumented using strain gauges on one surface and 3-D DIC (VIC-3D, Correlated Solutions, Inc.) on the other. For the Iosipescu shear test, a [0°/90°] stacked strain gauge rosette (Vishay Micro Measurements, CEA-13-062WT-120), oriented at ±45° to the specimen axes, was used; a single (axial) strain gauge was used for the tension tests. To enable use of digital image correlation, an artificial speckle pattern was created on the sample surface. This was accomplished by first painting the specimen surface uniformly white and then spraying fine black speckles onto the surface using an airbrush. The speckle size, measured using an autocorrelation technique, was approximately 50 μm. Two digital cameras (Point Grey Research Grasshopper), each with a CCD resolution of 2448 pixels × 2048 pixels and a 70–180 mm lens (Nikon ED AF Micro Nikkor), were used to acquire images for DIC. The focal length of the lenses was 70 mm, the aperture setting was F-11, and the angle between cameras ranged between 19° and 35°. Images were taken with a scale factor of 8–12 μm/pixel. To maximize the spatial resolution of the displacement measurement, the smallest possible subset size that ensured full correlation was chosen. This subset size (h_{sub}) was 30–45 pixels, or 270–370 μm. With this choice, the spatial resolution of displacements is well below the in-plane tow dimension (roughly 1 mm). The step size was selected to be $h_{sub}/10$, rounded to the nearest pixel.

6.2.3 Calculation of strains

Some subtleties are involved in the calculation of strains from the full-field displacement data generated by DIC, particularly for the Iosipescu test. For the tensile tests, the desired quantities are the axial and transverse strains; for the shear test, the desired quantity is the shear strain. These strains must be computed by averaging over a suitably-chosen area, A. The straightforward approach is to compute the area-averaged strain, $\overline{\epsilon}$, by differentiating displacements to find local strains and subsequently averaging these quantities over A. The average is equivalent to an integral, which is evaluated numerically as follows:

$$\overline{\epsilon}_{ij} = \frac{1}{A}\int\limits_{A} \epsilon_{ij}(x,y)\,\mathrm{d}A \approx \frac{1}{N}\sum_{k\in A} \epsilon_{ij}(x_k,y_k)\Delta A_k \tag{6.1}$$

where (x_k, y_k) are the coordinates of the k^{th} node within A, ΔA_k is its associated area, and N is the number of nodes within A. An alternative approach is to utilize the insight of Grédiac et al. (1994): notably, that the integral in Equation 6.1 can be transformed using Green's theorem. For instance, for shear strains,

$$\overline{\gamma} = \frac{1}{A}\int\limits_{A} \gamma(x,y)\,\mathrm{d}A = \frac{1}{A}\oint\limits_{\partial A} v(x,y)\,\mathrm{d}y - u(x,y)\,\mathrm{d}x \tag{6.2}$$

where the path integral is taken counterclockwise over the boundary of A, denoted ∂A. Once again, the integral is evaluated by discretizing over ∂A; specifically, the nodal displacement data obtained from DIC is interpolated in 2D and the integral of interest is evaluated by sampling the interpolation function over ∂A. The advantages of the latter approach are two-fold. First, it does not require the extra step of computing strains from displacements. Second, it avoids using local strains, which tend to be somewhat 'noisy' (since numerical differentiation is an inherently noisy process (Grédiac et al., 1994)). Therefore, the present work utilizes the path integral method for computing area-averaged strains.[1]

A second issue involves the selection of A. In uniaxial tension tests, the strain is nominally uniform and therefore A is chosen to be the entire area of the sample that lies within the field of view. For the Iosipescu shear test, however, there are competing considerations. Ideally, the experimental data would yield a function that relates the average shear stress to the average shear strain. The average stress is taken over the ligament, which is a rectangle lying within the yz-plane. However, the average strain is taken over A, which lies within the xy-plane. The width L_x (in the x-direction) of A must be large enough to ensure that a sufficient number of data points is used to compute the average,

---

[1] In practice, however, the two methods are found to give very similar results (differences of less than roughly 2 %) provided that full correlation is maintained.

but small enough to ensure that the strain distribution within the averaging area is uniform. Computations (not shown) indicate that a reasonable compromise is afforded by selecting L_x to be 0.8 mm, which is roughly equal to the notch radius, r.

A further issue that arises in the Iosipescu test is a discrepancy (on the order of tens of percent) between front-face and back-face strains. These differences arise for two reasons (Morton et al., 1992; Pierron, 1998). First, the specimen may undergo twisting (torsion) about the x-axis (Morton et al., 1992). (In the present experiments, DIC measurements of the out-of-plane displacement do indeed reveal some amount of twisting.) Second, Saint-Venant effects arise from the loading because the distance between the central ligament and the inner loading points is small. Either effect is sufficient to create a non-uniform distribution of shear strain in the through-thickness direction, z. Moreover, while the former effect can be suppressed by appropriately modifying the Iosipescu test fixture, the latter cannot (Pierron, 1998). However, both effects can be eliminated simply by averaging the front and back-face strains (Pierron, 1998). As a check on the fidelity of the resulting shear strain measurements, the measured shear modulus was compared with that predicted from elasticity using the elastic properties measured in the tension tests: the two agreed to within 5 %.

6.2.4 Results of mechanical testing

Axial and transverse strain measurements (from DIC) for the tension tests at 0° and 45° are shown in Figure 6.3(a) and (b). Shear stress-strain curves from the Iosipescu test are shown in Figure 6.3(c).[2] The latter strains were computed by averaging the DIC and strain gauge data on the two surfaces. The stress-strain curves exhibit little variation between specimens. For the purpose of calibrating the constitutive models (Sections 6.3 and 6.4), average stress-strain curves were calculated using a smoothing spline through the experimental data. The averages were computed only in the hardening regime (i.e. post-peak strain-softening was neglected). These curves are also depicted in Figure 6.3.

Five elastic constants can be calculated from the five stress-strain curves: the Young's moduli E_0 and E_{45} in the 0° and 45° directions, the corresponding Poisson's ratios ν_0 and ν_{45}, and the shear modulus G. Their average values are summarized in Table 6.1. From the theory of elasticity, only three of the constants are independent. Treating E_0, ν_0, and G as independent, the values of the other two quantities, E_{45} and ν_{45}, can be expressed as:

$$\begin{aligned} E_{45} &= \frac{4E_0G}{E_0 + 2G(1-\nu_0)} \\ \nu_{45} &= \frac{2E_0}{E_0 + 2G(1-\nu_0)} - 1 \end{aligned} \tag{6.3}$$

---

[2] All shear strains referred to herein are *engineering* shear strains.

The predicted values of E_{45} and ν_{45} are also shown in Table 6.1. The error between the elasticity prediction and the measurement for E_{45} is 3 %; the corresponding error for ν_{45} is 12 %, indicating that the experimental data is reasonably self-consistent.

The 0° tensile curve exhibits a nearly-bilinear response, with the change in tangent modulus occurring over the range of 100–200 MPa. The change in tangent modulus is relatively small: only about a factor of two. This behavior is reminiscent of that observed in both C/C and oxide-oxide composites with porous and/or microcracked matrices. In contrast, the curves in 45° tension and in shear exhibit nearly elastic-perfectly plastic behavior. In the latter cases, the tangent moduli in the post-cracking regimes are about an order of magnitude smaller than the corresponding elastic moduli. Additionally, the magnitude of the inelastic transverse strains for 45° loading are comparable to the inelastic axial strains, which is characteristic of a fiber 'scissoring' mechanism (Genin and Hutchinson, 1997). Similar macroscopic stress-strain behavior for off-axis loading has been observed in glass- and carbon-matrix composites (Cady et al., 1995a; Turner et al., 1995).

The effective elastic modulus of the (porous, microcracked) matrix can be extracted by employing an elastic analysis based on laminate theory (see Appendix B for pertinent formulae). Each woven cloth, comprising 0° and 90°

fibers, is partitioned into two unidirectional plies: one at 0° and the other at 90°. The volume fraction of fibers within each ply is taken to be equal to that of the overall composite, which is calculated from the manufacturer's reported weave properties (fiber areal weight and fiber density) and the number of plies and thickness of the composite panel. The resulting estimate is $V_f = 0.52$. The elastic properties of each ply are calculated using a well-accepted micromechanical model: the generalized self-consistent scheme (GSCS) (Christensen and Lo, 1979; Christensen, 1990). The GSCS model requires the constituent properties. The Young's modulus of the (isotropic) fiber (E_f) is taken from manufacturer data. The porous, cracked matrix is homogenized and represented by an isotropic effective medium with properties (E_m and ν_m) that are unknown *a priori*. Using the elastic constants of the plies, the elastic constants of the laminate are readily computed using standard relations from laminate theory. The remaining constituent properties (E_m, ν_m, and ν_f) are subsequently solved for by minimizing the error between the predicted and experimentally measured elastic constants of the laminate. The resulting property values are: $E_m = 43\,\text{GPa}$, $\nu_m = 0.15$, and $\nu_f = 0.18$. Using these values, the agreement between the predicted and measured elastic constants is excellent: the errors being less than 1 %.

Taken together, these results imply that, although the matrix in fully-dense form would be very stiff, its *effective* modulus is significantly less than that of the fibers ($E_m/E_f \approx 0.16$). The composite behavior is therefore expected to most closely resemble that of 'Class III' composites. For instance, shear banding should be the primary near-notch damage mechanism. (That this is indeed the case is demonstrated in Section 6.5.)

6.3 Assessment of existing constitutive models

6.3.1 Preliminaries

Based on the phenomenological constitutive models described in the introduction, the five stress-strain curves presented above are not all independent. For instance, the 45° tensile response is predicted to be dependent on the 0° tensile and shear responses. Here the internal consistency of the in-plane stress-strain curves stemming from both the remediated GH model (Chapter 4) and a model adapted from the work of Hahn (1973) on PMC laminates is assessed. The assessment is made using the test data for SiC/SiCN described above as well as comparable data previously reported for two other CMCs: (i) a cross-ply SiC/CAS laminate (Cady et al., 1995a), and (ii) a 2-D woven SiC/SiC composite (Camus, 2000; Aubard, 1992). The results presented below demonstrate that neither model is able to accurately predict the 45° tensile stress-strain curve from the 0° tensile and shear stress-strain curves for all material systems. But, the measured 45° tensile stress-strain curves are roughly bounded by the predictions of the two models.

In the following analysis, the axial and transverse strains for 0° tensile loading are represented by the functions $\epsilon_0 = f_0(\sigma)$ and $\epsilon_{0T} = f_{0T}(\sigma)$, respectively. Similarly, the axial and transverse strains for 45° tensile loading are $\epsilon_{45} = f_{45}(\sigma)$ and $\epsilon_{45T} = f_{45T}(\sigma)$, respectively. Finally, the shear stress-strain curve is $\gamma = f_s(\sigma)$.

6.3.2 GH model

The GH model is couched in terms of a tangent compliance matrix relating principal strains to principal stresses. In the inelastic regime, for principal strains oriented at 45° to the fibers, the constitutive equation takes the form:

$$\begin{bmatrix} \epsilon_I \\ \epsilon_{II} \end{bmatrix} = \begin{bmatrix} f'_{45}(\sigma_I) & f'_{45T}(\sigma_I)D_{45} + f'_{45T}(\sigma_{II})(1 - D_{45}) \\ f'_{45T}(\sigma_I) & f'_{45}(\sigma_I)D_{45} + f'_{45}(\sigma_{II})(1 - D_{45}) \end{bmatrix} \begin{bmatrix} \sigma_I \\ \sigma_{II} \end{bmatrix} \tag{6.4}$$

where the primes denote differentiation with respect to stress; the subscripts I, II denote the first and second principal strains/stresses, respectively; and the parameter D_{45} characterizes the tendency of the laminate to 'scissor' when loaded in tension in the 45° direction. As discussed in Chapter 4, for cross-ply laminates, a reasonable estimate for D_{45} is unity. In Section 4.5.5, Equation 6.4

was used to relate the 45° tensile response to the shear response of the CMC. The result, reproduced here, is:

$$f_s'(\sigma) \approx (1 + D_{45})(f_{45}'(\sigma) - f_{45T}'(\sigma)) \tag{6.5}$$

Equation 6.5 implies that if the stress, σ, is sufficient to cause significant inelasticity for 45° loading (i.e. to cause $f_{45}'(\sigma)$ and $f_{45T}'(\sigma)$ to become large in magnitude), it is sufficient to cause significant inelasticity in shear loading, and vice versa. In other words, the stress-strain curves for 45° tension and shear loading are expected to exhibit significant nonlinearity at the same stress level.

6.3.3 Hahn model

The Hahn model was originally developed for PMC laminates. It uses the contracted notation for stresses and strains: e.g. $\sigma_1 = \sigma_{11}$, $\sigma_6 = \sigma_{12}$, $\epsilon_6 = 2\epsilon_{12}$, etc., where the 1- and 2-directions are aligned with the fiber axes. The governing equations for cross-ply laminates in the original formulation of the model are (Hahn, 1973):

$$\begin{bmatrix} \epsilon_1 \\ \epsilon_2 \\ \epsilon_6 \end{bmatrix} = \begin{bmatrix} a_{11} & a_{12} & 0 \\ a_{12} & a_{22} & 0 \\ 0 & 0 & a_{66} + S_{6666}\sigma_6^2 \end{bmatrix} \begin{bmatrix} \sigma_1 \\ \sigma_2 \\ \sigma_6 \end{bmatrix} \tag{6.6}$$

Here nonlinearity is incorporated only in the shear response (through the quadratic term) and not in the 0° tensile response (Hahn, 1973). However, the model can be generalized to include nonlinearity in tension by using a tangent compliance formulation:

$$\begin{bmatrix} d\epsilon_2 \\ d\epsilon_2 \\ d\epsilon_6 \end{bmatrix} = \begin{bmatrix} f_0'(\sigma_1) & f_{0T}'(\sigma_2) & 0 \\ f_{0T}'(\sigma_1) & f_0'(\sigma_2) & 0 \\ 0 & 0 & f_s'(\sigma_6) \end{bmatrix} \begin{bmatrix} d\sigma_1 \\ d\sigma_2 \\ d\sigma_6 \end{bmatrix} \tag{6.7}$$

(If $f_0'(\sigma) = a_{11} = a_{22}$, $f_{0T}'(\sigma) = a_{12}$, and $f_s'(\sigma) = a_{66} + 3S_{6666}\sigma^2$, Equation 6.7 reduces to Equation 6.6.)

Here, again, the constitutive model can be used to relate the shear and 45° tensile responses. Doing so yields the relationships:

$$\begin{aligned} f_{45}'(\sigma) + f_{45T}'(\sigma) &= f_0'(\frac{\sigma}{2}) + f_{0T}'(\frac{\sigma}{2}) \\ f_{45}'(\sigma) - f_{45T}'(\sigma) &= \frac{1}{2} f_s'(\frac{\sigma}{2}) \end{aligned} \tag{6.8}$$

The latter is similar in form to Equation 6.5 in the GH model. However, in contrast to the GH model, the Hahn model predicts that if the 45° response exhibits nonlinearity at σ, then the shear response should exhibit nonlinearity at $\sigma/2$. That is, the predicted cracking stresses for 45° tension from the GH and the Hahn models differ by a factor of two.

6.3.4 Interpretation of experimental data

The predicted 45° tensile stress-strain curves from the two models are shown in Figure 6.4 for the three CMCs of interest: SiC/SiCN (present work), SiC/CAS (Cady et al., 1995a), and SiC/SiC (Camus, 2000).

For the composites with relatively stiff matrices (Figure 6.4(b) and (c)), the GH model yields reasonably accurate predictions of the cracking stresses and the inelastic hardening rates in 45° tension. The Hahn model, unsurprisingly, performs poorly in these cases, since its prediction of the plateau stress is approximately twice that of the GH model. In contrast, for the composite with a relatively compliant matrix (SiC/SiCN, Figure 6.4(a)), the Hahn model performs better than the GH model, though it overestimates the measured stresses by about 25 %. Closer examination of the functional forms of the two models reveals the origin of these differences: the GH model tacitly assumes that inelasticity is governed by the largest principal stress (as noted in Section 4.5.4) whereas the Hahn model assumes that it is governed by the larger of the tensile and shear stresses oriented with respect to fiber axes.

Experimental data compiled by Cady et al. (1995a) for several CMCs are broadly consistent with the trends reported here. That is, the ratio of the cracking stress in 45° tension and shear loading ranges from about 0.6 for stiff matrices (characterized by $E_m/E_f \gtrsim 1$) to roughly 2 for compliant matrices ($E_m/E_f \ll 1$). Furthermore, the theoretical model presented in Chapter 3 for steady-state matrix cracking in unidirectional CMCs under off-axis loading yields similar results. Specifically, in the absence of residual stress, the predicted ratio of cracking stresses for 45° tension and shear loading ranges from 1 for a rigid matrix to 2 for an infinitely compliant matrix. The key conclusion is that an alternative (more generalized) formulation is required to accurately capture the in-plane 'yield' surfaces of CMCs.

6.4 Formulation of new model

6.4.1 Preliminaries

The proposed model is based on the deformation theory of plasticity. Here strains are related to stresses via an effective compliance matrix that is a function of an 'effective stress,' $\overline{\sigma}$. The effective stress, in turn, is a function of the components of the stress tensor. (In the deformation theory of plasticity for isotropic metals, this would be the von Mises stress.) The effective stress function characterizes the yield/cracking surface of the material. By constructing this function appropriately, the ratio of the cracking stresses for different directions of loading is no longer a constant, as in the GH and Hahn models. Instead, it becomes a fitting parameter that can be calibrated with experimental data. Being a deformation theory, the model is expected to apply for (roughly) proportional stressing. The constitutive relationship is:

$$\epsilon_i = S_{ij}(\overline{\sigma})\sigma_j \tag{6.9}$$

where $i, j = 1, 2, 6$ (using, again, the contracted notation for stresses and strains). It is assumed that $\overline{\sigma}$ is scale-invariant (a homogeneous function of degree 1), which means that:

$$\overline{\sigma}(C\sigma_1, C\sigma_2, C\sigma_6) = C\overline{\sigma}(\sigma_1, \sigma_2, \sigma_6) \tag{6.10}$$

The cubic in-plane symmetry of the material implies that the 1- and 2-axes are equivalent. Imposing this condition yields the relations:

$$\begin{gathered} S_{11}(\overline{\sigma}) = S_{22}(\overline{\sigma}) \\ S_{12}(\overline{\sigma}) = S_{21}(\overline{\sigma}) \\ S_{16}(\overline{\sigma}) = S_{26}(\overline{\sigma}) \\ S_{61}(\overline{\sigma}) = S_{62}(\overline{\sigma}) \\ \overline{\sigma}(\sigma_1, \sigma_2, \sigma_6) = \overline{\sigma}(\sigma_2, \sigma_1, \sigma_6) \end{gathered} \tag{6.11}$$

The functions $S_{ij}(\overline{\sigma})$ are calibrated using the results of only two mechanical tests: notably, 0° tension and shear aligned with the two fiber axes (the 1- and 2-axes).

6.4.2 Mechanical tests for calibration

Uniaxial tension at 0°

For 0° tension, the effective stress becomes

$$\overline{\sigma} = \overline{\sigma}(\sigma_1, 0, 0) = C_0\sigma_1 \tag{6.12}$$

using the scale-invariance of $\overline{\sigma}$ (where $C_0 = \overline{\sigma}(1,0,0)$). Equation 6.9 then reduces to:

$$\begin{aligned} \epsilon_1 &= S_{11}(C_0\sigma_1)\sigma_1 \\ \epsilon_2 &= S_{21}(C_0\sigma_1)\sigma_1 \\ \epsilon_6 &= S_{61}(C_0\sigma_1)\sigma_1 = 0 \end{aligned} \tag{6.13}$$

The normal strains are given simply by the functions f_0 and f_{0T}, which characterize the 0° tensile stress-strain curves. After some algebra:

$$\begin{aligned} S_{11}(\overline{\sigma}) = S_{22}(\overline{\sigma}) &= \frac{f_0(\overline{\sigma}/C_0)}{\overline{\sigma}/C_0} \\ S_{21}(\overline{\sigma}) = S_{12}(\overline{\sigma}) &= \frac{f_{0T}(\overline{\sigma}/C_0)}{\overline{\sigma}/C_0} \\ S_{61}(\overline{\sigma}) = S_{62}(\overline{\sigma}) &= 0 \end{aligned} \tag{6.14}$$

Shear

In pure shear, the effective stress becomes

$$\overline{\sigma} = \overline{\sigma}(0,0,\sigma) = C_s\sigma \tag{6.15}$$

where $C_s = \overline{\sigma}(0,0,1)$. Using a procedure analogous to that utilized above, the following result is obtained:

$$\begin{aligned} S_{66}(\overline{\sigma}) &= \frac{f_s(\overline{\sigma}/C_s)}{\overline{\sigma}/C_s} \\ S_{16}(\overline{\sigma}) = S_{26}(\overline{\sigma}) &= \frac{f_{ns}(\overline{\sigma}/C_s)}{\overline{\sigma}/C_s} \end{aligned} \tag{6.16}$$

where $f_{ns}(\sigma)$ characterizes the normal strain induced by shear stressing. This function is difficult to measure in practice, largely because the strains are exceedingly small in CMCs. Here it is assumed that $f_{ns} = 0$, implying that the shear-extension coupling is negligible.

6.4.3 Tangent compliance

As demonstrated in Section 6.4.2, the tension and shear tests enable calibration of all of the unknown functions $S_{ij}(\overline{\sigma})$ in the constitutive equation. The final result is:

$$\begin{bmatrix} \epsilon_1 \\ \epsilon_2 \\ \epsilon_6 \end{bmatrix} = \begin{bmatrix} \frac{f_0(\overline{\sigma}/C_0)}{\overline{\sigma}/C_0} & \frac{f_{0T}(\overline{\sigma}/C_0)}{\overline{\sigma}/C_0} & 0 \\ \frac{f_{0T}(\overline{\sigma}/C_0)}{\overline{\sigma}/C_0} & \frac{f_0(\overline{\sigma}/C_0)}{\overline{\sigma}/C_0} & 0 \\ 0 & 0 & \frac{f_s(\overline{\sigma}/C_s)}{\overline{\sigma}/C_s} \end{bmatrix} \begin{bmatrix} \sigma_1 \\ \sigma_2 \\ \sigma_6 \end{bmatrix} \tag{6.17}$$

For ease of numerical implementation, the preceding results are re-expressed in terms of the tangent compliance tensor, $\partial\epsilon_i/\partial\sigma_j$. Assuming that the stresses are imposed proportionally, i.e. $\sigma_i = \Lambda_i\overline{\sigma}$, and differentiating Equation 6.17, yields:

$$\begin{bmatrix} d\epsilon_1 \\ d\epsilon_2 \\ d\epsilon_6 \end{bmatrix} = \begin{bmatrix} f_0'(\overline{\sigma}/C_0) & f_{0T}'(\overline{\sigma}/C_0) & 0 \\ f_{0T}'(\overline{\sigma}/C_0) & f_0'(\overline{\sigma}/C_0) & 0 \\ 0 & 0 & f_s'(\overline{\sigma}/C_s) \end{bmatrix} \begin{bmatrix} d\sigma_1 \\ d\sigma_2 \\ d\sigma_6 \end{bmatrix} \tag{6.18}$$

where the prime denotes differentiation with respect to stress. Equations 6.17 and 6.18 are mathematically equivalent for proportional stressing; the magnitude of the differences that arise when the stressing is non-proportional is presently unknown.

Equation 6.18 provides a basis for assessing the stability of the material model. The CMC undergoes softening if the eigenvalues of the tangent compliance matrix, given by Equation 6.18, are negative. From inspection, the conditions for softening are seen to be $f_s'(\overline{\sigma}/C_s) < 0$ or $f_0'(\overline{\sigma}/C_0) + f_{0T}'(\overline{\sigma}/C_0) < 0$. These quantities on the left-hand-sides of these inequalities are physically equivalent to the shear and biaxial compliances, respectively.

6.4.4 Predicted response for 45° tension

For 45° tension, the effective stress becomes

$$\overline{\sigma} = \overline{\sigma}(\frac{\sigma_{45}}{2}, \frac{\sigma_{45}}{2}, \frac{\sigma_{45}}{2}) = C_{45}\sigma_{45} \tag{6.19}$$

where $C_{45} = \overline{\sigma}(1/2, 1/2, 1/2)$. Employing the constitutive equation (Equation 6.18):

$$\begin{aligned} d\epsilon_1 = d\epsilon_2 &= \frac{1}{2}\left[f_0'(\frac{C_{45}}{C_0}\sigma_{45}) + f_{0T}'(\frac{C_{45}}{C_0}\sigma_{45})\right] d\sigma_{45} \\ d\epsilon_6 &= \frac{1}{2} f_s'(\frac{C_{45}}{C_s}\sigma_{45}) d\sigma_{45} \end{aligned} \tag{6.20}$$

Rewriting these equations in terms of f_{45} and f_{45T} yields:

$$f_{45}'(\sigma_{45}) + f_{45T}'(\sigma_{45}) = f_0'(\frac{C_{45}}{C_0}\sigma_{45}) + f_{0T}'(\frac{C_{45}}{C_0}\sigma_{45}) \tag{6.21}$$

and

$$f_{45}'(\sigma_{45}) - f_{45T}'(\sigma_{45}) = \frac{1}{2} f_s'(\frac{C_{45}}{C_s}\sigma_{45}) \tag{6.22}$$

Equations 6.21 and 6.22 imply that the *difference* between axial and transverse strains at 45° is related to the shear response, whereas their *sum* is related to the 0° tensile response. It is instructive to compare Equation 6.22 with the corresponding equations for the GH and Hahn models (Equations 6.5 and 6.8, respectively). When $C_s = C_{45}$, the GH model result is recovered (with $D_{45} = 1$). When $C_s = 2C_{45}$, the Hahn model result is recovered. In general, the model can capture an arbitrary ratio of cracking stresses in 45° tension and shear.

6.4.5 Effective stress

Heretofore general results have been derived using an arbitrary function $\overline{\sigma} = \overline{\sigma}(\sigma_1, \sigma_2, \sigma_6)$. For numerical implementation of the constitutive model, a specific function for the effective stress is required. To this end, a Hill-type effective stress (which straightforwardly extends the von Mises effective stress to anisotropic materials) is used:

$$\overline{\sigma} = \sqrt{A_{ij}\sigma_i\sigma_j} \tag{6.23}$$

After using material symmetry, this reduces to

$$\overline{\sigma} = \sqrt{A_{11}(\sigma_1^2 + \sigma_2^2) + 2A_{12}\sigma_1\sigma_2 + A_{66}\sigma_6^2} \tag{6.24}$$

One limitation of the effective stress in its current form is that it yield equivalent results in compression and in tension. To prevent spurious inelasticity in compression, σ_1 and σ_2 are replaced with $R(\sigma_1)$ and $R(\sigma_2)$, where R is the ramp function ($R(x) = (|x| + x)/2$).

Finally, the constitutive model requires the constants C_0, C_{45}, and C_s. Using the definition of the effective stress, it is found that:

$$\begin{aligned} C_0 &= \sqrt{A_{11}} \\ C_s &= \sqrt{A_{66}} \\ C_{45} &= \frac{1}{2}\sqrt{2A_{11} + 2A_{12} + A_{66}} \end{aligned} \tag{6.25}$$

Since the Hill-type effective stress essentially defines a yield surface, the constants A (or, equivalently, the constants C) must be related to the stresses at which the various stress-strain curves exhibit significant non-linearity. Taking these stresses to be σ_0, τ_0, and σ_{45}, for the three respective tests, the following result is obtained

$$C_0\sigma_0 = C_s\tau_0 = C_{45}\sigma_{45} \tag{6.26}$$

Using this equation, the constants A in the effective stress function can be evaluated (up to an arbitrary scale factor).

6.4.6 Comparison to experimental results

The present model predicts the 45° tensile response from the 0° tension and shear responses. (The prediction is not completely independent, since σ_{45} must be specified in order to solve for the unknown constants in the effective stress function.) Results are shown in Figure 6.5 for the three material systems examined in Figure 6.4. The stresses at which the stress-strain curves start to exhibit significant non-linearity are found by inspection. For the SiC/SiCN composite, $\sigma_0 = 170\,\mathrm{MPa}$, $\tau_0 = 82.5\,\mathrm{MPa}$, and $\sigma_{45} = 135\,\mathrm{MPa}$; for the SiC/CAS composite (Cady et al., 1995a), $\sigma_0 = 60\,\mathrm{MPa}$, $\tau_0 = 75\,\mathrm{MPa}$, and $\sigma_{45} = 70\,\mathrm{MPa}$; and for the SiC/SiC composite (Camus, 2000), $\sigma_0 = \sigma_{45} = 145\,\mathrm{MPa}$ and $\tau_0 = 170\,\mathrm{MPa}$.

The comparisons show that the agreement between measured and predicted stress-strain curves is excellent. The agreement supports the relationships presented in Equation 6.22: notably, that the strain-hardening rates in the shear and 45° tensile stress-strain curves are related by the scaling factor C_s/C_{45}. The GH model assumes this factor to be 1, while the Hahn-type model assumes it to be 2. The experimental data indicates that this ratio varies across materials: increasing with decreasing matrix stiffness. The present constitutive model appears to have enough generality to adequately capture this behavior.

6.5 Case study: open hole tension

The constitutive model developed in Section 6.4 is assessed through comparisons of predicted and measured displacements and strains in open-hole tension tests. Since all calibration data for the model were obtained entirely from (unnotched) tension and shear tests, the comparisons provide a true assessment of the predictive capability of the model.

6.5.1 Experiments

Rectangular specimens of length 114.3 mm and width 25.4 mm were used. Holes of 9.525 mm diameter (37.5 % of the total width) were machined using a diamond core drill. Two specimens were tested: one to failure, and the other to roughly 90 % of the failure stress. As in the unnotched tension tests, fiberglass tabs were adhered to the specimen ends and the specimens were loaded using hydraulic wedge grips.

Digital image correlation was again used to track specimen deformation. To maximize spatial resolution, only about one half of the full specimen width in the vicinity of the hole was imaged. Parameters for DIC were similar to the tension and shear tests, with the exception of the scale factor, which was slightly smaller (5.5–6 µm/pixel).

6.5.2 Finite element simulations

The constitutive model (Equation 6.18) was implemented in a user-material subroutine (UMAT) for use in ABAQUS. The equations were integrated explicitly using the modified Euler scheme described by Sloan et al. (2001). The scheme utilizes automatic sub-stepping to limit the error arising from the integration procedure to within a prescribed error tolerance for each time step.

The subroutine utilizes the measured functions f_0, f_{0T}, and f_s and the constants C. The smoothed, averaged stress-strain functions depicted in Figure 6.3 are used for this purpose. (Note that these curves neglect material softening.) The constants C are identical to those used previously (found by substituting $\sigma_0 = 170\,\text{MPa}$, $\tau_0 = 82.5\,\text{MPa}$, and $\sigma_{45} = 135\,\text{MPa}$ into Equation 6.26).

The finite element (FE) simulation was performed in ABAQUS Standard (Version 6.12-1, Dassault Systèmes). A quarter-symmetry FE model was employed, with four-noded, quadrilateral, plane-stress elements. The hole diameter was 0.375 of the plate width, as in the experiments. Displacement was monotonically applied at the top boundary in the y-direction. A study was performed to ensure that the quantities of interest (nodal displacements) converged with respect to mesh density. For comparison with the experimental data, the displacements (u, v) of every node within the model were extracted at 100 evenly spaced time increments, where the final time increment corresponds to an applied stress which exceeds the failure stress in the experiments.

6.5.3 Metrics for comparison

Several metrics were employed for comparison of experimental results with the FE simulations. To assess the agreement in *global* response, the nodal displacement data from experiments and simulation were used to compute macroscopic stress-strain curves. In this case, the net-section stress was plotted against the 'hole strain,' measured using a virtual longitudinal extensometer that spans the hole and is offset from the hole edge (see inset of Figure 6.6). To assess the correlations in the *local* fields, contour plots of the displacement in the direction of loading (v) and of the axial and shear strains (ϵ_{yy} and γ_{xy}, respectively) were constructed. The (scattered) data from DIC and from FEA was interpolated in x, y using Delaunay triangulation and subsequently evaluated on a common grid in x-y space. Strains were computed from displacements using an identical procedure for both sets of data. Specifically, the gridded data were differentiated with respect to the spatial coordinate using forward differences. The resulting strains were averaged using a Gaussian filter. The filter length, h_f, is physically equivalent to the gauge length for strain computation. It was selected to be equal to the tow width (1 mm), since the strains used to calibrate the constitutive model are macroscopic, *tow-averaged* strains. The standard deviation of the filter was $0.25h_f$.

6.5.4 Results

Macroscopic stress-strain curves from the FE simulation and from the two test specimens are shown in Figure 6.6. Two values of the offset, 1 mm and 3 mm, were selected. (The latter corresponds to the largest offset that lies within the field of view of the cameras.) At low stresses (< 50 MPa), the macroscopic stress-strain behavior is linear and the moduli from the simulation and the measurements are in excellent agreement. At higher stresses (50–300 MPa), the specimens exhibit significant macroscopic nonlinearity. The discrepancies between predicted and measured strains remain small, and less than the sample-to-sample variation. At yet higher stress levels (> 300 MPa), the agreement deteriorates somewhat: the simulated strains being slightly larger than the measured values (by roughly 10–30 %). (The fracture stress cannot be predicted since the constitutive law lacks an appropriate failure criterion.)

The shear strain distributions are depicted in Figure 6.7. With increasing stress, bands of large shear strain (in excess of 1 %) develop near the edge of the hole and expand parallel to loading direction. The shear bands are a consequence of the low shear cracking stress. The FE simulations appear to predict the size and shape of these bands with good accuracy. At yet higher stress levels (400 MPa), discrepancies between experiment and simulation become progressively more pronounced. However, as discussed later, these stresses fall outside the regime of proportional stressing. Some differences are also obtained between test specimens and between the two shear bands within an individual specimen. (The FE simulation assumes these bands to be identical, since the deformation is symmetric.) It is surmised that these effects are related to variations in fiber placement, matrix porosity, and other microstructural characteristics.

Predicted and experimental *tensile* strain fields are shown in Figure 6.8; corresponding line scans of tensile strain along the net-section are plotted in Figure 6.9(a). Here the measured strains do not vary smoothly in space. There appear to be multiple effects at play. First, there is measurement error associated with digital image correlation. For typical values of displacement noise and the filter length employed in the strain calculation ($h_f = 1\,\text{mm}$), the strain error in regions of relatively uniform strain should be on the order of a few hundred microstrain (Rajan et al., 2012). This value is evidently insufficient to explain all of the strain inhomogeneity. Second, there are stochastic variations in microstructural characteristics, as mentioned previously. Finally, there are also *non*-stochastic effects associated with the woven fiber architecture. Rajan et al. (2012) observed that, in 2-D woven composites, local strain enhancement occurs at tow 'crossovers': locations where undulating warp tows dive beneath flat weft tows. Similar effects may be responsible for the strain 'hotspots' observed in Figure 6.8. Despite some noisiness of the measured strain fields, however, the magnitude of the peak strains and their spatial decay away from the hole are similar to those seen in the simulated strain fields. The differences become more pronounced at stresses exceeding about 350 MPa. In this domain, the tensile strains exceed the (unnotched) tensile failure strain over a length scale comparable to the tow width (1 mm). Therefore, it is expected that significant fiber failure has occurred at this point in the experiment. At even higher stresses, a crack initiates at the hole edge and propagates across the ligament, leading to ultimate failure. Tensile softening due to fiber fracture and concomitant localization of deformation into a crack cannot be captured with the current modeling approach. Approaches based on cohesive zone concepts would be more suitable for this task (see, for instance, He et al. (1994) and Suo et al. (1993)).

The agreement between the measured and simulated axial displacements, shown in Figure 6.10, is similarly good, particularly for smaller values of applied stress. (The correlation is unsurprising, since both γ_{xy} and ϵ_{yy} are related to the axial displacement.) The accuracy of these predictions is assessed on the basis of the difference between predicted and experimental displacements, each normalized by the 'hole displacement'—the displacement (from the FE simulation) of a longitudinal extensometer that spans the hole diameter. The results are also plotted in Figure 6.10 for one of the test specimens. At stresses below about 200 MPa, the errors are very low ($< 5\,\%$ everywhere). The errors increase at higher stresses, especially within the shear bands and (to a lesser extent) in the hole 'wake' (the regions above and below the hole, to the right of the shear bands).

Finally, the simulation results are utilized to investigate near-notch *stresses*. (These quantities cannot be measured experimentally.) Figure 6.9(b) depicts local tensile stresses along the net-section, normalized by the applied net-section stress. In contrast to the local strain fields, no gauge averaging is performed to compute the stresses. As seen, inelasticity does not reduce the stress concentration factor directly at the hole edge, but it does reduce stresses over distances of 1–2 mm from the hole edge. Interestingly, these results are broadly consistent with the 'point stress' fracture criterion (Whitney and Nuismer, 1974), which is based on the attainment of a critical stress over a characteristic length. It has previously been used to rationalize the notch sensitivity of PMCs (Awerbuch and Madhukar, 1985) and CMCs (McNulty et al., 1999). In those studies, it had been found that, regardless of the matrix material, the characteristic length is on the order of 1 mm. The data presented herein is broadly consistent with these results; indeed, taking the critical stress to be the unnotched tensile strength, the inferred characteristic length is 1.3 mm.

6.5.5 Discussion

The agreement between predicted and experimental local displacement and strain fields mirrors the agreement between predicted and experimental global extensometer strains. Specifically, the agreement is excellent for smaller values of net-section stress (less than roughly 300 MPa), and noticeable discrepancies arise only at higher stresses. These discrepancies likely arise because, at higher stresses, the stress state within some material elements follows a non-proportional trajectory. The constitutive model, on the other hand, being based on deformation theory, assumes proportional stressing within every material element.

Deviations from proportional stressing can be assessed by computing ratios using the effective stress:

$$\begin{aligned}
\lambda_{xx} &= \frac{\overline{\sigma}(\sigma_{xx}, 0, 0)}{\overline{\sigma}(\sigma_{xx}, \sigma_{yy}, \sigma_{xy})} &&= \frac{\sigma_{xx}\sqrt{A_{11}}}{\overline{\sigma}} \\
\lambda_{yy} &= \frac{\overline{\sigma}(0, \sigma_{yy}, 0)}{\overline{\sigma}(\sigma_{xx}, \sigma_{yy}, \sigma_{xy})} &&= \frac{\sigma_{yy}\sqrt{A_{11}}}{\overline{\sigma}} \\
\lambda_{xy} &= \frac{\overline{\sigma}(0, 0, \sigma_{xy})}{\overline{\sigma}(\sigma_{xx}, \sigma_{yy}, \sigma_{xy})} &&= \frac{\sigma_{xy}\sqrt{A_{66}}}{\overline{\sigma}}
\end{aligned} \tag{6.27}$$

These ratios are of order unity. For instance, if the state of stress within the element is pure tension in the y-direction, then $\lambda_{yy} = 1$. If, instead, it is pure shear, $\lambda_{yy} = 0$. Therefore, changes in λ on the order of a few tenths over the loading history indicate significant non-proportional stressing. (Note, however, that only two of the ratios are independent.) Changes in λ are of consequence only if they are in regions of significant plastic strains. (In the elastic regime, non-proportional stressing does not induce errors.)

The absolute values of *changes* in λ_{xy} and λ_{yy} (with respect to their values in the regime of macroscopic elasticity) are depicted In Figure 6.11 for two values of net-section stress. There are two locations where significant changes in λ occur: 1) in the hole wake and 2) at the shear bands. In the former locations, the stresses are small and the plastic strains are negligible. However, in the latter location, plastic strains are obviously substantial. Non-proportional stressing within the shear bands appears to be related to the errors in displacement fields observed in Figure 6.10. If this hypothesis is correct, then tracking the ratios λ over the course of a simulation would provide some insight (albeit qualitative) into the regimes in which the constitutive model is expected to yield accurate results.

It should also be noted that the stress-strain curves used to calibrate the constitutive model omit any description of material softening. Errors arise from this assumption when the tensile and shear strains exceed the values corresponding to the peak tensile and shear stresses (roughly 0.63 % and 1.0 %, respectively). In the simulation, the condition for shear softening ($\gamma > \gamma_{peak}$) is first met at a net-section stress of approximately 220 MPa. Softening is expected to occur over a significant length scale (the tow width, 1 mm) at approximately 270 MPa. The corresponding values for tensile softening are 260 MPa and 290 MPa, respectively. These results imply that the effects of softening may become relevant when net-section stresses exceed roughly 250–300 MPa. Note, however, that material softening does not explain the discrepancies between measured and simulated displacement/strain fields: incorporation of softening would increase the compliance of the simulated specimen, causing the correlation between prediction and experiment to worsen. Further work is required to ascertain the effect of material softening on simulated displacement and strain fields and on the stress required for localization and fracture.

Table 6.1: Measured elastic constants. Predicted values of E_{45} and ν_{45} (from elasticity theory) are also shown.

	E_0 (GPa)	ν_0	G (GPa)	E_{45} (GPa)	ν_{45}
Measured	125	0.12	38	102	0.27
Predicted	–	–	–	99	0.30

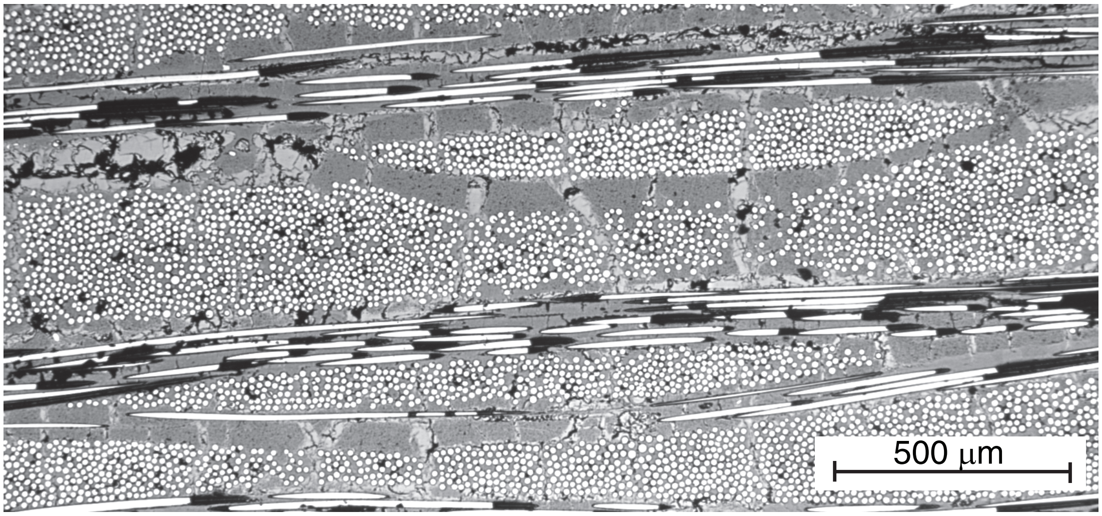

Figure 6.1: Optical micrograph of a polished cross-section through the composite.

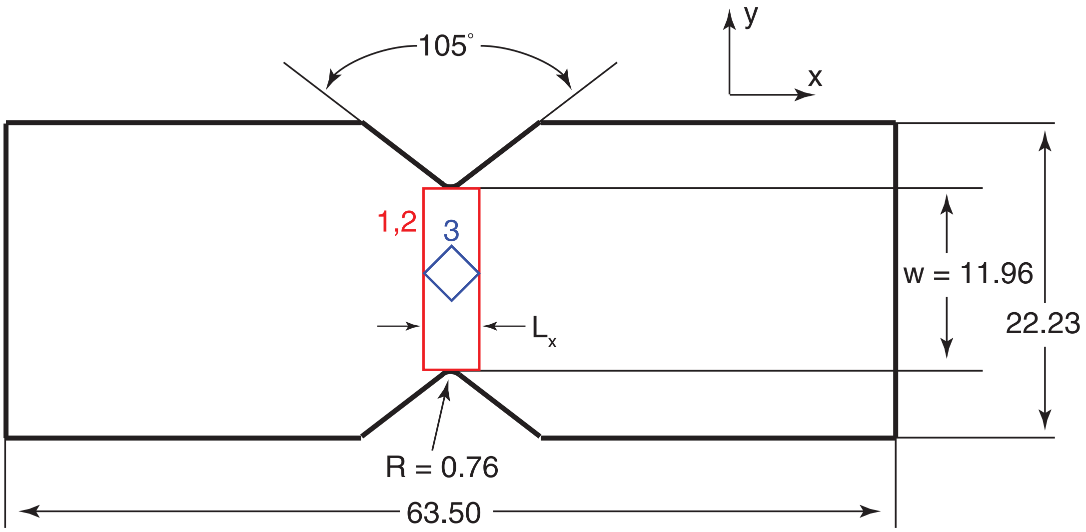

Figure 6.2: Schematic of Iosipescu test specimen (dimensions are in millimeters).

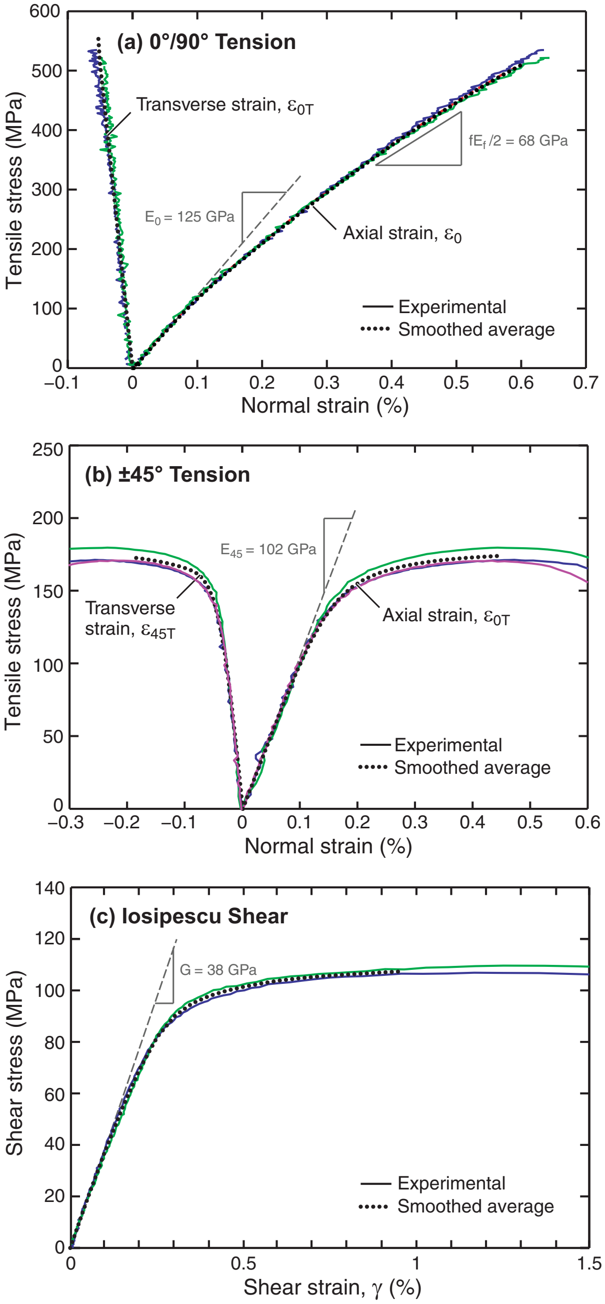

Figure 6.3: Measured stress-strain curves for (a) tension at 0°, (b) tension at 45°, and (c) shear. The normal strains in (a) and (b) were computed using DIC data whereas the shear strains in (c) were obtained by averaging the DIC and strain gauge data on the two faces, as described in the text. Also depicted are smoothed averages.

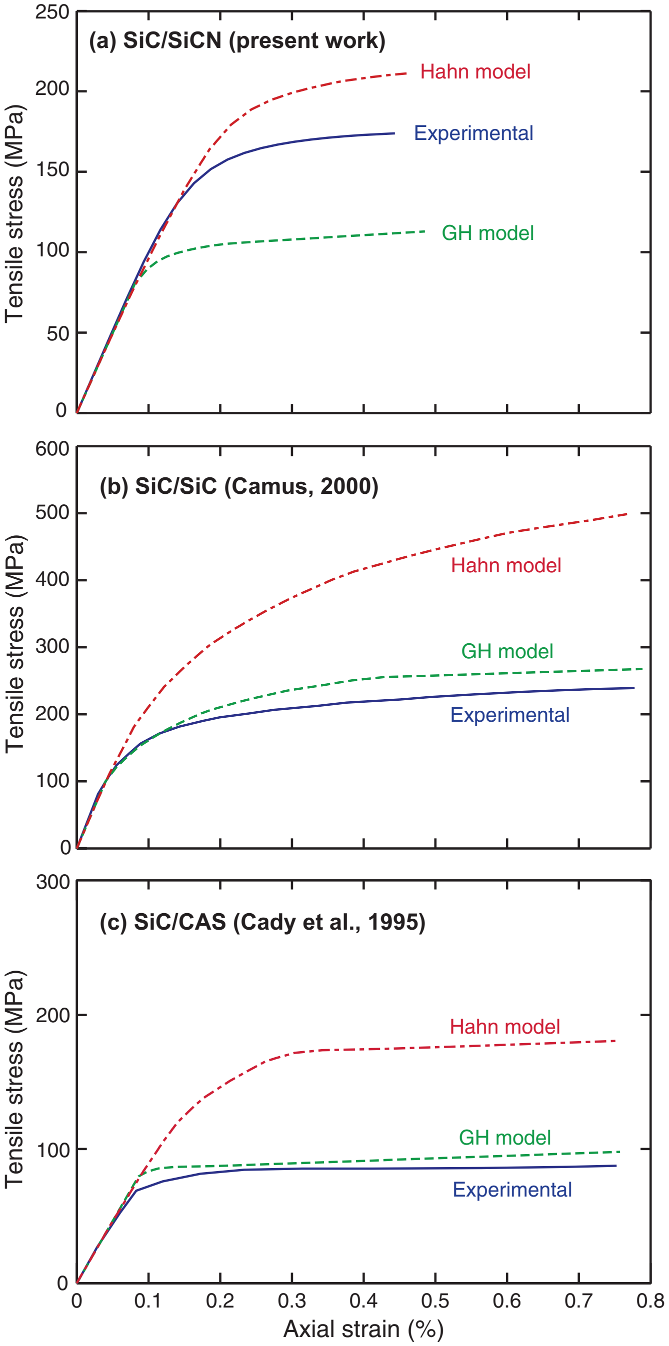

Figure 6.4: Comparisons of the GH and Hahn model predictions of the 45° axial stress-strain curve with experimental measurements on (a) SiC/SiCN composite (from the present work); (b) SiC/SiC composite (Camus, 2000) and (c) SiC/CAS composite (Cady et al., 1995a)).

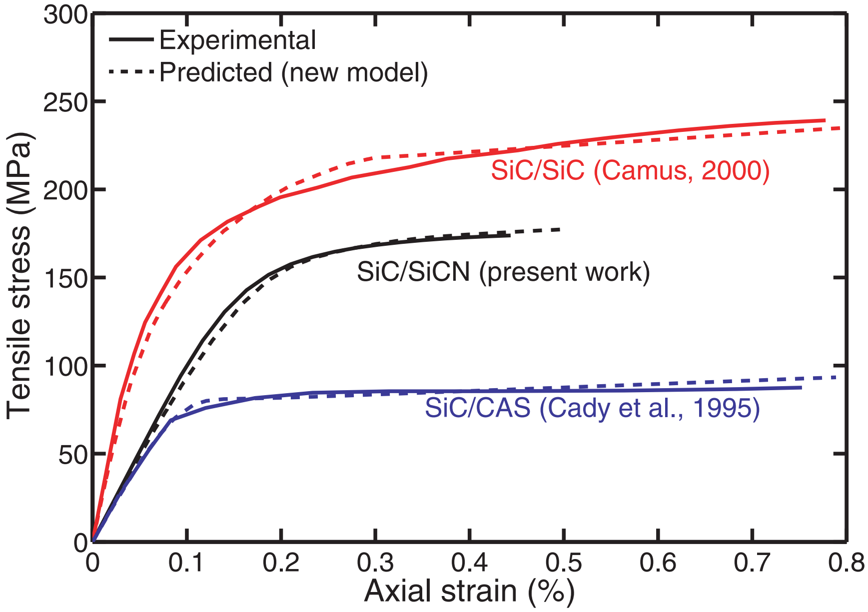

Figure 6.5: Comparisons of predicted and measured 45° axial stress-strain curves for the three composites in Figure 6.4.

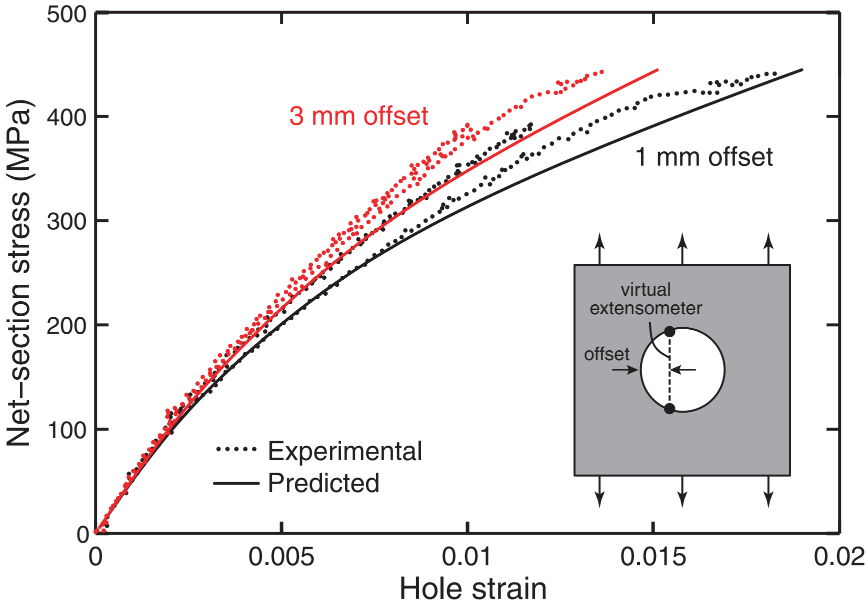

Figure 6.6: Comparisons of measured and predicted stress-strain curves for the open-hole tension test. The strain is that of a virtual extensometer that spans the hole and is offset from the hole edge, as shown in the inset. Strains were computed for two offsets: 1 mm and 3 mm. The hole radius is 4.76 mm.

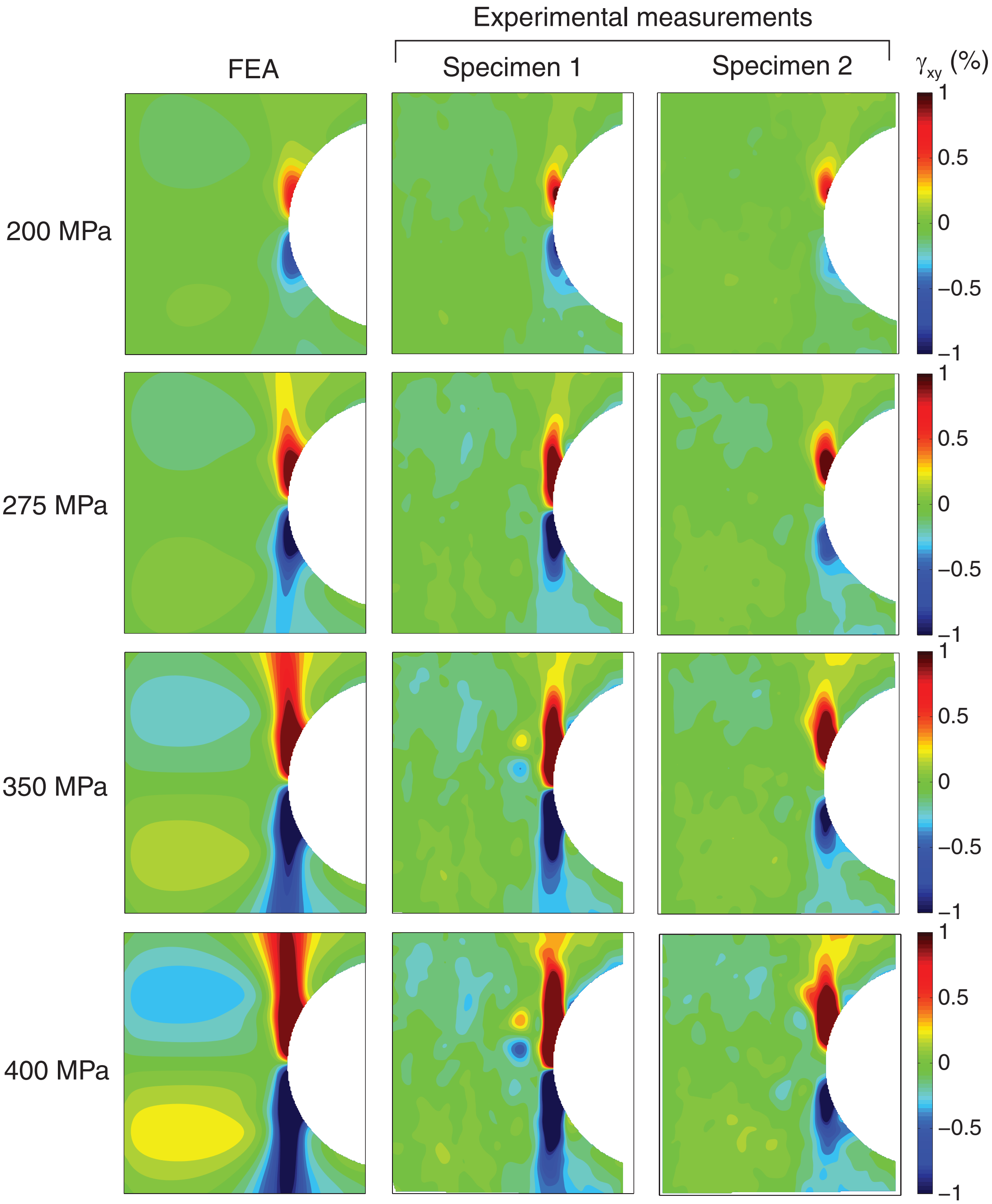

Figure 6.7: Comparisons of measured and predicted shear strain fields for the open-hole tension test.

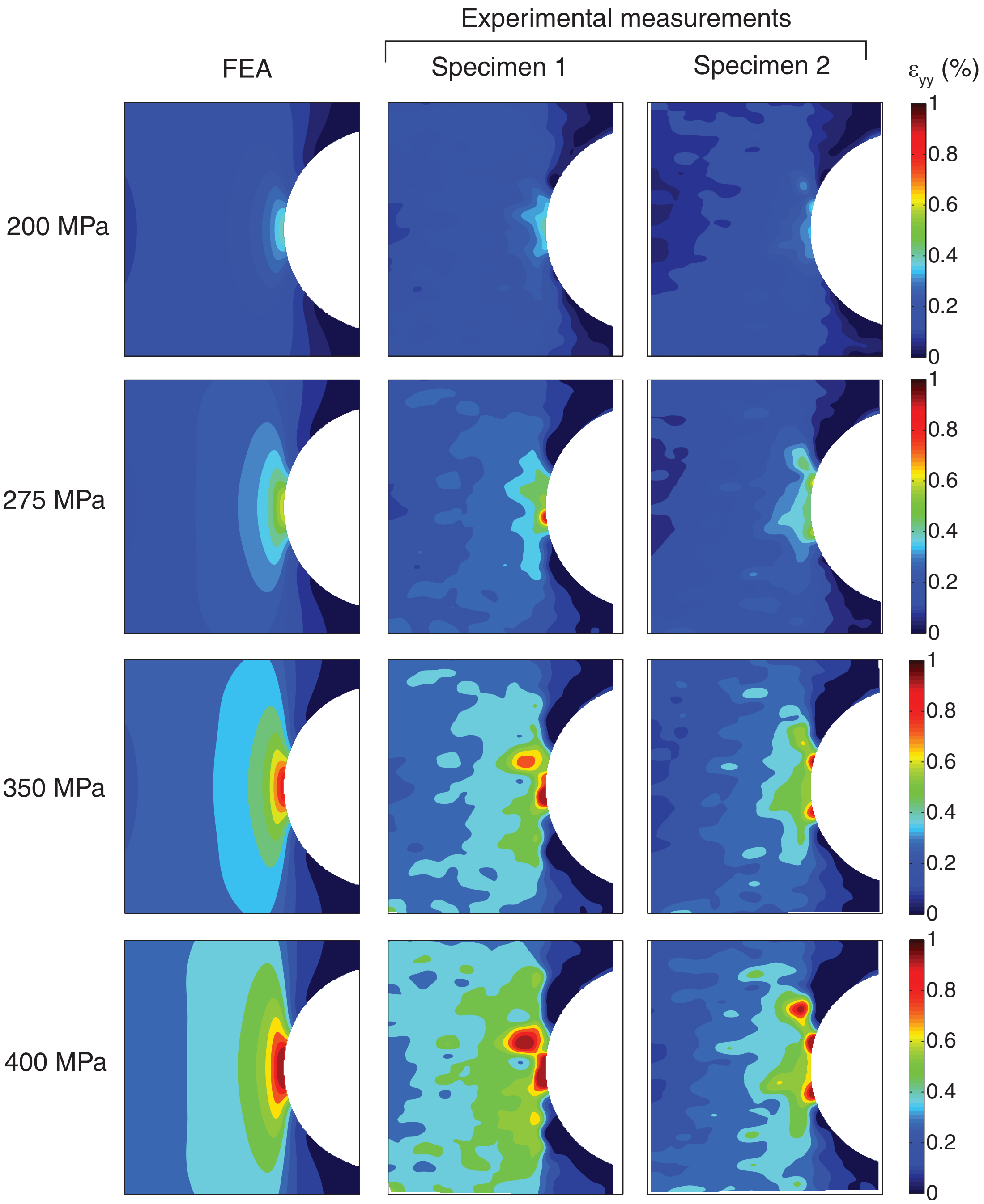

Figure 6.8: Comparisons of measured and predicted tensile strain fields for the open-hole tension test.

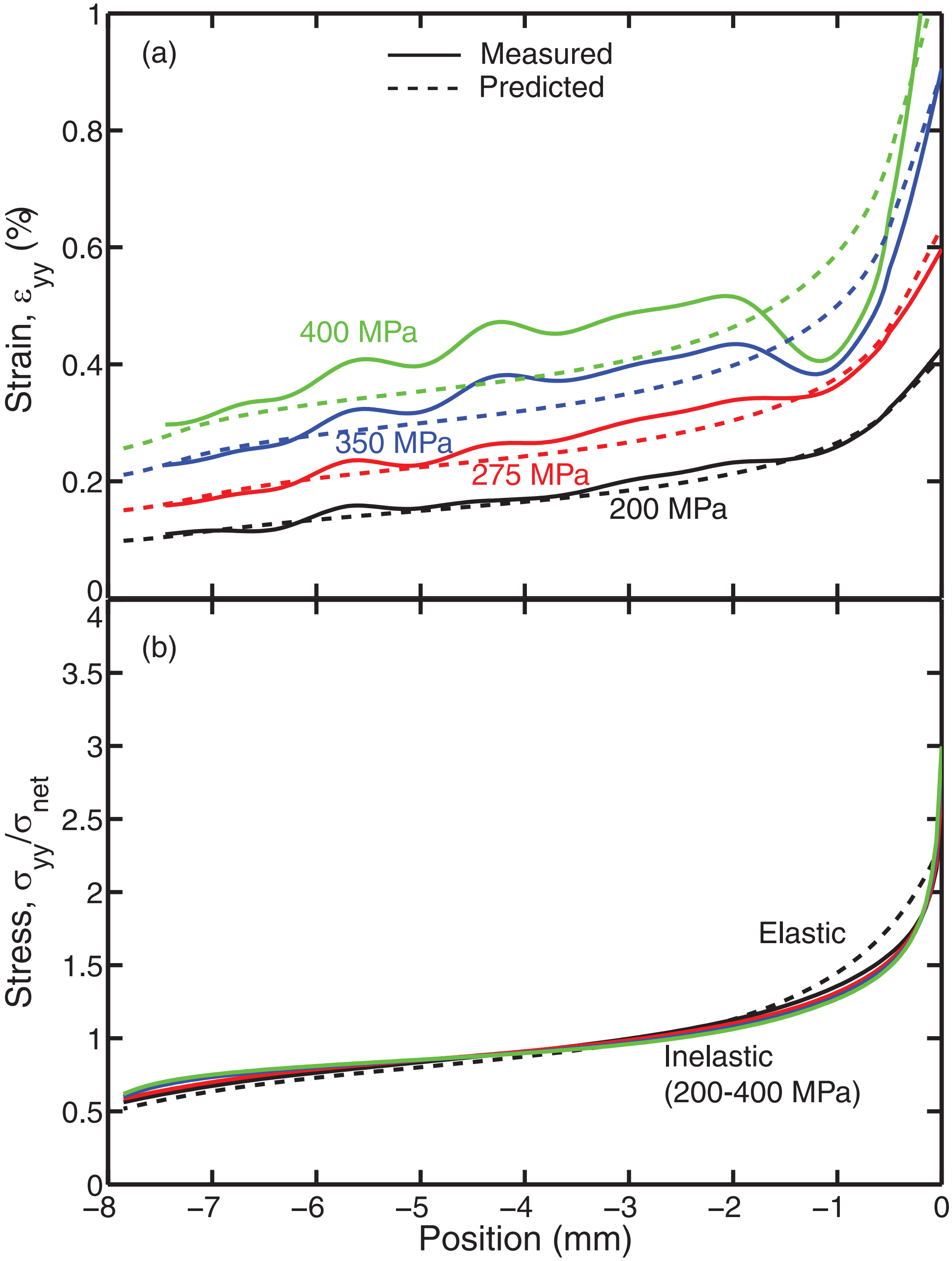

Figure 6.9: (a) Measured and predicted strains and (b) predicted stresses along the net-section plane for the open-hole tension test.

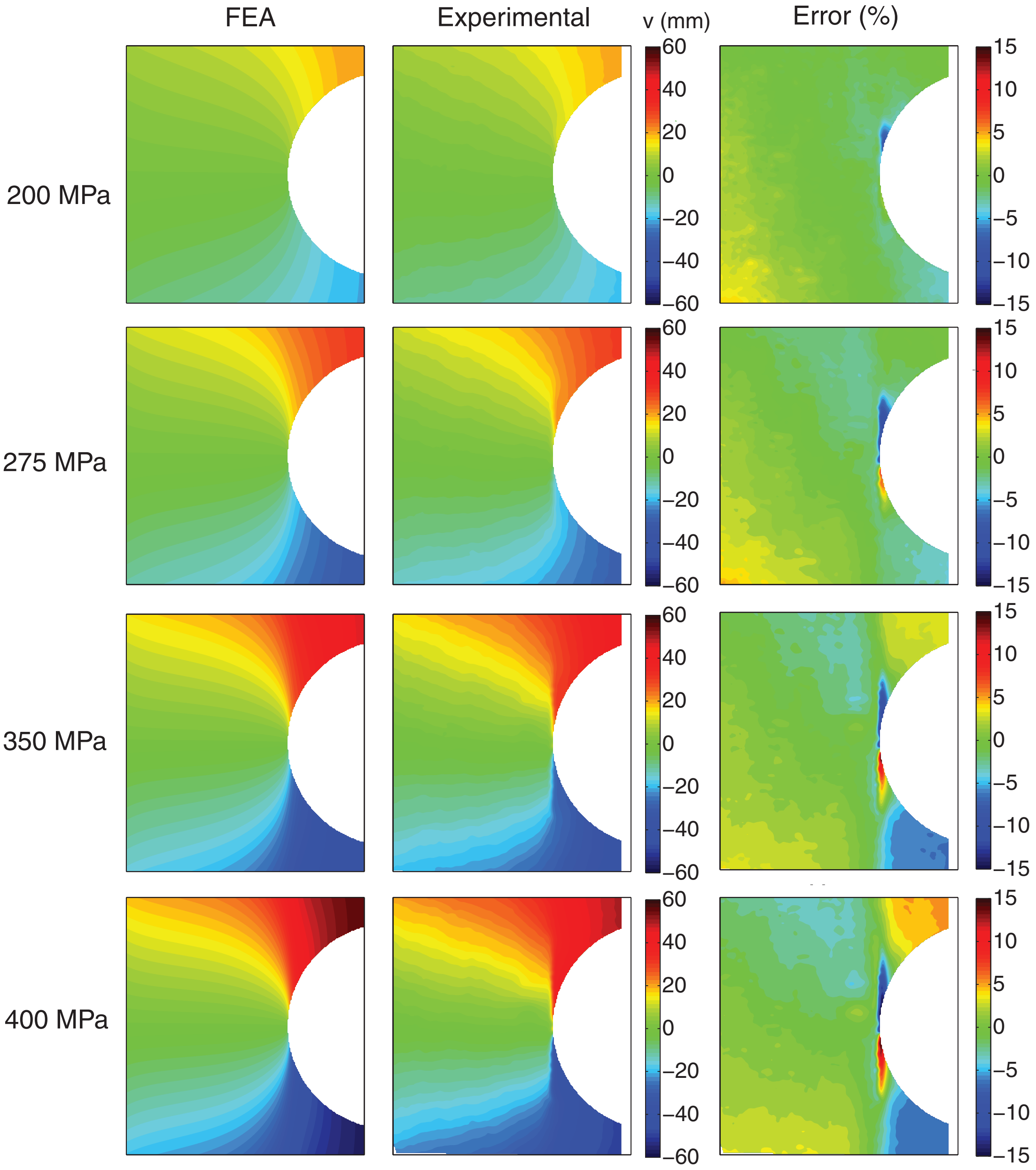

Figure 6.10: Comparisons of measured and predicted axial displacement fields (v) for the open-hole tension test as well as the error between them. (The error is the difference in displacements divided by the 'open hole displacement'; that is, the predicted displacement experienced by an extensometer that spans the hole diameter.)

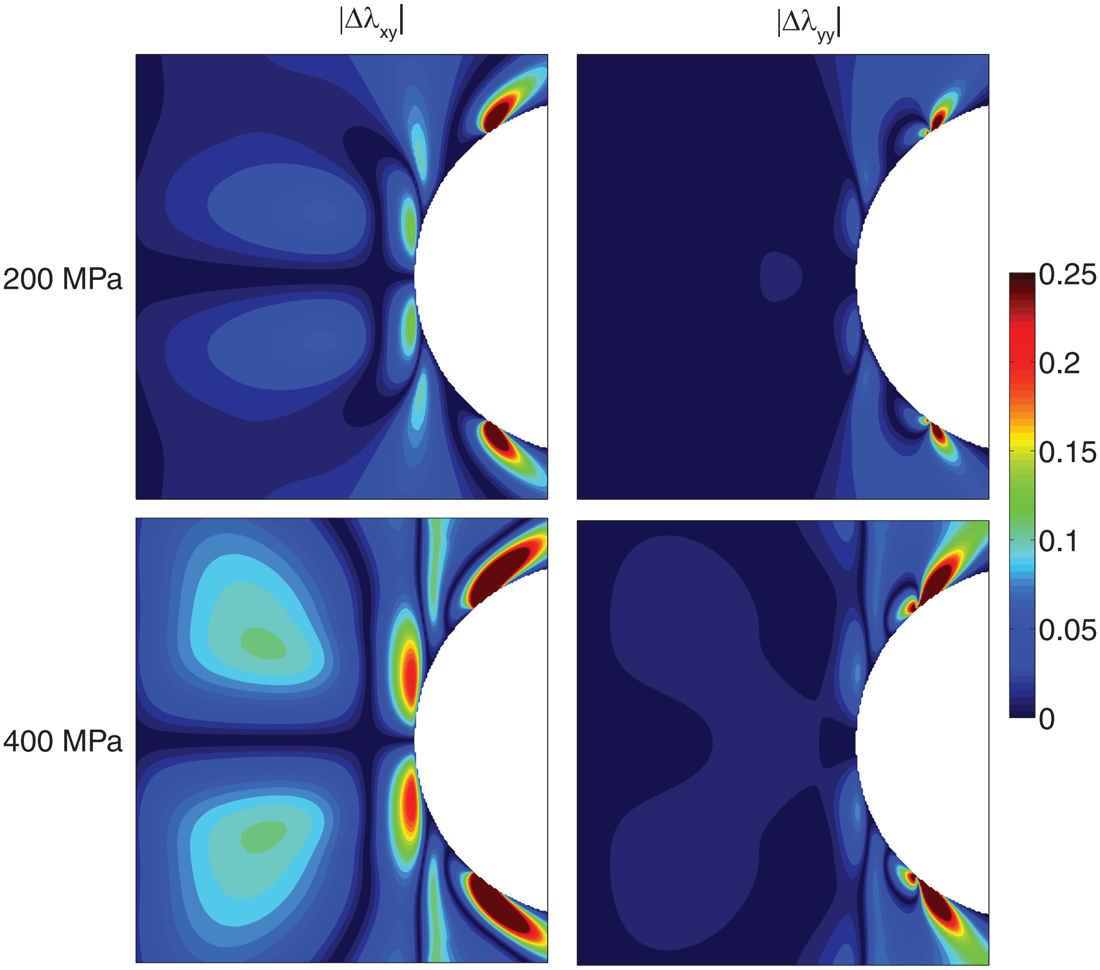

Figure 6.11: Changes in proportionality ratios, λ_{xy} and λ_{yy} from their values in the regime of global elasticity.

Chapter 7

Conclusions and future work

7.1 Summary and conclusions

An important distinction in CMC mechanics has been drawn between relatively simple 1-D loadings and more complex multiaxial 2-D loadings. For the former class of problems, the fundamental mechanics and physics underlying matrix cracking and fiber fragmentation are well-understood. As a consequence, the *deformation* of CMCs in 1-D loadings can be predicted with high fidelity. Prediction of *fracture*, however, remains to be fully resolved. Obviously, the constitutive description must be supplemented by a fracture criterion. As demonstrated in Chapter 2, criteria based on attainment of a critical local strain (as in Hild et al. (1994)) are inadequate for failure prediction when non-uniform strains are present. This deficiency was remedied through the development of a fracture criterion based on a global load maximum. The fracture criterion was combined with a constitutive law based on the mechanics of a fragmenting fiber bundle (Hui et al., 1995). The criterion implies that the first localization to initiate within the structure does not necessarily cause structural failure. Instead, because of structural (geometric) hardening (as manifested in a rising load-displacement curve), other localizations, remote from the first, are able to develop. Ultimate failure occurs once global (structural) softening commences. The corresponding failure predictions for four-point bending of CMC laminates were found to be in reasonably good agreement with available experimental data, as shown in Chapter 2.

The state of modeling for 2-D loadings is comparatively less mature. The key problems are two-fold. One lies in understanding the stress and strain fields, at the scale of the *constituents*, that arise in general in-plane loading of multidirectionally reinforced composites. As discussed in Chapter 3, the forms of these fields, couched in terms of the stresses on the constituent plies, can, in some instances, be obtained from analytical models. Their accuracy can be readily assessed using a finite element analysis of a representative volume element. In that chapter, the fields were subsequently used to estimate the steady-state matrix cracking stress, first for pure shear loading, and then for general in-plane loading. This was accomplished through an adaptation of the fracture mechanics analysis of Budiansky et al. (1986). In principle, the stress fields could also enable prediction of the *evolution* of damage, characterized, for instance, by the matrix crack density as a function of applied stress.

The second broad area of interest in the realm of multidirectional loadings is prediction of laminate behavior at *coarser* length scales: those relevant to engineering design (i.e. mm or cm). Unit cell models, such as those presented in Chapter 3, while useful for interrogating stress and strain distributions at the scale of µm, are difficult to 'scale up' to these larger length scales. As a consequence, prediction of laminate behavior is currently restricted to phenomenological models, based on either continuum damage mechanics (e.g. Talreja (1991); Camus (2000); Chaboche and Maire (2001)) or on elastic-plastic formulations (e.g. Genin and Hutchinson (1997)).

One of the latter type of models—the Genin-Hutchinson model—was examined in detail in Chapter 4. It was found to suffer from numerical convergence problems when used as a constitutive model in finite element calculations. Two distinct sources of instability were identified: one associated with incremental shearing of *elastically*-anisotropic laminates and the other with incremental transverse straining of *inelastically*-anisotropic laminates. Both instabilities are manifested only in the post-matrix cracking regime. The instabilities were remedied by two proposed modifications. In the first, shear-extension coupling after matrix cracking is assumed to be negligible (even if it exists in the elastic domain). In the second, a modified tangential compliance matrix is developed in order to account for fiber scissoring, assuming simultaneous operation of two modes of deformation: axial fiber stretching and fragmentation (which was described in the original GH model) and fiber rotation (which was not).

Using the remediated GH model, stress fields ahead of blunt notches in plates of CMC laminates were investigated in Chapter 5 using finite element analysis. A complementary analytical methodology, based on Neuber's law, was also developed. The methodology is based on a series of transformations of the corresponding elastic distribution. Within the *inelastic* zone, both the (original) elastic stress and the position coordinate are scaled using results from Neuber's law; within the *elastic* zone, the position coordinate of the original elastic stress is simply shifted. The predictions of the analytical model were found to be in excellent agreement with the simulation results.

In Chapter 6, the modified GH model, as well as a related model based on the work of Hahn (1973), was critically assessed using experimental data for three different materials: SiC/SiC (Camus, 2000), SiC/CAS (Cady et al., 1995a), and SiC/SiCN (present work). It was found that both constitutive models are overly restrictive and cannot accommodate the full range of behaviors of all composite types (i.e. 'Class II' and 'Class III' materials). To ameliorate this deficiency, a more generalized elastic-plastic model, based on the deformation theory of plasticity, was developed. Correlations between its predictions of strain fields and corresponding experimental measurements (from DIC) for open-hole tension tests are remarkably good. The principal utility of the model is in capturing CMC deformation in the intermediate stress regime, after elasticity ceases to apply but before effects of material softening and non-proportional stressing become important. Finally, where they existed, the discrepancies between the model predictions and the experimental data appeared to be correlated to the onset of non-proportional stressing. Some support for this hypothesis was provided through comparisons of changes in stress ratios with errors in predicted displacements. Indeed, the regions of largest error correspond to regions that experience a non-proportional loading history.

7.2 Future work

7.2.1 High-fidelity virtual tests

Background

Although, as discussed, analytical models and simulations have been developed for particular damage mechanisms present in CMCs—for instance, for matrix cracking and for fiber fragmentation—no model or simulation exists that can capture all such mechanisms simultaneously. Developing such a tool, particularly one that relaxes the assumptions commonly made in analytical models (on-axis loading, large slip lengths, global load sharing, steady-state cracking, etc.), would greatly advance the field of CMC mechanics. Indeed, it would represent a high-fidelity virtual test for structural composites (Cox and Yang, 2006). Virtual tests offer the possibility of 1) reducing the number of (expensive) experiments required to characterize the mechanical behavior of a single material system and 2) investigating material property space using simulations instead of trial-and-error-based testing. Several factors have converged to enable construction of this kind of tool today.

First, there is the crucial physical insight: notably, that all of the mechanical nonlinearity in CMCs can be attributed to interfaces within the material.

The term ‘interface’ is broadly construed: it refers not only to the fiber-matrix interface, but also to interfaces *within* the fiber and matrix along which cracks can form (see Figure 7.1).

Second, numerical capabilities for modeling interface inelasticity (sliding, damage, fracture, etc.) using cohesive elements have matured rapidly over the last 15 years. As discussed by Ortiz and coworkers (Camacho and Ortiz, 1996; Ruiz et al., 2001), cohesive models of fracture greatly expand the space of tractable problems relative to conventional fracture mechanics. They can handle arbitrarily interacting cracks/cohesive zones, material inhomogeneities, non-proportional loading, crack nucleation, etc., all of which are very difficult to analyze using classical methods. For instance, the He-Hutchinson problem of crack deflection/penetration at an interface (He and Hutchinson, 1989) was originally tackled by assuming a kink at the crack tip and comparing the energy release rate for the deflected kink with that for the penetrated kink. They developed a criterion for crack deflection based on the ratio of toughnesses between the substrate and the interface. A more modern and elegant treatment of the problem was carried out by Parmigiani and Thouless (2006), who assumed no such preexisting flaw. Instead, they used cohesive elements along the interface and in the substrate and assigned these elements different cohesive strengths/toughnesses. In doing so, they discovered that a general criterion for crack deflection must incorporate not only the substrate/interface toughness ratio, but also the *strength* ratio. The cohesive approach, therefore, unifies strength- and toughness-based failure criteria.

Furthermore, new techniques have been developed for tackling the more general problem in which the spatial pattern of damage is an output, not an input, to the simulation. (In other words, the crack paths are no longer predefined.) The most well-known of these methods are the extended finite element method (X-FEM) (Moës and Belytschko, 2002; Mariani and Perego, 2003) and the cohesive surface approach (Xu and Needleman, 1994).

Finally, increases in computational power have enabled much more ambitious models: i.e. larger geometries, 3-D simulations, finer meshes, etc. GPU parallelization is also an important development that has yet to be fully exploited.

Length scales of interest

The cohesive interface approach can be used to investigate CMCs at two scales. The first is that of the constituents (note preliminary efforts in this area by Walter et al. (1997) and Tang et al. (2010)). Particularly powerful is the use of cohesive simulations in conjunction with analytical models. For instance, a seminal contribution would be to simulate a unit cell, in which the interfaces have non-zero debond toughness and undergo frictional sliding after debonding, to analyze the mechanics of debonding and slip in CMCs under *off-axis* loading. The results, which would be analogous to those of Hutchinson and Jensen (1990) for on-axis loading, could be readily inserted into a steady-state matrix cracking analysis (such as that of Chapter 3) to predict cracking for general in-plane loading of CMCs with initially *bonded* interfaces. They could also be used to tailor constituent properties (residual stresses, fiber/matrix moduli, interfacial toughness and sliding stress) to maximize composite toughness/strength for off-axis loading.

The second scale of interest is the continuum-scale (mm or cm). The appropriate model in this case would be a representative volume element of a ply or a laminate, containing hundreds of fibers and associated matrix. For a single ply, the *entire* tensile stress-strain behavior could, in principle, be simulated. One could capture the stress at the onset of matrix cracking, the stress required to propagate a long matrix crack, the evolution of matrix crack density with applied stress, the onset of fiber fragmentation, global softening due to fiber fragmentation, the plateau stress after fiber fragmentation ceases, etc. In other words, such a simulation would represent a virtual tension test of a unidirectional ply. For a laminate, yet other problems could be tackled. For instance, virtual tests could be conducted for general in-plane loading (pure shear, 45°

tension, etc.) of CMC laminates. The resulting stress-strain curves could be used as inputs to a coarse-scale constitutive model (such as that of Chapter 6), thus rendering the modeling approach fully *multi-scale*. The shape of the 'yield/cracking surface' for the laminate, and its dependence on constituent properties, could also be predicted (and compared against the predictions of Chapter 3). Additionally, the simulation results could be used to improve existing constitutive models. For instance, non-proportional loading of CMC laminates could be studied, thereby enabling construction of a more sophisticated constitutive model that extends rudimentary elastic-plastic constitutive models of the type described in Chapter 6. Continuum damage mechanics models, such as that of Talreja (1991), could also be assessed. These models are typically based upon *ad hoc* damage evolution laws for internal variables such as crack density or crack area. In a cohesive fracture simulation, these variables would be outputs, not inputs.

7.2.2 Prediction of CMC fracture in non-uniform stress fields

As discussed in Chapters 2 and 6, fracture criteria for CMCs in non-uniform stress fields are often *ad hoc* and without any sound mechanistic basis. For instance, for prediction of notched fracture, a 'point stress' criterion, based on attainment of a critical stress at a critical distance (typically on the order of

1 mm), is often used. Such a criterion is obviously purely empirical.

Although experiments are useful for providing insight into the failure process, they often fail to produce measurements that are sufficiently detailed to discriminate between various (proposed) failure criteria. High-fidelity virtual tests, however, can overcome this deficiency. Parametric studies (varying specimen geometry, applied load, material system, etc.) can be performed rapidly, information from such tests can be extracted at a very small length scale, with no associated measurement noise, and, most importantly, information about the local stress state is available (as opposed to experiments, where typically only the strain state can be monitored). Virtual tests, therefore, are expected to be highly useful not only for assessing existing failure criteria but also for developing novel criteria that are more fundamentally sound Ibnabdeljalil and Curtin (1997b).

Two avenues seem particularly fruitful for investigating the newly-developed fracture criterion for 1-D loadings (Chapter 2). The first deals with direct observation of localizations. The global load criterion implies that an array of roughly periodically spaced localizations should form within the composite where the local strain is largest (e.g. on the tensile face in four-point bending). The displacement jumps associated with these localizations and their spatial distribution should be evident either in experiments (using

DIC) or in virtual tests. A second promising area is design of new mechanical tests designed to induce true tensile failure of CMCs under conditions of non-uniform strain. One possibility, worth further investigation, is to design a test that subjects a constrained specimen to an in-plane *thermal* gradient (Figure 7.2), thus avoiding the mechanical contact that results in premature shear or compressive failure in four-point bending.

For investigating fracture criteria for 2-D loadings (such as notched tension), a combination of virtual tests and experiments is again expected to be highly useful. For virtual tests, the major potential limitation is computational cost. For instance, explicit modeling of fibers and associated matrix in a notched CMC panel would be prohibitive. In this situation, an explicit multi-scale modeling approach (Curtin and Miller, 2003), wherein micro-scale modeling is used in regions of high damage and is coupled to continuum models remote from such regions, is potentially powerful. If feasible, the near-notch cohesive elements would capture material damage and fracture in a physically realistic way, and remote continuum elements would provide the proper coupling between the boundary conditions (applied loads) and the near-notch damage. Such virtual tests could be readily utilized to assess the accuracy of existing failure criteria for notched CMC laminates (McNulty et al., 1999), and to develop new criteria for notched fracture that are more accurate and physically sound.

To summarize, there exists a massive opportunity to apply the mathematical and computational machinery that has been developed for modeling material damage and fracture to relevant problems in CMC mechanics. One outcome would be the development of high-fidelity virtual tests with unprecedented realism and predictive power. Such tests could significantly accelerate the engineering design process as well as inform future materials development activities.

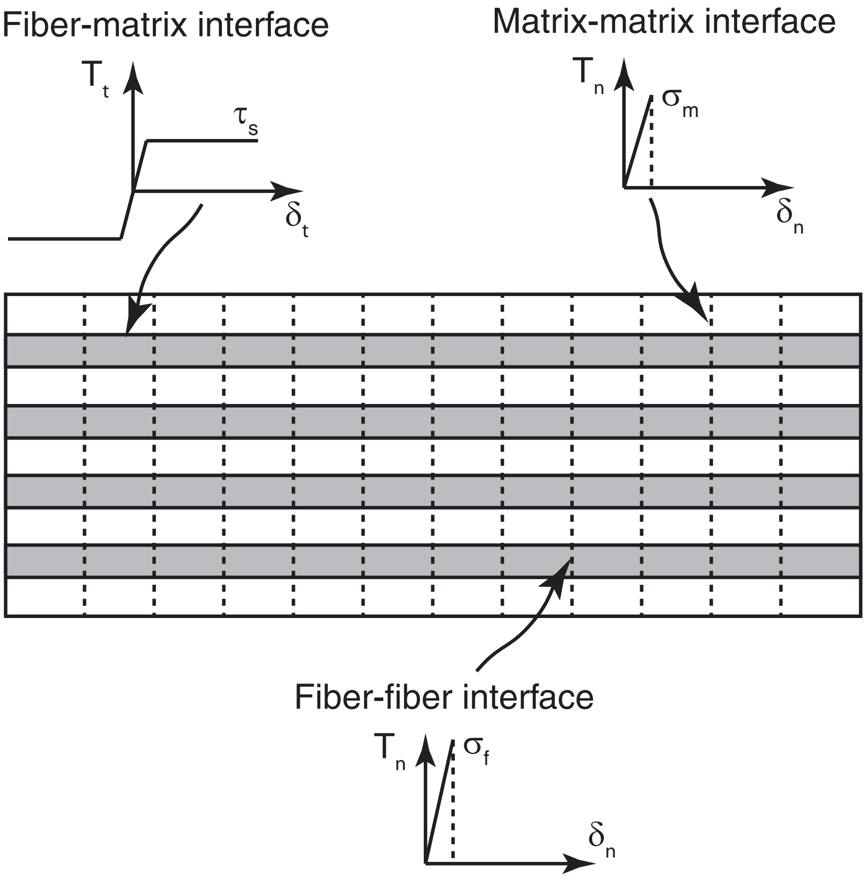

Figure 7.1: Modeling of damage and slip within a ceramic matrix composite using cohesive interfaces.

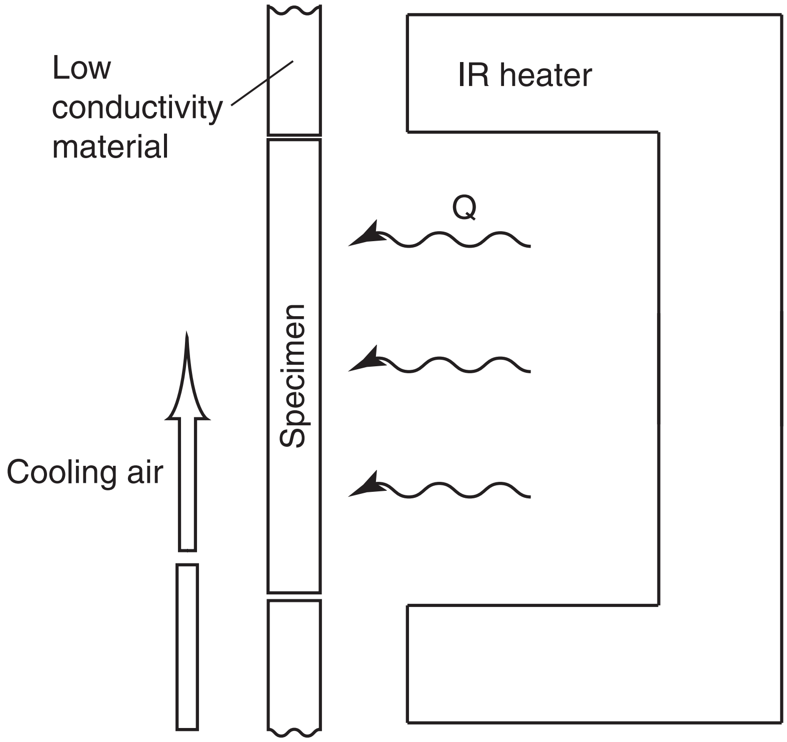

Figure 7.2: Schematic of test to impose a linear strain gradient, by creating a thermal gradient across the sample.

Appendix A

Exact fragmentation model

Here the exact analytical descriptions of the fragmentation model developed by Hui et al. (1995) are presented. The average stress is partitioned into three terms:

$$S(\Delta) = \int_{0}^{\Delta/2} \frac{\ell^2}{2} p_1(\Delta, \ell)\, \mathrm{d}\ell + \int_{\Delta/2}^{\Delta} \frac{\ell^2}{2} p_2(\Delta, \ell)\, \mathrm{d}\ell + \int_{\Delta/2}^{\Delta} \left[(\ell - \Delta)\Delta + \frac{\Delta^2}{2} \right] p_3(\Delta, \ell)\, \mathrm{d}\ell \tag{A.1}$$

The three integrals on the right side correspond to contributions from fragments of length $\ell < \Delta/2$, $\Delta/2 < \ell < \Delta$, and $\ell > \Delta$, respectively. The fragment lengths are normalized by the characteristic length, δ_c. The functions $p_i(\Delta, \ell)$ represent fiber fragment densities, given by

$$p_1(\Delta, \ell) = p(\ell) + 2\rho \int\limits_{\ell}^{2\ell} \frac{A_0(t)}{t} \exp\left[-t^\rho \left(\ell + \frac{t}{2}\right)\right] \, \mathrm{d}t \tag{A.2}$$

$$p_2(\Delta, \ell) = p(\ell) + 2\rho \int\limits_{\ell}^{\Delta} \frac{A_0(t)}{t} \exp\left[-t^\rho \left(\ell + \frac{t}{2}\right)\right] \, \mathrm{d}t \tag{A.3}$$

$$p_3(\Delta, \ell) = A_0(\Delta) \exp(-\Delta^\rho \ell) \tag{A.4}$$

where

$$p(\ell) = \ell^{2\rho} \exp\left[\frac{-\ell^{\rho+1}}{\rho+1}\right] \psi\left(\frac{\ell^{\rho+1}}{2}\right) \tag{A.5}$$

$$A_0(\ell) = \ell^{2\rho} \exp\left[\frac{\rho \ell^{\rho+1}}{\rho+1}\right] \psi\left(\frac{\ell^{\rho+1}}{2}\right) \tag{A.6}$$

and

$$\psi(x) = \exp\left[\frac{-2\rho}{\rho+1} \int\limits_{0}^{x} \frac{1-\exp(-t)}{t} \, \mathrm{d}t\right] \tag{A.7}$$

Appendix B

Elastic constants of cross-ply composite

The compliance matrix of a unidirectional ply (assumed to be in a state of plane stress) can be written in terms of the engineering constants as:

$$S_0 = \begin{bmatrix} 1/E_a & -\nu_t/E_t & 0 \\ -\nu_a/E_a & 1/E_t & 0 \\ 0 & 0 & 1/G_a \end{bmatrix} \tag{B.1}$$

The engineering constants, in turn, are found using the generalized self-consistent scheme (GSCS) (Christensen and Lo, 1979; Christensen, 1990). It is a micromechanical model that allows the macroscopic elastic constants of the fiber composite to be estimated using the elastic constants of the constituents.

The GSCS model yields the same result as the cylindrical composites assemblage (CCA) model (Hashin and Rosen, 1964; Hashin, 1983, 1979) for four of the composite elastic constants:

$$\begin{aligned}
E_a &= E_m V_m + E_f V_f + \frac{4(\nu_f - \nu_m)^2 V_m V_f}{V_m/k_f + V_f/k_m + 1/G_m} \\
\nu_a &= \nu_m V_m + \nu_f V_f + \frac{(\nu_f - \nu_m)(1/k_m - 1/k_f) V_m V_f}{V_m/k_f + V_f/k_m + 1/G_m} \\
G_a &= \frac{G_m(G_m V_m + G_f(1 + V_f))}{G_m(1 + V_f) + G_f V_m} \\
k &= \frac{k_m(k_f + G_m)V_m + k_f(k_m + G_m)V_f}{(k_f + G_m)V_m + (k_m + G_m)V_f}
\end{aligned} \tag{B.2}$$

where the subscripts f and m denote the fiber and effective medium, respectively. The shear modulus, G, and the transverse bulk modulus, k, are given by the expressions (for isotropic materials):

$$\begin{aligned}
G &= \frac{E}{2(1+\nu)} \\
k &= \frac{G}{1 - 2\nu}
\end{aligned} \tag{B.3}$$

A unidirectional ply is a transversely isotropic material, which possesses five independent elastic constants. The remaining constant, the transverse shear modulus, G_t, is only bounded by the CCA model. An exact solution, however, can be found by using the GSCS formula given in Christensen and Lo (1979) (the expression is quite lengthy and is thus not reproduced here). With these five constants, the transverse Young's modulus, E_t, and the transverse

Poisson's ratio, ν_t can be computed using the formulae (Hashin, 1979):

$$\begin{aligned} \nu_t &= \frac{k - mG_t}{k + mG_t} \\ E_t &= 2(1+\nu_t)G_t \end{aligned} \tag{B.4}$$

where

$$m = 1 + \frac{4k\nu_a^2}{E_a} \tag{B.5}$$

The compliance matrix for the 90° ply is obviously

$$\boldsymbol{S}_{90} = \begin{bmatrix} 1/E_t & -\nu_a/E_a & 0 \\ -\nu_t/E_t & 1/E_a & 0 \\ 0 & 0 & 1/G_a \end{bmatrix} \tag{B.6}$$

Then, using elasticity theory, the compliance matrix for the overall (cross-ply) composite is:

$$\boldsymbol{S}^c = 2([\boldsymbol{S}_0]^{-1} + [\boldsymbol{S}_{90}]^{-1})^{-1} \tag{B.7}$$

References

R. Eldrid, L. Kaufman, and P. Marks. The 7FB: The next evolution of the F gas turbine. Technical report, GE Power Systems, Schenectady, NY, 2001. 1.1

C. Epstein. GE's Passport 20 Engine program is on schedule for 2016 entry into service, 2013. URL `http://www.ainonline.com/aviation-news/nbaa-convention-news/2013-10-22/ges-passport-20-engine-program-schedule-2016-entry-service`. 1.1, 1.1

K. Wood. Ceramic-matrix composites heat up. *High-Performance Composites*, 21 (6), 2013. 1.1, 1.1

D. S. Beyerle, S. M. Spearing, F. W. Zok, and A. G. Evans. Damage and failure in unidirectional ceramic matrix composites. *Journal of the American Ceramic Society*, 75(10):2719–2725, 1992. 1.1, 1.2, 2.1

D. S. Beyerle, S. M. Spearing, and A. G. Evans. Damage mechanisms and the mechanical properties of a laminated 0/90 ceramic/matrix composite. *Journal of the American Ceramic Society*, 75(12):3321–3330, 1992. 1.1, 1.2

D. B. Marshall and A. G. Evans. Failure mechanisms in ceramic-fiber/ceramic-matrix composites. *Journal of the American Ceramic Society*, 68(5):225–231, 1985. 1.1, 1.2, 2.1

J. C. McNulty and F. W. Zok. Application of weakest-link fracture statistics to fiber-reinforced ceramic-matrix composites. *Journal of the American Ceramic Society*, 80(6):1535–1543, 1997. 1.1, 1.2, 1.5, 2.1, 2.4, 2.1

K. M. Prewo. Tension and flexural strength of silicon carbide fiber-reinforced glass ceramics. *Journal of Materials Science*, 21(10):3590–3600, 1986. 1.1, 1.2, 2.1

S. Jansson and F. A. Leckie. The mechanics of failure of silicon carbide fiber-reinforced glass-matrix composites. *Acta Metallurgica et Materialia*, 40(11): 2967–2978, 1992. 1.1, 2.1

F. W. Zok and S. M. Spearing. Matrix crack spacing in brittle matrix composites. *Acta Metallurgica et Materialia*, 40(8):2033–2043, 1992. 1.1, 1.2

S. M. Spearing and F. W. Zok. Stochastic aspects of matrix cracking in brittle matrix composites. *Journal of Engineering Materials and Technology*, 115:314–318, 1993. 1.1

W. A. Curtin. Multiple matrix cracking in brittle matrix composites. *Acta Metallurgica et Materialia*, 41(5):1369–1377, 1993. 1.1

M.-Y. He, B. Wu, and Z. Suo. Notch-sensitivity and shear bands in brittle matrix composites. *Acta Metallurgica et Materialia*, 42(9):3065–3070, 1994. 1.1, 6.5.4

J. Aveston, G. A. Cooper, and A. Kelly. Single and multiple fracture. In *The Properties of Fiber Composites*, pages 15–24. National Physical Laboratory, IPC Science and Technology Press Ltd., 1971. 1.1, 1.2, 1.3, 2.2.2, 3.1, 3.3.3, 3.6, 3.6

D. B. Marshall, B. N. Cox, and A. G. Evans. The mechanics of matrix cracking in brittle-matrix fiber composites. *Acta Metallurgica*, 33(11):2013–2021, 1985. 1.1, 1.2

B. Budiansky, J. W. Hutchinson, and A. G. Evans. Matrix fracture in fiber-reinforced ceramics. *Journal of the Mechanics and Physics of Solids*, 34(2):167–189, 1986. 1.1, 1.2, 1.3, 3.1, 3.2, 3.3.3, 3.7, 7.1

W. A. Curtin. Theory of mechanical properties of ceramic-matrix composites. *Journal of the American Ceramic Society*, 74(11):2837–2845, 1991. 1.1, 1.4, 2.1, 2.2.1

J. M. Neumeister. A constitutive law for continuous fiber reinforced brittle matrix composites with fiber fragmentation and stress recovery. *Journal of the Mechanics and Physics of Solids*, 41(8):1383–1404, 1993. 1.1, 2.1, 2.2.1

C.-Y. Hui, S. L. Phoenix, M. Ibnabdeljalil, and R. L. Smith. An exact closed form solution for fragmentation of weibull fibers in a single filament composite with applications to fiber-reinforced ceramics. *Journal of the Mechanics and Physics of Solids*, 43(10):1551–1585, 1995. 1.1, 1.2, 2.1, 2.2.1, 4.5.3, 7.1, A

S. J. Zhou and W. A. Curtin. Failure of fiber composites: a lattice Green function model. *Acta Metallurgica et Materialia*, 43(8):3094–3104, 1995. 1.1, 2.4

C. M. Landis, I. J. Beyerlein, and R. M. McMeeking. Micromechanical simulation of the failure of fiber reinforced composites. *Journal of the Mechanics and Physics of Solids*, 48(3):621–648, 2000. 1.1

F. Hild, J.-M. Domergue, F. A. Leckie, and A. G. Evans. Tensile and flexural ultimate strength of fiber-reinforced ceramic-matrix composites. *International Journal of Solids and Structures*, 31(7):1035–1045, 1994. 1.1, 2.1, 2.4, 7.1

P. Brøndsted, F. E. Heredia, and A. G. Evans. In-plane shear properties of 2-D ceramic matrix composites. *Journal of the American Ceramic Society*, 77(10): 2569–2574, 1994. 1.1, 1.3, 3.5.1

C. Cady, F. E. Heredia, and A. G. Evans. In-plane mechanical properties of several ceramic-matrix composites. *Journal of the American Ceramic Society*, 78(8):2065–2078, 1995. 1.1, 1.2, 1.3, 4.5.3, 4.5.4, 5.1, 6.2.4, 6.3.1, 6.3.4, 6.4.6, 6.4, 7.1

K. R. Turner, J. S. Speck, and A. G. Evans. Mechanisms of damage and failure in carbon-matrix composites subject to tensile and shear loading. *Journal of the American Ceramic Society*, 78(7):1841–1848, 1995. 1.1, 1.3, 6.2.4

D. B. Marshall and B. N. Cox. A J-integral method for calculating steady-state matrix cracking stresses in composites. *Mechanics of Materials*, 7(2):127–133, 1988. 1.2

W. A. Curtin. Exact theory of fibre fragmentation in a single-filament composite. *Journal of Materials Science*, 26(19):5239–5253, 1991. 1.2, 2.1, 2.2.1, 3.3.3, 4.5.2

Z. C. Xia, R. R. Carr, and J. W. Hutchinson. Transverse cracking in fiber-reinforced, brittle matrix cross-ply composites. *Acta Metallurgica et Materialia*, 41(8):2365–2376, 1993. 1.2

Z. C. Xia and J. W. Hutchinson. Matrix cracking of cross-ply ceramic composites. *Acta Metallurgica et Materialia*, 42(6):1933–1945, 1994. 1.2

J. C. McNulty, F. W. Zok, G. M. Genin, and A. G. Evans. Notch-sensitivity of fiber-reinforced ceramic-matrix composites: effects of inelastic straining and volume-dependent strength. *Journal of the American Ceramic Society*, 82(5): 1217–1228, 1999. 1.2, 1.4, 4.1, 4.5.5, 5.2.1, 6.5.4, 7.2.2

U. Ramamurty. Assessment of load transfer characteristics of a fiber-reinforced titanium-matrix composite. *Composites Science and Technology*, 65(11):1815–1825, 2004. 1.2

C. Cady, T. J. Mackin, and A. G. Evans. Silicon Carbide/Calcium Aluminosilicate: A notch-insensitive ceramic-matrix composite. *Journal of the American Ceramic Society*, 78(1):77–82, 1995. 1.4, 6.1

G. M. Genin and J. W. Hutchinson. Composite laminates in plane stress: Constitutive modeling and stress redistribution due to matrix cracking. *Journal of the American Ceramic Society*, 80(5):1245–1255, 1997. 1.4, 4.1, 4.2, 4.2, 4.5.5, 5.4.5, 6.1, 6.1, 6.2.4, 7.1

F. E. Heredia, S. M. Spearing, T. J. Mackin, M. Y. He, A. G. Evans, P. Mosher, and P. Brøndsted. Notch effects in carbon matrix composites. *Journal of the American Ceramic Society*, 77(11):2817–2827, 1994. 1.4, 6.1

C. G. Levi, J. Y. Yang, B. J. Dalgleish, F. W. Zok, and A. G. Evans. Processing and performance of an all-oxide ceramic composite. *Journal of the American Ceramic Society*, 81(8):2077–2086, 1998. 1.4

T. J. Mackin, T. E. Purcell, M. Y. He, and A. G. Evans. Notch sensitivity and stress redistribution in three ceramic-matrix composites. *Journal of the American Ceramic Society*, 78(7):1719–1728, 1995. 1.4, 6.1

T. J. Mackin, K. E. Perry, J. S. Epstein, C. Cady, and A. G. Evans. Strain fields and damage around notches in ceramic-matrix composites. *Journal of the American Ceramic Society*, 79(1):65–73, 1996. 1.4

V. A. Kramb, R. John, and L. P. Zawada. Notched fracture behavior of an oxide/oxide ceramic-matrix composite. *Journal of the American Ceramic Society*, 82(11):3087–3096, 1999. 1.4

S. Mall, D. E. Bullock, and J. J. Pernot. Tensile fracture behaviour of fibre-reinforced ceramic-matrix composite with hole. *Composites*, 25(3):237–242, 1994. 1.4

A. G. Evans, J.-M. Domergue, and E. Vagaggini. Methodology for relating the tensile constitutive behavior of ceramic-matrix composites to constituent properties. *Journal of the American Ceramic Society*, 77(6):1425–1435, 1994. 1.4, 6.1

B. N. Cox and F. W. Zok. Advances in ceramic composites reinforced by continuous fibers. *Current Opinion in Solid State and Materials Science*, 1(5):666–673, 1996. 1.4

R. Talreja. Continuum modelling of damage in ceramic matrix composites. *Mechanics of Materials*, 12(2):165–180, 1991. 1.4, 7.1, 7.2.1

G. Camus. Modelling of the mechanical behavior and damage processes of fibrous ceramic matrix composites: Application to a 2-D SiC/SiC. *International Journal of Solids and Structures*, 37(6):919–942, 2000. 1.4, 6.3.1, 6.3.4, 6.4.6, 6.4, 7.1

J. L. Chaboche and J. F. Maire. New progress in micromechanics-based CDM models and their application to CMCs. *Composites Science and Technology*, 61 (15):2239–2246, 2001. 1.4, 7.1

H. T. Hahn. Nonlinear behavior of laminated composites. *Journal of Composite Materials*, 7(2):257–271, 1973. 1.4, 6.1, 6.3.1, 6.3.3, 6.3.3, 7.1

R. M. Jones. Analysis of nonlinear stress-strain behavior of fiber-reinforced composite materials. *Journal of Aircraft*, 15(12):1669–1676, 1977. 1.4

R. S. Sandhu. Nonlinear behavior of unidirectional and angle ply laminates. *Journal of Aircraft*, 13(2):104–111, 1976. 1.4

M. D. Thouless and A. G. Evans. Effects of pull-out on the mechanical properties of ceramic-matrix composites. *Acta Metallurgica*, 36(3):517–522, 1988. 2.1

S. L. Phoenix. Statistical issues in the fracture of brittle-matrix fibrous composites. *Composites Science and Technology*, 48:65–80, 1993. 2.1

W. A. Curtin, B. K. Ahn, and N. Takeda. Modeling brittle and tough stress-strain behavior in unidirectional ceramic matrix composites. *Acta Materialia*, 46(10):3409–3420, 1998. 2.1

W. A. Curtin. Stochastic damage evolution and failure in fiber-reinforced composites. volume 36 of *Advances in Applied Mechanics*, pages 163–253. Elsevier, 1998. 2.1

M. Ibnabdeljalil and W. A. Curtin. Strength and reliability of fiber-reinforced composites: localized load-sharing and associated size effects. *International Journal of Solids and Structures*, 34(21):2649–2668, 1997. 2.1, 2.4

J. M. Neumeister. Bundle pullout: a failure mechanism limiting the tensile strength of continuous fiber reinforced brittle matrix composites and its implications for strength dependence on volume and type of loading. *Journal of the Mechanics and Physics of Solids*, 41(8):1405–1424, 1993. 2.1, 2.4

R. E. Bullock. Strength ratios of composite materials in flexure and in tension. *Journal of Composite Materials*, 8(2):200–206, 1974. 2.1

J. M. Whitney and M. Knight. The relationship between tensile strength and flexure strength in fiber-reinforced composites. *Experimental Mechanics*, 20 (6):211–216, 1980. 2.1

P. S. Steif and A. Trojnacki. Bend strength vs. tensile strength of fiber-reinforced ceramics. *Journal of the American Ceramic Society*, 77(1):221–229, 1994. 2.1, ii

H. L. Cox. The elasticity and strength of paper and other fibrous materials. *British Journal of Applied Physics*, 3(3):72–79, 1952. 2.2.1

A. G. Evans and F. W. Zok. The physics and mechanics of fibre-reinforced brittle matrix composites. *Journal of Materials Science*, 29(15):3857–3896, 1994. 2.2.2, 6.1

J. M. Hedgepeth and P. van Dyke. Local stress concentrations in imperfect filamentary composite materials. *Journal of Composite Materials*, 1(3):294–309, 1967. 2.4

H. Tada, P. C. Paris, and G. R. Irwin. *The stress analysis of cracks handbook*. Paris Productions Inc., St. Louis, Missouri, 2nd edition, 1985. 2

Z. Hashin and B. W. Rosen. The elastic moduli of fiber-reinforced materials. *Journal of Applied Mechanics*, 31(2):223–232, 1964. 3.1, 3.4.1, 3.4.2, B

E. Totry, J. M. Molina-Aldareguìa, C. González, and J. LLorca. Effect of fiber, matrix, and interface properties on the in-plane shear deformation of carbon-fiber reinforced composites. *Composites Science and Technology*, 70(6): 970–980, 2010. 3.3.1

P. Suquet. Elements of homogenization theory for inelastic solid mechanics. In E. Sanchez-Palencia and A. Zaoui, editors, *Homogenization Techniques for Composite Media*, pages 194–275. Springer-Verlag, Berlin, 1987. 3.3.2

Z. Xia, Y. Zhang, and F. Ellyin. A unified periodical boundary conditions for representative volume elements of composites and applications. *International Journal of Solids and Structures*, 40(8):1907–1921, 2003. 3.3.2, 3.5.2

Z. Hashin. Analysis of composite materials—A survey. *Journal of Applied Mechanics*, 50(3):481–505, 1983. 3.4.2, B

R. B. Pipes and N. J. Pagano. Interlaminar stresses in composite laminates under uniform axial extension. *Journal of Composite Materials*, 4(4):538–548, 1970. 3.8, 3.8

R. Hill. A general theory of uniqueness and stability in elastic-plastic solids. *Journal of the Mechanics and Physics of Solids*, 6:239–249, 1958. 4.4.1

Z. P. Bažant and L. Cedolin. *Stability of Structures: Elastic, Inelastic, Fracture and Damage Theories*. World Scientific Publishing Co. Pte. Ltd., Singapore, 2010. 4.4.1

G. Maier and T. Hueckel. Nonassociated and coupled flow rules of elastoplasticity for rock-like materials. *International Journal of Rock Mechanics and Mining Sciences*, 16(2):77–92, 1979. 4.4.1

D. Bigoni and T. Hueckel. Uniqueness and localization – I. Associative and non-associative elastoplasticity. *International Journal of Solids and Structures*, 28(2):197–213, 1991. 4.4.1, 4.4.1

Z. P. Bažant. Comment on orthotropic models for concrete and geomaterials. *Journal of Engineering Mechanics*, 109(3):849–865, 1983. 4.5.1, 4.5.1

S. W. Sloan, A. J. Abbo, and D. Sheng. Refined explicit integration of elastoplastic models with automatic error control. *Engineering Computations*, 18 (1/2):121–154, 2001. 4.6.1, 6.5.2

H. Neuber. Theory of stress concentration for shear-strained prismatical bodies with arbitrary nonlinear stress-strain law. *Journal of Applied Mechanics*, 28(4): 544–550, 1961. 5.1, 5.3.1, 5.3.1

J. A. Heathcote, X.-Y. Gong, J. Y. Yang, U. Ramamurty, and F. W. Zok. In-plane mechanical properties of an all-oxide ceramic composite. *Journal of the American Ceramic Society*, 82(10):2721–2730, 1999. 5.1

C. S. Lynch and A. G. Evans. Effects of off-axis loading on the tensile behavior of a ceramic-matrix composite. *Journal of the American Ceramic Society*, 79(12): 3113–3123, 1996. 5.2.1

G. M. Genin and J. W. Hutchinson. Failure at attachment holes in brittle matrix laminates. *Journal of Composite Materials*, 33(17):1600–1619, 1999. 5.2.2

G. Agnihotri. Calculation of elastic-plastic strains and stresses in notches under torsion load. *Engineering Fracture Mechanics*, 51(5):823–835, 1995. 5.3.1, 5.3.2

W. Guo, C. H. Wang, and L. R. F. Rose. *Elastoplastic analysis of notch-tip fields in strain hardening materials*. Report DSTO-RR-0137, DSTO Aeronautical and Maritime Research Laboratory, Melbourne, Victoria, 1998. 5.3.1, 5.3.2, 5.4.2, 5.4.5

Y. Jiang and B. Xu. Deformation analysis of notched components and assessment of approximate methods. *Fatigue and Fracture of Engineering Materials and Structures*, 24(11):729–740, 2001. 5.3.1

A. Moftakhar, A. Buczynski, and G. Glinka. Calculation of elasto-plastic strains and stresses in notches under multiaxial loading. *International Journal of Fracture*, 70(4):357–373, 1995. 5.3.1, 5.4.5

Z. Zeng and A. Fatemi. Elasto-plastic stress and strain behaviour at notch roots under monotonic and cyclic loadings. *The Journal of Strain Analysis for Engineering Design*, 36(3):287–300, 2001. 5.3.1, 5.4.5

G. Härkegård and T. Mann. Neuber prediction of elastic-plastic strain concentration in notched tensile specimens under large-scale yielding. *Journal of Strain Analysis for Engineering Design*, 38(1):79–94, 2003. 5.3.1

G. Glinka. Calculation of inelastic notch-tip strain-stress histories under cyclic loading. *Engineering Fracture Mechanics*, 22(5):839–854, 1985. 5.3.2, 5.4.5

G. R. Irwin. Plastic zone near a crack and fracture toughness. In *Proceedings of the Seventh Sagamore Conference*, pages IV–63, 1960. 5.3.2

J. R. Rice. *Mechanics of crack tip deformation and extension by fatigue*, pages 247–311. American Society for Testing and Materials, Philadelphia, PA, 1967. 5.4.1

M. Zappalorto and P. Lazzarin. Analytical study of the elastic-plastic stress fields ahead of parabolic notches under antiplane shear loading. *International Journal of Fracture*, 148(2):139–154, 2007. 5.4.1

Q. Yang and B. Cox. Cohesive models for damage evolution in laminated composites. *International Journal of Fracture*, 133(2):107–137, 2005. 5.4.4

K. S. Chan, M.-Y. He, and J. W. Hutchinson. Cracking and stress redistribution in ceramic layered composites. *Materials Science and Engineering A*, 167(1/2): 57–64, 1993. 5.4.4

K. Molski and G. Glinka. A method of elastic-plastic stress and strain calculation at a notch root. *Materials Science and Engineering*, 50(1):93–100, 1981. 5.4.5

M. Hoffman and T. Seeger. A generalised method for estimating multiaxial elastic-plastic notch stresses and strains, part I: Theory. *Journal of Engineering Materials and Technology*, 107(4):250–254, 1985. 5.4.5

D. F. Adams and D. E. Walrath. Current status of the Iosipescu test method. *Journal of Composite Materials*, 21(6):494–507, 1987. 6.2.2

M. Grédiac, F. Pierron, and A. Vautrin. The Iosipescu in-plane shear test applied to composites: A new approach based on displacement field processing. *Composites Science and Technology*, 51(3):409–417, 1994. 6.2.3, 6.2.3

J. Morton, H. Ho, M. Y. Tsai, and G. L. Farley. An evaluation of the Iosipescu specimen for composite materials shear property measurement. *Journal of Composite Materials*, 26(5):708–750, 1992. 6.2.3

F. Pierron. Saint-Venant effects in the Iosipescu specimen. *Journal of Composite Materials*, 32(22):1986–2015, 1998. 6.2.3

R. M. Christensen and K. H. Lo. Solutions for effective shear properties in three phase sphere and cylinder models. *Journal of the Mechanics and Physics of Solids*, 27(4):315–330, 1979. 6.2.4, B, B

R. M. Christensen. A critical evaluation for a class of micro-mechanics models. *Journal of the Mechanics and Physics of Solids*, 38(3):379–404, 1990. 6.2.4, B

X. Aubard. *Mechanical Behaviour Models of 2-D SiC-SiC Composites*. PhD thesis, University of Paris VI, France, 1992. 6.3.1

V. P. Rajan, M. N. Rossol, and F. W. Zok. Optimization of digital image correlation for high-resolution strain mapping of ceramic composites. *Experimental Mechanics*, 52(9):1407–1421, 2012. 6.5.4

Z. Suo, S. Ho, and X. Gong. Notch ductile-to-brittle transition due to localized inelastic band. *Journal of Engineering Materials and Technology*, 115(3):319–326, 1993. 6.5.4

J. M. Whitney and R. J. Nuismer. Stress fracture criteria for laminate composites containing stress concentrations. *Journal of Composite Materials*, 8(3): 253–265, 1974. 6.5.4

J. Awerbuch and M. S. Madhukar. Notched strength of composite laminates: Predictions and experiments—a review. *Journal of Reinforced Plastics and Composites*, 4(1):3–159, 1985. 6.5.4

B. N. Cox and Q. D. Yang. In quest of virtual tests for structural composites. *Science*, 314(5802):1102–1107, 2006. 7.2.1

G. T. Camacho and M. Ortiz. Computational modelling of impact damage in brittle materials. *International Journal of Solids and Structures*, 33(20–22):2899–2938, 1996. 7.2.1

G. Ruiz, A. Pandolfi, and M. Ortiz. Three-dimensional cohesive modeling of dynamic mixed-mode fracture. *International Journal for Numerical Methods in Engineering*, 52(1–2):97–120, 2001. 7.2.1

M.-Y. He and J. W. Hutchinson. Kinking of a crack out of an interface. *Journal of Applied Mechanics*, 56(2):270–278, 1989. 7.2.1

J. P. Parmigiani and M. D. Thouless. The roles of toughness and cohesive strength on crack deflection at interfaces. *Journal of the Mechanics and Physics of Solids*, 54(2):266–287, 2006. 7.2.1

N. Moës and T. Belytschko. Extended finite element method for cohesive crack growth. *Engineering Fracture Mechanics*, 69(7):813–833, 2002. 7.2.1

S. Mariani and U. Perego. Extended finite element method for quasi-brittle fracture. *International Journal for Numerical Methods in Engineering*, 58(1):103–126, 2003. 7.2.1

X.-P. Xu and A. Needleman. Numerical simulations of fast crack growth in brittle solids. *Journal of the Mechanics and Physics of Solids*, 42(9):1397–1434, 1994. 7.2.1

M. E. Walter, G. Ravichandran, and M. Ortiz. Computational modeling of damage evolution in unidirectional fiber reinforced ceramic matrix composites. *Computational Mechanics*, 20(1–2):192–198, 1997. 7.2.1

C. Tang, M. A. Sheikh, and D. R. Hayhurst. Finite element modeling of transverse deformation in representative volume elements of ceramic matrix composites (cmcs). *Journal of Multiscale Modelling*, 2(1–2):107–126, 2010. 7.2.1

J. W. Hutchinson and H. M. Jensen. Models of fiber debonding and pullout in brittle composites with friction. *Mechanics of Materials*, 9(2):139–163, 1990. 7.2.1

M. Ibnabdeljalil and W. A. Curtin. Strength and reliability of notched fiber-reinforced composites. *Acta Materialia*, 45(9):3641–3652, 1997. 7.2.2

W. A. Curtin and R. E. Miller. Atomistic/continuum coupling in computational materials science. *Modelling and Simulation in Materials Science and Engineering*, 11(3):R33–R68, 2003. 7.2.2

Z. Hashin. Analysis of properties of fiber composites with anisotropic constituents. *Journal of Applied Mechanics*, 46(3):543–550, 1979. B, B